IMPROVED MATHEMATICAL MODELS AND DYNAMIC ANALYSIS OF LIGHT ROTOR-BEARING SYSTEMS UNDER UNBALANCE AND STOCHASTIC EXCITATION

Emam Ahmed Hashish

A Thesis

in

The Faculty

of

Engineering

and

Computer Science

Presented in Partial Fulfillment of the Requirements
for the degree of Doctor of Philosophy at
Concordia University
Montreal, Quebec, Canada

February 1981

TO MY PARENTS

ABSTRACT

IMPROVED MATHEMATICAL MODELS AND DYNAMIC ANALYSIS OF LIGHT ROTOR-BEARING SYSTEMS UNDER UNBALANCE AND STOCHASTIC EXCITATION

E. Hashish, Ph.D.
Concordia University, 1981

Detailed stability analysis and accurate evaluation of the response of light rotor-bearing systems are presented using improved mathematical models for both the rigid and the flexible states of the rotor. The nonlinear stiffness and damping of the finite bearing are specified through a numerical approach maintaining a practical treatment for the cavitation boundaries and leading to decoupled equations of motion from the hydrodynamic pressure equation. Using both linear and nonlinear approaches, modified stability boundaries are defined and further details about the nonlinear behaviour are obtained.

The equations of motion for the general case of flexible rotor-bearing are assembled using the finite element method and taking into account the gyroscopic moments, the rotary inertia, the shear deformation, the internal damping and the bearing support flexibility preserving the dimensions of the constructed system to a minimum. General modal analysis is applied on the nonsymmetric dynamical systems for the evaluation of both the deterministic and stochastic responses. Error bounds for justification of the linearized rotor-bearing system are provided in a chart form and comparisons with previous studies are made. An application of the present analysis on a grinding machine spindle wheel system is carried out with a new emphasis on the definition of rotor rigidity.

ACKNOWLEDGMENTS

The author expresses sincerest appreciation to his supervisor Dr. T.S. Sankar for his guidance and encouragement in the course of the work reported in this thesis. The author is also grateful to the thesis co-supervisor Dr. M.O.M. Osman for his valuable help and discussion.

Helpful review and discussion of the work by Dr. J.S. Rao is greatly appreciated. Thanks are also due to A. Carbone for his help and to Mrs. I. Crawford and Mrs. L. Saab for typing the manuscript of the thesis.

The financial support provided by the Department of Mechanical Engineering of Concordia University and the Natural Sciences and Engineering Research Council of Canada is gratefully acknowledged.

TABLE OF CONTENTS

LIST OF FIGURES

LIST OF TABLES

NOMENCLATURE

A	Cross sectional area of a beam element
$[A_g]$	Matrix in an algebraic system
$[A_\ell]$	Matrix in linearized bearing equations
A_n, B_n	Coefficients of Fourier harmonic series
B_{ij}	Coefficients in eccentricity functions
c	Radial clearance
c_b	Damping coefficient of bearing support
$[c_s]$	Damping matrix of a system of second order equations
$c_{xx}, c_{xy}, \ldots$	Damping coefficients in the linearized bearing equation
c_d	coefficients of internal viscous damping
$C_{XX}, C_{XY}, \ldots$	Nonlinear damping functions
d	Journal diameter
$[D_d]$	Internal viscous damping matrix of an element, factor of displacements
$[D_h]$	Hysteretic damping matrix of an element
$[D_v]$	Internal viscous damping matrix of an element
$[D_y]$	Dynamic matrix, of order 2N
e	Eccentricity ratio = ε/c
$\dot{e}$	Squeeze velocity
e_o	Static eccentricity ratio
e_r, e_t	Unit vectors in the radial and tangential directions
E	Modulus of elasticity

$E_1, E_2, \ldots E_6$	Eccentricity functions
F_c, f_c	Mean and random cutting forces
F_r, F_t	Radial and tangential film forces
F_X, F_Y	Nonlinear film forces in the X and Y directions
F_x, F_y	Linearized film forces
g_1, g_2	Functions of velocities and displacements
G	L/d
[G]	Gyroscopic matrix of an element
G_s	Modulus of elasticity in shear
$[G_y]$	Gyroscopic submatrix of an element
h	film thickness
H	Dimensionless film thickness
$H(\omega)$	Complex frequency response function
I	Cross sectional transverse moment of inertia
[I]	Unity matrix
J_T, J_z	Lateral and axial mass moments of inertia per unit length
[k]	Stiffness matrix of an element
k_b	Stiffness of a bearing support
$[k_s]$	Stiffness matrix of a system of second order equations
$k_{xx}, k_{xy}, \ldots$	Stiffness coefficients of the linearized bearing equations
[K]	Convential stiffness matrix, of order 2N
K_j^*	jth generalized stiffness
$K_{XX}, K_{XY}, \ldots$	Nonlinear stiffness functions
ℓ	Length of an element

L	Length of the bearing
L_g	Lagrangian
L_p	Liapunov function
m	Journal mass
m_b	Bearing mass
m_z	Mass per unit length of an element
$[M]$	Conventional mass matrix of order 2N
M^*	Axial number of divisions of the developed bearing
M_j^*	jth generalized mass
$[M_{t_1}], [M_{r_1}]$	Submatrices in the translation and rotation mass matrices of an element
M_x, M_y	Flexural bending moments
N	Number of degrees of freedom of a dynamical system
N^*	Number of divisions in θ direction of the developed bearing
N_i, N_{ri}	Shape functions
O_b	Bearing centre
O_j	Journal centre
p	Hydrodynamic pressure distribution
p_1, p_2	Shear and squeeze pressure components
$p_f(f)$	Probability density of the cutting force f_c
p_x, p_y	Distributed forces on the element
P	Potential energy
$\bar{q}$	Vector of phase space variables, of order 2N

$\bar{q}_s$	Displacement vector of a dynamical system, of order N
$\bar{q}^e$	Nodal coordinates of an element
$\bar{Q}^e$	Vector of generalized forces of an element
$\bar{Q}_s$	Global generalized forces, of order N
r	Journal radius
$[R(\tau)]$	Autocorrelation matrix
S	Bearing dynamic parameter, given by equation (2.18a)
S_o	Input spectral density, constant
S_{or}	Sommerfeld number
$[S(\omega)]$	Spectral density matrix
t	Time
T	Kinetic energy
$\bar{u}$	Principle coordinates, of order 2N
$\bar{U}$	Input vector in the principal coordinates, of order 2N
U_n	Unbalance force
U_θ, V_θ	Tangential and radial velocities of a point on the journal in (e_r, e_t)
v_c, v_w, v_h	cross feed, workpiece and grinding wheel velocities
V_x, V_y	Shear forces
W	Applied load
W_n	Dimensionless load = $W/cm\omega_j^2$
x,y	Cartesian coordinates specified from an equilibrium point

z	Dimensionless axial coordinate
z^*	Vector of phase space variables in the non-linear equations
Z	Axial coordinate
Z^*	Nonlinear functions in z^*
α	Angular displacement in the XZ plane
α_j	jth modal damping exponent
β	Angular displacement in the YZ plane
β_ℓ^*	Load angle
β_c	Angle of cutting force
β_j	jth damped natural frequency
γ	Shear coefficient
γ_e	Inclination angle of the major axis of the orbit from the load direction
γ_h	Hysteretic angle
δ_{cj}	jth logarithmic decrement
ε	Eccentricity of the journal centre
η_h	Hysteresis factor
θ	Circumferential coordinates
θ_1, θ_2	Boundary angles of positive pressure
λ_j	jth eigenvalue
μ	Dynamic viscosity
ρ	Coefficient of effective area in shear
τ	Dimensionless time, or time lag in auto-correlation function
ϕ_1, ϕ_2	Dimensionless shear and squeeze pressure components

$\bar{\phi}_j$	jth right eigenvector
ϕ_{sx}, ϕ_{sy}	Shear angles in XZ and YZ planes
ψ	Angle of the line of centres with X direction
$\dot{\psi}$	Whirling speed
$\mathring{\psi}$	Whirling speed ratio = $\dot{\psi}/\omega_j$
$\bar{\psi}_j$	jth left eigenvector
ω	Frequency
ω_j	Journal speed
ω_r	Rotor speed
ω_s	Dimensionless speed

Legend for Figs. 5.11 to 5.15, 6.12, 6.13 and 6.15

Denotation of Mode Shape

E = Even Mode

O = Odd Mode

Denotation of Precession Direction

B = Backward Precession

F = Forward Precession

M = Mixed Precession (Backward/Forward)

CHAPTER 1

INTRODUCTION AND LITERATURE REVIEW

1.1 General Objectives

Light rotor-bearing systems are distinguished with small geometrical configuration and light applied loads. When the operating speeds of such systems are high, they may be located in a rather sensitive stability region where a precise assessment of the stability parameters are vital to the design procedure. In addition, appropriate mathematical modelling and consequently accurate evaluation and control of the system response is also important. In this sense, light rotor-bearings can be seen as the most general case of rotor-bearing system as a whole.

Generally, a rotor-bearing system is flexible and possesses nonlinear characteristics. Special conditions may exist when the rotor may be assumed to be rigid or the non-linear system can be linearized. These special cases may be utilized to simplify the analyses and to obtain results of general nature but with approriate justifications. The applied loads in the case of a light rotor are primarily the external loads which may lead to either even or opposite suspension. Therefore, the dynamic analysis should be of a general nature to accommodate such consequences, with the knowledge that these loads contribute to the stiffness

and damping of the fluid film bearings.

Hydrodynamic film bearings have always been recognized as appropriate suspension supports due to their damping ability. To study the effectivness of these bearings, an accurate modelling of the journal bearing that considers its finite width and still preserves the simplicity of the known approximations for long and short bearing, must be carried out. This is to be followed by a detailed stability analysis, preferably using a nonlinear model, for appropriate emphasis on the details of the regions of stability.

A realistic representation of the rotor itself should include all the secondary effects such as the gyroscopic moments, rotary inerita, shear deformation, internal viscous damping and hysteretic damping, all of which play a significant role particularly at high operating speeds of the rotor. Another practical consideration is to include the flexibility of the bearing support in the machine frame as is done in the present investigation.

An important application of light rotor-bearing analyses is on the grinding machine spindle. An example of surface grinding machine spindle is shown in Fig. 1.1. grinding process is a finish machining operation where the output is a modified surface roughness and is directly related to the machine dynamic performance. This, therefore, demands an accurate evaluation and control of the machine

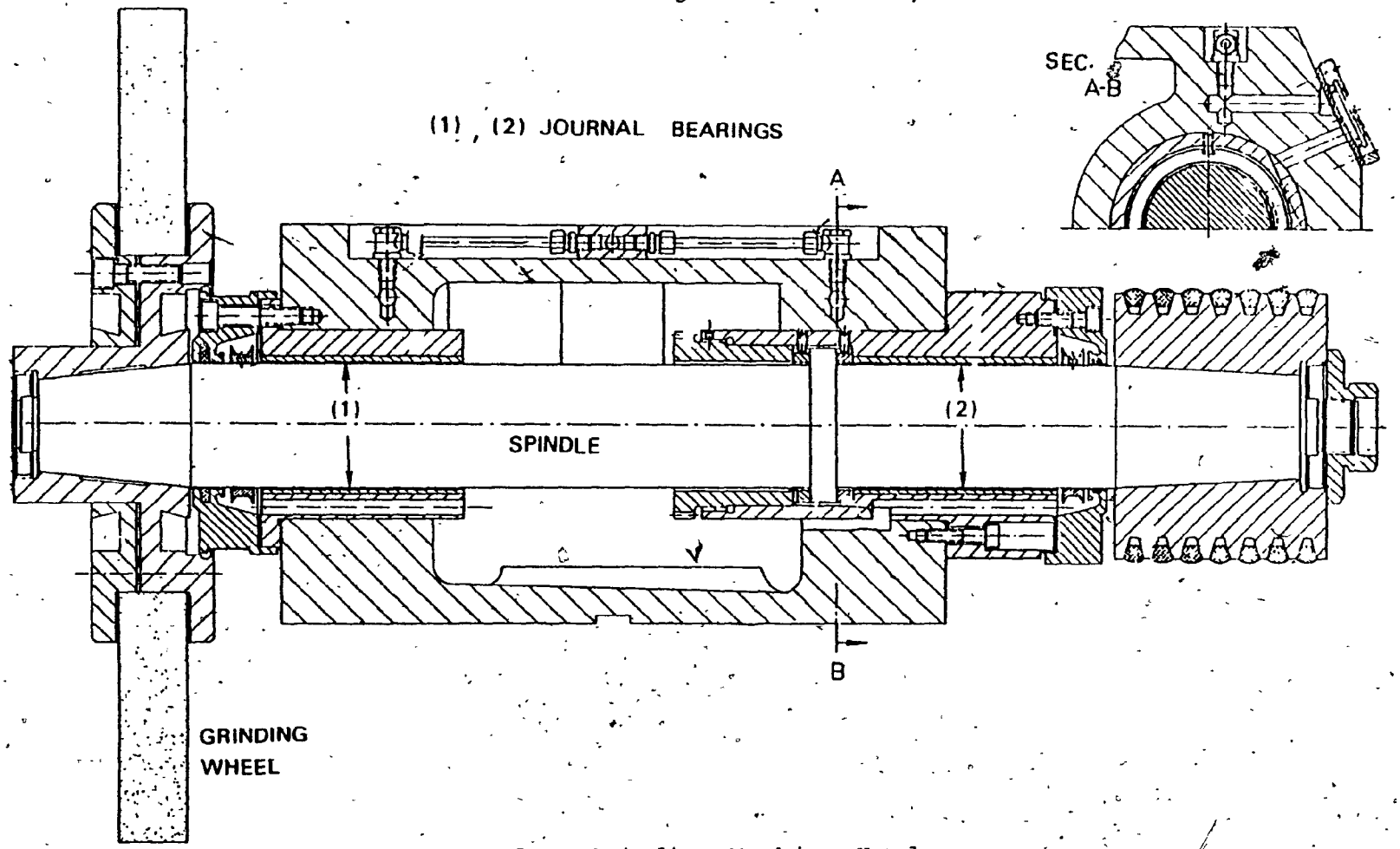

Fig. 1.1 A Surface Grinding Machine Head.
Courtesy: Werkzeugmaschinen Atlas by Prof. W. Schmidt

response and stability which in turn requires appropriate mathematical modelling of the grinding machine under operating conditions to replace the simple and approximate mathematical models that have been used so far. Two types of input to the grinding machine spindle system are of interest which are the unbalance and cutting forces. Cutting forces in general are essentially random in nature and a solution for the stochastic response need to be established with minimum limitations on the statistical description of the random input.

It is then the objective of this investigation to provide an accurate mathematical modelling for the particular case of light rotors under a general form of excitation that includes all the above mentioned details. It is also worthwhile to evolve an effective approach that utilizes the special cases of rotor rigidity and system linearity whenever they can be accommodated without loss of accuracy by further modifying the mathematical modelling techniques and the methods of dynamic analysis for such special conditions.

A literature survey, grouped in a sequence of development of the major work directly applicable to the present investigation, is presented in the next section followed by a brief introduction on the scope of the present investigation.

1.2 Literature Review

The general subject of discussion here is the dynamics of rotor-bearing system in both rigid and flexible conditions. The assumption of rotor rigidity introduces great simplifications in the dynamic analysis and can be considered valid if the rotor running speed is well below its first bending critical speed.* The literature available on all different aspects of the present subject is quite numerous. A representative but covering sufficiently the major contributions in the bibliography are discussed in sections 1.2.1 to 1.2.3.

The first subsection 1.2.1, deals with the bearing element and the dynamic behaviour of rigid rotors. The bearing treated is the plain journal bearing with incompressible fluid film. The various approaches to the mathematical modelling of the hydrodynamic film forces, the treatment of the cavitated film, suitable methods for solving the bearing equations and stability analysis are considered in these publications. The second subsection, 1.2.2 is devoted to the contributions in the area of flexible rotor modelling and response calculations. The final subsection, 1.2.3, covers the literature dealing with the grinding machine cutting forces and evaluation of the stochastic response of the rotor system in such cases.

---

*One main conclusion of this thesis is that the assumption of rotor rigidity is also dependent on the type of input excitation.

1.2.1 The Finite Journal Bearing

The hydrodynamic pressure in a journal bearing is generated due to the relative motion between the journal and bearing surfaces and is given by the well known Reynolds' equation [1]. No analytical solution for the Reynolds' equation in its general dynamic form is available so far in the literature. Most bearing dynamical analyses employ approximate solutions to the Reynolds' equation by considering it in a simplified one-dimensional form. The two approximations for such solutions are namely the assumptions of infinitely long bearing known as the Sommerfeld solution; and the infinitely short bearing, Ocvirk solution [2-4]. Due to their simplicity, these approximations are suitable for certain aspects of dynamic analysis, particularly, the calculation of nonlinear transient response. However, the range of validity of the results for both these approximations is quite limited. The long bearing approximation is suitable for L/d ratio over 2 whereas the short bearing is applicable for L/d ratio less than 1/4. Another approximation, later introduced, utilizes a weighted sum of both the long and short bearing solutions [5].

There are a few analytical solutions to the Reynolds' equation for a full oil film and in the steady state condition of the journal. Hays [6] formulated a solution to the Reynolds' equation in a series expansion form using the variational approach. Under similar assumptions Reynolds'

equation was also solved using the method based on the separation of variables [7-11]. All these solutions involve minor numerical computations and series truncation.

Two of the approaches, using the method of separation of variables, are of particular interest in bearing dynamic analysis, since they accommodate a general journal motion [12,13]. The first is due to Warner [12] who introduced a compensation to the long bearing approximation by an end leakage factor. Recently, Barrett, Allaire and Gunter [13] introduced another solution which is essentially a correction to the short bearing solution extending its validity up to a value of $L/d = 1.25$. More recently the validity of solutions based on the separation of variables were questioned by Day [14] who found that such solutions are limited to special cases of the shape of the film thickness.

Another approach for evaluating the hydrodynamic pressure in a journal bearing, is through numerical solutions. There is no difficulty in solving the Reynolds' equation in the steady state condition for the purpose of bearing design [15], or around an equilibrium point for the evaluation of linearized stiffness and damping coefficients [16,17]. The finite difference method was used in [15-17] and the finite element method was applied to the lubrication problem [18-21]. Through an effective use of the variational principles, the finite element approach has become an attractive method with the combination of ease and fast convergence towards an

accurate solution. For dynamic investigations, integrating the equation of motion of the journal while simultaneously solving the Reynolds' equation [22], is recognized to be very heavy on computation time [23,24]. Such an approach is associated with a compromise on the integration step size or on the required solution duration, namely the number of cycles, which negates the advantages of a finite bearing consideration.

In practice, the oil film is cavitated due to its negligible tensile strength. Studies on cavitation in thin oil film [25-38] present a well defined film boundary in the steady state condition and emphasized the kinematic nature of the cavity. If such a detailed treatment is extended to the dynamic case, the whole process will then be on an instantaneous basis and must have to be repeated for every time step which is quite impractical. However, experimental evaluations on the film extent in the general dynamic case is not as well defined as that in the steady state. The observations on the nature of cavitation [26] can still serve as a base for developing appropriate mathematical or analytical hypothesis.

Once the equation of motion is constructed, the analysis following it branches to a quantitative type for response calculations and a qualitative type for stability analysis. The quantitative analysis includes a variety of approaches such as perturbation technique [39], analog integration [4, 40], numerical integration using various

methods [22,24,40,51] and kinematics simulation in phase space [41]. Due to scaling difficulties in analog solutions [4,40] and because of the advances in digital computing equipment, digital computations present the most efficient approach, whereas other approximate analytical solutions such as in the vicinity of limit cycle region [39] are good only for getting some general design results.

The qualitative aspect of the dynamic analysis is concerned with defining the stability characteristics of the journal motion. Linear stability analysis using Routh-Hurwitz criterion provides general results in the dynamic range where the linear approximation for the system remains acceptable. Using linear analysis, the full film bearing is found unstable for all values of the bearing parameters whereas the partial film (cavitated film) bearing is associated with a stable region [42-44]. These results were obtained using the long bearing approximation by Reddi and Trumpler [42], extended for the finite bearing by Holmes [43] and modified by Badgley and Booker [44] using short, long and Warner's finite bearing. Badgley and Booker [44] included nonlinear stability analysis in their study which is executed by integrating the nonlinear equations of the journal numerically. Stability boundary lines for different L/d ratios in [43,44] intersected with each other in several places which is an inappropriate trend that can not be supported by physical or mathematical reasons.

Nonlinear stability analysis included, besides numerical

integration of the equation of motion, examining approximate analytical solution of the equation of motion using perturbation methods [39,45] and Liapunov direct method [46]. Liapunov direct method is often regarded as the general method for stability, but no such general results are evident in [46] that are to be expected from such analysis.

1.2.2 Flexible Rotor-Bearing System

Modelling methods for flexible rotor-bearing system is reviewed in a report by Eshleman [47] mainly dealing on critical speed and response calculations along with a historical background that included the very early work in rotor dynamics. However, a review on the modelling approaches for flexible rotor-bearing system is provided here with an emphasis on the recent literature and as an extension of [47].

A first approximation to a rotor-bearing system is a single mass rotor with massless flexbile shafts. This simple treatment allows the extraction of certain general results and conclusions. Utilizing the above simple approximation Gunter [48,49], who also provided an excellent background and discussion on the nonsynchronous whirl in rotor-bearing systems, found that support flexibility and damping improve the rotor stability and demonstrated how two similar rotors that incorporate shrink fits may vary in their onset speeds of instability. Vance and Lee [50] extended the above study by considering a different type of external damping such as air drag which is not necessarily parallel to the support

flexibility and defined the possibility of a rotor operating above the significant critical speed. Simple flexible rotor-bearing models lack the accuracy in response calculations and are not versatile enough for details other than just general conclusions.

A direct detailed treatment of a rotor-bearing system is done by multimass section modelling of the rotor beam using the flexibility influence coefficients and including the gyroscopic moments, rotary inertia, bearing nonlinear stiffness and damping [51,52]. Lund and Orcutt [53] modified the Prohl-Myklestad method, which is a transfer matrix approach for obtaining the natural frequencies, to allow for the distributed parameters in shaft sections. This transfer matrix method is then made to suit steady state response calculations such as unbalance response and found to produce results in good agreement with the experimental observations [53]. The transfer matrix method has also been used in modal analysis for calculating the damped natural frequencies and the associated natural modes [54-56]. This particular method has the advantage of small computer memory requirements, but the equations of motion using such a procedure are not explicitly written and it was found in [53] that accurate unbalance response calculation using transfer matrix method requires a number of rotor stations that are 4 to 5 times the highest anticipated natural frequency. Large numbers of such solutions are associated with numerical instabilities [56] and therefore the choice

of the number of stations must be made with some compromise.

The finite element method is a relatively recent method to be applied on rotor-bearing systems. The output of the finite element application on a rotor-bearing system is an explicitly written general dynamic system independent of prespecifying the input excitation. Additional details such as bearing support flexibility can be accounted for easily in the finite element formulation. Ruhl and Booker [57] carried a comparison between the finite element method and the Prohl method with a discrete system formulation. The lumped mass stations in a discrete formulation must be many times the number of elements in a finite element formulation to achieve the same accuracy in response results and further the number of finite elements needed only to exceed the highest anticipated critical by just one [57]. The finite element formulation can also account for shear deformation in the system [58-61] as applied specifically on rotor dynamics by Rouch and Kao [62,63].

Implementing shear deformation can be by either a simple Timoshenko beam element [58,60,61] in which only the shape functions over the element are modified or through incorporating additional variables to account for the shear angle. As demonstrated by Thomas et al [59], a proper representation for the simple Timoshenko beam [58,60,61] produces results with negligible deviation as compared to the more sophisticated 12 nodal variable element [59,62,63].

The extra variables per element lead to a larger global dynamic system and may demand the use of a reduction process which requires the stiffness matrix to be symmetric [63]. The reduction technique also increases the system potential energy and consequently the estimate of critical speeds and the system response. But the finite element procedure already generates an upper bound estimate to the exact solution since the method approaches the solution from the high side [57]. Therefore the advantage of incorporating a higher order dynamical system is countered by a loss in accuracy in the form of getting a higher estimate to the system output, if a reduction technique is used.

Other finite element simulations of a rotor-bearing system taking the rotary inertia, axial load [64] and internal damping [65] into account besides the gyroscopic moment, were considered in the previous studies, but they ignored the shear deformation. Although the neglect of shear deformation simplifies the finite element procedures significantly, this must be taken into account for a thick beam where the diameter to the length ratio of the element is not negligible and when higher modes are encountered [59].

1.2.3 The Grinding Machine and the Grinding Process

Grinding operation is correlated with various operational parameters [66] with the cutting forces being random in nature [67,68]. Therefore the system has to be investigated using probabilistic techniques. Dynamic analysis of

grinding machines still employ simple model for the machine head where the spindle is considered essentially as a rigid body [69]. This approach can only be considered as a simple first approximation.

Application of stochastic analysis to rotor-bearing problems is scarce. Using a simple 3 mass model to represent rotor, the bearing and the housing, the bearings performance is studied for axially applied random excitation in [70]. Sankar and Osman [71] modelled a general machine tool spindle into a simple one degree-of-freedom system in a study of the spindle response to the randomly varying cutting forces. The response solution is determined using the Fokker-Planck technique for stationary and nonstationary excitations. Such basic approaches are valuable for extracting rough estimates of the machine dynamic behaviour under probabilistic considerations and in these cases where solutions to the more extensive and complex mathematical models are not possible through available techniques. A comprehensive stochastic analysis on a flexible rotor-bearing system is carried out by Lund [72] using a transfer matrix technique. This approach is extended in the present analysis to a general dynamic system which is the output of the finite element formulation.

1.3 Scope of the Present Investigation

The objective of the present study is to provide accurate, yet simple, mathematical models for rigid and

flexible rotor-bearing systems. Through such improved modelling of the rotor-bearing system, it is attempted later to provide a reasonable accurate assessment of the system stability and response when under deterministic and stochastic input forces.

In Chapter 2, improved mathematical models for finite bearing with partial film profiles are developed. A sequence of decomposition of the pressure equation into different components, rearranging the equations in terms of dimensionless pressure forms, description of an efficient solution using the finite element technique, curve fitting with a proper polynomial form and finally an appropriate setting of the partial film, are described. A comparison of the present results with past experimental and recent theoretical work is also carried out.

Chapter 3 commences with a comment on different numerical intregration techniques followed by a comparison of the present finite bearing with previous experimental results for the full film case. Then a stability analysis is carried out using both the linearized and nonlinear system of equations of motion and an appropriate numerical technique.

In Chapter 4, the linearized equations for the finite bearing is solved by modal analysis method. Fundamental parameters, for a rigid symmetric rotor are valuable in design but never available before, such as the damped natural frequencies and complex frequency response, are evaluated.

The complex frequency response is particularly important for later calculations of the system's stochastic response. Error analysis on the deviation of the solution based on linearized system from the corresponding solution of the original nonlinear one is discussed and charts for such error estimation are constructed and presented.

In Chapter 5, a flexible rotor-bearing system is simulated in detail using the finite element technique. The mathematical model takes into account the gyroscopic moment, rotary inertia, shear deformation, internal viscous damping, hysteretic damping, linear as well as nonlinear stiffness and nonlinear damping for the finite bearing and bearing support flexibility. Modal analysis procedure for such a general nonsymmetric system are emphasized. A comparison with previous experimental and theoretical work is presented. A comparison between two distinctive types of support flexibility namely bearing support flexibility and Hertzian contact flexibility is also carried out.

Chapter 6 is devoted to the application of this rotor dynamic analysis on the grinding machine. The random cutting forces are represented as the stochastic input and a solution by modal analysis is outlined. At this point in Chapter 6, the four mathematical models previously developed are summarized. Depending on the spindle rigidity and running speed, the choice of rigid or flexible rotor treatments of the problem can be made. Also the size of the journal orbit

in the hydrodynamic bearing determines which of the linear or the nonlinear analysis is appropriate (the nonlinear behaviour, as considered here, is only due to the film bearing). However, a solution for the stochastic problem is provided for only the linearized system that is rigid or flexible. An application of flexible rotor with finite bearing is carried out on a grinding machine spindle and the response of the system to unbalance and random excitation is determined.

Conclusions on the overall contributions of this investigation, a summarized version of the discussion of the results and comparisons are presented in Chapter 7 as well as recommendations for future work. This is followed by an extensive bibliography that contributed to the development of this work. Finally, the different details that are necessary for the completion and understanding of the presentation are separately presented in Appendices at the end of the thesis.

CHAPTER 2

EQUATIONS OF MOTION OF THE FULL AND THE PARTIAL FILM FINITE BEARING

2.1 Background

In this part of the study, a simple but an efficient approach is followed to evaluate the hydrodynamic forces of a finite bearing in a form that combines the accuracy of taking into account the bearing finite width yet the simplicity of the short and long bearing approximations. The hydrodynamic pressure forces are generated in the fluid film between the surfaces of the journal and the bearing due to the relative motion between surfaces. These hydrodynamic forces are the outcome of integration of the shear and normal pressure distributions as given by the Reynolds' equation [1]. In reality the fluid film is partially ruptured. In the present study, the evaluation of the hydrodynamic pressure forces for such a practical case, for any general journal motion, begins with the evaluation of the full film hydrodynamic forces. Later the full film forces will be used, in part, for the evaluation of the partial film forces. The hydrodynamic pressure equation, known as the Reynolds' equation, is derived from the Navier-Stokes equation under the assumption that:

i) the flow is laminar,

ii) the body force of the oil film is negligible,

iii) the radius of curvature of the moving surfaces is large as compared to the film thickness,

iv) the pressure across the oil film in the radial direction is invariant,

and for incompressible fluid film this equation can be written as [1,12]

$$\frac{1}{r^2}\frac{\partial}{\partial\theta}\left(\frac{h^3}{12\mu}\frac{\partial p}{\partial\theta}\right)+\frac{\partial}{\partial z}\left(\frac{h^3}{12\mu}\frac{\partial p}{\partial z}\right)=\frac{1}{2r}\frac{\partial}{\partial\theta}(U_\theta h)-V_\theta \qquad (2.1)$$

where μ is the oil viscosity, U_θ and V_θ are the tangential and normal velocities respectively of a point on the journal at an angle θ from the line of centers O_jO_b as seen in Fig. 2.1. The velocities U_θ and V_θ are viewed from the rotating coordinates e_t, e_r as can be seen from the diagram and are given by the relations

$$\begin{aligned} U_\theta &= r\omega_j + \varepsilon\dot{\psi}\cos\theta - \dot{\varepsilon}\sin\theta \\ V_\theta &= \varepsilon\dot{\psi}\sin\theta + \dot{\varepsilon}\cos\theta \end{aligned} \qquad (2.2)$$

where $\dot{\psi}$ is the whirling speed. The film thickness h in equation (2.1) is given by

$$h = c - \varepsilon\cos\theta \qquad (2.3)$$

which is an approximated relation obtained by assuming ε/r to be negligible [1].

The radial and tangential film forces F_r and F_t are

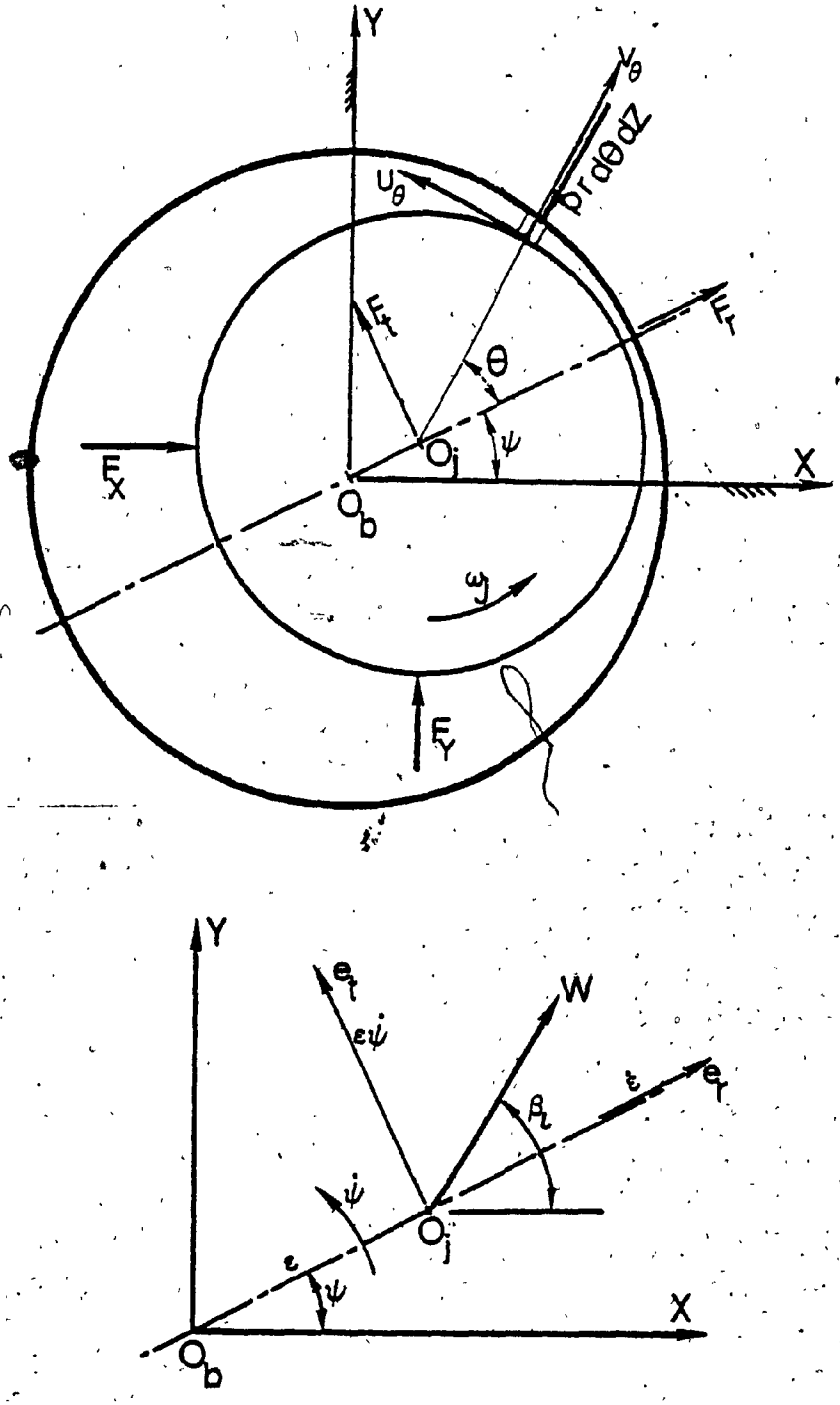

Fig. 2.1 Journal Bearing Coordinate System.

evaluated by integrating the pressure p and are

$$F_r = -r \int_{\theta_1}^{\theta_2} \int_0^L p \cos\theta \; dZd\theta$$

$$F_t = -r \int_{\theta_1}^{\theta_2} \int_0^L p \sin\theta \; dZd\theta \qquad (2.4)$$

where θ_1 and θ_2 define the pressure boundaries in the circumferential direction. In general, the angles θ_1 and θ_2 are functions of the journal displacements and velocities. For the case of full film and including the negative pressure, the angles θ_1 and θ_2 take the values

$$\theta_1 = 0 \qquad \theta_2 = 2\pi$$

Once the hydrodynamic forces are evaluated, the journal equations of motion in the x direction can be written as

$$m\bar{a}_x = \bar{F}_x + \bar{W}_x \qquad (2.5)$$

where m is the journal mass, a_x is the journal acceleration in the x direction, W_x is the applied load and F_x is the hydrodynamic force given by

$$F_x = F_r \cos\psi - F_t \sin\psi \qquad (2.6)$$

Similarly the y directional equation can be written with

$$F_Y = F_r \sin\psi + F_t \cos\psi \qquad (2.7)$$

The evaluation of the radial and tangential hydrodynamic forces F_r and F_t, are, therefore, the basis for constructing the journal equations of motion. The evaluation of the integrals in equation (2.4) is the main aspect under study in the following parts.

2.2 Rearrangement of Reynolds' Equation

For the plain journal bearing that is under consideration, the Reynolds' equation is solved under the following assumptions:

i) The viscosity μ is invariant over time and space.

ii) The journal and bearing axes are parallel.

iii) The supply pressure is negligible in comparison to the hydrodynamic pressure.

Introducing the nondimensional quantities

$$z = Z/L$$

$$H = h/c = 1 - e\cos\theta$$

$$G = L/d$$

into equation (2.1), substituting expressions for U_θ and V_θ from equation (2.2) into equation (2.1), expanding the right hand side, neglecting terms of the order c/d less than other terms and using the linearity of Reynolds' equation for the present incompressible case, equation (2.1) can be shown to take the following decomposed form

$$\frac{\partial}{\partial\theta}\left(H^3\frac{\partial\phi_i}{\partial\theta}\right)+\left(\frac{l}{2G}\right)^2\frac{\partial}{\partial z}\left(H^3\frac{\partial\phi_i}{\partial z}\right)=f_i(\theta) \qquad (2.8)$$

with

$$\phi_i=\left(\frac{c}{d}\right)^2\frac{l}{\mu}\frac{p_i}{g_i} \quad , \quad i=1,2$$

$$f_1(\theta)=\frac{3}{2}\,e\,\sin\theta$$

$$f_2(\theta)=-3\,\cos\theta$$

$$g_1=\omega_j-2\dot{\psi}$$

$$g_2=\dot{e}$$

Here p_1 is the shear or wedge pressure component and p_2 is the squeeze pressure component. It may also be noted that ϕ_1 and ϕ_2 are the nondimensional shear and squeeze pressure components. The two nondimensional parameters G and e are the only quantities that are needed to be specified to determine the solution of equations (2.8).

2.3 The Boundary Conditions

For a full film bearing the pressure distribution including the negative pressure, is a continuous periodic function along the circumferential coordinate θ with a period 2π and therefore can be represented by a Fourier harmonic series. Furthermore, replacing θ by $-\theta$ on the right hand side of equation (2.8) with $i=1$ gives

$$\frac{3}{2}\,e\,\sin(-\theta)=-\frac{3}{2}\,e\,\sin\theta$$

whereas replacing θ by $-\theta$ on the left hand side does not

change the sign. This means that ϕ_1 is an odd function in θ. By a similar arguement it can be shown that ϕ_2 is an even function in θ. These properties of $\phi_1(z,\theta)$ and $\phi_2(z,\theta)$ allow the introduction of the following boundary conditions:

$$\phi_1(0,z) = 0 \qquad \text{and} \qquad \phi_1(\pi,z) = 0$$
$$\phi_2\left(\frac{\pi}{2},z\right) = 0 \qquad \text{and} \qquad \phi_2\left(\frac{3\pi}{2},z\right) = 0 \tag{2.9a}$$

along with the axial boundary conditions

$$\phi_i(\theta,0) = 0 \quad \text{and} \quad \phi_i(\theta,1) = 0 \quad , \quad i = 1,2 \tag{2.9b}$$

2.4 Solution by the Finite Element Method

Different procedures may be used in applying the finite element method to a linear partial differential equation [18]. The variational approach is the natural choice if a variational integral can be found for the problem on hand. The variational approach has the advantage of accelerating the convergence of the numerical solution through minimization of the deviation between the exact solution and the approximating one as shown by Reddi [19].

The bearing is developed in the dimensionless coordinates θ and z as shown in Fig. 2.2 with elements of triangular shape. Two types of elements represent an appropriate choice and these are the triangular and the rectangular elements. While the rectangular element has an obvious geometrical fit with the rectangularly developed

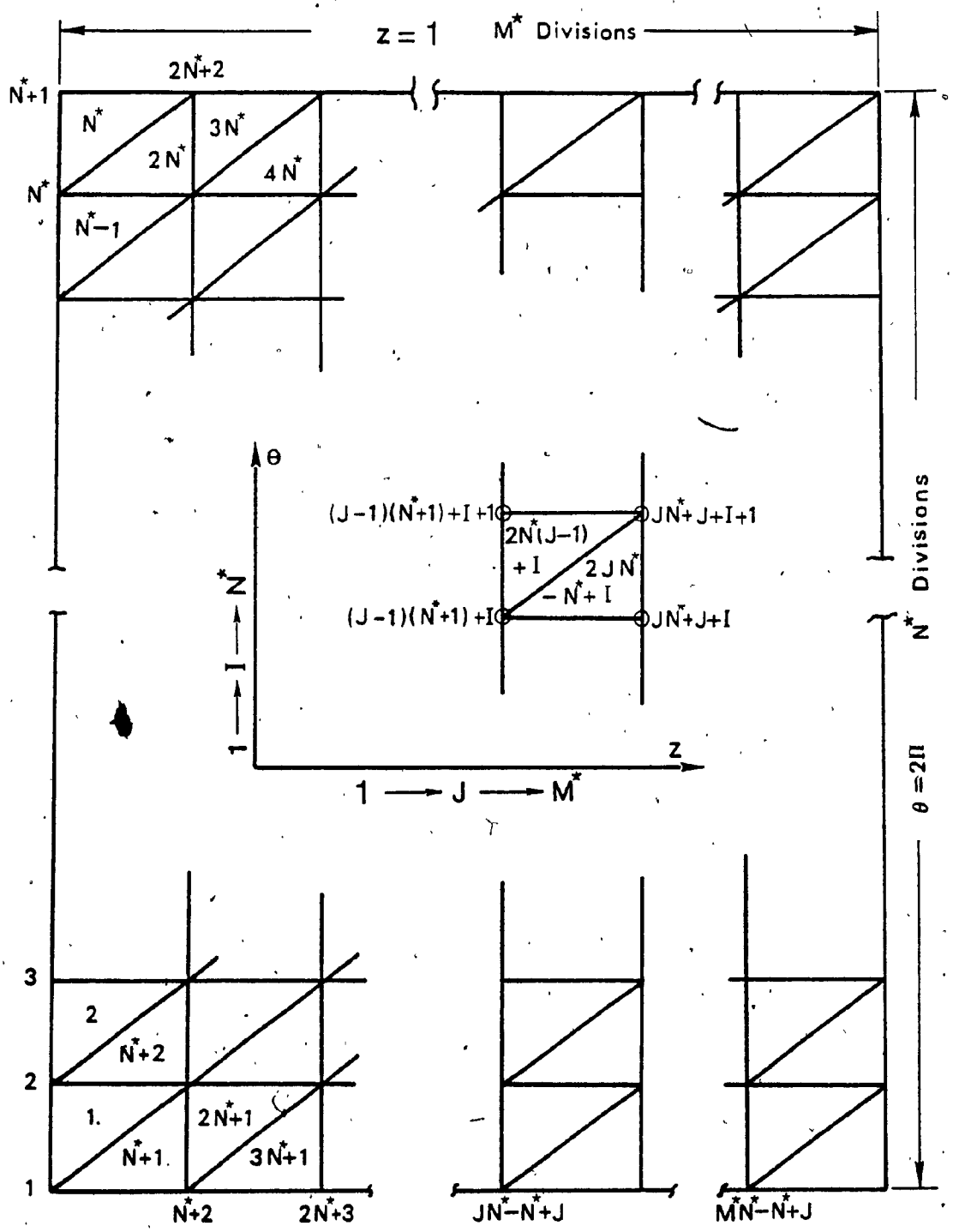

Fig. 2.2 The Bearing Developed in Nondimensional Coordinates with Triangular Element Arrangement.

bearing, the triangular element with minimum number of nodes, namely 3, is associated with a simple linear approximating function where in such a case the integrations over the element can be evaluated from tabulated values [18]. The arrangement with rectangular element results in half the number of elements compared to a triangular element arrangement but in both cases the overall number of nodes, which is also the order of the resulting global algebraic system, remains the same. A comparison was made between the results obtained using a triangular element with that using a rectangular elemental arrangement and was found to be in close agreement. Based on this fact, the simpler triangular element is employed in this finite element analysis.

The finite element method begins by assuming an approximating function over the element, a linear function in this case, evaluating this polynomial at the element nodes and expressing the resulting equations in terms of the function nodal values, substituting into the variational intregral, evaluating the resulting integrations over the element and finally extremizing the variational integral with respect to the function nodal values. This results in an algebraic system of an order equal to the number of the element nodes, namely 3 [18,19]. The equations of all elements are then summed up into a single global system which can be written as follows:

$$[A_g]\ \{\phi_g\} = \{f_g\} \qquad (2.10)$$

with an order n_o = overall number of nodes

= $(N^* + 1)$ $(M^* + 1)$ with reference to Fig. 2.2.

The functional nodal values $\bar{\phi}_g$ in turn are determined through the solution of the above algebraic system.

2.5 The Finite Element Program

The number of divisions N^* and M^* can be arranged to be the only input to the program, for a specified L/d and eccentricity ratios, through automatic mesh generation employing a general element as shown in Fig. 2.2. The numerical solution proceeds beginning with starting values for M^* and N^* which are, then, progressively increased until no significant improvement in the obtained solution is achieved. The starting values in the present investigation were set as $N^* = 16$ and $M^* = 6$ and the final values are $N^* = 36$ and $M^* = 12$. The improvement in the evaluated dimensionless pressure function ϕ_1 at $G = 1$, $\theta = 90°$ and different eccentricity values is 2 to 7% which roughly indicates a fast convergence toward the exact solution with a fewer number of elements.

A straight forward construction and solution of the algebraic system (2.10), which is of order $n_o = 481$ for the final values of N^* and M^*, will require excessive computer time and memory. However certain facts may be employed for reducing the complexity of the problem. They are:

i) ϕ_1 is an odd function in θ,

ii) ϕ_2 is an even function in θ,

iii) ϕ_1 and ϕ_2 are symmetric around $z = \frac{1}{2}$ for all θ,

iv) $[A_g]$ is a symmetric banded matrix,

v) all elements have the same area and every two rows in the θ or z direction are identical,

vi) all nodes in the z direction for certain values of θ other than those at $z = 0$ and $z = 1$ will be under the same values of the film function H and under the same participation from similar elements in number and shape.

From (i),(ii) and (iii) it is necessary to consider just one quarter of the domain, which is essentially a process of decoupling the system at the lines of symmetry. In fact, the condition (iii) corresponds to exchanging the boundary conditions (2.9b) by the new boundary conditions:

$$\left.\frac{\partial \phi_i}{\partial z}\right|_{z=\frac{1}{2}} = 0 \quad , \quad i = 1,2$$

From (iv) only the band of matrix A_g need to be stored. Finally, from statements (v) and (vi) only the first four rows, rows in the circumferential direction, of elements are required to be constructed. Using this simplifying procedure the computer storage needed can be reduced to less than 2% of the originally required amount.

The Pyne-Iron method is used for introducing the boundary conditions into the algebraic system (2.10) which in

turn is solved employing the Gauss-Jordan technique. The dimensionless pressure functions can now be integrated for the evaluation of hydrodynamic forces.

2.6 Evaluation of the Full Film Forces

The integrals in the tangential and radial hydrodynamic force expressions (2.4), can be written for the non-dimensional shear and squeeze pressure functions ϕ_1 and ϕ_2 as

$$\int_0^{2\pi}\int_0^{L} p \sin\theta \cdot dZd\theta = L\mu \left(\frac{d}{c}\right)^2 [g_1 I_1 + g_2 I_2]^*$$

$$\int_0^{2\pi}\int_0^{L} p \cos\theta \, dZd\theta = L\mu \left(\frac{d}{c}\right)^2 [g_1 I_3 + g_2 I_4]$$

where (2.11)

$$I_i = \int_0^{2\pi}\int_0^{1} \phi_i \sin\theta \, dzd\theta \quad , \quad i = 1,2$$

$$I_{i+2} = \int_0^{2\pi}\int_0^{1} \phi_i \cos\theta \, dzd\theta \quad , \quad i = 1,2$$

and g_1, g_2 are defined in equation (2.8).

The shear and squeeze nondimensional functions ϕ_1 and ϕ_2 can be expanded in the θ direction in terms of Fourier sine and cosine series respectively.

---

*Valid for the present case with the integrations over the axial coordinate Z is carried out using any of the Newton-Cotes formulaes.

$$\phi_1(\theta)\Big|_{z=z_j} = \sum_{n=1}^{\infty} B_n \sin n\theta$$

$$\phi_2(\theta)\Big|_{z=z_j} = \sum_{n=0}^{\infty} A_n \cos n\theta \qquad (2.12)$$

where z_j is a specified discrete value in the z direction. Applying the expansions (2.12) into the integrals I_i (i=1,2,3, 4) in equation (2.11) it can easily be shown that

$$I_1(z_j) = B_1\pi$$

$$I_2(z_j) = I_3(z_j) = 0 \qquad (2.13)$$

$$I_4(z_j) = A_1\pi$$

Hence the integrations in the θ direction only requires the evaluation of the coefficients A_1 and B_1 of the fundamental terms in the Fourier series. The integrations,

$$I_i = \int_0^1 I_i(z)\, dz \quad , \quad i = 1,2,3,4$$

are carried out using Newton-Cotes formulae [18].

Here a check is made by using a large value of G, say G = 100, and comparing the solution obtained with the infinitely long bearing solution. At an arbitrary chosen eccentricity ratio e = .5, the maximum observed error over ϕ_1 and ϕ_2 is less than 1% verifying a reasonably good accuracy of the overall numerical procedure followed which started by the finite element solution, followed by the evaluation of Fourier series coefficients for ϕ_1 and ϕ_2 in θ

direction and finally the numerical integration over z.

The values of the integrals I_i lead to complete the evaluation of the hydrodynamic forces of the full film bearing. These values are still discrete over the eccentricity e and L/d ratio given by G. The values of the nonvanishing integrals I_1 and I_4 over e and G will be referred to as E_1 and E_2 from now on throughout this thesis.

2.7 Curve Fitting of Eccentricity Ratio Functions E_1 and E_2 for the Finite Bearing

For infinitely long bearing, the expressions for the eccentricity functions E_1 and E_2 are [1]:

$$E_1 = \frac{-3\pi e}{(2+e)\sqrt{1-e^2}}$$

$$E_2 = \frac{3\pi}{(1-e^2)^{3/2}} \qquad (2.15)$$

Using these functions as the base for normalizing the finite bearing eccentricity functions E_1 and E_2, it is found that the finite bearing eccentricity functions are not separable in e and G. That is,

$$E_i(e,G) \neq E_{i_1}(e)\, E_{i_2}(G)$$

which imposes a restriction on the validity of those journal bearing solutions which are of separable form [7-13]. This conclusion also means that the curve fitting of the eccentricity functions E_i over e and G, is not possible by a function of

a simple form. Instead of using a complicated form of a curve fitting fucntion, the eccentricity functions are curve fitted over the eccentricity ratio e only, which is a variable in the journal equation of motion, for different L/d ratios, which is only a parameter for a given journal bearing case.

It would be convenient if the form of the curve fitting function possess the following advantages, namely:

i) simplicity in handling for the use of computer programming;

ii) accommodates the eccentricity functions E_1, E_2 as well as those eccentricity functions that will be presented in the latter part of this chapter;

iii) flexibility in expansion that can provide various requirements on accuracy and simplicity.

Recognizing that these eccentricity functions tend to infinity at e = 1, different forms that can exhibit such a trend are tested starting by functions similar to those of the infinitely long bearing given by equations (2.15). Among the many tested forms, a polynomial that satisfies all above requirements is considered, and is found to be of the form

$$E_j = B_{jo} + \sum_{i=1}^{m_1} B_{ji}\, e^i + \tan\frac{\pi e}{2} \sum_{i=m_1+1}^{m_2} B_{ji}\, e^i, \qquad j = 1,2 \tag{2.16}$$

The factor $\tan\frac{\pi e}{2}$ helps to accelerate the convergence at high eccentricity values while the second term increases the

the fitting accuracy at small eccentricity. Using property (iii) presented above, the choice of the polynomial order given by m_2 as well as m_1, can now be made based on a required combination of accuracy and efficiency. Although the polynomial (2.16) with $m_1 = 3$ and $m_2 = 6$ achieves satisfactory accuracy, a final choice of $m_1 = 4$ and $m_2 = 8$ is made since a higher accuracy is demanded in the present investigation. A sample set of curve fitted eccentricity functions is presented in Table A.1 in Appendix A to show the adequacy of the curve fitting polynomial chosen. Also the polynomial coefficients B_j for eccentricity functions E_1 and E_2 are presented in Tables A.2 and A.3 in Appendix A.

The plots of the eccentricity functions E_1 and E_2 are presented in Figs. 2.3 and 2.4, respectively, along with the corresponding long and short bearing eccentricity functions. The infinitely long bearing can be seen as only an upper bound to the finite bearing curves whereas it is obvious that the validity of the short bearing approximation is limited for small L/d ratios, say less than .25, and small eccentricity ratio.

2.8 The Equation of Motion of the Full Film Finite Bearing

With the eccentricity functions E_1 and E_2 defined in equation (2.16), the tangential and radial film forces F_t and F_r can be written as

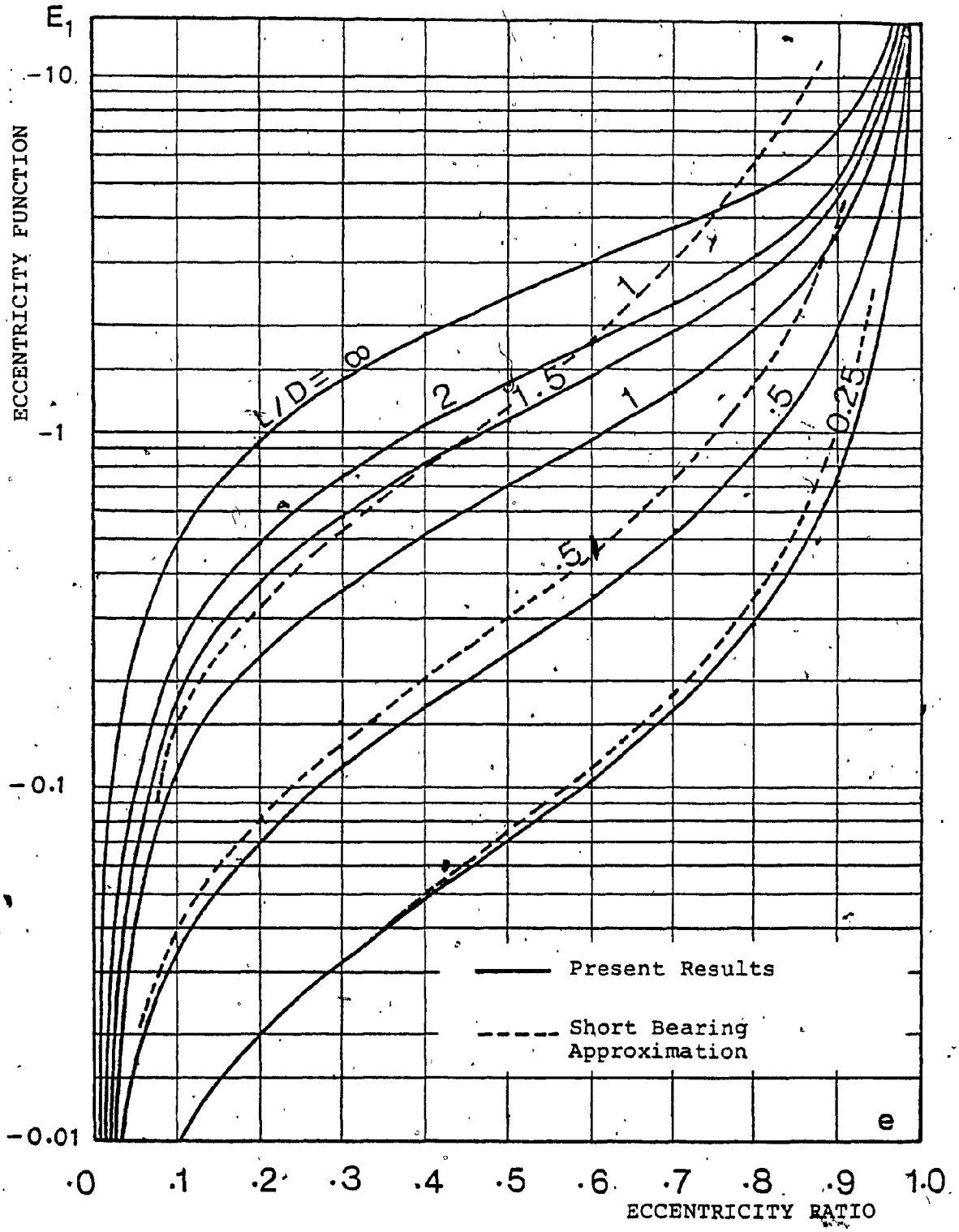

Fig. 2.3 Eccentricity Function E_1 for Different L/d Ratios with the Corresponding Long Bearing and Some Short Bearing Results.

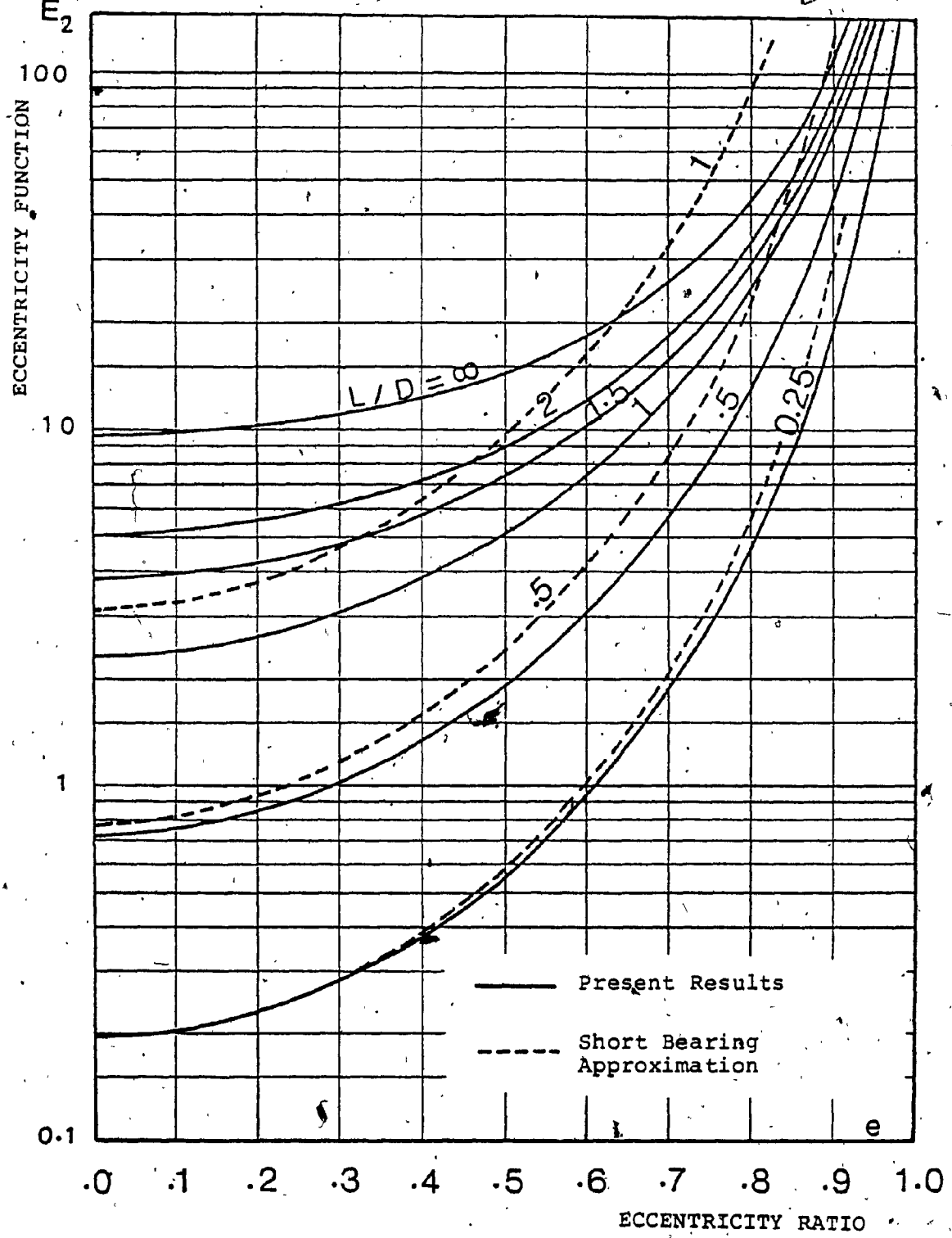

Fig. 2.4 Eccentricity Function E_2 for Different L/d Ratios with the Corresponding Long Bearing and Some Short Bearing Results.

$$F_t = -\frac{Ld^3}{2c^2}\ \mu\ (\omega_j - 2\dot{\psi})\ E_1$$

$$F_r = -\frac{Ld^3}{2c^2}\ \mu\ \dot{e}\ E_2 \tag{2.17}$$

The equations of motion of the journal bearing for a full film can be expressed in a dimensionless form by dividing them by $cm\omega_j^2$ and further utilizing the nondimensional time $\tau = t\omega_j$ and are given by

$$\ddot{e} - e\dot{\psi}^2 = -\frac{S}{2}\ \dot{e}\ E_2 + W_n \cos(\beta_\ell - \psi)$$

$$e\ddot{\psi} + 2\dot{\psi}\dot{e} = -\frac{S}{2}\ (1 - 2\dot{\psi})\ E_1 + W_n \sin(\beta_\ell - \psi) \tag{2.18}$$

Here S is the dimensionless dynamic bearing parameter given by

$$S = \frac{\mu L}{m\omega_j}\left(\frac{d}{c}\right)^3, \tag{2.18a}$$

dot above the variables indicate differentiation with respect to τ, and the dimensionless applied load $W_n \triangleq W/(cm\omega_j^2)$ is spaced by an angle β_ℓ with the horizontal as can be seen in Fig. 2.1b. The static equilibrium position for the finite full film bearing is given, with reference to Fig. 2.1, by the equations

$$\beta_\ell - \psi = \frac{3\pi}{2}$$

$$W_n = -\frac{S}{2} E_1 \tag{2.19}$$

The equations of motion of the finite bearing with full film along with its associated eccentricity functions E_1 and E_2

are of limited practical value but serve as a base for the practical film models that are developed later in this chapter.

2.9 Cavitation in Thin Oil Film

Under practical operating conditions negative pressure values as may be given by solving the Reynolds' equation are sufficiently large to cause a film rupture. In the steady state condition, accurate determination of the cavitation boundary is quite manageable in terms of computation even if it requires iterating the Reynolds' equation along with the flow continuity equation [25,30]. In the dynamic case, such a treatment is practically impossible and so a simpler treatment is usually adopted, say for example, by disregarding the negative pressure in the divergent zone of the film. However, the hypothesis on the kinematics of the cavities and the effect of the cavitation region on the bearing dynamic performance must be clearly defined to support the arguments involved in constructing a partial film model in the dynamic case of the bearing. For this a few important facts about the nature of cavitation in thin oil film are extracted from previous experimental studies [26] and may be briefly stated as follows:

i) cavities in thin oil film, which are mostly gaseous or formed from the dissolved gases in the oil, are either ventilated at ambient pressure or partially ventilated at a pressure due to the ambient [27]. Therefore, the cavitation region can be assigned a zero pressure value for

practical considerations,

ii) the cavities stretch along the cavitation region in the direction of motion, leaving only oil streamers with narrow width [30] which can be thought of as very narrow successive bearings, and have negligible effect on the bearing behaviour [32],

iii) the cavities can somtimes be moving but mostly are fixed cavities that have the ability to fluctuate in length with a high ratio between expanded and shrunk lengths at a high frequency [27,38],

iv) some experiments on the dynamically loaded bearing [36] recorded a rotating cavitation region similar to the one in the steady state condition and a relative motion between the cavity and surface was also observed.

From (i) and (ii), the assumption of neglecting the pressure in the cavitation region is well supported as being practical. The last two points (iii) and (iv) make it possible to assume that the cavitation region can move, shrink on one side and expand at the other with high frequency that can follow a general motion of the journal in the dynamic case. These facts are useful in supporting the theoretical partial film models presented in the following sections.

2.10 Dynamic Pressure Boundaries

An extensive treatment that considers the pressure

gradient at the commencement of the cavitation zone as well as the flow continuity in a procedure toward establishing a very precise cavitation boundary similar to the treatment of the steady state conditions [25,30] is quite impractical in the dynamic case. On the other hand, an appropriate adjustment to the pressure components of the full film bearing as done here, may lead to an efficient and practical dynamic film model.

A superposition of the shear and squeeze pressure components p_1 and p_2 presented in Fig. 2.5 gives all the four possibilities of positive and negative pressure positions and consequently giving the location possibilities for the resultant pressure profile. The dynamic boundary angles θ_1 and θ_2 are given by the relation

$$p_1/p_2 = -1$$

but from equation (2.8)

$$p_i = \left(\frac{d}{c}\right)^2 \mu \, g_i \, \phi_i \quad , \quad i = 1,2$$

then

$$\frac{p_1}{p_2} = 1 = -\left(\frac{g_1}{g_2}\right)\left(\frac{\phi_1}{\phi_2}\right) = \frac{-(\omega_j - 2\dot{\psi})\,\phi_1}{\dot{e}\,\phi_2} \qquad (2.20)$$

Instead of evaluating ϕ_1/ϕ_2 for a finite bearing, the upper and lower bounds corresponding to the short and long bearings are considered. For a short bearing the dynamic pressure distribution is [4],

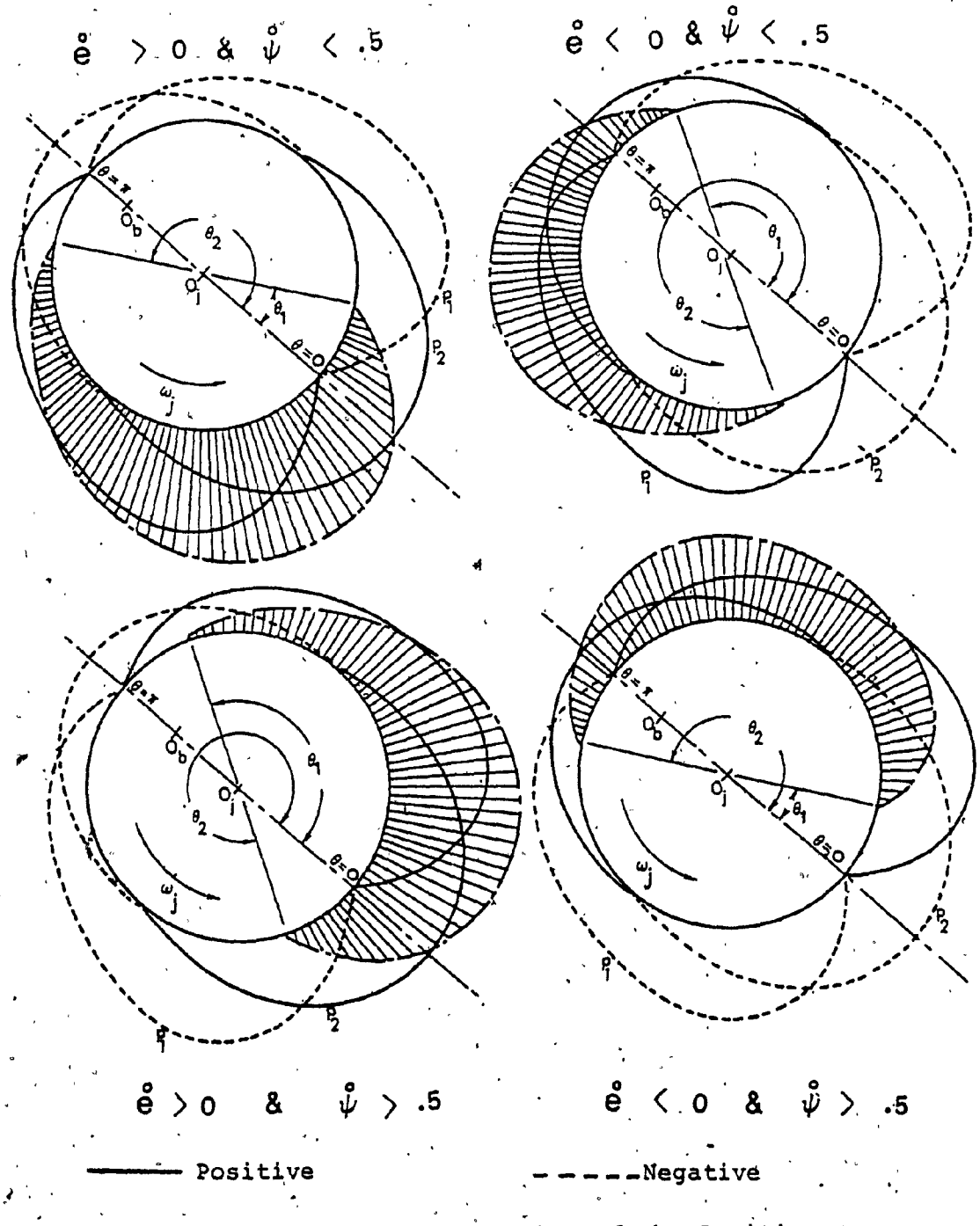

Fig. 2.5 Possibilities of Location of the Positive Pressure Profile of the Basic Dynamic Film Model.

$$p = 3\mu\ (d/c)^2\ G^2[z(z-1)]\ (1/H^3)\ [2g_2\cos\theta - eg_1\sin\theta]$$

from which

$$-\frac{p_2}{p_1} = 1 = \frac{2\dot{e}\cos\theta}{e(\omega_j - 2\dot{\psi})\sin} \quad \text{or} \quad \theta = \tan^{-1}\frac{2\dot{e}}{e(\omega_j - 2\dot{\psi})} \tag{2.21}$$

The long bearing pressure distribution [1] can be written as

$$p = \frac{3\mu}{2}\left(\frac{d}{c}\right)^2\left[\frac{-g_1 e\ (2 - e\cos\theta)\ \sin\theta}{(2 + e^2)\ H^2} + \frac{g_2}{e}\left(\frac{1}{H^2} - 1\right)\right]$$

from which (2.22)

$$\theta = \tan^{-1}\ \frac{\dot{e}(2 + e^2)}{e(\omega_j - 2\dot{\psi})}$$

Then for short and long bearings the boundary angles are given by equations (2.21) and (2.22) and therefore the corresponding relation for the finite bearing, in general, will also be in the arc tangent form. Consequently, if the boundary angle θ_1 is determined by any such arc tangent relations, then θ_2 is given by the relation

$$\theta_2 = \theta_1 + \pi$$

Therefore, in the dynamic case, the positive pressure profile will always be extended over half the circumference and as the quantities $e, \dot{e}$ and $\dot{\psi}$ change in sign and magnitude, the transition between one pressure profile from the four possibilities in Fig. 2.5, to another causes the cavitation region to shrink on one side, along θ direction, and to expand on the other. The cavity has the ability to follow the motion with high frequency as mentioned earlier.

The partial film model presented still maintain those boundary angles that are dependent on the displacements and velocities of the journal which means that the journal equation of motion will always be coupled with the Reynolds' equation. Consequently, two partial film models are considered namely the $3\pi/2$ and the π film models. Both film models are decoupled from the Reynolds' equation and are shown to be upper and lower bounds for the time dependent boundary model presented above and will be referred to as the basic film model.

2.11 The $3\pi/2$ Film Model

This model was first used for the short bearing case [4]. The name implies the angle of the arc along which the film extends. In this film model the negative pressure is disregarded in both the shear and squeeze pressure components. The pressure profile is then constructed from the superposition of the remaining positive pressure components, as shown in Fig. 2.6 which presents the four possibilities for the location of the pressure profile. These possibilities are determined by the sign of the velocity function g_1 and g_2 given by equation (2.8).

The evaluation of the hydrodynamic forces for the $3\pi/2$ film is illustrated by the diagram 2.7. In Fig. 2.7, the signs of the quantities $\dot{e}$ and $(1-2\dot{\psi})$ are first projected on the pressure distributions corresponding to the respective component. Disregarding the negative pressure and evaluating

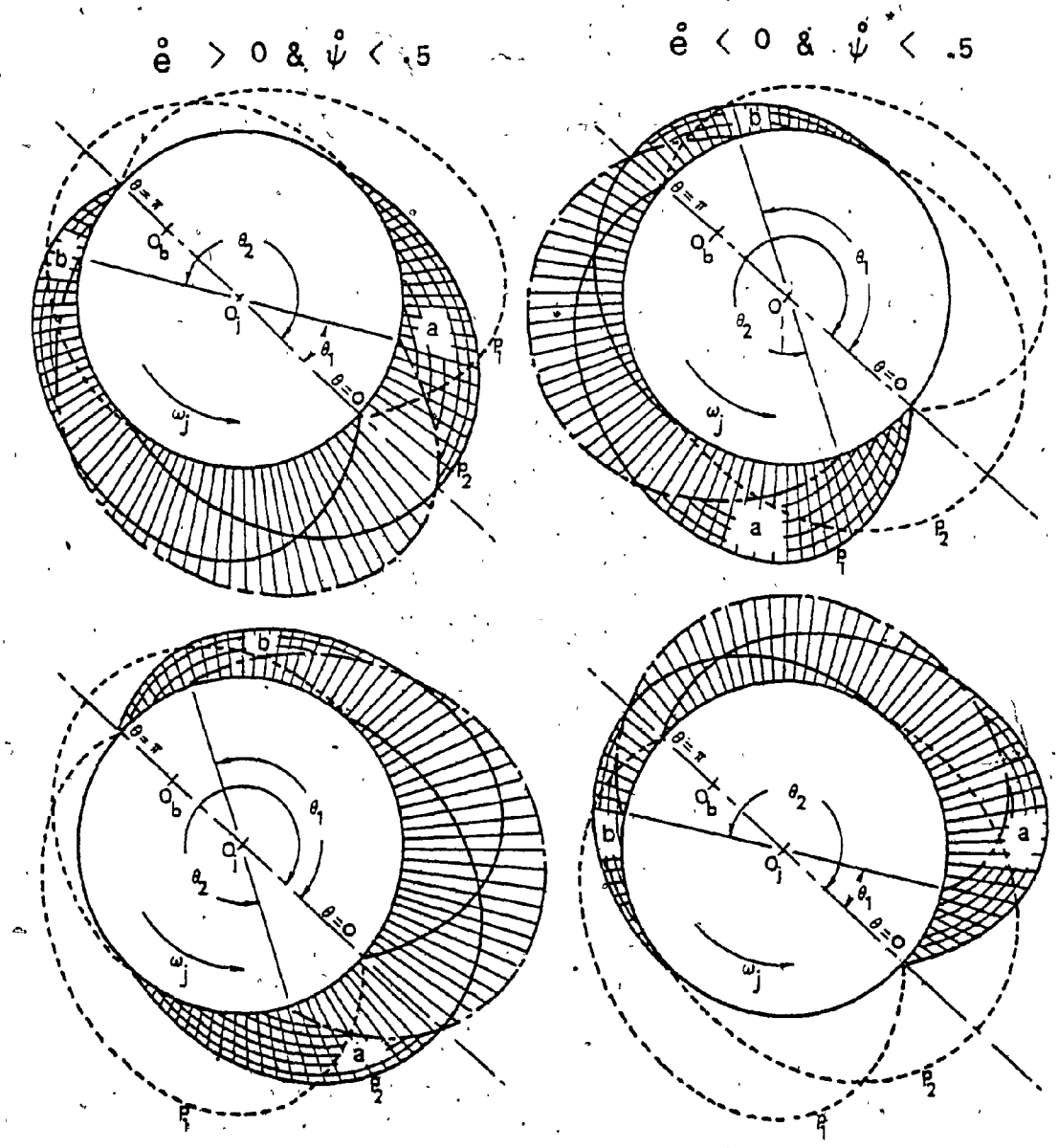

Fig. 2.6 Possibilities of Location of the Positive Pressure Profile of the $3\pi/2$ Film Model.

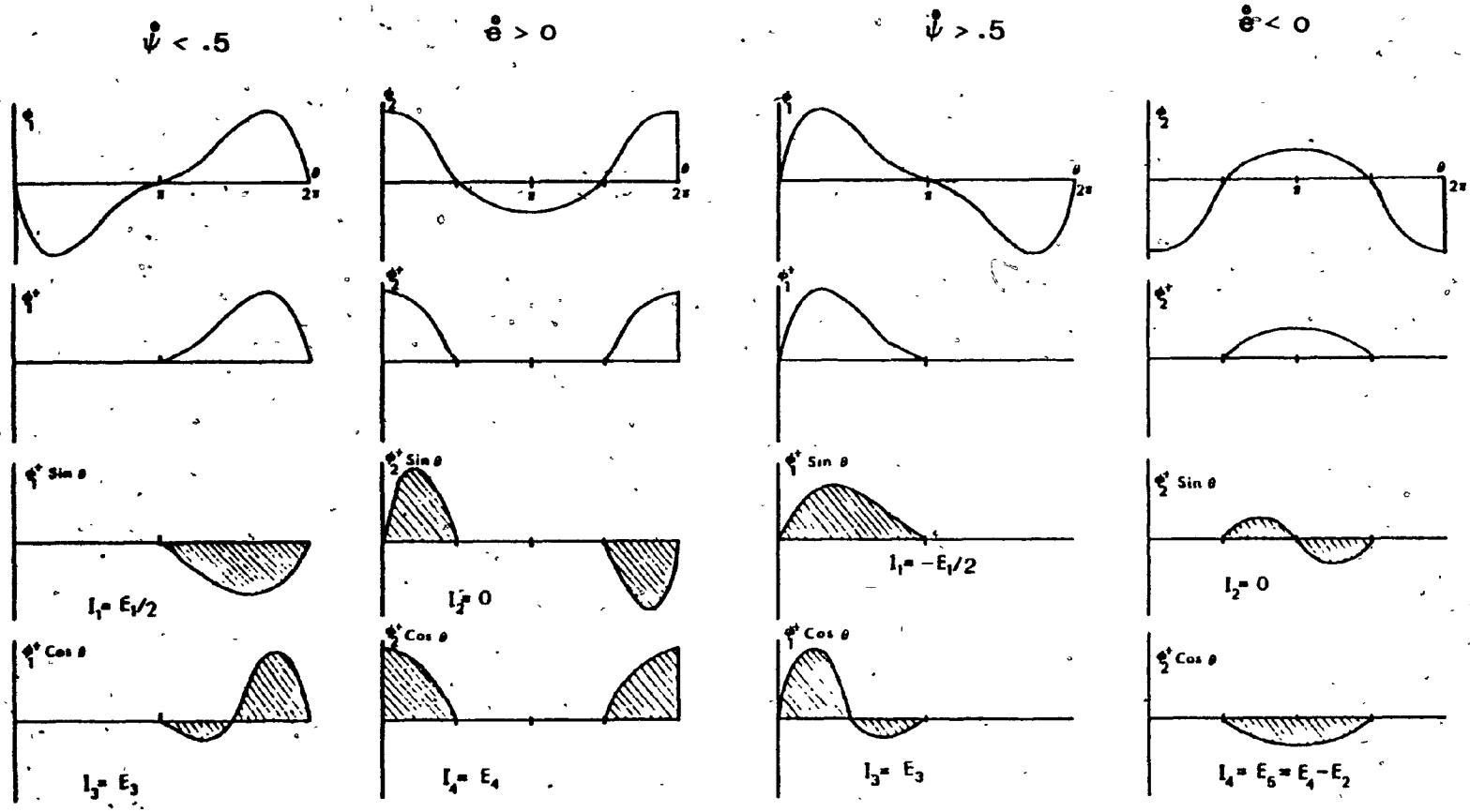

Fig. 2.7 Simplified Procedure for Evaluating the Hydrodynamic Forces for the $3\pi/2$ Film Model.

the integrals in equations (2.11), but with the new limits, yields

$$I_1 = \int_0^1 \int_0^{\pi} \phi_1 \sin\theta \, d\theta dz = \int_0^1 \frac{1}{2} B_1 \pi \, dz$$

$$I_2 = 0$$

$$I_3 = \int_0^1 \int_0^{\pi} \phi_1 \cos\theta \, d\theta dz = \int_0^1 \left(\sum_{n=2}^{\infty} B_n \frac{-2n}{n^2-1} \right) dz$$

$$I_4 = \int_0^1 \int_0^{\frac{\pi}{2}} \phi_2 \cos\theta \, d\theta dz = \int_0^1 \left(2A_0 + A_1 \frac{\pi}{2} \right) dz \qquad (2.23)$$

where A_n and B_n are the coefficients of the Fourier cosine and sine series in the expansions of the nondimensional pressure components ϕ_2 and ϕ_1 at discrete axial locations. Two additional eccentricity functions, namely E_3 and E_4, arise from the new boundary conditions as can be seen in Fig. 2.7. Finally returning the signs of the resulting quantities back to the velocities $\dot{e}$ and $(1-2\dot{\psi})$, the radial and tangential force components for the $3\pi/2$ film can be written as

$$F_t = -\frac{L\mu d^3}{4c^2} \left[(\omega_j - 2\dot{\psi}) \, E_1 \right]$$

$$F_r = -\frac{L\mu d^3}{2c^2} \left[\dot{e} \, E_5 + |\omega_j - 2\dot{\psi}| E_3 \right] \qquad (2.24)$$

and

$$E_5 = E_4 \text{ for } \dot{e} > 0$$

$$= E_2 - E_4 \text{ for } \dot{e} < 0$$

The eccentricity functions E_3 and E_4 are curve fitted using the polynomial form (2.16) and corresponding coefficients are presented in Tables A.5 and A.5 in Appendix A. The plots of the eccentricity functions E_3 and E_4 are presented in Figs. 2.8 and 2.9 for different L/d ratios. The corresponding eccentricity functions for the short and long bearings are evaluated and plotted in Figs. 2.8 and 2.9 for ready comparison. The conclusion, following a similar comparison for E_1 and E_2 in Figs. 2.3 and 2.4, can now be extended for all eccentricity functions in the sense that the short bearing approximation shows inadaquate accuracy at L/d > .25 and high eccentricity ratio values whereas the long bearing curve is only an upper bound to the finite bearing and otherwise a rough approximation for L/d < 2.

2.12 The π Film Model

This film model is frequenctly used and is developed here for the finite bearing by disregarding the full film pressure distribution in the divergent zone. The four possibilities for the location of the pressure profile are presented in Fig. 2.10. A similar procedure as that described in Fig. 2.7 earlier can be used to identify the new film forces. In this case the integral I_2 of equation (2.11) does not vanish as in the cases of the full film and $3\pi/2$ film models. The integral I_2 can then be written as

$$I_2 = \int_0^1 \int_{\pi}^{2\pi} \phi_1 \sin\theta \, d\theta dz = \int_0^1 \left(\sum_{n=0,2,4}^{\infty} \frac{2A_n}{n^2-1} \right) dz$$

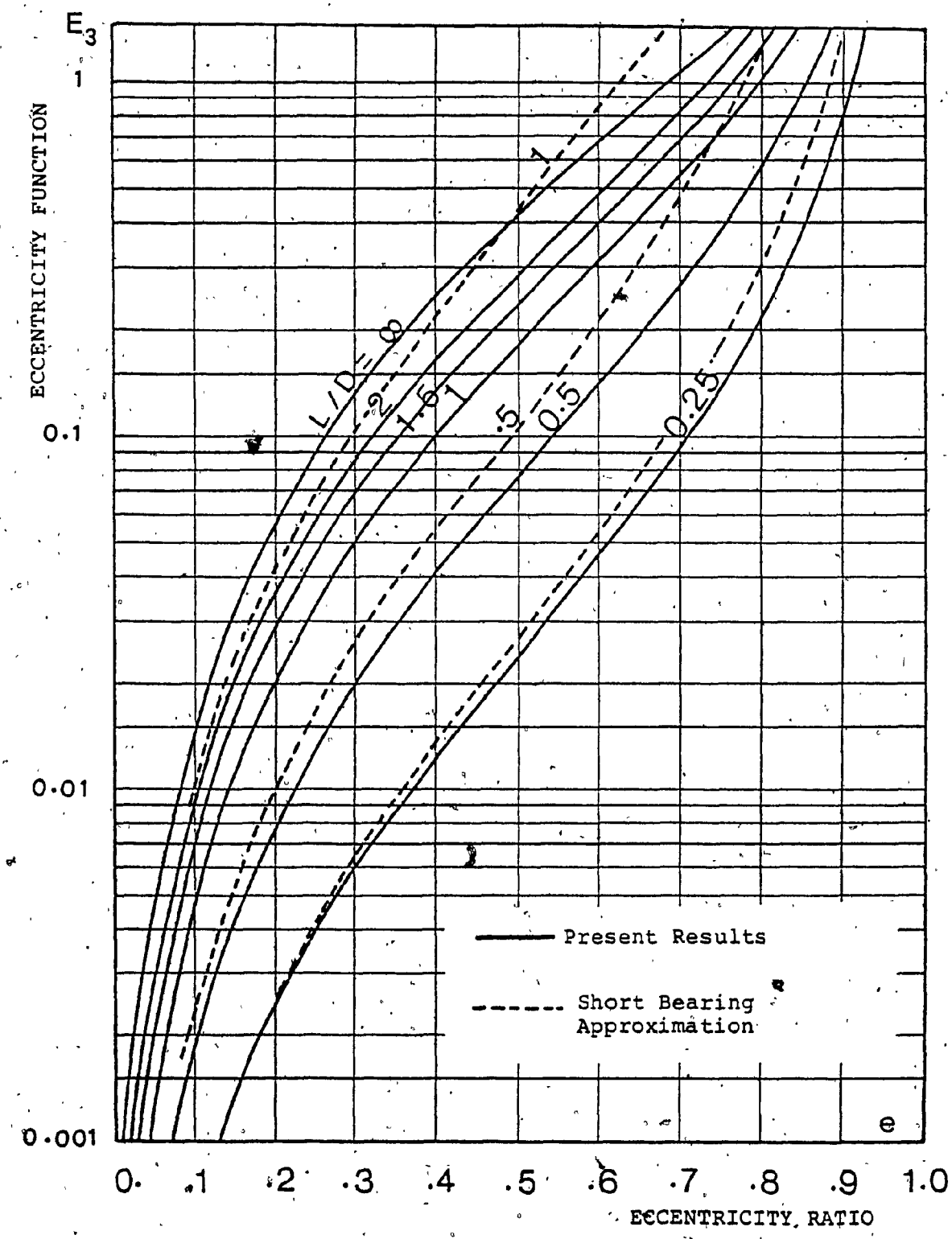

Fig.-2.8 Eccentricity Function E_3 for Different L/d Ratios with the Corresponding Long Bearing and Some Short Bearing Results.

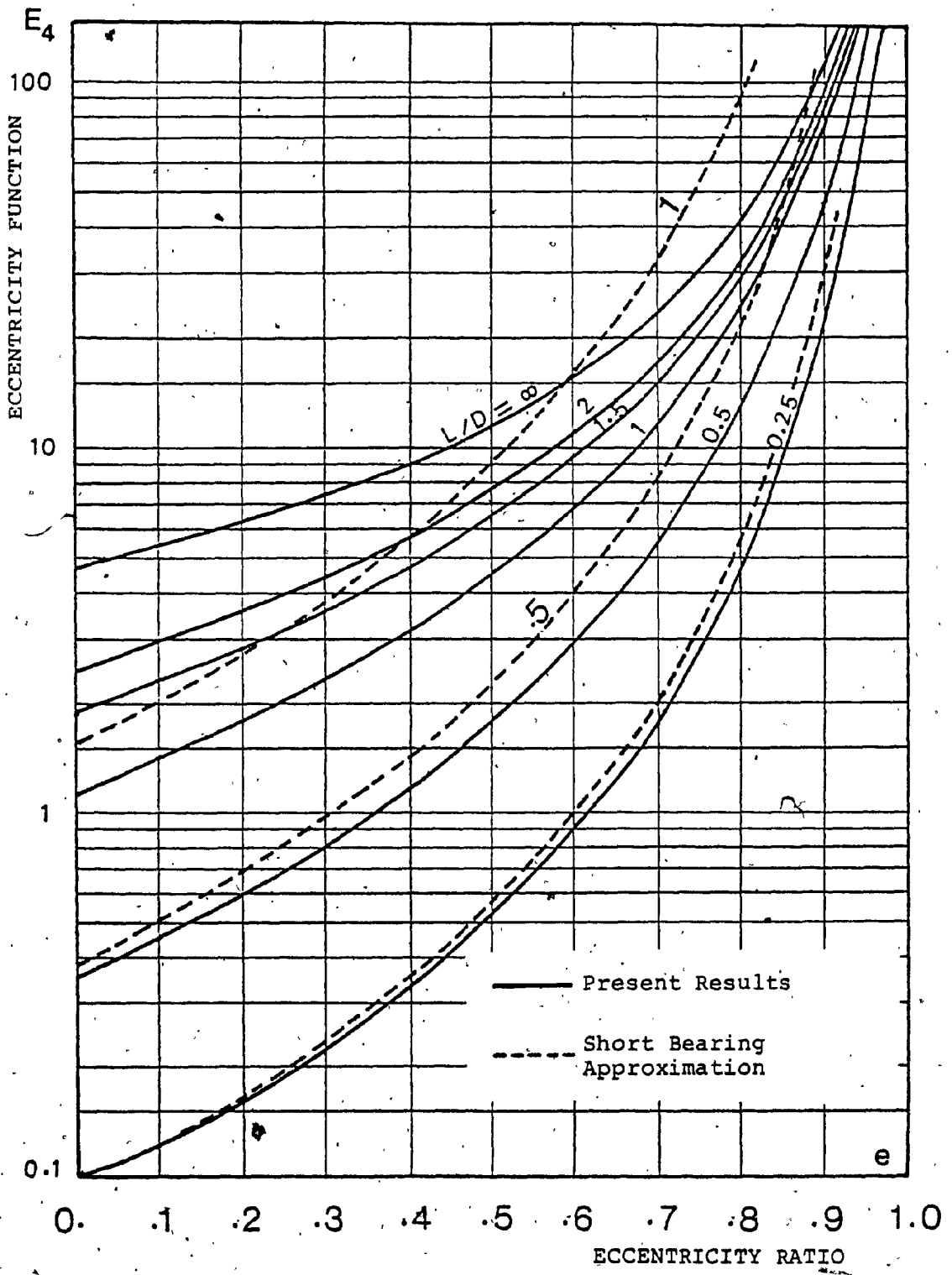

Fig. 2.9 Eccentricity Function E_4 for Different L/d Ratios with the Corresponding Long Bearing and Some Short Bearing Results.

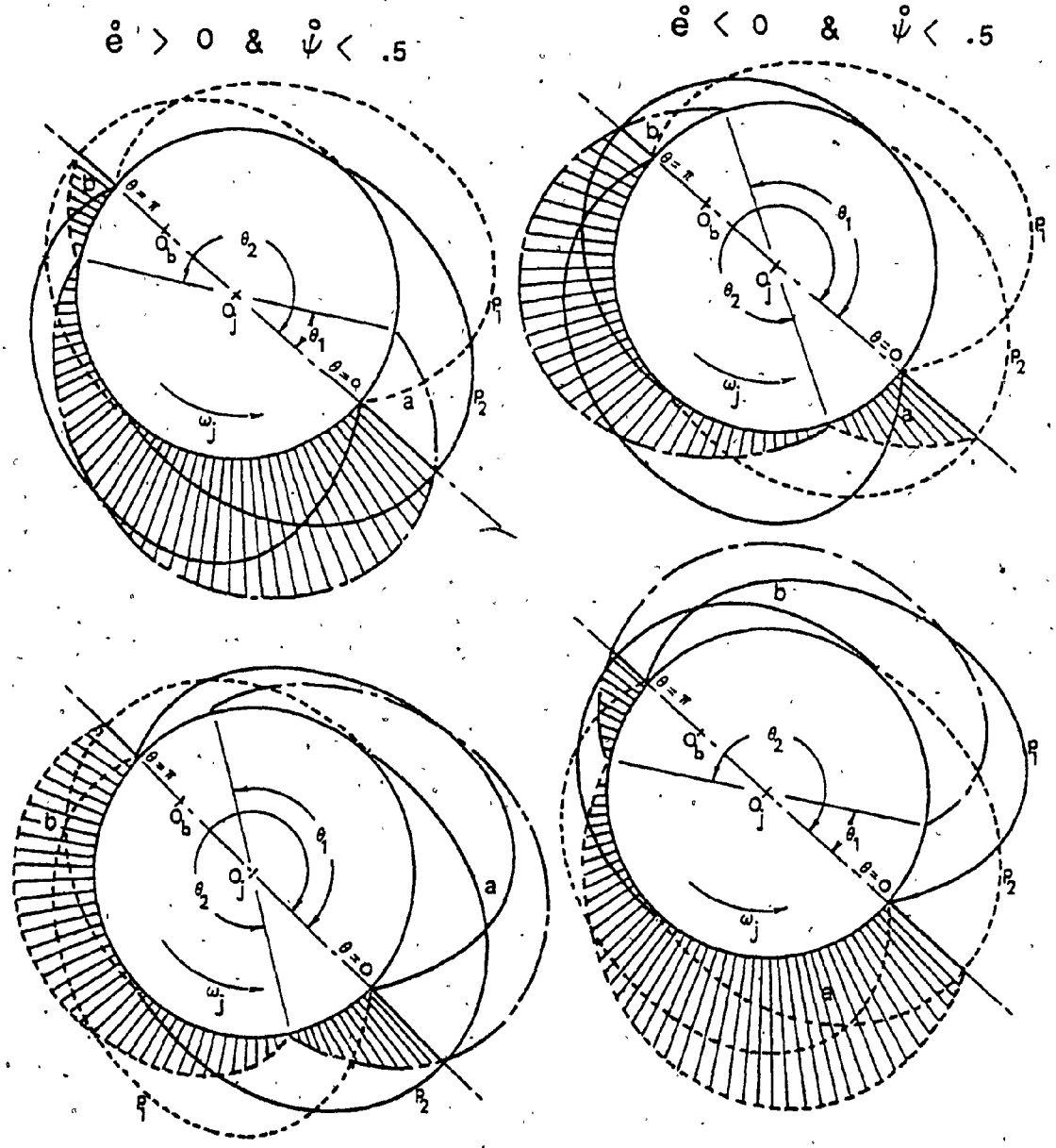

Fig. 2.10 Possibilities of Location of the Pressure Profile of the π Film Model.

This results in a new eccentricity function E_6 which is also curve fitted using polynomial (2.16) and the coefficients of the polynomial are presented in Table A.6, Appendix A. The new eccentricity function E_6 is also plotted in Fig. 2.11 for different L/d ratios. Once the integrals I_1, I_2, I_3 and I_4 are available, the radial and tangential film force can be written and are

$$F_t = -\frac{L\mu d^3}{2c^2}\left[(\omega_j - 2\dot{\psi})\frac{E_1}{2} + \dot{e}\,E_6\right]$$

$$F_r = -\frac{L\mu d^3}{2c^2}\left[(\omega_j - 2\dot{\psi})\,E_3 + \dot{e}\,\frac{E_2}{2}\right] \qquad (2.25)$$

2.13 Discussion on the $3\pi/2$ and π Film Models

A simple qualitative procedure is used to define the deviation of the $3\pi/2$ and π film models from the basic film model. The difference between any of the partial film models and the basic film model is represented by regions that are denoted by a and b on the pressure profiles in Figs. 2.6 and 2.10. The pressure profile of the basic film is always contained entirely in the profile of the $3\pi/2$ film at all possibilities as shown in Fig. 2.6. Consequently, the pressure distribution in zones a and b is always positive, so is the difference (a-b). On the other hand, the zones a and b may not be included in the pressure profile of the π film and may also be of a negative pressure distribution. In both figures and for all the possibilities shown, each area that is denoted by a is bigger than that marked b due to their individual

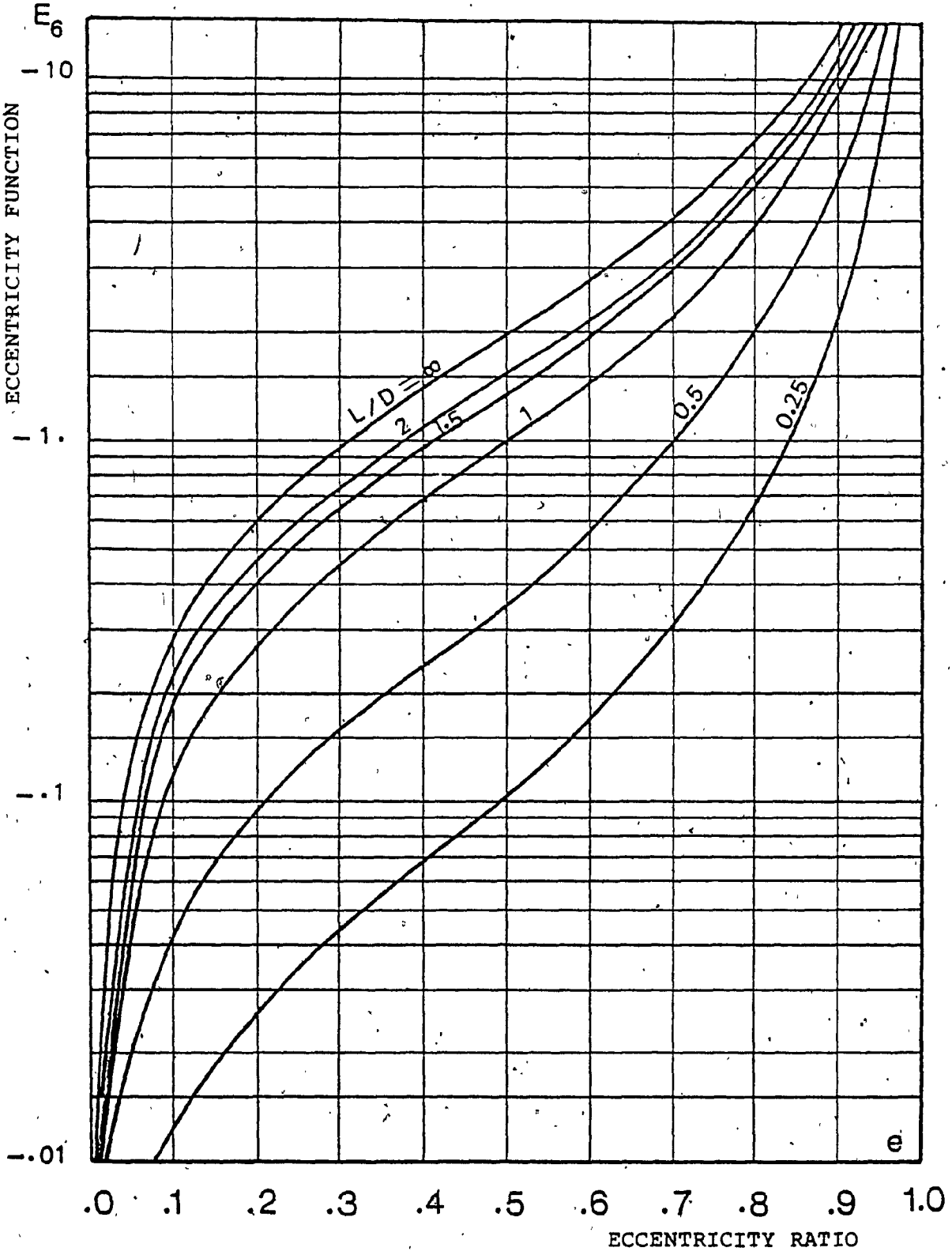

Fig. 2.11 Eccentricity Function E_6 for Different L/d Ratios.

location with respect to the eccentricity direction of the journal center. These two zones are consistently of opposite nature and therefore the deviation from the basic model is only the difference (a-b) which then generates two minor forces F_r^* and F_t^* that are directed either along or opposite to the forces of the basic film.

Let a representative force for the basic film profile be located at any point on that quarter of the journal circumference which is completely occupied by that profile. Next, let the residual force be placed anywhere on the quarter where the zone a is located. Then by analyzing these forces in terms of their radial and tangential componets, assessment of the deviations of the $3\pi/2$ and the π film models can be made. For example, considering the case with $\overset{o}{\psi} < .5$ and $\overset{o}{e} > 0$ in Fig. 2.6, the residual force due to (a-b) is located somewhere on the first quadrant given by $\theta = 0$ to $\pi/2$, and the force for the basic film model should be located on the fourth quadrant which is entirely contained in the basic film profile. Then it can be identified that F_r^* is added to the radial component of the basic film force F_r while F_t^* is subtracted from the tangential component F_t. The conclusion for all possibilities and for both partial film models is summarized in Table 2.1.

As can be seen from Table 2.1 the effect of constructing the $3\pi/2$ film starting from the basic film model gives an opposite effect compared to that of the π film. Only the radial component F_r^* in the lower two cases, with $\overset{o}{\psi} > .5$, are

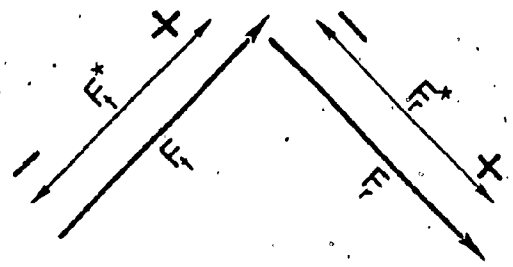

	$3\Pi/2$ FILM		Π FILM	
	F_t^*	F_r^*	F_t^*	F_r^*
$\dot{e} > 0$ $\dot{\psi} < .5$	−	+	+	−
$\dot{e} < 0$ $\dot{\psi} < .5$	+	−	−	+
$\dot{e} > 0$ $\dot{\psi} > .5$	−	+	+	+
$\dot{e} < 0$ $\dot{\psi} > .5$	+	−	−	−

Table 2.1 Signs of the Residual Forces for the $3\pi/2$ and π Film Models.

similar. Then it can be stated that the opposite effects of the $3\pi/2$ and π film models on the basic film, place these film models as upper and lower bounds for the basic film particularly for cases where $\overset{\circ}{\psi}$ does not exceed .5 significantly.

2.14 The Equation of Motion and the Steady State Equilibrium Locus

Substituting the tangential and radial film forces into the equation of motion and utilizing a dimensionless pattern as used previously for the full film bearing in equation (2.18), the equation of motion in a nondimensional form for all different film models can be written as

$$\begin{aligned} \overset{\infty}{e} - e\overset{\circ}{\psi}^2 &= -\frac{S}{2}\left[(1-2\overset{\circ}{\psi})\ E_i + \overset{\circ}{e}\ E_j\right] + W_n \cos\ (\beta_\ell - \psi) \\ e\overset{\infty}{\psi} + 2\overset{\circ}{\psi}\overset{\circ}{e} &= -\frac{S}{2}\left[(1-2\overset{\circ}{\psi})\ E_k + \overset{\circ}{e}\ E_\ell\right] + W_n \sin\ (\beta_\ell - \psi) \end{aligned} \tag{2.26}$$

Here β_ℓ is the load angle as explained in Fig. 2.1 and S is the bearing dynamic parameter given by equation (2.18a). The eccentricity functions E_i, E_j, E_k and E_ℓ are summarized in Table 2.2 for all the different film models.

The equilibrium position is then given by;

$$\begin{aligned} \frac{S}{2} E_3 &= W_n \cos\ (\beta_\ell - \psi) \\ \frac{S}{4} E_1 &= W_n \sin\ (\beta_\ell - \psi) \end{aligned} \tag{2.27}$$

for both the $3\pi/2$ and π film models.

	2π model (full film)	$\frac{3\pi}{2}$ model	π model
E_i	0	ζE_3	E_3
E_j	E_2	E_5	$E_2/2$
E_k	E_1	$E_1/2$	$E_1/2$
E_ℓ	0	0	E_ℓ

$$\zeta = 1 \text{ for } \mathring{\psi} \leq 1/2$$
$$= -1 \text{ for } \mathring{\psi} > 1/2$$

$$E_5 = E_4 \text{ for } \mathring{e} > 0$$
$$= E_2 - E_4 \text{ for } \mathring{e} < 0$$

Table 2.2 Eccentricity Functions for all Film Models.

Equation (2.27) can be written in terms of the well known Sommerfeld number S_{or} as

$$S_{or} = \frac{\mu \omega_j L d}{8\pi W} \left(\frac{d}{c}\right)^2 = \frac{1}{2\pi} \frac{1}{\sqrt{E_1^2 + 4 E_3^2}} \qquad (2.28)$$

The attitude angle $(\psi - \beta_\ell)$ which is the angle between the load and the line of centers is then

$$\psi - \beta_\ell = \tan^{-1} \frac{-E_1}{2E_3} \qquad (2.29)$$

Relations (2.28) and (2.29) are plotted in Figs. 2.12 and 2.13 respectively, for different L/d ratios.

2.15 Comparison of the Present Results with Other Investigations

Ocvirk [2] reported an experimental study on a bearing with L/d ratio, G = 1 and Sommerfeld number $S_{or} = .1598$. This value of S_{or} corresponds to a steady state eccentricity ratio e = .41 and an attitude angle of 60°. Ocvirk measured experimentally the attitude angle as 60° whereas the steady state eccentricity ratio was not measured. Using the curves for L/d = 1 in Fig. 2.12, the steady state eccentricity that corresponds to $S_{or} = .1598$ is .566. It is interesting to notice that the two eccentricity lines e = .41 and e = .566 in Fig. 2.13 intersect the short bearing line and the L/d = 1 line, respectively, to give nearly the same attitude angle of 60° despite the significant difference between the two contour levels. Perhaps this agreement may have not taken place if

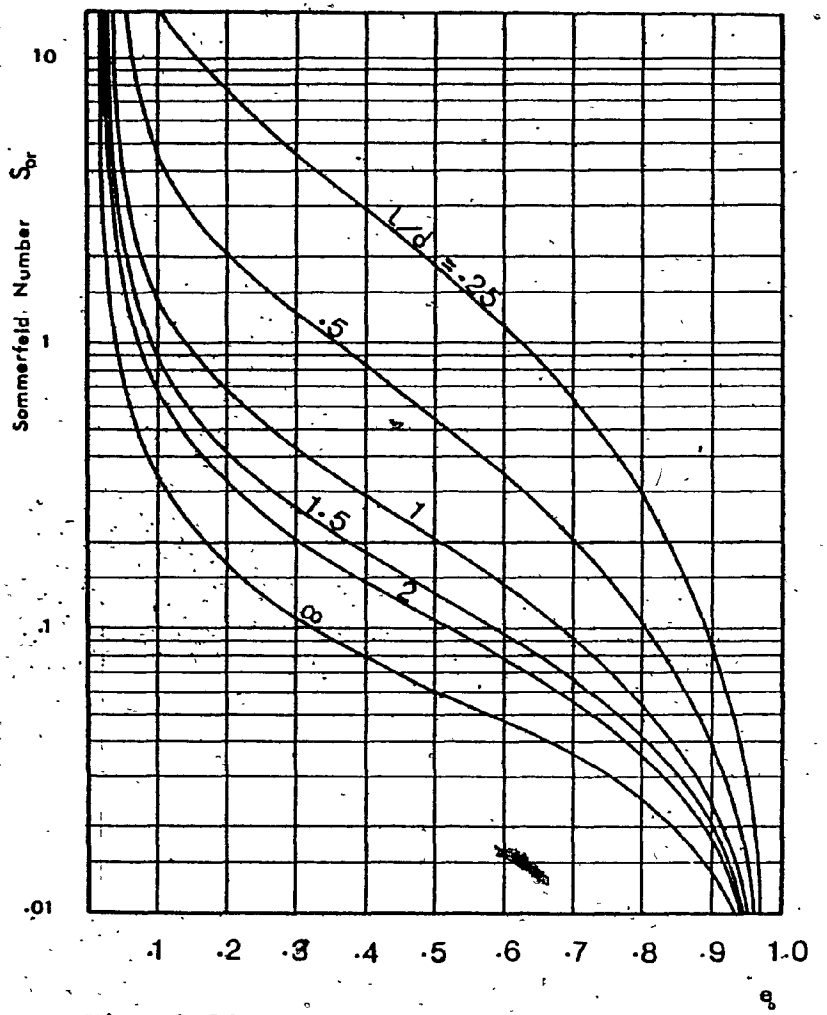

Fig. 2.12 The Sommerfeld Relation for the Present Finite Bearing.

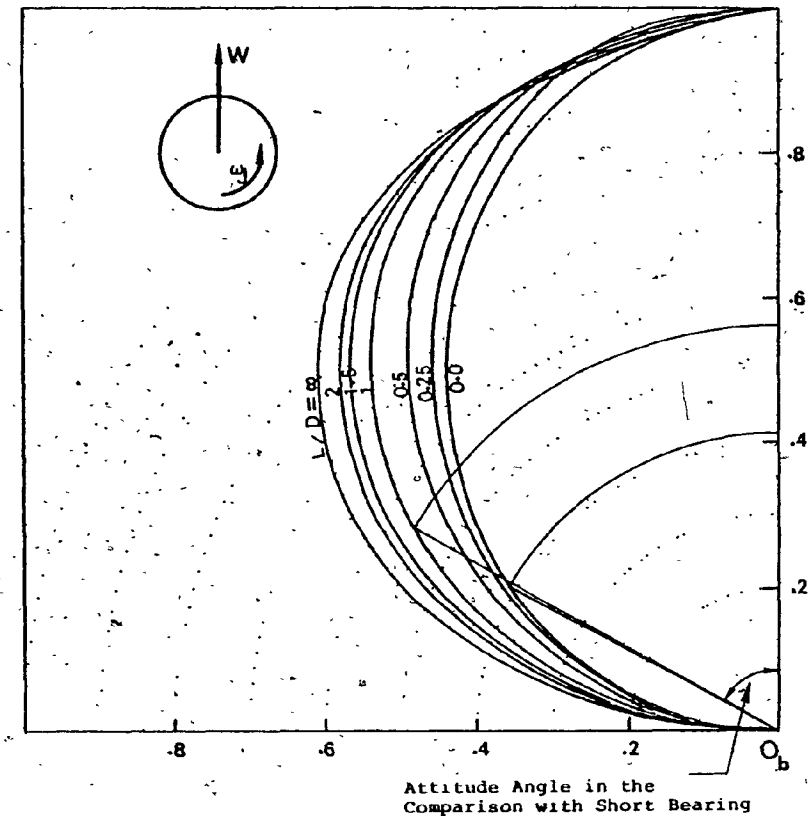

Fig. 2.13 Polar Plot of the Static Locus of the Journal.

the loading on the bearing was different, i.e. different S_{or}.

Another comparison may be carried out with recent results by Barrett, Allaire and Gunter [13] in which a modified short bearing theory is presented extending the range of short bearing application to L/d = 1.25 using a correction factor. The cases that are used for comparison are the steady state condition and the pure squeeze motion and for both cases analytical solutions that are based on variational methods are available [6,73]. The modified Sommerfeld number $4G^2S_{or}$, $G = L/d$, is plotted against the steady state eccentricity ratio e_o for L/d ratios .5 and 1.25 in Fig. 2.14. Besides the short bearing and the corrected short bearing curves [13], the present and other analytical solutions are also presented in Fig. 2.14. The corrected short bearing is in good agreement with the analytical solution particularly at the smaller L/d ratio whereas the finite bearing of the present analysis is in better agreement with the analytical solution independent of the L/d value.

In Fig. 2.15 a comparison is made for a pure squeeze condition which represents a case of a squeeze film damper. Neglecting the cavitation region, the film force due to squeeze velocity only can be determined from equation (2.24) and is

$$F_r = -\frac{L\mu d^3}{2c^2}\,\dot{e}\,E_4 \quad \text{for } \dot{e} > 0$$

This value of F_r is used in plotting the finite bearing curves in Fig. 2.15, again for L/d ratios .5 and 1.25. As it can be

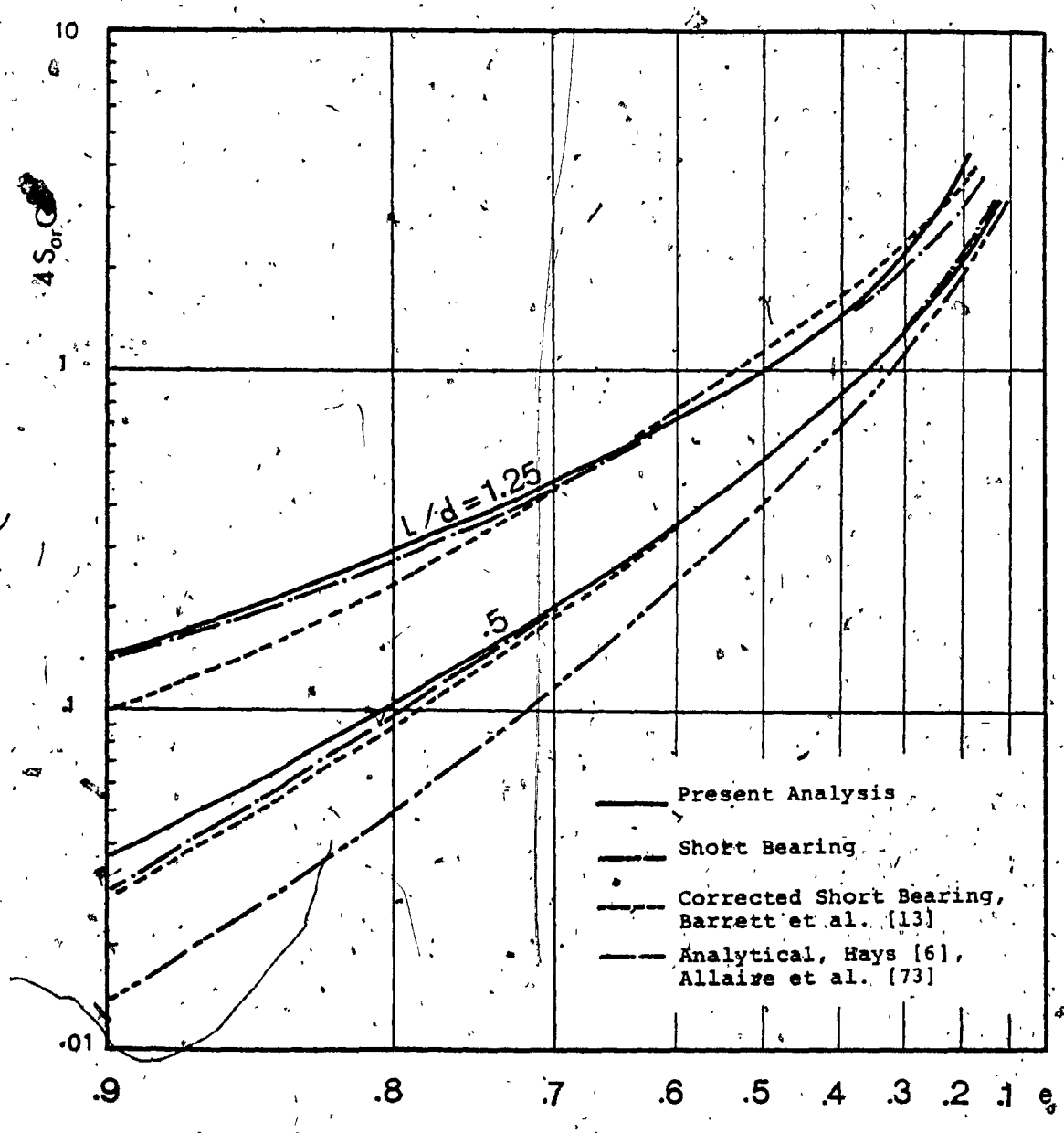

Fig. 2.14 Comparison Between Present and Previous Results in the Steady State Condition.

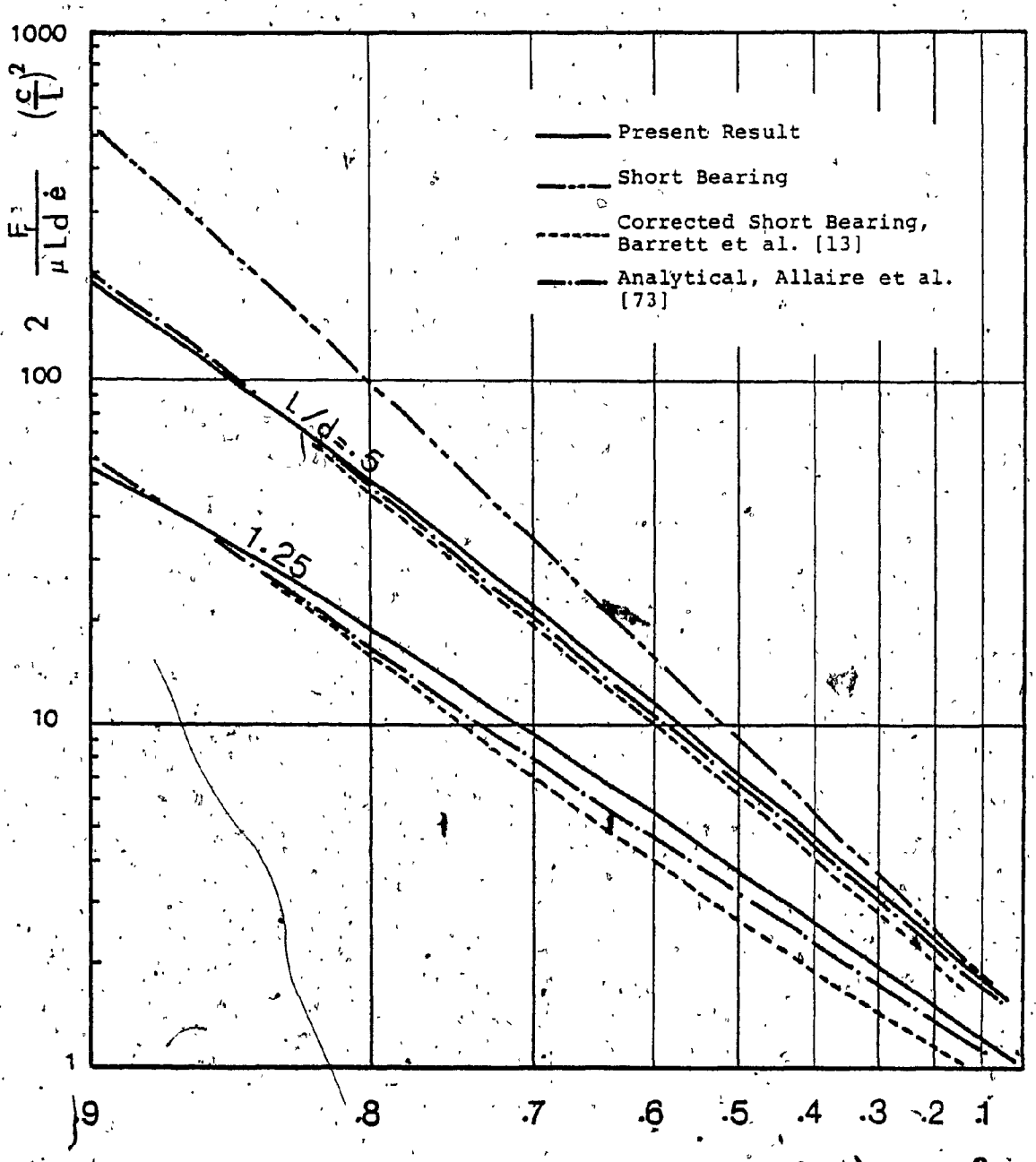

Fig. 2.15 Comparison Between Present and Previous Analysis for a Squeeze Motion Case.

seen from Fig. 2.15, the finite bearing curves and the corrected short bearing curves are both in good agreement with the analytical curves [73]. However, it must be emphasized that the finite bearing results presented here have the versatility in application for any L/d ratio with the simplicity of the well known long and short bearing approximations.

2.16 Discussion

The equation of motion of the finite journal bearing is developed with an appropriate treatment for the partial film case. The hydrodynamic forces derived are particularly adequate for nonlinear dynamic analysis since they are decoupled from the Reynolds' equation and therefore preserve the simplicity of the short and long bearing solutions but with better accuracy.

Two partial film models are developed for the finite bearing, namely the π film and the $3\pi/2$ film models which can be used either independently or jointly. The $3\pi/2$ film can be used adequately for small eccentricity ratios when the supply pressure is significant compared to the hydrodynamic pressure and also for a pure squeeze film case, otherwise the π film model is the one to be used. Both film models are shown to be upper and lower bounds for the time dependent boundary model which is the basic film model, and consequently the qualitative behaviour of the latter film model can be examined with certainty by evaluating the corresponding solutions of

both film models. The comparison presented demonstrates the accuracy of the developed model independent of the L/d ratio. The next chapter is devoted to the solution and stability analysis of the finite bearing equations.

CHAPTER 3

NUMERICAL SOLUTION AND STABILITY ANALYSIS FOR LINEAR AND NONLINEAR EQUATIONS OF MOTION OF THE FINITE JOURNAL BEARING

3.1 Numerical Solution of the Equation of Motion and the Numerical Methods

Stability of a numerical integration procedure is a joint property between the differential equation under solution and the numerical technique employed whereas the system instability is a basic property of the system itself and can not be altered by changing the numerical technique chosen. However, in case an instability of the solution procedure is observed, it is a fair bet to switch to a different numerical technique.

The fourth order Runge-Kutta and the Hamming's predictor-corrector methods are both used alternatively in the present analysis. Whereas Hamming's predictor-corrector was reported to exhibit numerical instability when applied on a nonlinear rotor system [51], it was found to be sufficiently accurate in solving the short and long bearing equations [40]. A comparison was made by applying both numerical techniques on the finite bearing equation (2.26) and for all the different examples investigated including the stable and the unstable cases, the difference between the solutions obtained using the Runge-Kutta method and

Hamming's method were so small that it can not be distinguished on a computer plot. Since the Hamming's predictor-corrector method requires considerably less computation time than the Runge-Kutta method, the former method is used in most cases whereas the latter method is used only as a check in those cases where instability is observed.

A one hundred step per journal revolution, namely 2π for the dimensionless system (2.26), is used throughout this investigation whereas the step size is automatically reduced to half its value if the set error bound is violated. An error bound of $e \times 10^{-3}$ to $e \times 10^{-4}$ is used in this case.

It should be noted that, besides the initial conditions, the solution is completely defined for specific L/d ratio by any two of the following three parameters:

S , the bearing dynamic parameter

e_0 , steady state eccentricity ratio

W_n , dimensionless load or alternatively the dimensionless speed $\omega_s = \sqrt{1/W_n}$

An alternative formulation of the journal bearing equation of motion (2.26) in the cartesian form is

$$\begin{aligned} \overset{oo}{X} + C_{XX}(X,Y)\overset{o}{X} + C_{XY}(X,Y)\overset{o}{Y} + K_{XX}(X,Y)X + K_{XY}(X,Y)Y &= W_{nX} \\ \overset{oo}{Y} + C_{YX}(X,Y)\overset{o}{X} + C_{YY}(X,Y)\overset{o}{Y} + K_{YX}(X,Y)X + K_{YY}(X,Y)Y &= W_{nY} \end{aligned} \tag{3.1}$$

where the equilibrium position is given by:

$$K_{XX}(X_0,Y_0)X_0 + K_{XY}(X_0,Y_0)Y_0 = W_{nX}$$

$$K_{YX}(X_0,Y_0)X_0 + K_{YY}(X_0,Y_0)Y_0 = W_{nY} \qquad (3.2)$$

Here C_{XX}, K_{XX}, ... are nonlinear functions in the displacement X and Y only and are presented in Appendix B.

One direct advantage of this formulation is that the linearized damping coefficients that correspond to an equilibrium point (X_0,Y_0) are obtained by the evaluation of $C_{XX}(X,Y)$, ... at (X_0,Y_0) which can also be utilized later in the stability analysis.

3.2 Comparison of the Numerical Results with Experimental Results for the Full Film Case

The main reason for this comparison is not only to investigate the accuracy of the finite full film bearing solutions, but also to provide an additional support to all the developed eccentricity functions E_1, E_2 ... which are developed jointly in the past Chapter. In an experiment reported by Mitchell, Holmes and Byrne [40], a bearing with a diameter, d = 1.25 in, length L = .75 in., and a circumferential groove of .11 in. was used. The experiment started with a partial film with the journal being stationary. Then the supply pressure was raised suddenly to a value just enough to allow a full film formation. The journal, in turn, climbed on an unstable spiral. The traces recorded for four different combinations of the dimensionless load W_n and the

steady state eccentricity ratio e_0 are reproduced in Fig. 3.1.

The L/d ratio, taking the groove into account, is approximately calculated to yield G = .5. The comparative solutions using the present finite bearing equations for the same values of W_n and e_0 are presented in Fig. 3.2. The numerical solutions in Fig. 3.2 show a very good agreement with the corresponding experimental records in Fig. 3.1. The shape and the number of loops are almost the same before the journal orbit surrounds the origin. The present analytical solution shows the orbits growing faster to circular shapes than the corresponding experimental results. Mitchell, Homes and Byrne [40] also noticed that the journal never reaches the clearance circle but rests in a circular limit cycle with a diameter little less than the clearance circle diameter. This is in contradiction to the theoretical solution which shows a continual growth in the orbit. This point is discussed in detail in a separate section after the stability analysis.

3.3 Comparison Between the Different Partial Film Models

The effect of the film extent on the journal transient behaviour may be demonstrated by a comparative analysis between the π and the $\frac{3\pi}{2}$ film models. The journal stability status varies between asymptotic stability, orbital stability and instability depending on the steady state eccentricity e_0, the dimensionless speed ω_s and the L/d ratio. In Fig. 3.3 a case of asymptotic stability with L/d = .25, e_0 = .75 and

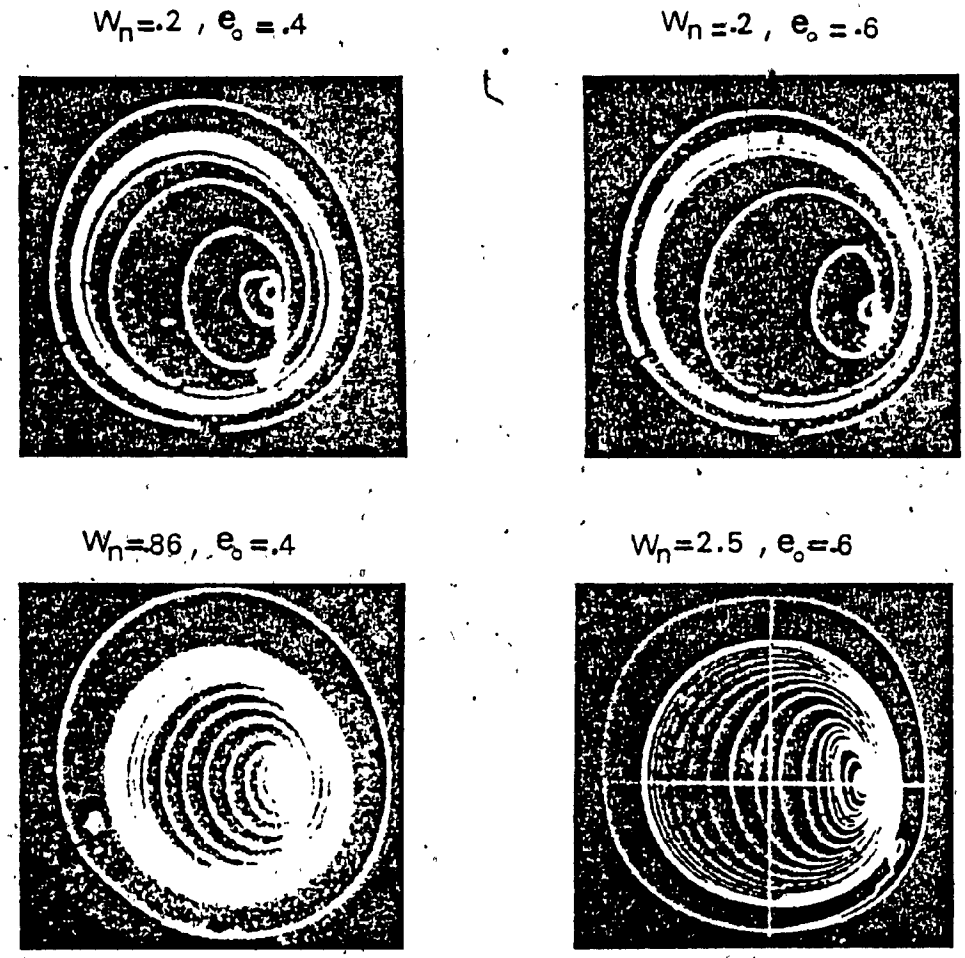

Fig. 3.1 Experimental Traces for Full Film Bearing.
Courtesy; Mitchell, Holmes and Byrne [40].

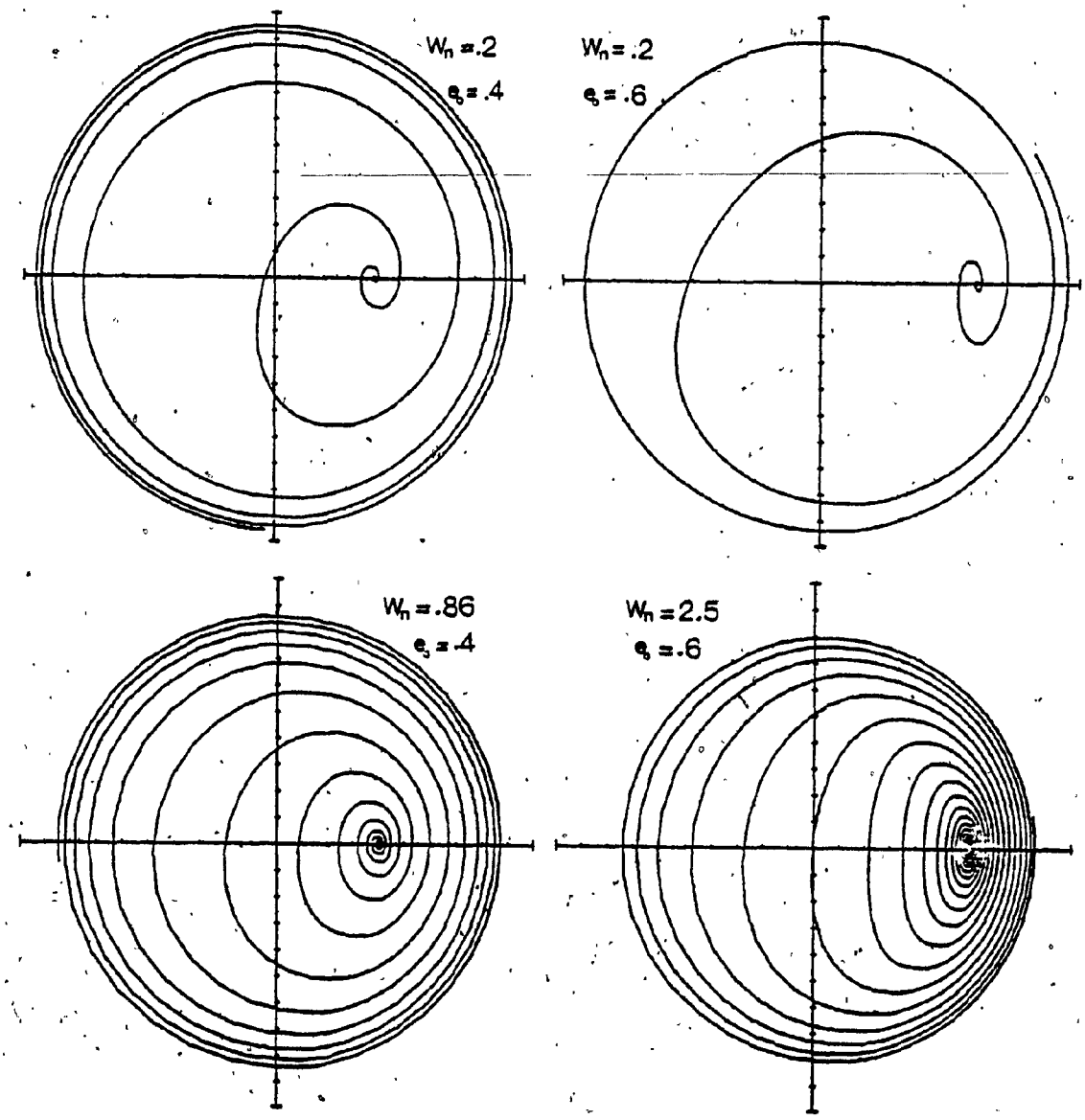

Fig. 3.2 Numerical Solutions of the Full Film Bearing for Comparison with the Experimental Traces.

$\omega_s = 3$, are presented for the $3\pi/2$ and the π film models. It may be seen that the qualitative behaviour of both the partial film models is roughly the same. As can be seen from the figure, the unstable transient solutions of the π model grows almost immediately into larger loops close to the clearance circle whereas those unstable solutions that correspond to the $3\pi/2$ film progress closer to the clearance circle through a few intermediate loops. In the stable cases shown, the solution corresponding to the π film approaches the equilibrium point faster than that corresponding to the $3\pi/2$ film model. It can also be concluded that the transient solutions of the $3\pi/2$ film in both stable and unstable conditions behave more smoothly than those of the π film model. A stronger conclusion would then be that the journal must be stable for a case when both film models predict stability and the same is valid for instability since it was previously verified that the $3\pi/2$ film and π film are essentially the upper and lower bounds for the basic dynamic film extension with a time dependent boundary.

Fig. 3.4 presents a case of orbital stability for the $3\pi/2$ film model associated with the corresponding solution using the π film. The transient solution of the π film in Fig. 3.4 decays asymptotically to the equilibrium point whereas the solution corresponding to the $3\pi/2$ film model reaches a definite limit cycle. These limit cycles exist in the vicinity of the stability boundary. Therefore the $3\pi/2$ film extension provides a wider range of orbital stability

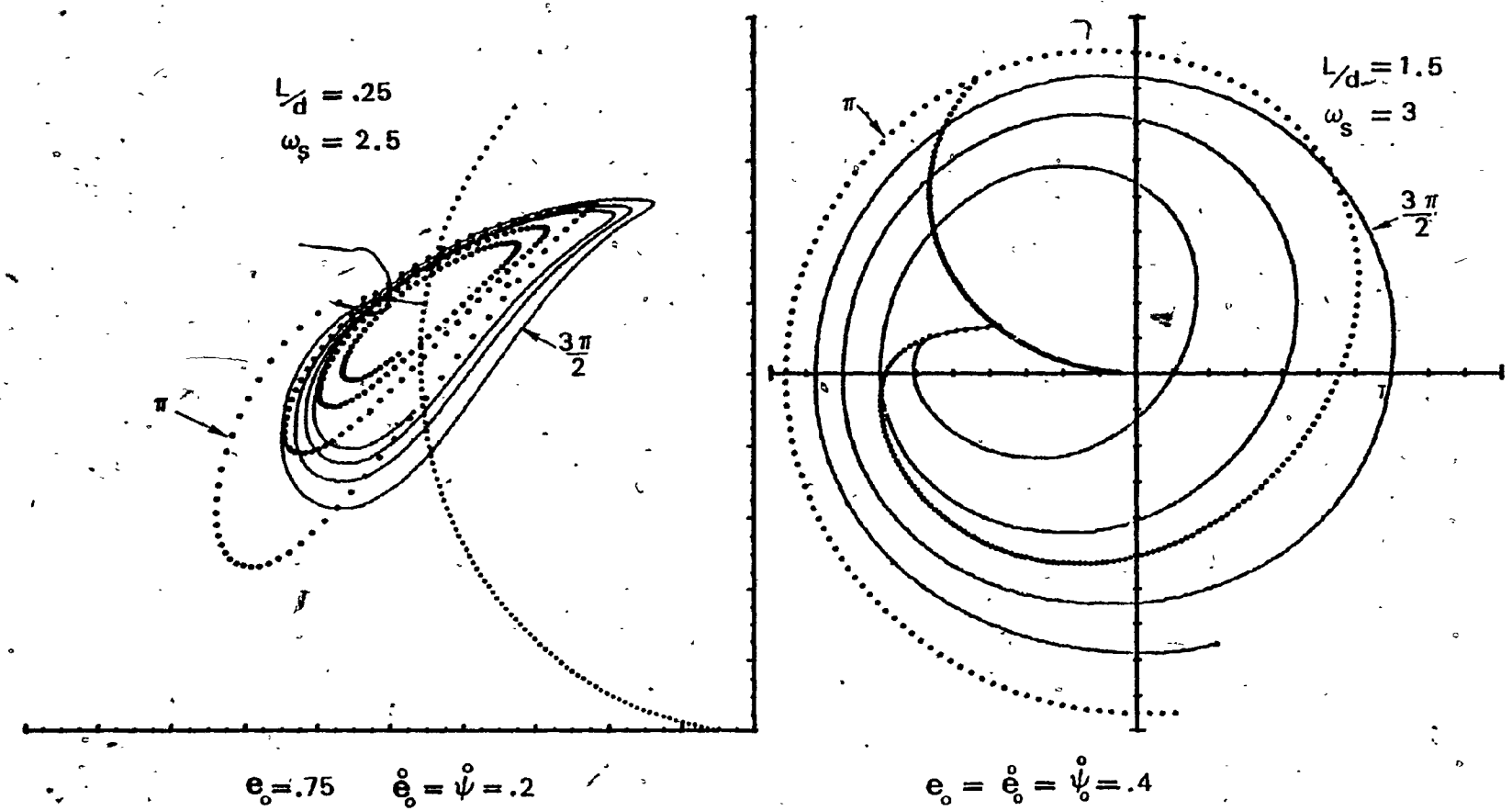

Fig. 3.3 Comparison Between the $3\pi/2$ and the π Film Models in the Stable and the Unstable Conditions.

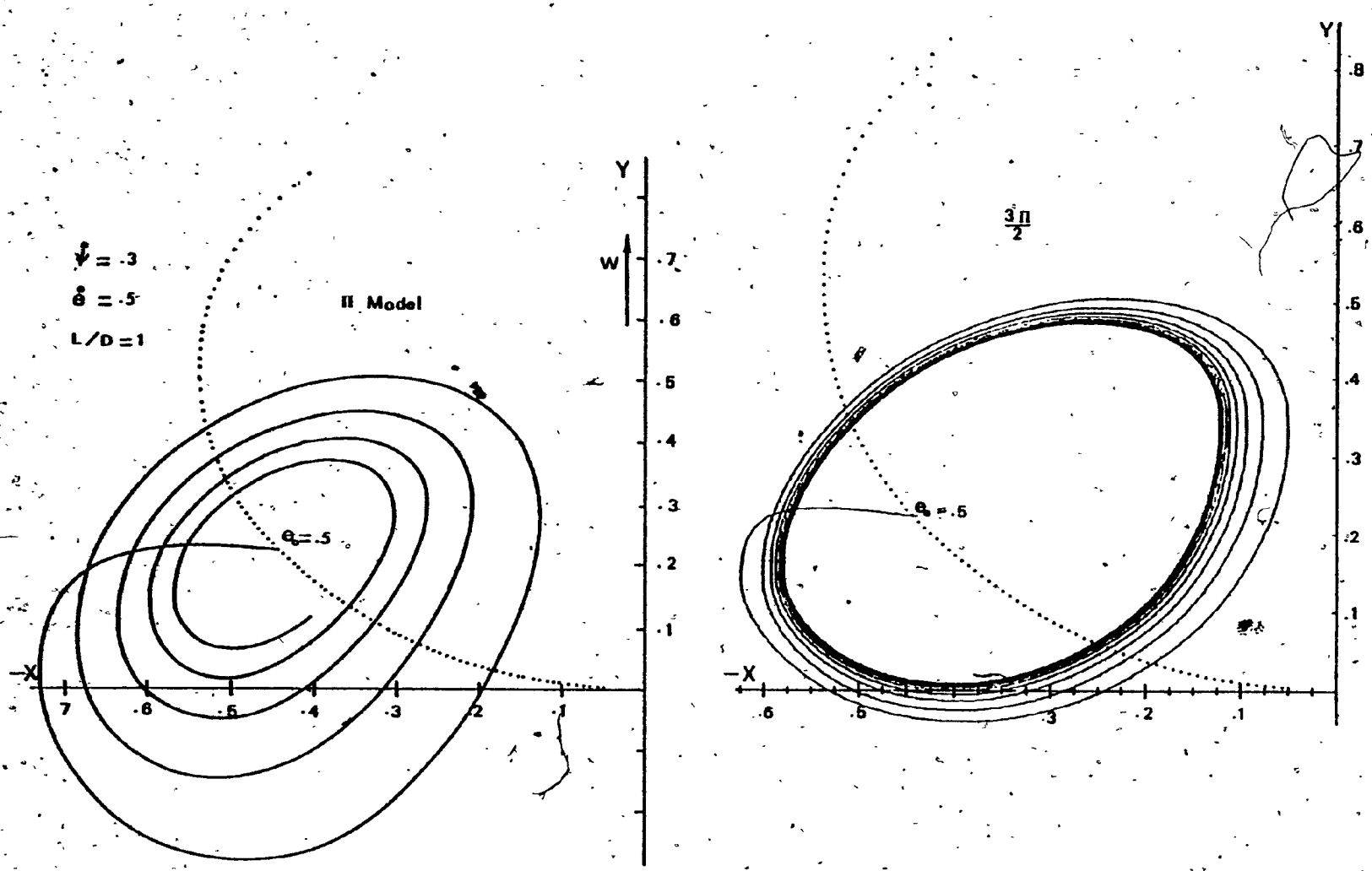

Fig. 3.4 A Limit Cycle Case for the 3π/2 Film Model and the Corresponding Solution of the π Film Model.

than the π film model. Specific and conclusive details about the qualitative behaviour of the journal bearing can only be deduced with an organized investigation for a stability analysis.

3.4 Stability Analysis

Two equilibrium states are of interest. They are: (i) the stationary equilibrium solution and (ii) the orbital equilibrium solution, which is essentially a periodic solution. Correspondingly, two well known stability definitions are: (i) the stability in the sense of Liapunov which defines the stability of a stationary equilibrium solution and (ii) the stability in the sense of Poincare which defines the orbital stability [79]. The following statements correspond to both of the above stability theories with the general term equilibrium state referring to either a stationary equilibrium solution or an orbital equilibrium solution.

If the trajectories of the perturbed motion tend to remain in a bounded region in the neighbourhood of the equilibrium state, the equilibrium state is said to be stable. If the trajectories approach the equilibrium state asymptotically, the equilibrium state is asymptotically stable. If the perturbed motion does not behave in accordance to the above two cases, the equilibrium state is then unstable. Stability in the large implies stability under any arbitrarly large perturbation. In the present analysis,

it will be sufficient to define a case of closed journal orbit as an orbital stability case without involving further details on orbital stability.

The stability analysis branches to linear and non-linear approaches in the following sections.

3.4.1 Stability Investigation Using a Linear Analysis

Stability using a linear approach is a process of examining the roots of the characteristic equation of the dynamical system around an equilibrium point. Such an approach is limited to cases of infinitesimal perturbations which is an assumption that qualifies the linear system itself but unfit in extracting detail features such as orbital stability [79]. However, the linear analysis serves at least as a base for detailed conclusions that only a nonlinear analysis can provide. In some special cases the assumption of infinitesimal perturbations is quite tolerable and consequently the results of the linear methods may be expected to represent those of the nonlinear system closely which is the case observed here for the π film model as may be seen later in this section.

Considering the equations of motion of the finite bearing in the space variables and presented in the compact form

$$\{\overset{0}{Z}^{*}\}_{4x1} = \{Z^{*}(z_1^{*}, z_2^{*}, \ldots)\}_{4x1} \qquad (3.3)$$

which is written in detail for both cartesian and polar

coordinate systems in equations (C.1) and (C.2) in Appendix C. Here $\bar{Z}^*$ are general nonlinear functions in the phase variables $\bar{z}^*$ or z_j^* with $j = 1,2,3,4$. It is assumed that the journal undergoes a small perturbed motion specified in the phase space by the variables $\bar{q}$ from an initial equilibrium position given by the coordinates $\bar{z}_0^*$ which is determined from the system of equation (3.3) with

$$\{0\} = \{Z^*(Z_{10}^*, Z_{20}^* \ldots)\}$$

Then expanding the nonlinear functions $\bar{Z}^*$ around the equilibrium point $\bar{z}_0^*$, by the Taylor series and retaining only the first order terms in the expansion, yields the homogenous linear system

$$\{\dot{q}\} = [A_\ell]\{q\} \tag{3.4}$$

with

$$a_{ij} = \left.\frac{\partial Z_i^*}{\partial z_j^*}\right|_{\bar{z}^* = \bar{z}_0^*}$$

The a's are listed in Appendix D. System (3.4) describes the perturbed motion from an equilibrium position. The characteristic equation for the above system is determined as

$$\lambda^4 + C_1\lambda^3 + C_2\lambda^2 + C_3\lambda + C_4 = 0 \tag{3.5}$$

where the coefficients C_1, C_2, C_3 and C_4 are given by

$$
\begin{aligned}
C_1 &= \frac{S}{2}\,(E_j - 2E_k/e) \\
C_2 &= \frac{S}{2e}\,[S(E_iE_\ell - E_jE_k) + E_i'e + E_i] \\
C_3 &= \frac{S^2}{4e}\,[E_kE_\ell + E_iE_j + 2E_k'E_i - 2E_kE_i'] \\
C_4 &= \frac{S^2}{4e}\,[E_i'E_i + E_k'E_k]
\end{aligned}
\tag{3.6}
$$

and are evaluated at the equilibrium point $\bar{z}_0^*$. The prime on the eccentricity function, namely E', indicates the total derivative $\frac{dE}{de}$ since E_i, E_j ... are functions of the eccentricity functions E listed in Table 2.2, but are used here with the adjustments, $\zeta = 1$ and $E_5 = E_4$ which are needed in the present linearization procedure. The first restriction is justified by the assumption of small perturbations while the second considers a positive squeeze velocity from the two cases given in Table 2.2.

A necessary and sufficient condition for the equilibrium point $\bar{z}_0^*$ to be asymptotically stable is that all the real parts of the roots $\lambda_j (j = 1,2,3,4)$ of equation (3.5) be negative. The Routh-Hurwitz criterion defines the necessary and sufficient condition, for all the roots λ_j to have negative real parts, to be that all the minor determinants of the matrix

$$
\begin{bmatrix}
C_1 & 1 & 0 & 0 \\
C_3 & C_2 & C_1 & 1 \\
0 & C_4 & C_3 & C_2 \\
0 & 0 & 0 & C_4
\end{bmatrix}
$$

be positive. There are then four such minor determinants given by

$$D_1 = C_1$$

$$D_2 = C_1C_2 - C_3$$

$$D_3 = C_3D_2 - C_1^2C_4$$

$$D_4 = C_4D_3$$

Using the expression (3.6), and since E_i and E_j are always positive and E_k is always negative for all possible values of e and L/d and for all film models, referring to Table 2.2, it can be shown that

$$C_1 > 0 \quad \text{and} \quad C_4 > 0$$

This means that D_1 is always positive and the condition $D_4 > 0$ is implicitly included in the condition $D_3 > 0$. Therefore only two conditions to be satisfied are

$$D_2 > 0 \tag{3.7}$$

and $$D_3 > 0 \tag{3.8}$$

By inspection, it can be stated that condition (3.8) is stronger than (3.7). That is, if conditon (3.8) is satisfied then condition (3.7) is automatically satisfied. Using equation (3.6) in condition (3.8) gives,

$$S > e\,\frac{Q_4Q_5}{Q_2Q_3} + \frac{Q_3}{Q_2Q_4} - \frac{Q_1}{Q_2} \tag{3.9}$$

where

$$Q_1 = E_i' e + E_i$$

$$Q_2 = E_i E_\ell - E_k E_j$$

$$Q_3 = E_k E_\ell + E_i E_j + 2E_k' E_i - 2E_k E_i'$$

$$Q_4 = E_j - 2E_k/e$$

$$Q_5 = E_i E_i' + E_k E_k'$$

and

S is the bearing dynamic parameter given by equation (2.18a).

For the full film bearing

$$Q_1 = Q_3 = 0$$

whereas Q_2, Q_4 and Q_5 possess a definite value. This gives the indefinite condition

$$S > \infty \quad , \text{ for the full film case} \qquad (3.10)$$

Condition (3.10) implies that a full film bearing is unstable for all values of the governing parameters. The equality limit which can be obtained from the inequality (3.9) describes the stability boundary for the partial film models. The stability boundaries for the $3\pi/2$ and π film models are plotted in Figs. 3.5 and 3.6 respectively, for different values of the L/d ratios. The ordinate ω_s in these figures are the dimensionless speed, which is frequently called the critical mass, expressed by

$$\omega_s = 1./\sqrt{W_n} = \omega_j \sqrt{cm/W}$$

and it is introduced in relation (3.9) through the use of equation (2.28).

For both the partial film models, every stability boundary line for a specific L/d ratio lies entirely between the two lines of the next longer and next shorter bearings, that is next larger and next smaller L/d curves. This trend is different from some of the results reported by Holmes [43] as well as by Badgely and Booker [44] where curves that correspond to different L/d ratios, such as the long bearing and Warner's finite bearing in [44], intersect and crossover. There is no physical or mathematical reason, other than the use of perhaps inappropriate mathematical models, for such a trend. The condition (3.9) is built from the eccentricity functions $E_1, E_2, \ldots$ and their derivatives with respect to the eccentricity ratio e. As can be seen from the figures for the eccentricity functions in Chapter 2, no intersection takes place between any of the different finite bearing curves over the entire eccentricity range. For this particular reason the intersections in Fig. 3.5 between different curves take place at a single common point where $e_0 = .77$ and after which all curves are reversed. Still, every one of these curves lies entirely between the two curves corresponding to the next shorter and longer bearings. However the stability boundary line of the short bearing for small perturbation [44] can be identified as the upper limit for the stability curves of the π model.

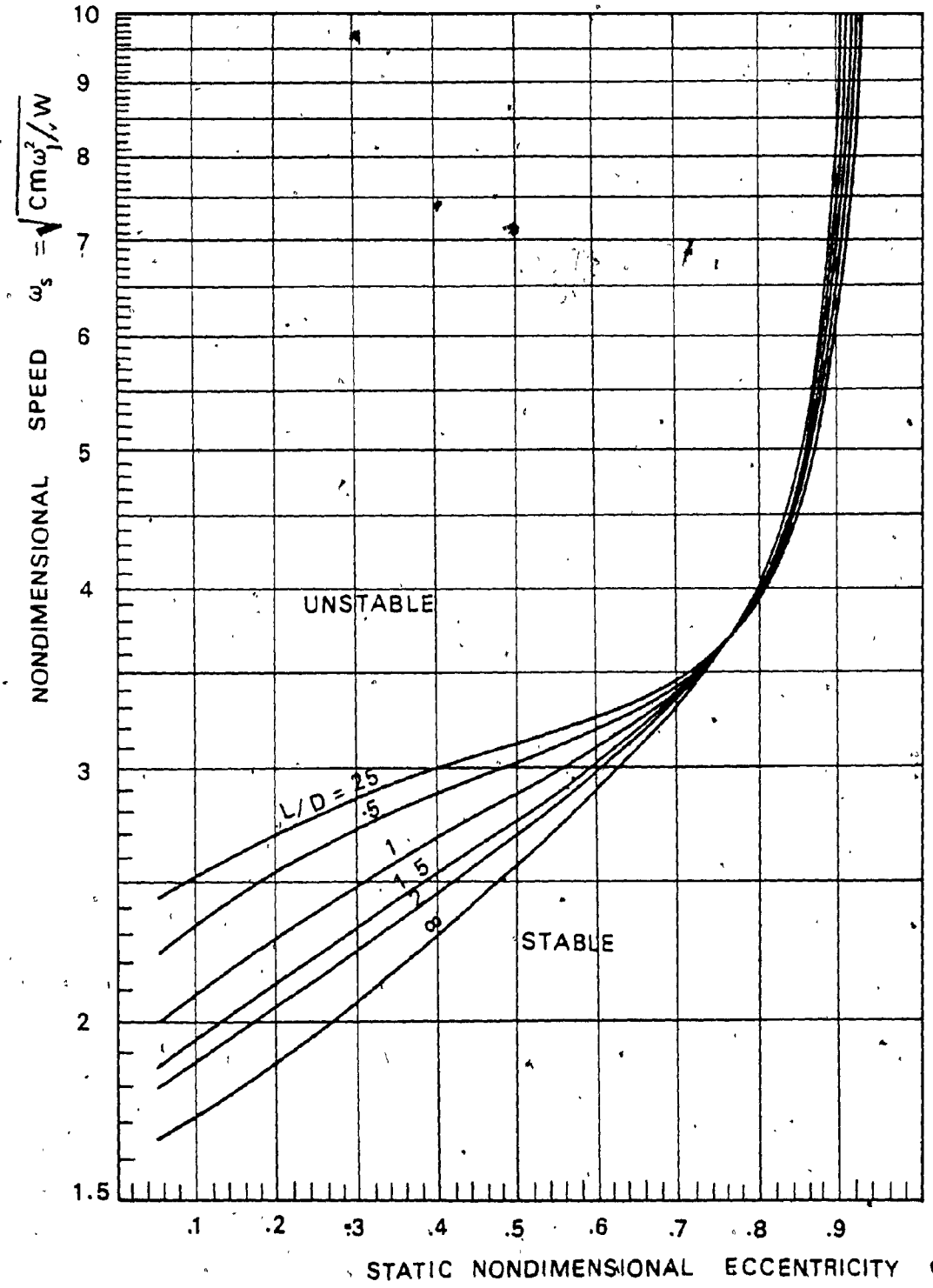

Fig. 3.5 Stability Limit for the $3\pi/2$ Film Bearing by Linear Analysis.

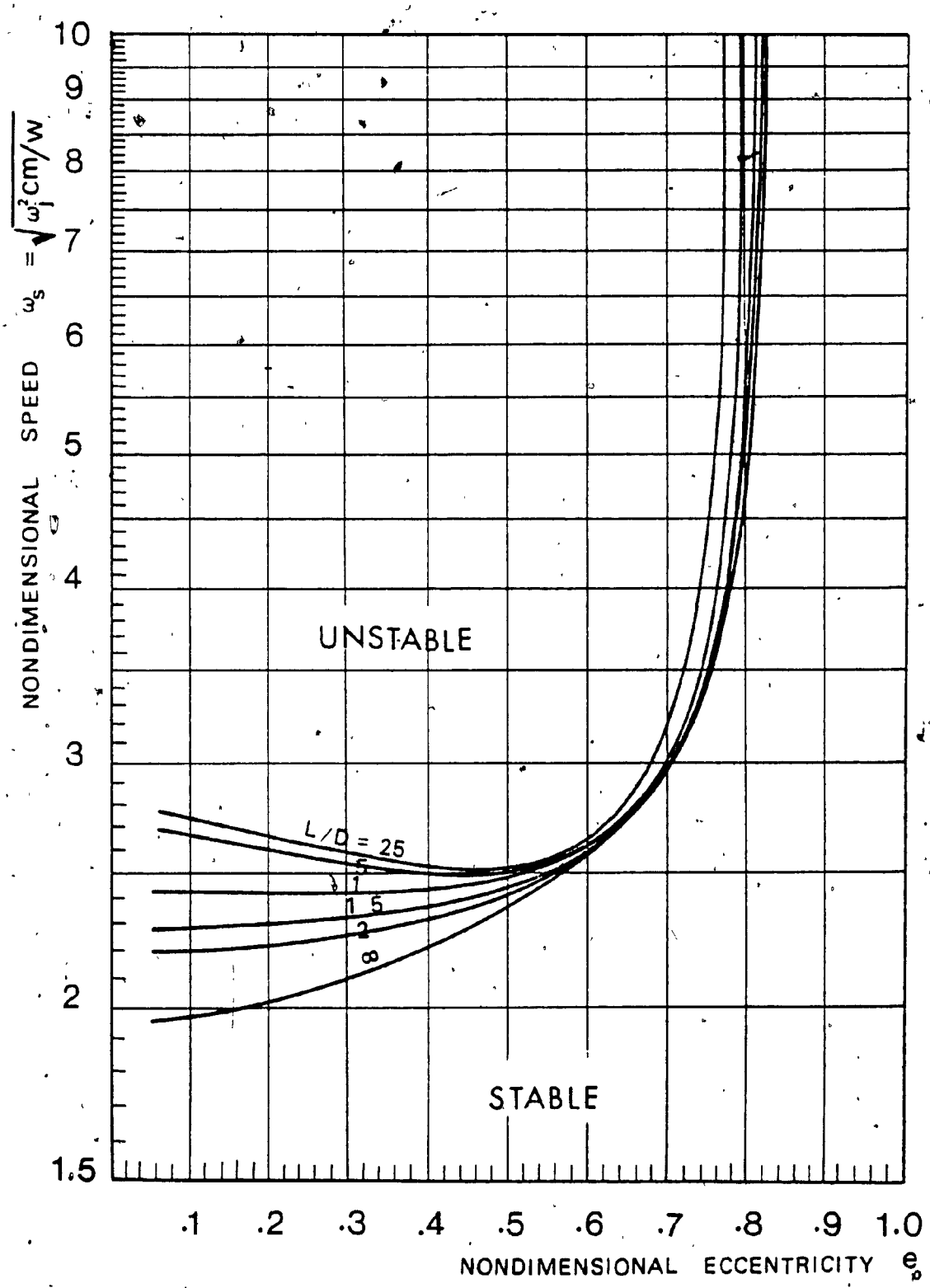

Fig. 3.6 Stability Limit for the π Film Bearing by Linear Analysis.

Numerous transient solutions of the equation of motion with the $3\pi/2$ film have indicated the existence of a different stability region than that shown in Fig. 3.5. A considerable part of these solutions was found to yield limit cycles. The observed difference is due to two reasons: (i) the linearization procedure of the $3\pi/2$ film model included the assumption that $\overset{0}{e} > 0$ or $E_5 = E_4$, with reference to Table 2.2, (ii) the orbital stability cannot be assessed using linear models. The assumption $\overset{0}{e} > 0$ is not that severe while the point (ii) is stronger since the nonlinear stability analysis actually extends the stability region of the $3\pi/2$ film model but with an orbital stability subregion as will be seen in the next section.

3.4.2 Stability Behaviour Using Nonlinear Analysis

Further details on the stability and instability regions can now be investigated in the neighbourhood of the stability boundary that is already presented. As mentioned earlier, the linear approach for stability analysis is incapable of deducing the orbital stability information and is limited to infinitesimal perturbations. Therefore an assessment on the stability details may require examining the nonlinear system itself and is done by integrating the equations of motion numerically. For this nonlinear study, a bearing with a L/d ratio 1 is considered. The rate of decay or growth of the journal loops defines the proximity of the investigated system status (e_0, ω_s) from the limiting

stability border line. The solution process in the vicinity of the stability boundary may require a considerably large number of loops to distinguish between a stable orbit, instability or asymptotic stability as the case may be.

In this analysis, the π film model is found to be most susceptible to slight changes in the dimensionless speed ω_s and to the initial velocity conditions. A relatively small change in the initial velocities is introduced to check the sensitivity of this model. For example, Fig. 3.7 presents two solutions for the π film model with the parameters $e_0 = .3$, $\omega_s = 2.4$ and different initial conditions. Here a change in the initial velocities from $\overset{0}{e}_0 = .2$ and $\overset{0}{\psi}_0 = .2$ to $\overset{0}{e}_0 = .3$ and $\overset{0}{\psi}_0 = .3$ changes the state of the system from asymptotic stability to instability. The effect of the change in dimensionless speed ω_s on the stability status of the π film model is represented by two solutions in Fig. 3.8. As shown in the figure, a reduction in the ω_s from a value 2.5 to 2.4, which is quite small, changes the state of stability from an orbital stability state to an asymptotically stable condition.

The $3\pi/2$ film model has smoother characteristics than the π film model. For the $3\pi/2$ film model, an increase in the dimensionless speed ω_s changes the stability state from asymptotic stability to orbital stability, which starts with a very small orbit size and smoothly grows bigger with increasing ω_s. As ω_s is further increased, the size of the orbit grows and takes a more circular shape. The diameter

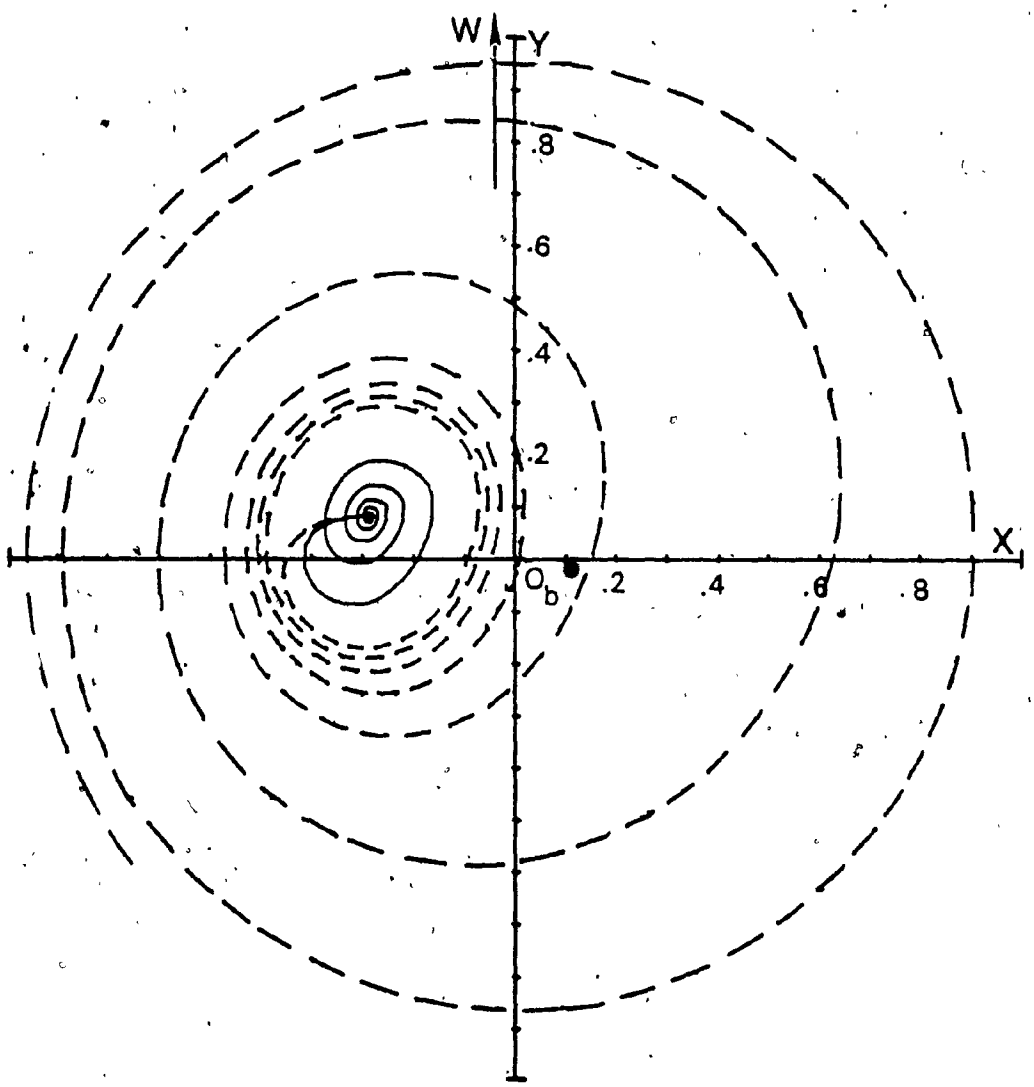

$e_o = \cdot 3$ $\omega_s = 2.4$ Π Model

——— $\dot{\psi}_o = .2$ & $\dot{e}_o = .2$

– – – $\dot{\psi}_o = .3$ & $\dot{e}_o = .3$

(Initial Conditions)

Fig. 3.7 Effect of Initial Velocities on the Transient Behaviour of the π Film Bearing.

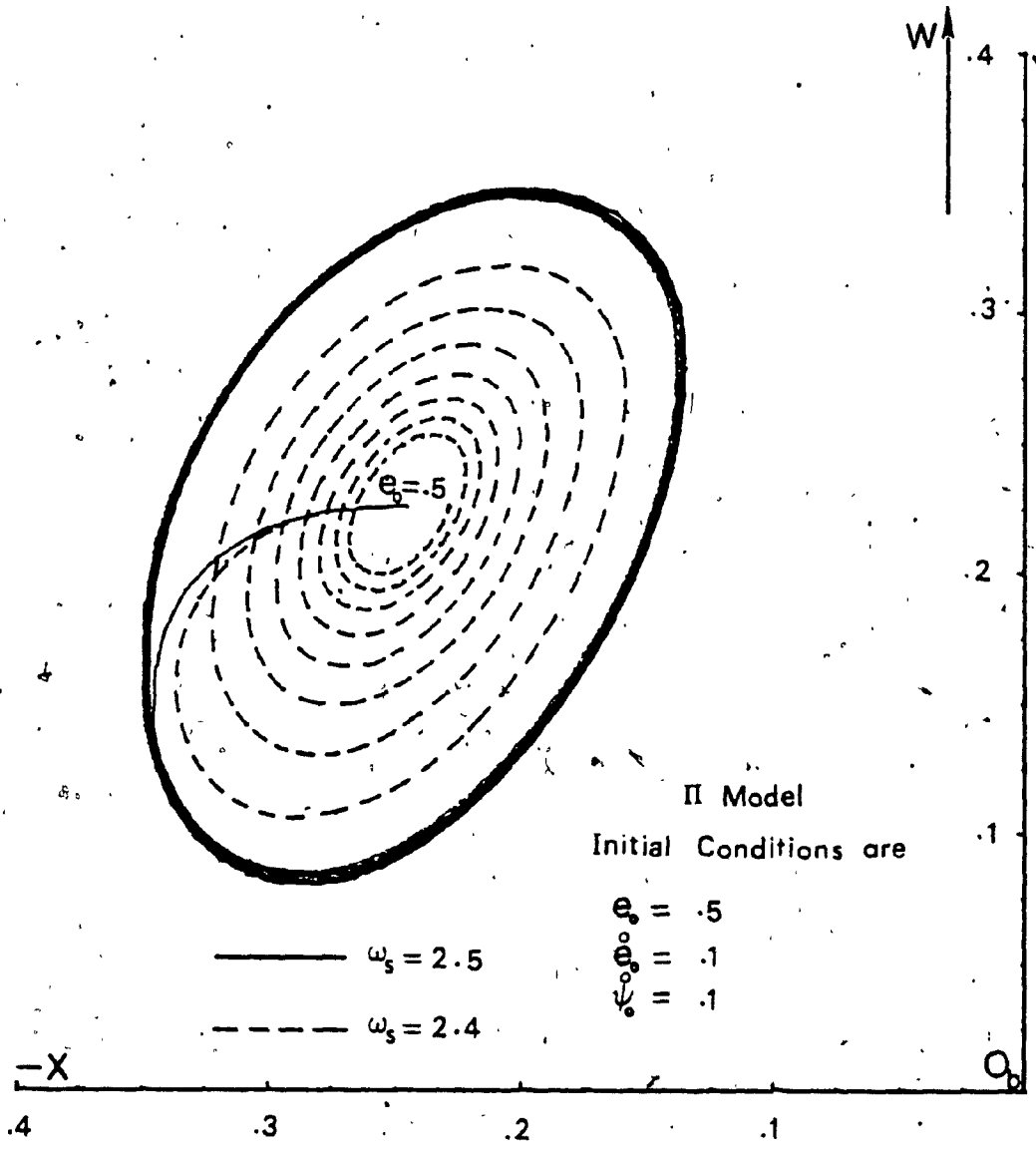

Fig. 3.8 Effect of Change in ω_s Near the Stability Limit on the Transient Behaviour of the π Film Bearing.

of the circular orbit, in turn, approaches the diameter of the clearance circle asymptotically as ω_s approaches its critical value at the instability limit line. This process is symbolized by two solutions in Fig. 3.9. The $3\pi/2$ film model is also less sensitive to initial perturbations. This property can be demonstrated best in a region close to the stability boundary where the system is supposed to be most sensitive to the magnitude of the applied perturbations. A case of orbital stability is presented in Fig. 3.10. When the initial velocities are changed from $\overset{0}{e}_0 = .1$ and $\overset{0}{\psi}_0 = .1$ to $\overset{0}{e}_0 = .5$ and $\overset{0}{\psi}_0 = .5$, which is relatively a large difference, the final limit cycle is unaffected and only the number of intermediate loops is decreased.

The adjustments arising from the nonlinear analysis for the stability boundaries of the π and $3\pi/2$ film models are presented in Figs. 3.11 and 3.12. The cases indicated as stability in the large refer to cases of asymptotic stability that remain unchanged despite the large initial perturbation applied whereas those indicated as stability in the small refer to cases that can be destabilized by a relatively large initial pulse. The magnitude of this destabilizing pulse depends on the proximity of the system to the stability boundary. It turns out that a precise determination of the stability in the large would require several parallel curves each of which would define the magnitude of the initial perturbation beyond which the system is unstable. This is found to be most tedious to achieve

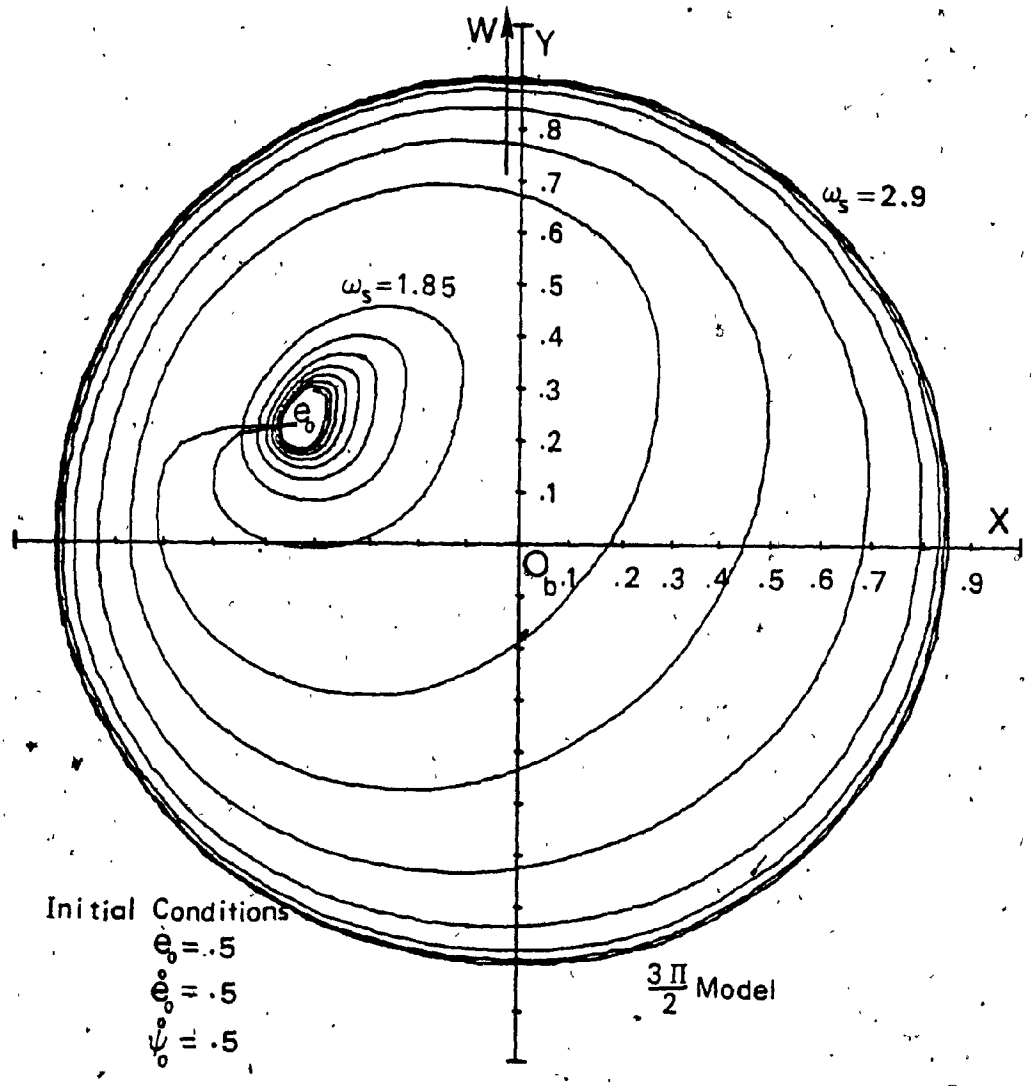

Fig. 3.9 Change of the Orbit Size Across the Orbital Stability Subregion for the $3\pi/2$ Film Bearing.

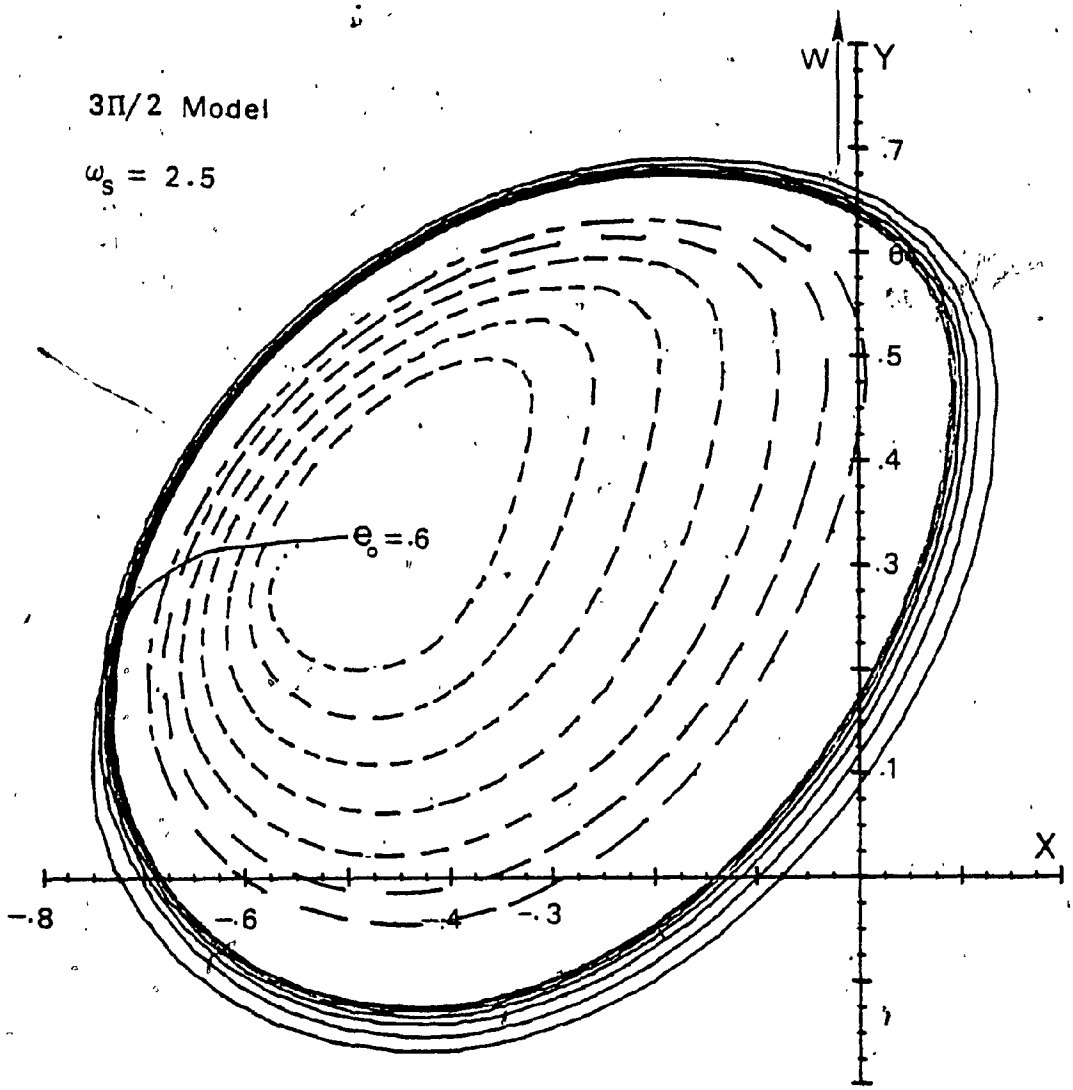

Fig. 3.10 Effect of Initial Velocities on the Transient Behaviour of the 3π/2 Film Bearing in the Orbital Stability Subregion.

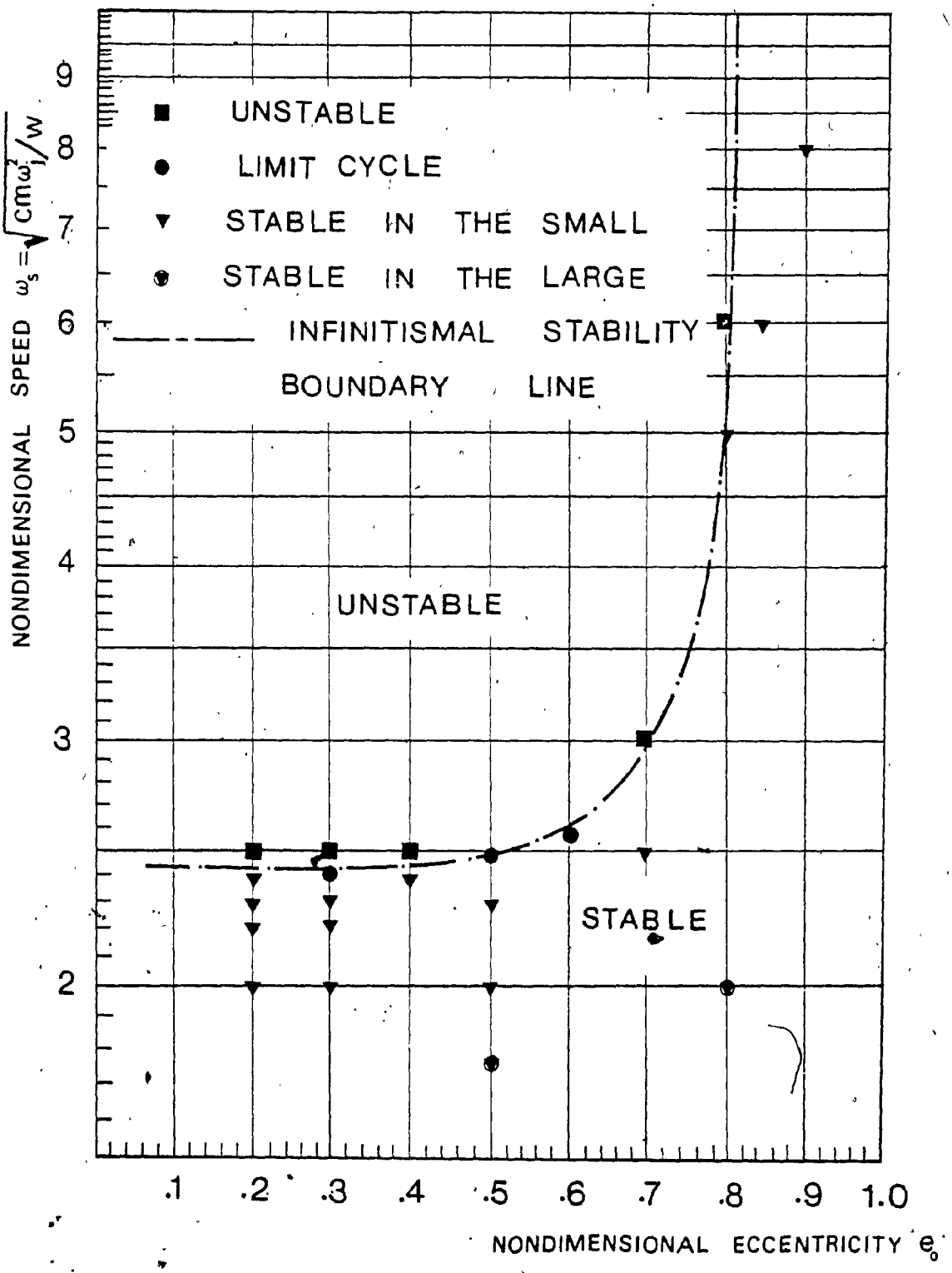

Fig. 3.11 Adjustments to the Stability Limit for the π Film Bearing, L/d = 1.

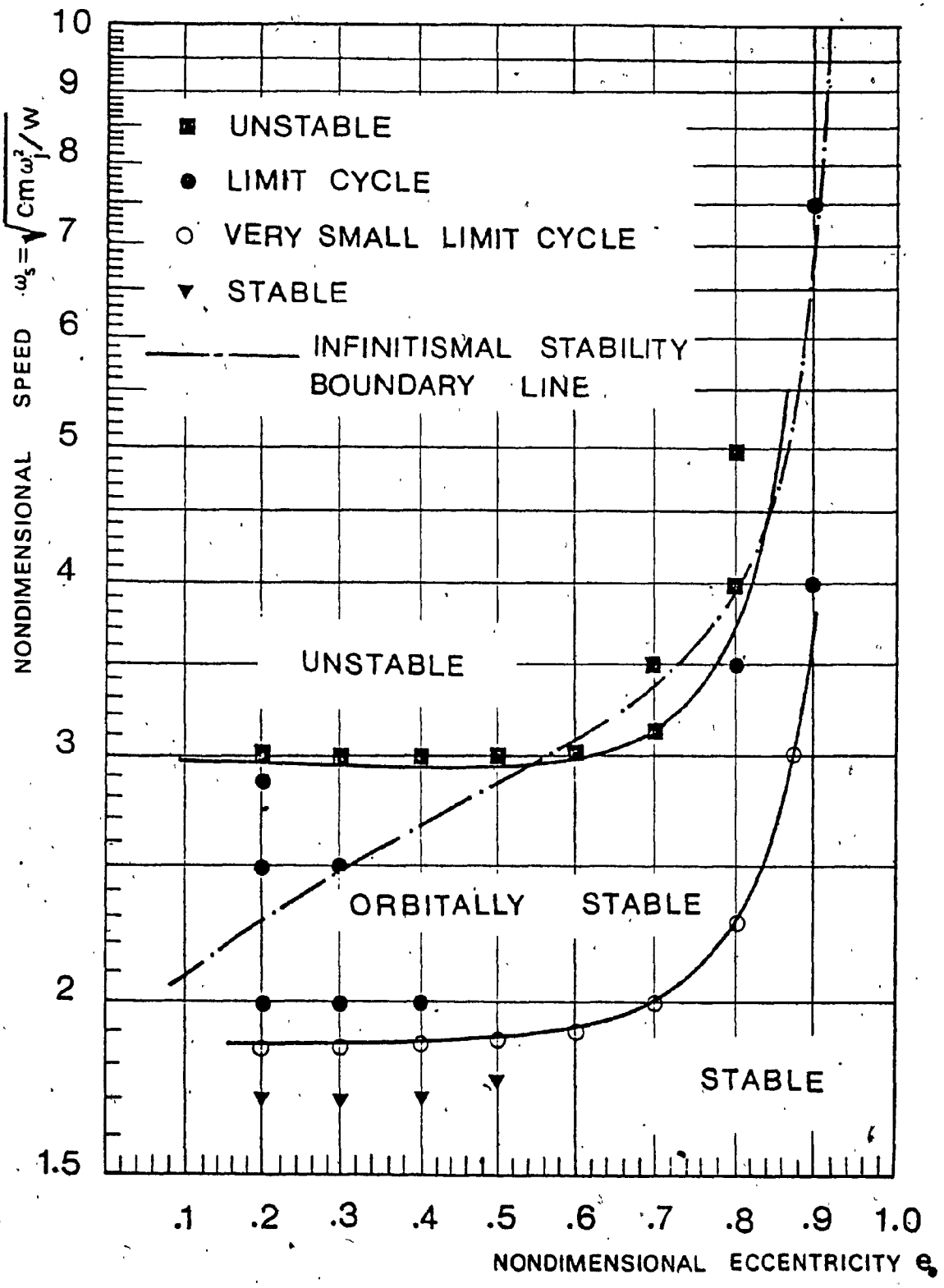

Fig. 3.12 Adjustments to the Stability Limit for the $3\pi/2$ Film Bearing, L/d = 1.

since possible sets of combinations of different magnitudes for the different initial conditions are numerous. The orbital stability subregion of the π film model is very narrow and is also dependent on the magnitude of the initial conditions. Because of this, the points in the plot for orbital stability are not connected in Fig. 3.11. On the other hand, for the $3\pi/2$ film model a relatively large subregion of orbital stability exists as seen in Fig. 3.12. However for small initial disturbances, the asymptotic stability region of the π film bearing is larger than that of the $3\pi/2$ film model.

As mentioned earlier, the state of instability of the $3\pi/2$ film model is reached rather smoothly from large orbits as ω_s approaches its critical value. The instability boundary in Fig. 3.12 corresponds to a limit cycle with a diameter greater than 95% of the clearance circle diameter where the search for the instability boundary is stopped at that particular limit value. The orbital stability region shown in Fig. 3.12 is well defined and stands well for relatively large range of values of the initial disturbances.

3.5 New Explanation on the Full Film Model Instability

The contradiction in the behaviour of the full film bearing between the limit cycle that is often observed experimentally [40] with the corresponding theoretical results of the present as well as previous [22,40] studies, can be explained by a logical argument in view of a comparison

between the orbital stability subregions of both the partial film models, namely the π and $3\pi/2$ film models presented in Figs. 3.11 and 3.12. If the nonlinear analysis based stability plots in Figs. 3.11 and 3.12 are superimposed over each other, it will be evident that not only is the orbital stability subregion of the $3\pi/2$ film model larger than that of the film model but also the orbital stability subregion of the $3\pi/2$ film model extends above and below that of the π film model.

By an inspection of Figs. 2.5 and 2.10 in Chapter 2, it can be shown that the π film model has positive and negative pressure profiles, same as those of the basic dynamic film profiles, but the difference is only in the pressure magnitude and since it is shown in Chapter 2 that the $3\pi/2$ and π film models are upper and lower bounds for the basic dynamic film model. Then the basic dynamical film model can be expected to have a slightly larger orbital stability region than that of the π film. Therefore, in the presence of an effective pressure supply and/or in the case of lightly loaded bearing, the positive pressure profile may be posted such that its extent will be, more or less, similar to that of the $3\pi/2$ film model shown in Fig. 2.6 in Chapter 2. Also the larger the extension of the positive pressure profile, the wider the orbital stability subregion will be and consequently the higher the possibility of occurrence of large circular limit cycles such as those shown in Fig. 3.9. It may be recognized that the circumstances of effective supply

pressure and light loading, are typical to those cases for which a full film exists. In the event of instability, the journal climbs on an orbit with a large eccentricity ratio which means a higher hydrodynamic pressure magnitude, both positive and negative in sense. Then, to maintain a full film case, it requires a posting of the pressure supply which consequently forms a positive pressure profile similar to that of the $3\pi/2$ film model resulting in a case of orbital stability that dominates the journal behaviour.

3.6 Alternative Methods

For the sake of completion of the present stability discussions using nonlinear analysis, applicable for bearings with different L/d ratios without extensive integration of the equation of motion, the Liapunov's method which is often regarded as the general method for stability analysis, is briefly presented. The Liapunov's direct method is reduced to one of finding an "appropriate" Liapunov function L_p, which is a scalar function in the space variables. If L_p is positive definite and if the total time derivative $\dot{L}_p$ is negative definite at the origin or at the equilibrium point investigated, then the system is asymptotically stable.

For the present problem, a Liapunov function was constructed in the form of a total energy expression which ensures its positive definiteness but the total derivative $\dot{L}_p$ was found to provide inappropriate condition for the analysis since the bearing dynamic parameter S can be factored out from $\dot{L}_p$, which means that the condition for

stability is only dependent on the applied perturbations.

Another approach was also followed using the Lienard transformation [80,81] which starts by reformulating the equations of motion using the Lienard's variables u_*, v_* as

$$u_* = \dot{x} + \int_0^x C_{XX}(\eta,y)d\eta + \int_0^y C_{XY}(x,\xi)d\xi = \dot{x} + I_{XX} + I_{XY}$$

$$v_* = \dot{y} + \int_0^x C_{YX}(\eta,y)d\eta + \int_0^y C_{YY}(x,\xi)d\xi = \dot{y} + I_{YX} + I_{YY} \qquad (3.11)$$

$$\dot{u}_* \triangleq - \left[K_{XX}(x + X_0) + K_{XY}\ (y + Y_0)\ -W_X\right] = - f_x(x,y)$$

$$\dot{v}_* = - \left[K_{YX}(x + X_0) + K_{YY}\ (y + Y_0)\ -W_Y\right] = - f_y(x,y)$$

where K_{XX}, C_{XX}, ... are the nonlinear stiffnesses and damping given by equation (B.1) in Appendix B and $x = X-X_0$, $y = Y-Y_0$.

The Lienard function, which is also a Liapunov function, is given for the present problem, by

$$L_p = \frac{1}{2}\ (u_*^2 + v_*^2) + \int_0^x f_X(\eta,y)d\eta + \int_0^y f_y(x,\xi)d\xi \qquad (3.12)$$

Then the total time derivative of (3.12) using equation (3.11) is

$$\dot{L}_p = -(I_{XX} + I_{XY})\ f_X(x,y) - (I_{YX} + I_{YY})\ f_y(x,y) + T_1 + T_2 \qquad (3.13)$$

where T_1 and T_2 are

$$T_1 = x \frac{\partial}{\partial x} \int_0^y f_y(x;\xi)d\xi$$

$$T_2 = y \frac{\partial}{\partial y} \int_0^x f_x(\eta,y)d\eta$$

To complete the check for asymptotic stability of the equilibrium point (X_0,Y_0), the signs of L_p and $\dot{L}_p$ have to be determined. But this requires an analytical evaluation of the integrals in equations (3.12) and (3.13) which was found too complicated to achieve.

3.7 Summary

A comparison between the results developed for the finite bearing with the availabe experimental results for the full film case shows a good agreement that not only supports the suggested full film model but mainly establishes the accuracy of all the eccentricity functions which are derived in Chapter 2. Modified stability boundaries, based on both linear and nonlinear analysis, are constructed for an accurate assessment of the stability behaviour of a rigid symmetric rotor. The $3\pi/2$ film model is found to be distinguished by a considerably large orbital stability region compared to the π film bearing model. This provides a logical explanation for the limit cycle often observed experimentally in the behaviour of the full film bearing.

CHAPTER 4

SOLUTION OF THE LINEAR EQUATION OF MOTION OF THE FINITE BEARING THROUGH MODAL ANALYSIS AND ERROR BOUNDS

4.1 General

In cases where the assumptions of rotor rigidity and linearity of hydrodynamic forces are justifiable, a great simplification in the dynamic analysis of the rotor-bearing system can be accomplished. With such simplification, general results can be obtained and the system response to complicated excitation such as stochastic forces can be calculated easily and efficiently.

Solutions that are obtained using linear bearing equations were found to be in "surprisingly" good agreement [53] with the corresponding solutions of the nonlinear system as long as the journal eccentricity ratio does not exceed a value of .75. Different validity bounds for the linear hydrodynamic stiffness and damping, that are based on eccentricity ratio only can be found frequently in the literature. Neither an all inclusive parameter that defines what can be called the range of valid linear approximation nor charts for the specific determination of the error involved in utilizing the linear system, are available. Such an objective is attempted in this chapter.

Besides providing an error measure for the deviation

of the linearized bearing system from the nonlinear one, a solution by modal analysis for the linearized equation of a rigid symmetric rotor is obtained. Through a solution by modal analysis, many basic and important dynamic characteristics of the journal bearing system such as damped natural frequencies, modal logarithmic decrement and the complex frequency response are calculated and presented particularly the complex frequency response is a basic quantity necessary for the evaluation of the stochastic response of the system using the spectral density approach.

4.2 Solution of the Linearized Bearing System by Modal Analysis

The linearized equations of motion of the finite journal bearing are developed and presented in Appendix E. Stiffness coefficients k_{xx}, k_{xy}, ... for both partial film models, namely the $3\pi/2$ and the π films, are the same whereas the damping coefficients C_{xx}, C_{xy}, ... are different. All the stiffness and damping coefficients are presented in Fig. 4.1 for a bearing with a $L/d = 1$. Here, the π film model is used, along with the corresponding coefficients that are developed by impedance method [5] where the finite bearing was treated as a weighted sum of the short and long bearings. For some of the stiffness and damping coefficients the differences between the present finite bearing and those of [5] are considerable over most of the range of the eccentricity ratio e_o.

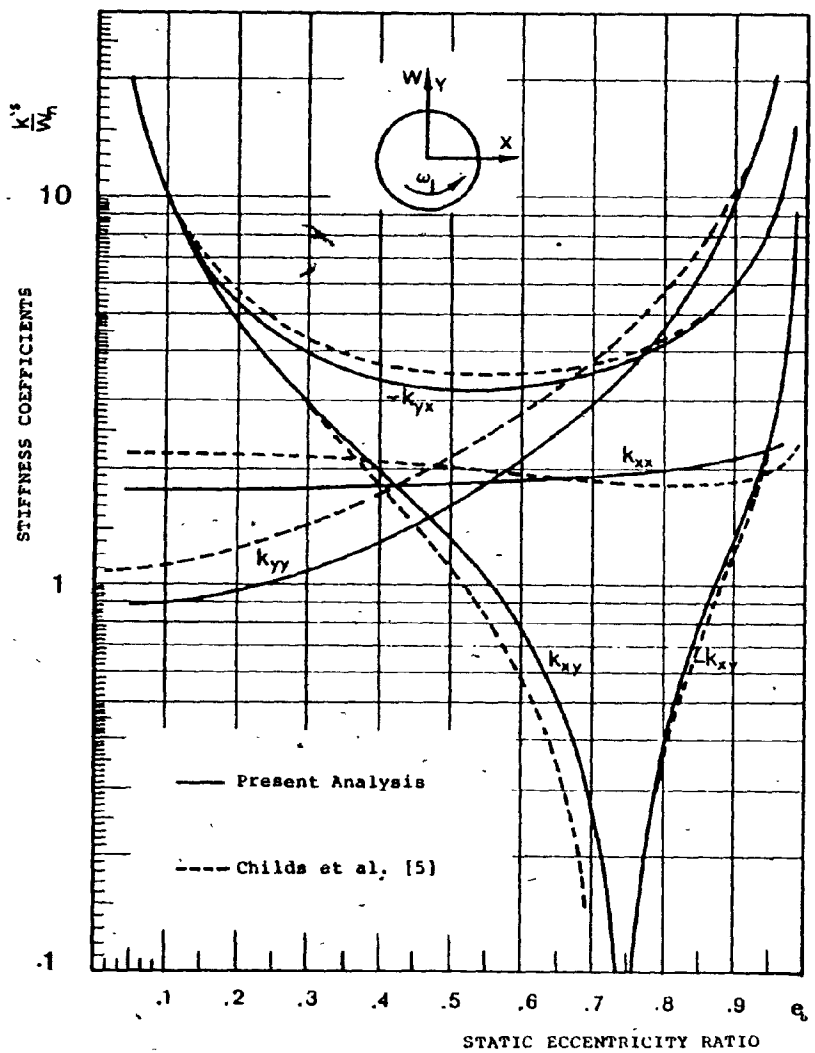

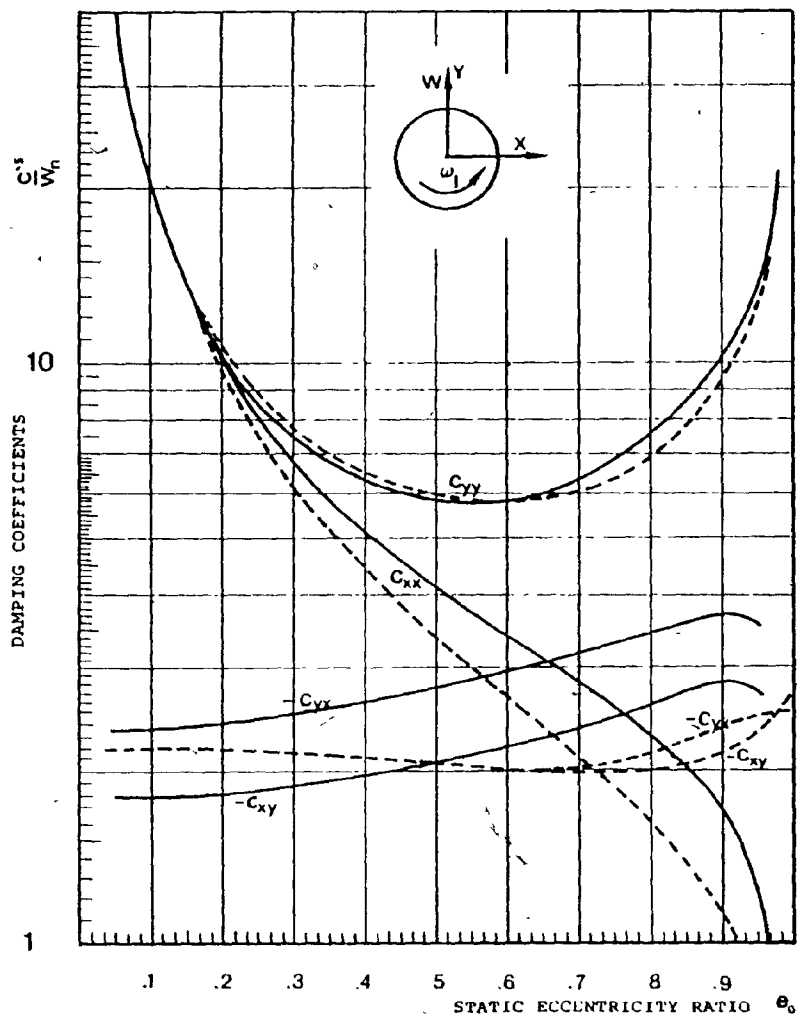

Fig. 4.1 Comparison Between the Present and the Previous Results for the Coefficients of the Linearized Equations.

It should be noted that the curves plotted in Fig. 4.1 are exclusive to the particular load and the rotational speed direction as specified at the top of the figure. If a solution is carried out with a given load angle β_{ℓ_1} and then repeated with different load angle β_{ℓ_2}, keeping the same bearing parameters and running speed direction, the new solution will be identical to the first except that it will be oriented with an angle $(\beta_{\ell_2} - \beta_{\ell_1})$ from the first solution. The stiffness and damping coefficients will be different in both cases since they depend on the coordinates of the different equilibrium points. This is demonstrated by the two solutions for an unbalance response and presented in Fig. 4.2.

Shifting the axes to the equilibrium point (X_o, Y_o), the linearized equation of motion of the finite journal bearing in the new coordinates

$$x = X - X_o \quad \text{and} \quad y = Y - Y_o$$

can be written in dimensionless form as

$$\begin{bmatrix} 1 & 0 \\ 0 & 1 \end{bmatrix} \begin{Bmatrix} \ddot{x} \\ \ddot{y} \end{Bmatrix} + \begin{bmatrix} c_{xx} & c_{xy} \\ c_{yx} & c_{yy} \end{bmatrix} \begin{Bmatrix} \dot{x} \\ \dot{y} \end{Bmatrix} + \begin{bmatrix} k_{xx} & k_{xy} \\ k_{yx} & k_{yy} \end{bmatrix} \begin{Bmatrix} x \\ y \end{Bmatrix} = \begin{Bmatrix} w_x(\tau) \\ w_y(\tau) \end{Bmatrix}$$

$$\text{or} \quad [I]\{\ddot{q}_s\} + [c_s]\{\dot{q}_s\} + [k_s]\{q_s\} = \{w_s\} \qquad (4.1)$$

where the excitation components $w_x(\tau)$ and $w_y(\tau)$ are the remainder of the applied load after excluding the static equilibrium load W_n. The stiffness and damping matrices

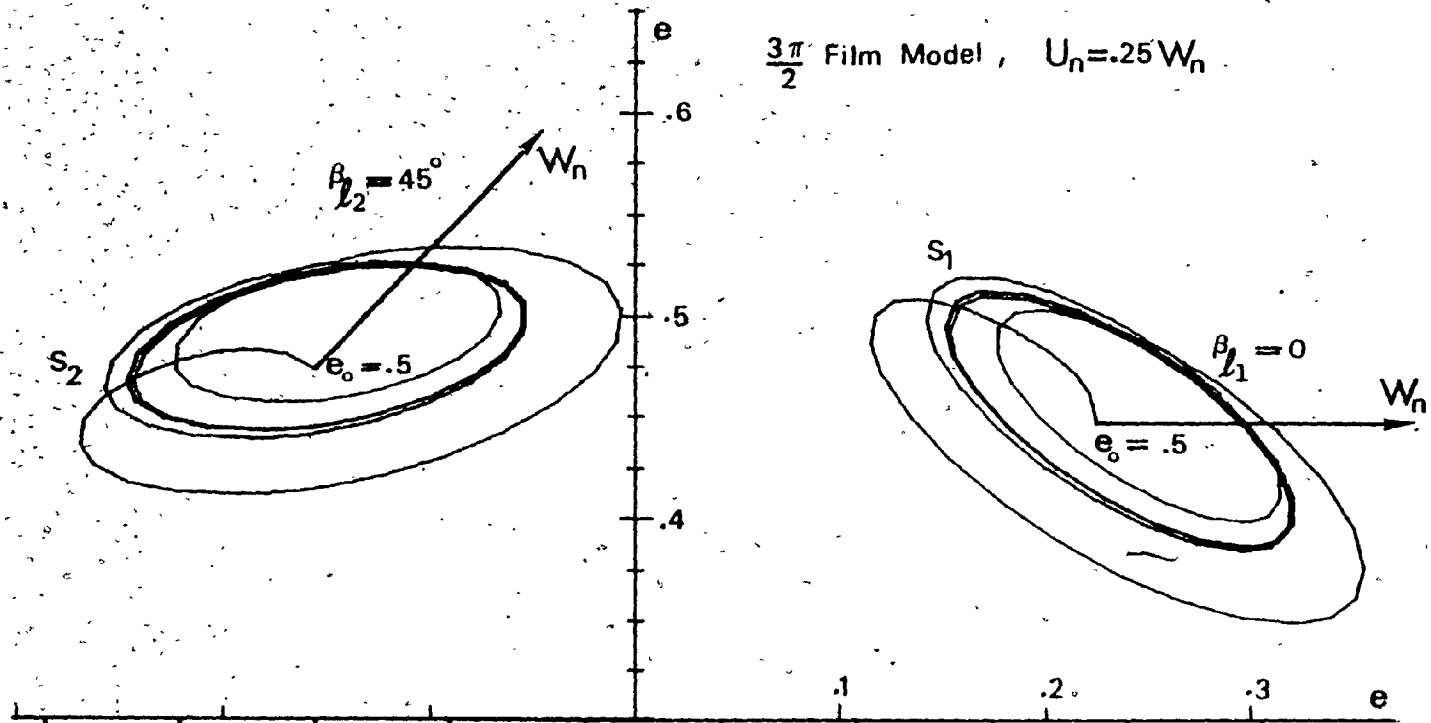

	c_{xx}	c_{xy}	c_{yx}	c_{yy}	k_{xx}	k_{xy}	k_{yx}	k_{yy}
S_1	23.71	11.56	18.74	37.32	6.417	12.77	-5.282	7.308
S_2	15.36	-10.39	-3.213	45.67	3.115	8.583	-9.475	10.61

Fig. 4.2 Two Solutions with the Same Bearing Parameters for Different Load Angles.

$[k_s]$ and $[C_s]$ are nonsymmetric. System of equations (4.1) can be solved by modal analysis and for this the equations are written in the first order form as

$$\{\dot{q}\}_{4x1} = [D_y]_{4x4} \{q\} + \{w\} \qquad (4.2)$$

where

$$\{\dot{q}\} = \begin{Bmatrix} \dot{\bar{q}}_s \\ \bar{q}_s \end{Bmatrix}, \quad \{w\} = \begin{Bmatrix} \bar{w}_s \\ \bar{0} \end{Bmatrix} \quad \text{and} \quad [D_y] = \begin{bmatrix} -[C_s] & -[k_s] \\ [I] & [0] \end{bmatrix}$$

The roots of the characteristic equation

$$\det \left| [D_y]_{4x4} - [I]_{4x4} \right| = 0$$

are generally complex. They then exist as the complex conjugate pairs

$$\lambda_j = \alpha_j \pm i\, \beta_j \quad , \quad j = 1,2 \qquad (4.3)$$

which are dimensionless in the present case. Here α_j is the modal damping exponent and β_j is the damped natural frequency of the jth mode. Every pair of roots is called eigenvalue λ_j [54].

A quantity of significant practical importance is the logarithmic decrement defined by

$$\delta_{cj} = \frac{-2\pi\alpha_j}{\beta_j} \quad , \quad j = 1,2$$

corresponding to the jth mode of the dynamic system.

The damped natural frequencies and logarithmic decrements

of the dynamic system (4.1) are calculated in a scanning search over most of the stable region and around the stability boundary line, with reference to stability figures in Chapter 3, represented by the bounds $.2 \leq e \leq .8$ and $.5 \leq \omega_s \leq 2.5$ for $L/d = 1$. The results obtained for these properties for different e_o and ω_s values are presented in Tables 4.1 through 4.4. It is found that over almost all the stable region of the journal, in the $\omega_s - e$ plane, only one eigenvalue exists as a complex conjugate pair whereas the other splits into two real unequal roots. The real roots represent a nonoscillating mode and in such a case only one damped natural frequency and consequently the corresponding logarithmic decrement are listed in Tables 4.1 to 4.4. Only in the vicinity of the stability boundary both modes are oscillating and if one, or both, logarithmic decrement is negative then it refers to a case of instablity of the system.

The magnitudes of the logarithmic decrements indicate the proximity of the journal status to the stability boundary. A combination of the information in Table 4.2 and Fig. 3.5 in Chapter 3, or that in Table 4.4 and Fig. 3.6, gives comprehensive details on the damping ability of the finite bearing and how this damping gradually decreases or increases in the stable region. Therefore the logarithmic decrements obtained completes the linear stability analysis presented in Chapter 3 which only defines the journal condition of being stable or unstable. The damped natural frequencies specify the

e_o ↓	NONDIMENSIONAL SPEED ω_s				
	.5	1.5	1	2	2.5
.2	.422	.424	.424	.420	.408 , .357
.3	.399	.404	.406	.400	.384 , .268
.4	.386	.394	.398	.390	.369 , .115
.5	.380	.393	.401	.390	.363
.6	.382	.403	.415	.397	.362
.7	.394	.431	.446	.411	.365
.8	.429	.499	.495	.432	.373

Table 4.1 Damped Natural Frequencies of the Journal Bearing with $3\pi/2$ Film Model and L/d = 1.

.2	1.062	.888	.606	.236	35.600 , -.175
.3	1.618	1.370	.978	.488	35.700 , -.008
.4	2.192	1.867	1.347	.742	75.000 , .187
.5	2.800	2.368	1.684	.956	.363
.6	3.460	2.868	1.950	1.100	.498
.7	4.200	3.323	2.060	1.134	.570
.8	5.050	3.562	1.890	1.040	.577

Table 4.2 Logarithmic Decrement of the Journal Bearing with $3\pi/2$ Film Model and L/d = 1.

.2	.500	.510	.519	.516	.496 , .324
.3	.502	.525	.545	.532	.490 , .338
.4	.505	.551	.582	.546	.486 , .359
.5	.513	.600	.624	.550 , .120	.480 , .392
.6	.530	.690	.658	.560 , .240	.473 , .440
.7	.571	.810	.677	.550 , .257	.462 , .516
.8	.693	.900	.683	.540 , .510	.648 , .445

Table 4.3 Damped Natural Frequencies of the Journal Bearing with π Film Model and L/d = 1.

.2	1.783	1.520	1.075	.500	32.300 , -.090
.3	2.708	2.250	1.478	.614	21.560 , -.100
.4	3.674	2.920	1.692	.638	16.200 , -.070
.5	4.700	3.420	1.674	.618 , 9.760	12.800 , -.010
.6	5.930	3.516	1.505	.602 , 28.600	10.500 , .090
.7	7.050	2.970	1.287	.600 , 19.300	8.770 , .227
.8	8.230	2.220	1.080	.614 , 14.570	7.400 , .370

Table 4.4 Logarithmic Decrement of the Journal Bearing with π Film Model and L/d = 1.

transient oscillating frequency of the journal and they are around a value of .5 in the vicinity of the stability boundary, particularly for the π film model. This is in contrast with the well known whirling speed ratio $\mathring{\psi} = \dot{\psi}/\omega_j$ of the oil whip [39]. However no assured conclusion about orbital stability can be deduced from a linear analysis.

The complex frequency response functions can easily be evaluated using modal analysis and they are of particular interest for two reasons: (i) they represent the system transfer function and therefore contain all the system properties and indicate the frequencies at which the dynamical system is most sensitive and (ii) they are basic elements in the evaluation of the response of the system (4.1) particularly under random excitation which will be presented later in this thesis for a grinding machine application. For the present two-degrees-of-freedom system, the frequency response functions are evaluated in the principal coordinates and then transformed back to the coordinates of the phase space. Then for every frequency component of the input force, the input-output relation is

$$\begin{Bmatrix} x(\omega_i) \\ y(\omega_i) \end{Bmatrix} = \begin{bmatrix} H_{xx}(\omega_i) & H_{xy}(\omega_i) \\ H_{yx}(\omega_i) & H_{yy}(\omega_i) \end{bmatrix} \begin{Bmatrix} w_x(\omega_i) \\ w_y(\omega_i) \end{Bmatrix} \tag{4.3}$$

Here ω_i is a dimensionless frequency given by $\omega_i = \omega/\omega_j$ and $x(\omega_i)$, $w(\omega_i)$, ... are the standard Fourier transform of the quantities $x(\tau)$, $w(\tau)$, ...

The behaviour of the complex frequency response $H_{xx}(\omega_i)$ with respect to changes in the steady state eccentricity ratio e_o, the dimensionless speed ω_s and the bearing L/d ratio, is demonstrated by three samples in Figs. 4.3, 4.4 and 4.5 as relations between $|H_{xx}(\omega_i)|^2$ and ω_i. It may be noted that the complex frequency response $H_{xx}(\omega_i)$ is also dimensionless. As can be seen from Figs. 4.3 through 4.5, the system's ultimate sensitivity indicated by its resonance tendancy is not at $\omega_i = 1$, which is the case for synchronous excitation such as unbalance, but rather around $\omega_i = .5$ particularly in these cases close to instability. For example, the resonant case in Fig. 4.4 with $\omega_s = 2.5$ occurs at $\omega_i = .48$ which in this particular resonant case defines the onset speed of an oil whip state. On the other hand the system transfer function may be almost flat for a journal status that is located deep in the stable region, such as the case in Fig. 4.4 with $\omega_s = .5$, which defines that the system response is almost independent of the frequency of the input force.

An important purpose of the application of modal analysis on the bearing system (4.1) is the calculation of the steady state response to unbalance excitation for use in evaluating the acceptability region of the bearing linear system (4.1) for such studies. Besides the accuracy available in defining the journal orbit, the modal analysis provides a saving in computer time, as compared to numerical integration, for a steady state solution in the order of 50 times. The unbalance excitation may be represented as,

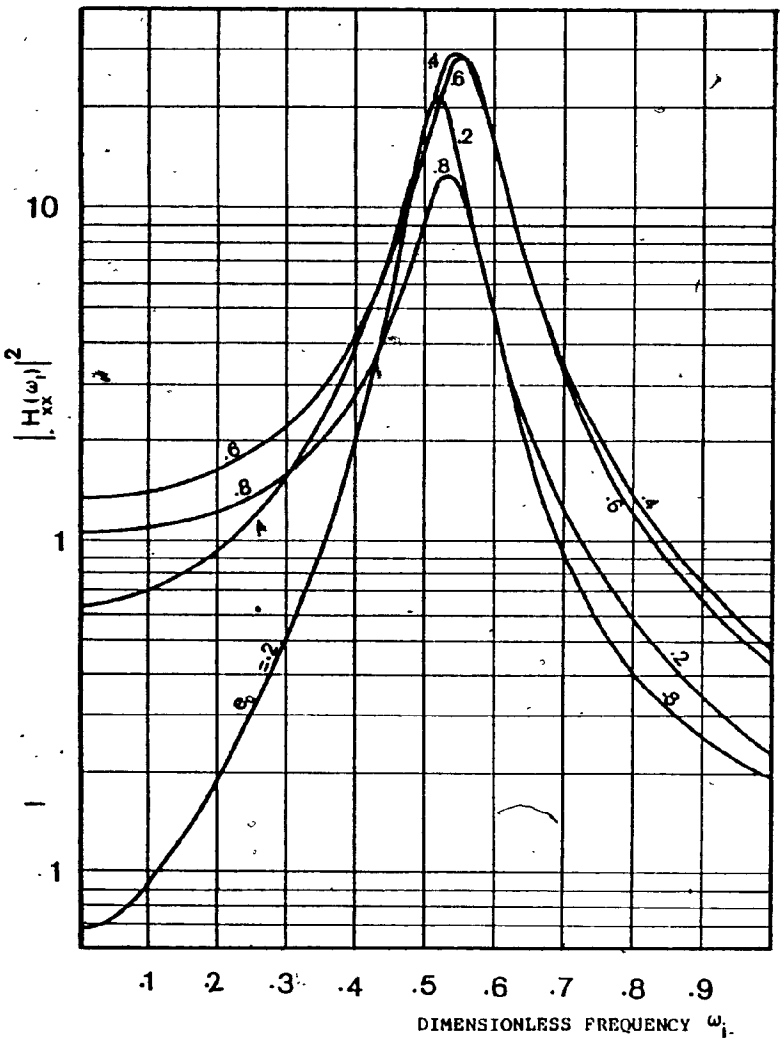

Fig. 4.3 Effect of Static Eccentricity Ratio on the Complex Frequency Response Function, $\omega_s = 2$ and L/d = 1.

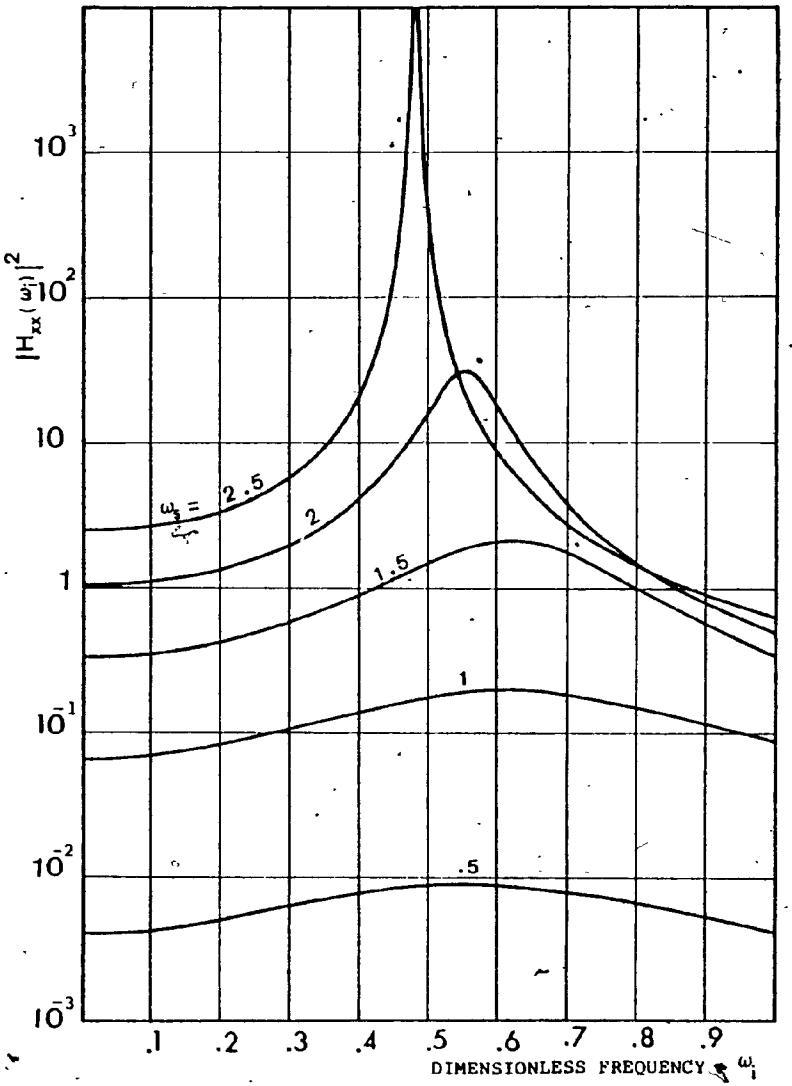

Fig. 4.4 Effect of the Dimensionless Speed on the Complex Frequency Response Function, $e_o = .5$ and L/d = 1.

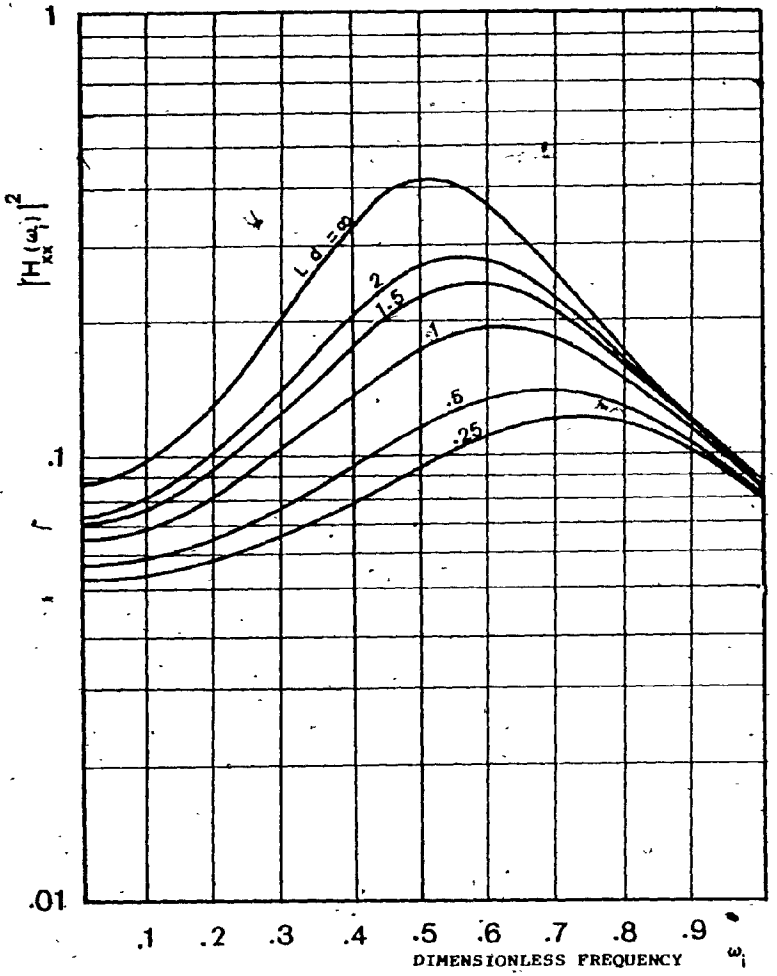

Fig. 4.5 Effect of Bearing Width on the Complex Frequency Response Function, $e_o = .5$ and $\omega_s = 1$.

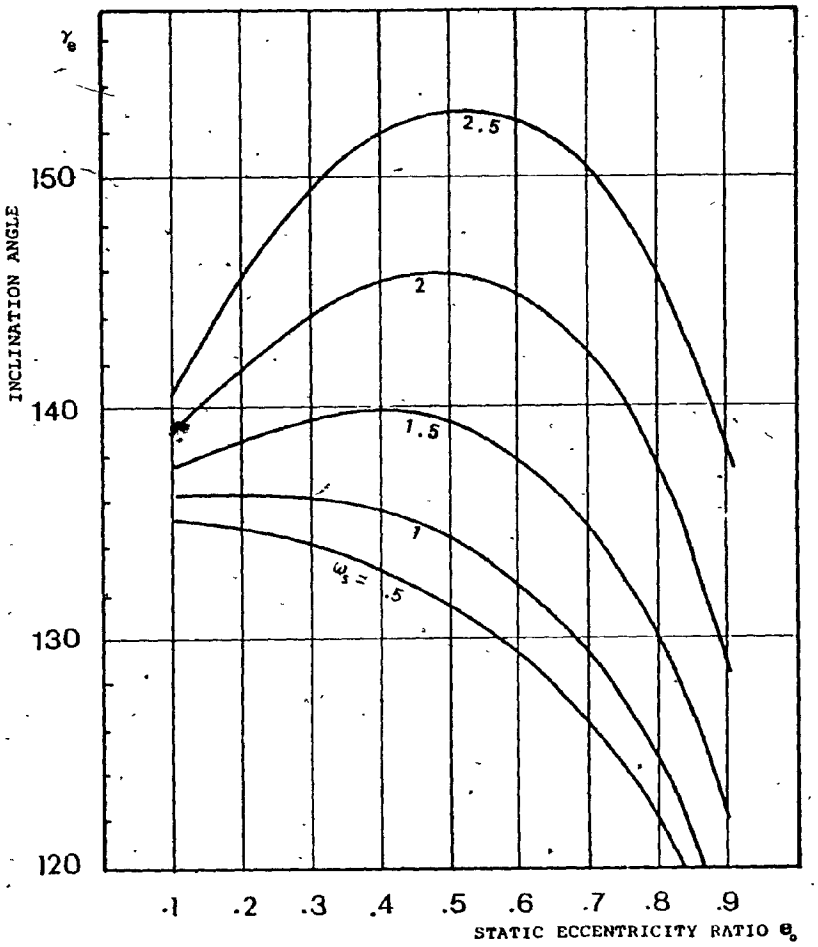

Fig. 4.6 Inclination Angle of the Major Axis with the Load Direction.

$$\begin{Bmatrix} w_x(\tau) \\ w_y(\tau) \end{Bmatrix} = U_n \begin{Bmatrix} \cos\tau \\ \sin\tau \end{Bmatrix}$$

where U_n is the dimensionless unbalance amplitude.

The steady state response is then of the form

$$\begin{aligned} x &= a_x \cos\tau + b_x \sin\tau \\ y &= a_y \cos\tau + b_y \sin\tau \end{aligned} \tag{4.5}$$

The parametric equations (4.5) may be rewritten in the cartesian system of coordinates as

$$\frac{y^2}{\rho_2^2} + \frac{x^2}{\rho_1^2} - \frac{2xy}{\rho_1\rho_2} \sin(\varepsilon_2 - \varepsilon_1) = \cos^2(\varepsilon_2 - \varepsilon_1) \tag{4.6}$$

where
$$\rho_1 = \sqrt{a_x^2 + b_x^2},$$

$$\rho_2 = \sqrt{a_y^2 + b_y^2},$$

$$\varepsilon_1 = \tan^{-1}\frac{-b_x}{a_x},$$

$$\varepsilon_2 = \tan^{-1}\frac{a_y}{b_y}$$

Equation (4.6) is essentially the equation of an ellipse with oblique axes. If the coordinates (x,y) are rotated to a new position (x_1, y_1) to coincide with the directions of the major and minor axes of the ellipse, equation (3.6) will be of the form

$$\frac{x_1^2}{d_1^2} + \frac{y_1^2}{d_2^2} = 1$$

Here $2d_1$ and $2d_2$ are the major and minor axes of the ellipse given by the relations

$$\frac{1}{d_1^2} = \eta_1 \left[\frac{\rho_1}{\rho_2} \sin^2\gamma_e + \frac{\rho_2}{\rho_1} \cos^2\gamma_e - \eta_2\right],$$

$$\frac{1}{d_2^2} = \eta_1 \left[\frac{\rho_1}{\rho_2} \cos^2\gamma_e + \frac{\rho_2}{\rho_1} \sin^2\gamma_2 + \eta_2\right], \tag{4.7}$$

$$\text{with} \quad \frac{1}{\eta_1} = \rho_1\rho_2 \cos^2(\varepsilon_2 - \varepsilon_1)$$

$$\frac{1}{\eta_2} = \sin(2\gamma_e) \sin(\varepsilon_2 - \varepsilon_1) .$$

γ_e is the orientation angle of the new coordinates system (x_1,y_1) from the original system (x,y) and is expressed as

$$\gamma_e = \frac{1}{2} \tan^{-1}\left[\frac{2\ \rho_1\rho_2}{\rho_1^2 - \rho_2^2} \sin(\varepsilon_2 - \varepsilon_1)\right] \tag{4.7a}$$

The inclination angle γ_e is invariant under any change of the unbalance load U_n for a specified system status (ω_s,e_o) and L/d ratio. For L/d = 1 the inclination angle is presented in Fig. 4.6 for different dimensionless speeds ω_s. Solution (4.5) and the orbit parameters d_1, d_2 and γ_e can be used in a comparative analysis with the nonlinear system to determine the acceptable region of the steady state response of the linear system under unbalance excitation. But first, a discussion of a simple parameter for measuring the error that is associated with the linear system is carried out in the following section.

4.3 Simple Measures of Error Due to Linearization of the System

The simple form of stating the nonlinear damping and stiffness functions in the cartesian coordinates (3.1) may be used for developing a comparison between the results for the actual nonlinear and approximated linearized bearing systems. Nonlinear damping and stiffness C_{XX}, ... and K_{XX}, ... in (B-1) Appendix B are functions of the displacements X and Y and the bearing dynamic parameter S which is separable such that

$$C^*_{XX}(X,Y) = C_{XX}(X,Y,S)/S$$

It is easy to define the residual nonlinearity as

$$\Delta C^*_{XX} = C^*_{XX}\Big|_{e=e_o} - C^*_{XX} \quad \text{where } e_o \text{ is an equilibrium point.}$$

The percentage error of the deviation ΔC^*_{XX} in the neighbourhood of an equilibrium point $e_o = .5$ with $L/d = 1$ in a π film is presented in Fig. 4.7 in a contour form. Similar graphs may be constructed for all C_{XY}, ..., and K_{XX}, ..., and different equilibrium points. Then a journal orbit that has been calculated, say the steady state response, is placed on such graphs for error estimation of the damping and stiffness coefficients used. However, this approach may be misleading in terms of the behaviour of the overall dynamic system and will also be independent of the system stability status which is given by the dimensionless speed ω_s besides the eccentricity ratio e. A comparison between the nonlinear and the

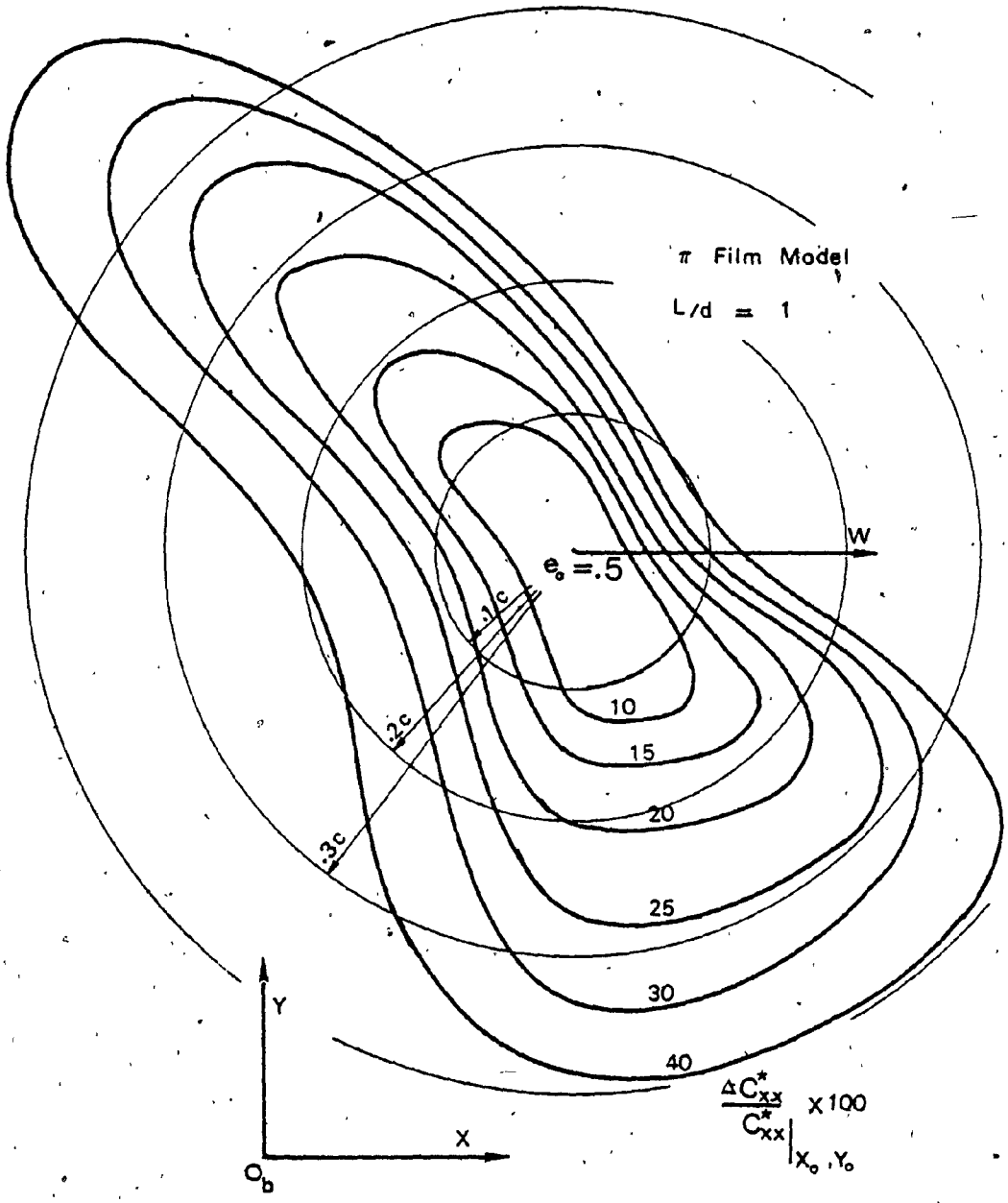

Fig. 4.7 Contour Lines of Percentage Deviation Error for C_{XX}.

corresponding linear bearing equations, that is based on steady state response to unbalance excitation, shows much closer agreement than the larger percentage error which is associated with the individual damping and stiffness components as can be seen in Fig. 4.7.

4.4 Evaluation of the Error Bounds for the Linearized System Using Numerical Integration and Modal Analysis

The nonlinear equation of motion (3.1) is integrated numerically for a wide range of parameters and under different values of the unbalance amplitude. The solution is continued until the steady state is attained. An example of the solution obtained is presented in Fig. 4.8 for $L/d = 1$, $\omega_s = .5$ and an unbalance amplitude $U_n = .25W_n$. Only the steady state solution is presented in Fig. 4.8. The major and minor axes of the elliptical orbit of the corresponding linear system are also plotted in Fig. 4.8. Using similar data as those for Fig. 4.8, the error arising from the linearized approach can be measured graphically. The major axes of the distorted ellipses of the nonlinear solutions are assumed to be the distances between peaks. As can be noticed from the sample solutions in Fig. 4.8, with the minor axis as a base for comparison, a closer matching between the linear and nonlinear solutions may be noticed. Consequently, if the major axis is used as a base, a conservative estimate will result.

The major axis, which is also dimensionless, is plotted

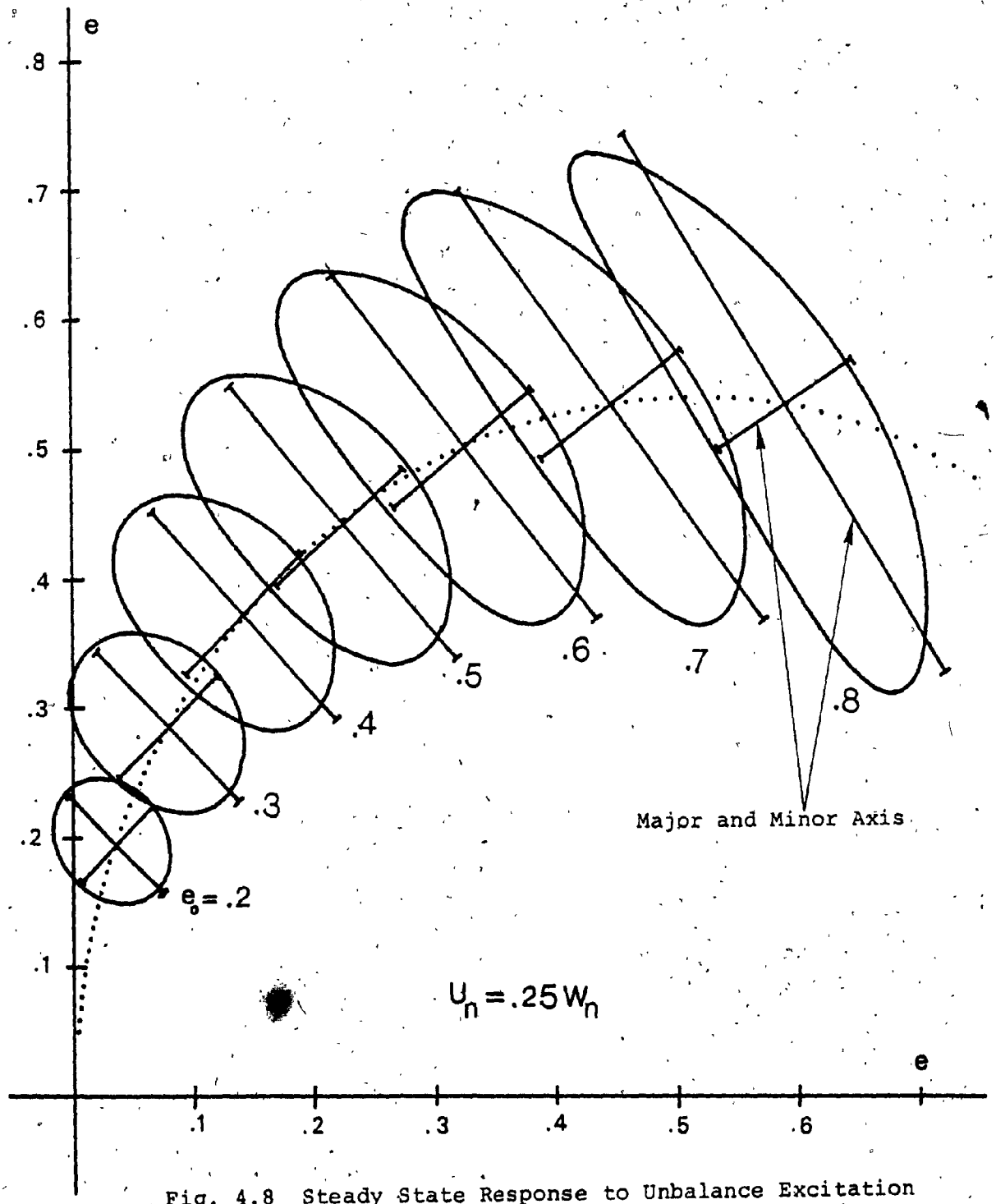

Fig. 4.8 Steady State Response to Unbalance Excitation of Both the Nonlinear and the Linearized Bearing Equations.

against the eccentricity ratio e in Fig. 4.9 for $\omega_s = .5, 1, 1.5$ and 2 and for the unbalance amplitudes $U_n = .25W_n, .5W_n$ and $.75W_n$ where W_n is the steady state equilibrium load of the respective eccentricity ratio, for a bearing with $L/d = 1$. The percentage error values are written along the curves at different points and the letter "C" defines "complicated path" which is the case when the response of the nonlinear system becomes completely distorted from the elliptical shape where, in most of these cases, a double loop is formed. The cases of complicated path are observed close to the stability boundary, that is for large values of ω_s, as can also be seen from Fig. 4.9. The chart can be used by first calculating the dimensionless speed of the rotor-bearing system, which may be rigid or flexible, as well as the eccentricity ratio, say, for example, $\omega_s = 1.5$ and $e_o = .5$. Now, (i) if an error bound is specified to be, say 5%, then the major axis of the orbit must not be allowed to exceed 30% of the radial clearance, (ii) if the unbalance response is already obtained, say the major axis of the orbit at the bearing center line is 60% of the radial clearance, then the error involved in using the linear stiffness and damping of the bearing is 13%.

4.5 Conclusion

A solution by modal analysis is carried out for the linear equation of motion of the finite bearing, which is essentially a nonsymmetric dynamical system. The solution obtained is most adequate for calculating the stochastic

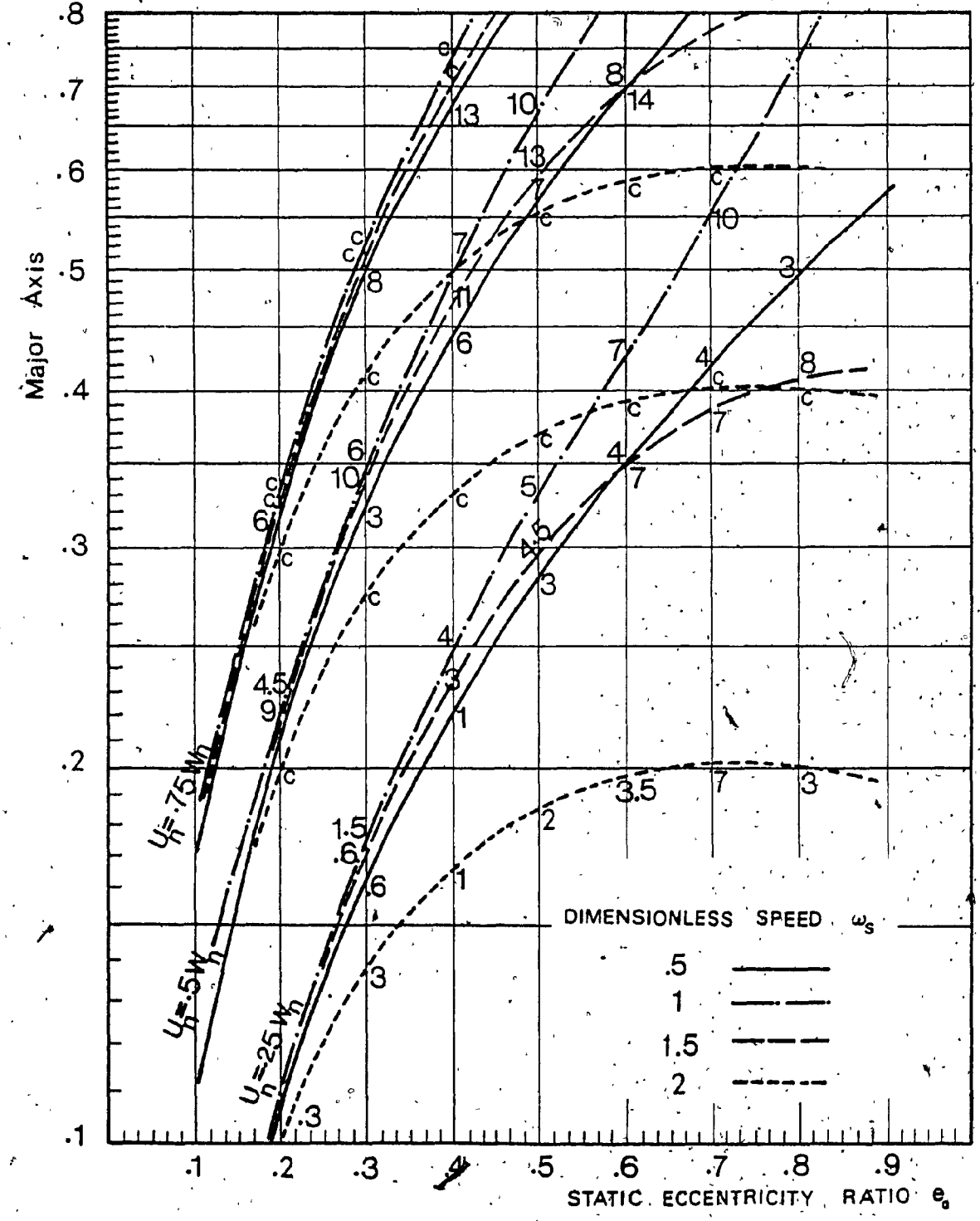

Fig. 4.9 Chart of Percentage Error in Deviation of the Linearized Equation System, L/d = 1.

response in the application of rotor bearing dynamics on a grinding machine spindle discussed in Chapter 6, whenever the case of rotor rigidity and system linearity applies. Fundamental parameters of the finite bearing such as the damped critical speeds, the logarithmic decrement and the complex frequency response are calculated. These parameters provide further details on the stability of the finite journal bearing and define the system sensitivity over the input frequency. A chart for the error involved in the linear approximation of the hydrodynamic forces is provided for the case of $L/d = 1$ and the use of such charts for rigid and flexible rotors are illustrated.

CHAPTER 5

FINITE ELEMENT REPRESENTATION OF A ROTOR-BEARING SYSTEM AND SOLUTION BY MODAL ANALYSIS

5.1 Objectives

The flexible-rotor-bearing equations are solved by the finite element method with the gyroscopic moments, the shear deformation, the rotary inertia, the internal damping and the bearing support flexibility all taken into account. Previous applications of the finite element method on the rotor-bearing problem included the shear deformation by introducing 4 additional degress-of-freedom per element to account for the shear angles and thus increasing the size of the final dynamical system by 50% [62,63]. The present approach utilizes a simple Timoshenko element which was shown by Thomas et al [59], as applied on a simple beam, leading to practically negligible error in the calculated natural frequencies in comparison to the more complicated element. This therefore avoids the unnecessary increase in the size of the dynamical system which may require the use of a reduction technique [63] resulting in considerable disadvantages and limitations as mentioned in Chapter 1.

Previous approaches [62,64,65] utilized a unified spatial rotational direction which introduces unnecessary complexities in the procedure for developing the element equations. Instead, in the present analysis, an analogous treatment of both the planes of motion is used. The

nonconservative moments due to the hysteretic damping are also appropriately introduced into the element equations. Since modal analysis of a general dynamical system with nonsymmetric characteristics are not well known or clearly stated for nonstandard applications, a standard proof as well as the necessary relations for the modal analysis are briefly indicated for direct use in calculating the system response under any deterministic excitation.

The final part of this section is devoted to a check on the procedure through a comparison with previous theoretical and experimental results as well as a detailed comparison with the different effects of the two types of support flexibility is presented. The various interpretations of the results are discussed and later used in an example to bring out their application.

5.2 The Equation of Motion of a Rotating Beam

The equation of motion for a rotating Timoshenko beam, with shear deformation included, in two perpendicular planes of motion XZ and YZ and as described by Fig. 5.1 can be written as follows [53]:

$$\frac{\partial}{\partial Z}\left[\rho A G_s\left(\frac{\partial X}{\partial Z}-\alpha\right)\right]+p_x(Z,t)=m_z\frac{\partial^2 X}{\partial t^2}$$

$$\frac{\partial}{\partial Z}\left[\rho A G_s\left(\frac{\partial Y}{\partial Z}-\beta\right)\right]+p_y(Z,t)=m_z\frac{\partial^2 Y}{\partial t^2}$$

$$\frac{\partial}{\partial Z}\left(EI\frac{\partial \alpha}{\partial Z}\right)+\rho A G_s\left(\frac{\partial X}{\partial Z}-\alpha\right)=J_T\frac{\partial^2 \alpha}{\partial t^2}+\omega_r J_z\frac{\partial \beta}{\partial t}$$

$$\frac{\partial}{\partial Z}\left(EI\frac{\partial \beta}{\partial Z}\right)+\rho A G_s\left(\frac{\partial Y}{\partial Z}-\beta\right)=J_T\frac{\partial^2 \beta}{\partial t^2}-\omega_r J_z\frac{\partial \alpha}{\partial t} \qquad (5.1)$$

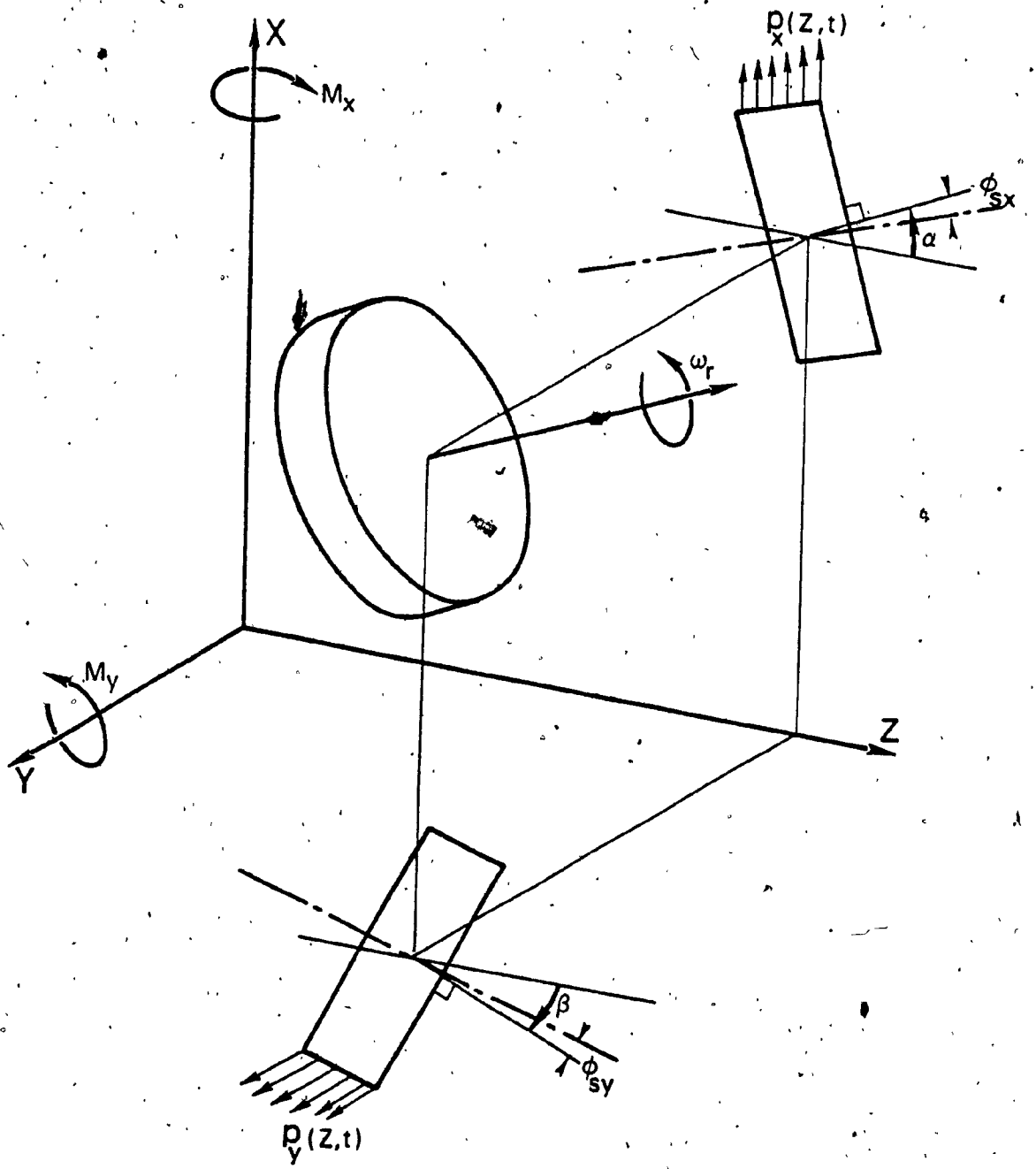

Fig. 5.1 A Beam Segment and the Analogous Motion Planes.

Here the relations

$$\alpha = \frac{\partial X}{\partial Z} + \phi_{sx} \quad \text{(with the shear angle } \phi_{sx} = \frac{V_x}{\rho G_s A}\text{)} \tag{5.2}$$

and $$M_y = EI \frac{\partial \alpha}{\partial Z} \tag{5.3}$$

in the XZ plane and the corresponding relations in the YZ plane are employed. Further p_x and p_y are the distributed external forces with respect to the XZ and YZ planes respectively, ρ is the shear form factor (=.75 for circular beam section [55], m_z, J_T and J_z are the mass and lateral and axial mass moments of inertia, all specified per unit length of the beam; V_x and M_y are the shear and moment in the XZ plane.

The kinetic and potential energies T and P for the beam segment with a length ℓ are

$$T = \frac{1}{2} \int_0^{\ell} \left\{ m_z \left[\left(\frac{\partial X}{\partial t}\right)^2 + \left(\frac{\partial Y}{\partial t}\right)^2 \right] + J_T \left[\left(\frac{\partial \alpha}{\partial t}\right)^2 + \left(\frac{\partial \beta}{\partial t}\right)^2 \right] + \omega_r J_z \left(\beta \frac{\partial \alpha}{\partial t} - \alpha \frac{\partial \beta}{\partial t} \right) \right\} dZ \tag{5.4a}$$

$$P = \frac{1}{2} \int_0^{\ell} \left\{ EI \left[\left(\frac{\partial \alpha}{\partial Z}\right)^2 + \left(\frac{\partial \beta}{\partial Z}\right)^2 \right] + \rho A G_s \left[\left(\frac{\partial X}{\partial Z} - \alpha\right)^2 + \left(\frac{\partial Y}{\partial Z} - \beta\right)^2 \right] \right\} dZ \tag{5.4b}$$

As can be seen from Fig. 5.1, the moments and the rotational displacements are in different direction in both XZ and YZ planes. However, the rotations α and β as well as

the shear angles in both planes retain a similarity such that the relation (5.3) is similar for both planes. This convention will be referred to as the analogous planes treatment. Another treatment that will be discussed in the development of this investigation is one that considers a consistent rotational direction in both planes of motion [62,64,65] which will be referred to as the unified sign treatment. The effect of the unified sign treatment on the equations of motion (5.1) is represented by a sign change for the gyroscopic moment terms, $(\omega_r J_Z \frac{\partial \beta}{\partial t})$ and $(\omega_r J_Z \frac{\partial \alpha}{\partial t})$, and consequently affecting the sign of the gyroscopic term in the kinetic energy expression (5.4a). This can be easily distinguished by examining the relation

$$\bar{T}_g = J_z \bar{\Omega}_p \times \bar{\Omega}_r$$

where T_g is the gyroscopic moment, $\bar{\Omega}_p$ is the precessional speed and $\bar{\Omega}_r$ is the spinning speed.

5.3 The Finite Element Solution

The solution by the finite element technique of the partial differential equations (5.1) is carried out over the space dimension Z rendering a set of ordinary differential equations, with respect to time only. Then the output of the finite element solution is a dynamical system independent of the rotor-bearing configuration. This represents an advantage of the finite element method over the transfer matrix methods.

The solution of equations (5.1) is achieved through the process of dividing the beam into a number of elements which are assumed to have uniform properties in the context of the present analysis. An element of the beam is described in Fig. 5.2 in the XZ plane. The displacement X(Z,t) is assumed to be expressed in terms of the nodal variables X_1, α_1, X_2 and α_2, or q_i^e, i = 1,2,3,4, using the weighted sum relationship

$$X(Z,t) = \sum_{i=1}^{4} N_i(Z)\, q_i^e(t) \tag{5.5}$$

where $N_i(Z)$ are called the shape functions which must satisfy the boundary conditions of the element and otherwise arbitrary.

The natural approach for deducing the shape functions is through the use of the static equilibrium condition of the beam. The static equilibrium equations are derived from equations (5.1) by letting all the time derivatives and the applied load be zero. Then using equations (5.2) and (5.3), the static equilibrium equations are

$$\frac{dV_X}{dZ} = 0$$

$$\frac{dM_Y}{dZ} = V_X \tag{5.6}$$

Further, using equation (5.2) in (5.3) gives

$$\frac{d^2X}{dZ^2} + \frac{d\phi_{sX}}{dZ} = \frac{M_Y}{EI} \tag{5.7}$$

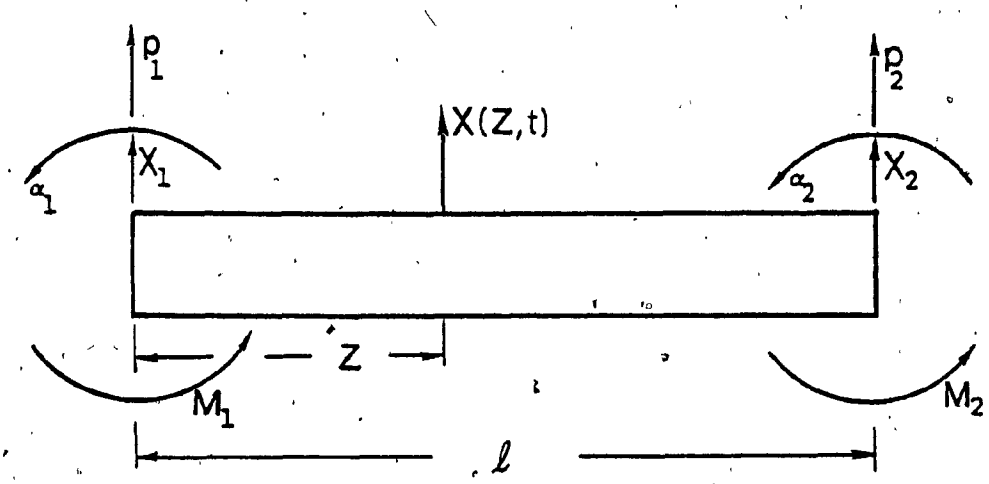

$$\begin{matrix} X_1 \\ \alpha_1 \\ X_2 \\ \alpha_2 \end{matrix} \equiv \begin{matrix} q_1^e \\ q_2^e \\ q_3^e \\ q_4^e \end{matrix}$$

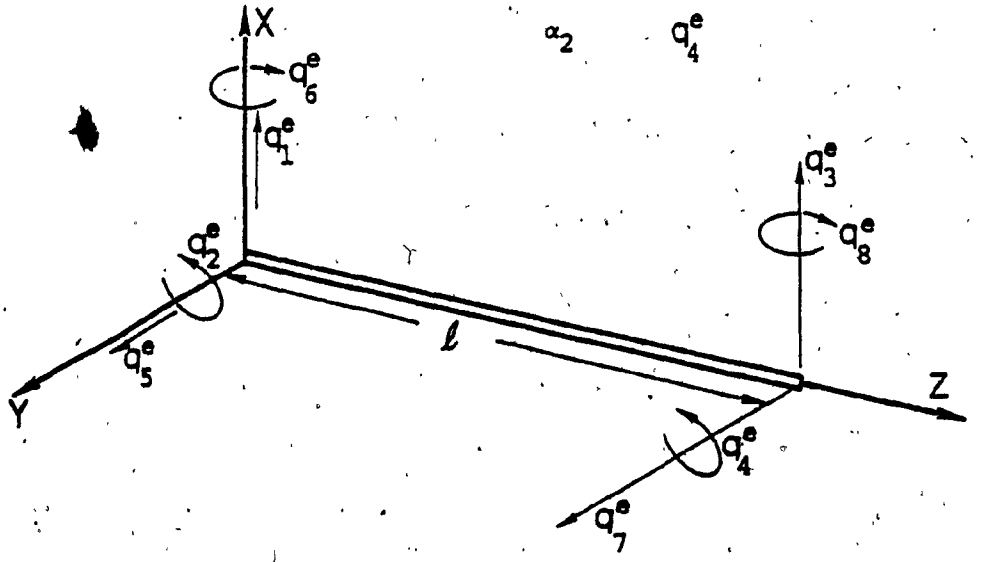

Fig. 5.2 Primary Arrangements of the Element Nodal Coordinates.

Integrating equations (5.6) and (5.7) gives the expression for static deflection as

$$X = \frac{1}{EI} \left(a_1 \frac{Z^3}{6} + a_2 \frac{Z^2}{2} + a_3 Z + a_4 \right)$$

where a_1, a_2, ..., are constants to be determined from the boundary conditions. For $N_1(Z)$, the boundary conditions are

$$N_1(0) = 1;\ N_1(\ell) = 0;\ \left(\frac{dN_1}{dZ} + \phi_{sX}\right)_{Z=0} = 0;\ \left(\frac{dN_1}{dZ} + \phi_{sX}\right)_{Z=\ell} = 0;$$

and similarly for N_2, N_3 and N_4. Evaluating the constants a_i for every set of boundary conditions, the shape functions can now be derived and written as [58]

$$\begin{aligned}
N_1 &= \frac{1}{(1+\gamma)} \left(1 + \gamma - \gamma g_e - 3g_e^2 + 2g_e^3\right) \\
N_2 &= \frac{\ell}{2(1+\gamma)} \left(2g_e + \gamma g_e - 4g_e^2 - \gamma g_e^2 + 2g_e^3\right) \\
N_3 &= \frac{1}{(1+\gamma)} \left(\gamma g_e + 3g_e^2 - 2g_e^3\right) \\
N_4 &= \frac{\ell}{2(1+\gamma)} \left(-\gamma g_e - 2g_e^2 + \gamma g_e^2 + 2g_e^3\right)
\end{aligned} \tag{5.8}$$

where $\gamma = \dfrac{12EI}{\rho G_s A \ell^2}$

and

$$g_e = \frac{Z}{\ell}$$

The displacement $Y(Z,t)$ in the YZ plane can be derived by an exact "analogous" procedure. The rotational displacement

$\alpha(Z,t)$ can be described in a similar fashion as

$$\alpha(Z,t) = \sum_{i=1}^{4} \cdot N_{ri}(Z)\ q_i^e(t) \qquad (5.9)$$

and analogously for $\beta(Z,t)$.

The shape functions $N_{ri}(Z)$ are not presented in any of the previous work [58-63] but different procedures are used to develop the stiffness and mass matrices. The evaluation of such shape functions is important for including the effects such as hysteresis where the rotational displacements must be defined. Construction of the stiffness and mass matrices are also simplified by the explicit definition of the rotational displacments. The shape functions N_{ri} for the rotational displacements are developed simultaneously with the shape functions N_i, in equation (5.8), and can be written as

$$\begin{aligned}
N_{r_1} &= \frac{1}{\ell(1+\gamma)}\ (-6g_e + 6g_e^2) \\
N_{r_2} &= \frac{1}{(1+\gamma)}\ (1 + \gamma - 4g_e - \gamma g_e + 3g_e^2) \\
N_{r_3} &= \frac{1}{\ell(1+\gamma)}\ (6g_e - 6g_e^2) \\
N_{r_4} &= \frac{1}{(1+\gamma)}\ (-2g_e + \gamma g_e + 3g_e^2)
\end{aligned} \qquad (5.10)$$

Substituting the displacements X,Y,α and β along with their derivatives in the kinetic and potential energy

expressions (5.4) and carrying out the integrations over the element, the Lagrange's equations may be developed in the form

$$\frac{d}{dt}\left(\frac{\partial T}{\partial \dot{q}_i^e}\right) - \frac{\partial T}{\partial q_i^e} + \frac{\partial P}{\partial q_i^e} = Q_i^e \quad , \; i = 1,2,\ldots,8$$

where Q_i^e are the nonconservative forces which are introduced into the system through the virtual work expression

$$\delta W_x = \int_0^{\ell} p_x(Z,t)\ \delta X(Z,t)\ dZ$$

and since

$$\delta X(Z,t) = \sum_{i=1}^{4} N_i\ \delta q_i^e$$

which yields

$$Q_i^e = \int_0^{\ell} p_x(Z,t)\ N_i\ dZ \quad , \quad i = 1,2,\ldots,4 \qquad (5.11)$$

Similar expressions can be derived for the YZ plane. The element equations of motion in a matrix form can be written as

$$\begin{bmatrix} [M_{t_1}] & [0] \\ [0] & [M_{t_1}] \end{bmatrix} \{\ddot{q}^e\} + \begin{bmatrix} [M_{r_1}] & [0] \\ [0] & [M_{r_1}] \end{bmatrix} \{\ddot{q}^e\} + \begin{bmatrix} [0] & [G_y] \\ -[G_y] & [0] \end{bmatrix} \{\dot{q}^e\} + \begin{bmatrix} [k_1] & [0] \\ [0] & [k_1] \end{bmatrix} \{q^e\} = \{Q^e\} \qquad (5.12)$$

Here the subscript t refers to translation and the subscript r refers to rotation. All submatrices $[M_{t_1}]$, $[M_{r_1}]$, $[G_y]$ and $[k_1]$ are symmetric and are of the order 4. Submatrices $[M_{t_1}]$,

$[M_{r_1}]$ and $[k_1]$ are presented in Appendix F. $[G_y]$ is given by

$$[G_y] = [M_{r_1}] \frac{J_z}{J_T} \omega_r$$

5.4 Comparison Between the Present Finite Element Procedure and the Unified Rotational Sign Treatment

The unified rotational sign procedure considers a specific angular direction for both planes [64,65]. In the unified sign treatment, the slope of the beam centre line in the YZ plane is altered to keep the angular displacement β in a positive direction; that is,

$$\beta = - \frac{\partial Y}{\partial Z}$$

Here the shear deformation is not considered which was also the case with the studies [64,65]. The displacements X,Y, α and β in turn will be

$$\begin{aligned} X(Z,t) &= \sum_{i=1}^{4} N_i \, q_i^e \\ Y(Z,t) &= \sum_{i=1}^{4} (-1)^{i+1} N_i \, q_{i+4}^e \\ \alpha(Z,t) &= \sum_{i=1}^{4} N_i' \, q_i^e \\ \beta(Z,t) &= \sum_{i=1}^{4} (-1)^{i} N_i' \, q_{i+4}^e \end{aligned} \qquad (5.14)$$

and the equations of motion of the element will be

$$\begin{bmatrix} [M_{t_1}] & [0] \\ [0] & [M_{t_2}] \end{bmatrix} \{\ddot{q}^e\} + \begin{bmatrix} [M_{r_1}] & [0] \\ [0] & [M_{r_2}] \end{bmatrix} \{\ddot{q}^e\} + \begin{bmatrix} [0] & [G^*] \\ -[G^*]^T & [0] \end{bmatrix} \{\dot{q}^e\}$$

$$+ \begin{bmatrix} [k_1] & [0] \\ [0] & [k_2] \end{bmatrix} \{q^e\} = \{Q^e\} \qquad (5.15)$$

Submatrices $[M_{t_1}]$, $[M_{r_1}]$ and $[k_1]$ are the same as those of system (5.12) with the shear factor $\gamma = 0$ and the new matrices $[M_{t_2}]$, $[M_{r_2}]$, $[k_2]$ and $[G^*]$ are presented in Appendix F. Also, the first 4 elements in the vector $\{Q^e\}$ are similar to those in (5.11), but the last 4 are defined by

$$Q_i^e = \int_0^{\ell} p_y(Z,t)\ N_{i-4}\ (-1)^{i+1}\ dZ\ ,\quad i=5,6,7,8 \qquad (5.16)$$

It is clear from equations (5.15) and (5.16) that the unified rotational sign system [62,64,65] is associated with a complicated procedure. These complications will even be magnified when the stage is reached to add further details to the system such as internal damping and bearing's stiffness, damping and pedestal flexibility. The final solutions for a rotor bearing system using either of these two conventions are exactly the same in terms of the eigenvalues, the precessional direction of the modes and the dynamic response with the exception that the sign of the angular response β will be different. For these reasons and because of the procedural simplicity, the analogous motion plane method is adopted in this analysis.

5.5 Internal Damping

Internal damping can be divided into two distinctive parts, namely, viscous damping component and a hysteretic component. Viscous damping is induced in a rotating beam due to its internal resistance to strain. The viscous damping forces presented by Gunter [48] for a single mass rotor are

$$F_{Xd} = -C_d(\dot{X} + \omega_r Y)$$
$$F_{Yd} = -C_d(\dot{Y} - \omega_r X) \tag{5.17}$$

and can be introduced to the element equations as distributed forces through the virtual work expression as

$$Q_i^e = -\int_0^\ell C_d(\dot{X} + \omega_r Y)\, N_i \, dZ \quad \text{(XZ plane)}$$
$$= -\int_0^\ell C_d(\dot{Y} - \omega_r X)\, N_{i-4} \, dZ \quad \text{(YZ plane)} \tag{5.18}$$

with the velocities $\dot{X}$ and $\dot{Y}$ given by

$$\dot{X} = \sum_{i=1}^{4} N_i \dot{q}_i^e \; ; \quad \dot{Y} = \sum_{i=1}^{4} N_i \dot{q}_{i+4}^e \tag{5.19}$$

The velocity terms in equation (5.18) add a new matrix $[D_v]$ to the system (5.12) which is exactly similar to the translation matrix $[M_t]$ but with C_d in the place of m_z. That is

$$[D_v]\{\dot{q}^e\} = \frac{C_d}{m_z}\begin{bmatrix}[M_{t_1}] & [0] \\ [0] & [M_{t_1}]\end{bmatrix}\{\dot{q}^e\} \tag{5.20}$$

The displacement terms in expressions (5.18) introduce a

skew symmetric matrix $[D_d]$ such that

$$\left[D_d\right]\left\{q^e\right\} = \frac{c_d\,\omega_r}{m_z}\begin{bmatrix}[0] & [M_{t_1}]\\ -[M_{t_1}] & [0]\end{bmatrix}\left\{q^e\right\} \tag{5.21}$$

Hysteretic damping is the second form of internal damping and is induced in a vibrating beam under the action of cyclic stresses. Hysteresis, is a material property and is independent of the frequency of the cyclic stress. The lag angle γ_h of the neutral stress line induces a coupling between the flexural bending moments such that [54]

$$\begin{Bmatrix}M_y\\ M_x\end{Bmatrix} = EI\begin{bmatrix}\cos\gamma_h & \sin\gamma_h\\ -\sin\gamma_h & \cos\gamma_h\end{bmatrix}\begin{Bmatrix}\alpha'\\ \beta'\end{Bmatrix} \tag{5.22}$$

where γ_h is called the loss angle and is given by

$$\sin\gamma_h = \frac{\eta_h}{\sqrt{1+\eta_h^2}} \tag{5.23}$$

and $\pi\eta_h$ is the logarithmic decrement of the damping in the beam [54].

Introduction of the primary moments, represented by the diagonal terms in equation (5.22), into the potential energy expression is straight forward and is accomplished by multiplying the stiffness matrix by $\cos\gamma_h$. The components of the nonconservative moments which are the off diagonal terms in equation (5.22), should be introduced in a similar manner as the nonconservative forces of expression (5.11). The moment equations of the system (5.1) may be rewritten as

$$J_T \frac{\partial^2 \alpha}{\partial t^2} + \omega_r J_z \frac{\partial \beta}{\partial t} + \rho A G_x \left(\alpha - \frac{\partial X}{\partial Z}\right) - \frac{\partial}{\partial Z} \left(EI \cos\gamma_h \frac{\partial \alpha}{\partial Z}\right)$$

$$= \frac{\partial}{\partial Z} \left(EI \sin\gamma_h \frac{\partial \beta}{\partial Z}\right)$$

$$J_T \frac{\partial^2 \beta}{\partial t^2} - \omega_r J_z \frac{\partial \alpha}{\partial t} + \rho A G_s \left(\beta - \frac{\partial Y}{\partial Z}\right) - \frac{\partial}{\partial Z} \left(EI \cos\gamma_h \frac{\partial \beta}{\partial Z}\right) \quad (5.24)$$

$$= -\frac{\partial}{\partial Z} \left(EI \sin\gamma_h \frac{\partial \alpha}{\partial Z}\right)$$

The coupling moments can then be introduced through the principle of virtual work as explained below.

$\delta W_{XZ} = \int_0^\ell M_{XZ}\, \delta\alpha\, dZ$ with respect to the XZ plane

where $M_{XZ} = \frac{\partial}{\partial Z} \left(EI \sin\gamma_h \frac{\partial \beta}{\partial Z}\right)$

and the analogous moment equation with respect to the YZ plane can be determined similarly.

Then,

$$\delta W_{XZ} = \int_0^\ell \frac{\partial}{\partial Z} \left(EI \sin\gamma_h \frac{\partial \beta}{\partial Z}\right) \delta\alpha \; dZ, \text{ for the XZ plane}$$

$$= \left[EI \sin\gamma_h \frac{\partial \beta}{\partial Z}\, \delta\alpha\right]_0^\ell - \int_0^\ell EI \sin\gamma_h \frac{\partial \beta}{\partial Z}\, \delta\alpha'\, dZ \quad (5.25)$$

The first term forms the natural boundary conditions and vanishes for, at least, a free-free beam. The second term introduces a skew symmetric matrix $[D_h]$ to be added to the stiffness matrix of the element equation system (5.12). The matrix $[D_h]$ is developed in Appendix G.

5.6 The Bearing Element and the Flexibility of the Bearing Suspension

The bearings represent a flexible restraint on the rigid body motion of the rotating beam. As can be seen from Fig. 5.3, the bearing hydrodynamic forces F_X and F_Y are assumed to be located at a distance Z_c from one end of element, say the left node, such that

$$F_X = F_X(X_c, Y_c, \dot{X}_c, \dot{Y}_c) \qquad \}$$

and similarly for F_Y. The hydrodynamic forces F_X and F_Y are then introduced into the element equations (5.12) through the principle of virtual work given by

$$\delta W_X = F_X \, \delta X_c$$

and similarly for the Y direction.

The finite element modelling of a rotating beam as an explicitly written set of equations of motion represents an advantage due to the simplicity in the adaptation of the non-linear hydrodynamic forces F_X and F_Y. For added convenience a particular adjustment by considering $Z_c = 0$ or $Z_c = \ell$ is proposed, which will allow the nonlinear stiffnesses and damping expressions, given in (B.1) of Appendix B, to be introduced into the dynamical system directly as they are stated.

For linearized hydrodynamic forces, the coordinates are moved to the static equilibrium location of the journal O_j° and can be seen from the axial view of Fig. 5.3b, which

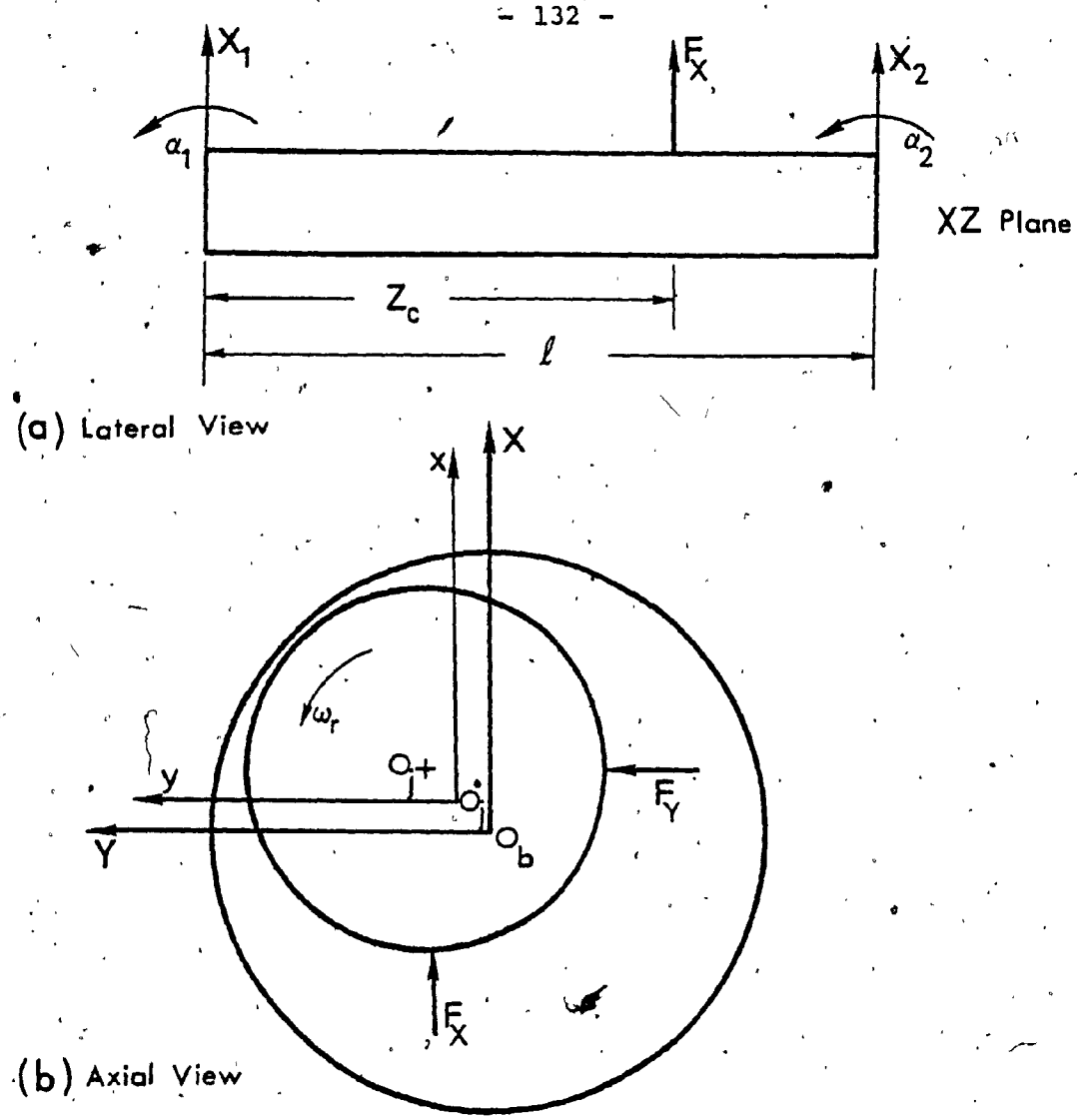

Fig. 5.3 Bearing-Element Coordinates System.

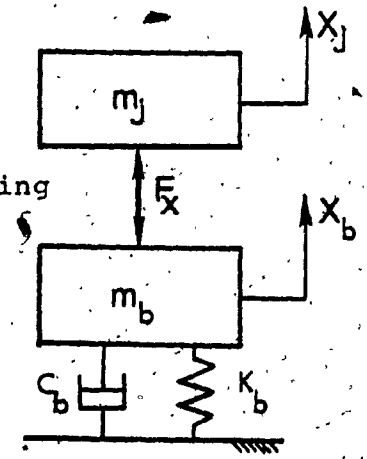

$x = X_j - X_b$

$y = Y_j - Y_b$

$F_X = F_X(x, y, \dot{x}, \dot{y})$

XZ Plane

Fig. 5.4 Sketch of the Journal, Bearing and Support.

corresponds to a specific load, spinning speed ω_r and bearing parameters. Expanding the nonlinear hydrodynamic forces around the equilibrium point, using Taylor series and retaining only the first order derivatives, the hydrodynamic forces can be written in the form

$$F_x = -k_{xx}\, x - k_{xy}\, y - c_{xx}\, \dot{x} - c_{xy}\, \dot{y}$$

and similarly for F_y. Here, it is understood that the displacements in the above expression are such that

$$x = x(Z,t)\Big|_{Z=Zc} \quad \text{and} \quad y = y(Z,t)\Big|_{Z=Zc}$$

The interaction between the bearing and the supporting structure represents a positive step towards a realistic simulation of a rotor bearing system. This particular step starts with an approach that can be further extended to include a complete machine structure into a one general dynamic system. A simplified model for the journal, the bearing and the bearing support is presented in Fig. 5.4. The bearing mass m_b represents a moving reference. The displacements, X_j and Y_j will be the rotor coordinates in terms of a new stationary reference. The linearized hydrodynamic forces make it easy to introduce the support effect. In this case, the hydrodynamic force F_x is given by

$$F_x = F_x(x,y,\dot{x},\dot{y})$$

$$= F_x(X_j,Y_j,\dot{X}_j,\dot{Y}_j) - F_x(X_b,Y_b,\dot{X}_b,\dot{Y}_b)$$

where X_b, Y_b are the bearing displacements.

Details of the arrangements of the bearing element and the bearing support with stiffness and damping coefficients are presented in Appendix H.

5.7 Global Assembly of the Rotor Elements

The element equations (5.12) with the internal damping may be expressed in the form

$$\left[[M_t] + [M_r]\right]\left\{\ddot{q}^e\right\} + \left[[G] + [D_v]\right]\left\{\dot{q}^e\right\} + \left[\cos\gamma_h[k] + [D_d] + [D_h]\right]\left\{q^e\right\} = \left\{Q^e\right\} \tag{5.26}$$

which is of order 8. The coordinates q^e are arranged such that

q_i^e take $i = 1,2,3,4$ with respect ot XZ plane

q_i^e take $i = 5,6,7,8$ with respect to YZ plane

Before arranging the elements into a global assembly, a local coordinate arrangement is first made, as can be seen from Fig. 5.5, with

q_i^e take $i = 1,2,3,4$ for left hand side node

q_i^e take $i = 5,6,7,8$ for right hand side node.

The assembly of all the elements into one global system is then straight forward since the elements are all aligned in a one-dimensional space. All similar coordinates from the adjacent elements are then simply added together. The bearing coefficients are included in the element equations as presented in Appendix H. However, the bearing support

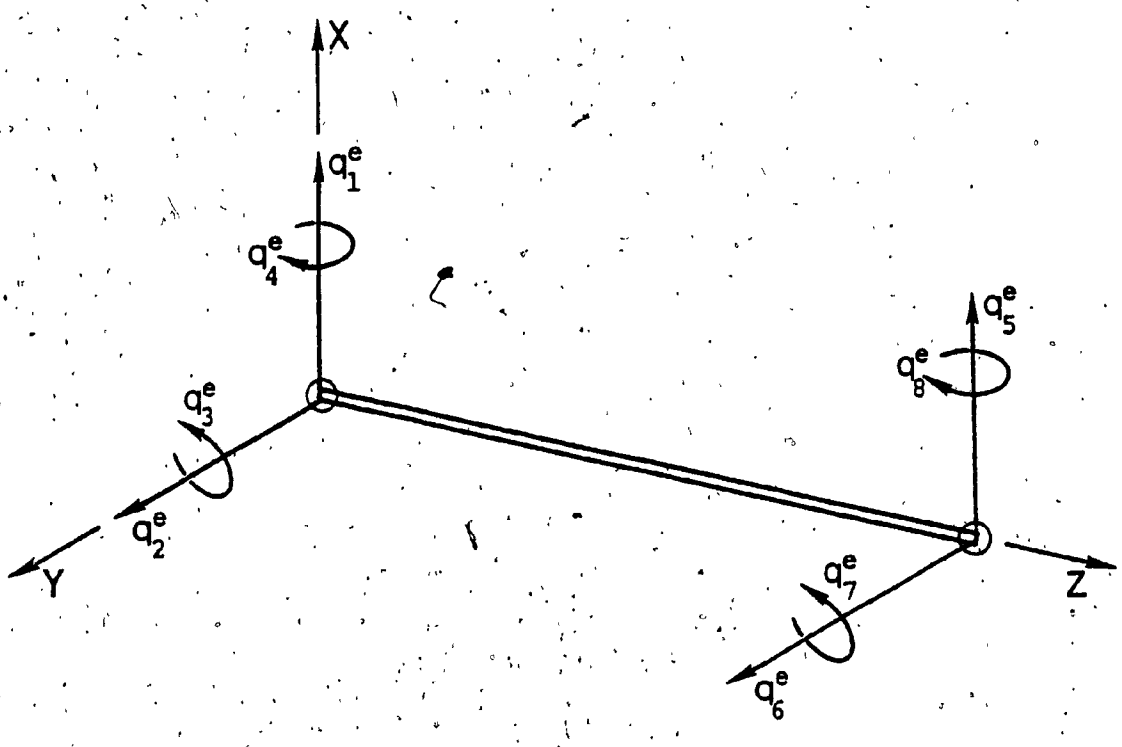

Fig. 5.5 Adjusted Element Coordinates for Global Assembly.

coefficients and the bearing equations are to be added into the global assembly of the elements. The final global system will then be

$$[m_s]\{\ddot{q}_s\} + [c_s]\{\dot{q}_s\} + [k_s]\{q_s\} = \{Q_s\} \qquad (5.27)$$

which is a dynamical system with N degrees-of-freedom where N is given by

$$N = 4(n+1) + 2(b)$$

with n = number of elements

b = number of bearing flexible supports

Matrices $[c_s]$ and $[k_s]$, with the addition of the bearing stiffness and damping coefficients are nonsymmetric in character.

5.8 Solution of the Rotor System by Modal Analysis

The second order differential equations (5.27) form a linear system with unsymmetric damping and stiffness marices. A proper approach to the solution of this problem is to transform the system into its natural or principal coordinates in which the equations will be decoupled for an easy solution. The decoupling of the equations of motion can be carried out utilizing a similarity transformation [88] which is applicable to a general dynamic system such as (5.27). However this technique involves the inversion of two matrices of order 2N where N is the number of degrees-of-freedom of the dynamical system. Further, one of the matrices to be

inverted is the modal matrix which is made up of complex elements.

A simpler approach would be to determine the solution by a modal analysis. Due to the linear independence of the eigenvectors, the system response at a given time can be calculated as a weighted sum of the natural modes of the system. This weighted sum signifies the contribution due to each independent mode. Since the significance of the higher modes in the calculation of the response decreases as compared to the contriubtion of these modes in the neighbourbood of the excitation frequencies, only a finite number of eigenvalues and eigenvectors need to be calculated.

Modal analysis for undamped systems and for damped symmetric systems with the damping matrix proportional to any or both of the mass and stiffness matrices, is known in the literature [75,88]. In case of a general damped symmetric system there exists a modal analysis [76] which starts by rewriting the system in its first order form to provide a square modal matrix which is necessary for the linear transformation to the principle coordinates. The system is rewritten as a set of first order equations as follows:

$$[M]\ \{\dot{q}\} + [K]\ \{q\} = \{Q\} \tag{5.28}$$

where

$$[M]_{2NX2N} = \begin{bmatrix} [0] & [m_s] \\ [m_s] & [C_s] \end{bmatrix} \qquad [K]_{2NX2N} = \begin{bmatrix} [-m_s] & [0] \\ [0] & [k_s] \end{bmatrix}$$

$$\{q\} = \begin{Bmatrix} \{\dot{q}_s\} \\ \{q_s\} \end{Bmatrix} \qquad \{Q\} = \begin{Bmatrix} \{0\} \\ \{Q_s\} \end{Bmatrix}$$

Very little information is available on the modal analysis of a general nonsymmetric system. However, there is a general modal analysis treatment [77] which was applied to the rotor dynamic problem by Lund [55] through a transfer matrix technique. Neither the statements and proofs of the orthogonality relations given by Lancaster [77] are in a standard form [75,76,88] nor the procedure due to Lund [55] is suitable for a general dynamical system. Therefore, a standard proof as well as the necessary relations for modal analysis of a general dynamical system are breifly presented below.

Along with the eigenvalue problem

$$\lambda[M]\{\phi\} + [K]\{\phi\} = \{0\} \tag{5.29}$$

consider the complementary eigenvalue problem of the transpose of the dynamic system (5.28)

$$\lambda[M]^T\{\psi\} + [K]^T\{\psi\} = \{0\} \tag{5.30}$$

The eigenvalues λ_j (j=1,2,....,2N) of both of the above problems are identical. However, for a general nonsymmetric system, the corresponding eigenvectors $\bar{\phi}_j$ and $\bar{\psi}_j$ are different. Here the roots of the characteristic equations λ_j are referred to as the eigenvalues[1] where it is understood [75] that they are the eigenvalues of the dynamic matrix $[M]^{-1}[K]$. The vectors $\bar{\phi}_j$ and $\bar{\psi}_j$ are called the j^{th} eigenvector and the j^{th} complementary eigenvector respectively, or the j^{th} right eigenvector and the j^{th} left eigenvector [75].

[1] In some dynamical analysis the term eigenvalue is used to define a pair of complex conjugate roots [55].

For an eigenvalue λ_j and a right eigenvector $\bar{\phi}_j$, the relation

$$\lambda_j [M]\{\phi_j\} + [K]\{\phi_j\} = \{0\} \tag{5.31}$$

is satisfied. Similarly for an eigenvalue λ_k and a left eigenvector $\bar{\psi}_k$, the relation

$$\lambda_k \{\psi_k\}^T[M] + \{\psi_k\}^T[K] = \{0\}^T \tag{5.32}$$

is also satisfied.

Premultiplying (5.31) by $\bar{\psi}_k{}^T$ and postmultiplying (5.32) by $\bar{\phi}_j$ and then subtracting (5.32) from (5.31) gives

$$(\lambda_j - \lambda_k)\{\psi_k\}^T[M]\{\phi_j\} = \{0\} \tag{5.33}$$

which leads to the relation

$$\{\psi_k\}^T[M]\{\phi_j\} = \{0\} \quad , \quad j \neq k \tag{5.34}$$

Assuming that all the eigenvalues to be distinct and summing up all similar relations (5.34), gives the following orthogonality relation:

$$[\Psi]^T[M][\Phi] = [M^*] \tag{5.35}$$

similarly, it can be shown that

$$[\Psi]^T[K][\Phi] = [K^*] \tag{5.36}$$

where M^* and K^* are diagonal matrices. The orthogonality relations (5.35) and (5.36) are general and hold true for any dynamical system.

Introducing the linear transformation

$$\{q\} = [\Phi]\{u\} \tag{5.37}$$

in equation (5.28) and multiplying throughout by $[\Psi]^T$ yields

$$[\Psi]^T[M][\Phi]\{\dot{u}\} + [\Psi]^T[K][\Phi]\{u\} = [\Psi]^T\{Q\}$$

which is in the form

$$[M^*]\{\dot{u}\} + [K^*]\{u\} = \{U\} \tag{5.38}$$

System (5.38) is a set of decoupled first order ordinary differential equations that can be solved in a closed form.

Using the orthogonality relations, it can be shown that

$$\lambda_j M_j^* = -K_j^*$$

which can be used in equation (5.38) and results in a simpler form for the decoupled first order equation. This, in a scalar form, is

$$\dot{u}_j - \lambda_j u_j = \frac{1}{M_j^*} U_j \quad , \quad j = 1,2,\ldots,2N \tag{5.39}$$

5.9 The Transient and Forced Response of the Rotor System

The solution of the global equation of motion (5.27) is now reduced to finding the solution of equation (5.39). A general solution of equation (5.39) can be shown to take the form [75;88]

$$u_j = a_j \exp(\lambda_j t) + \frac{1}{M_j^*} \int_0^t U_j(\zeta) \exp[\lambda_j(t-\zeta)]d\zeta \quad , \quad j=1,2,\ldots,2N \tag{5.40}$$

The first part of the solution represents the transient response where the constants a_j , $j = 1,2,\ldots,2N$ are to be evaluated from the initial conditions which are given in the principle coordinates $\bar{u}$ by

$$\{u(0)\} = \text{Real } [\Phi]^{-1}\{q(0)\} \qquad (5.41)$$

The steady state response, in turn, can also be calculated through the evaluation of the integral in equation (5.40) for a specified excitation $\bar{Q}(t)$. An example of the steady state response of an unbalance excitation is presented in Appendix I.

The linear transformation (5.37) can, alternatively, be written as

$$q_k = \sum_{j=1}^{2N} \phi_{kj}\, u_j \quad , \qquad k = 1,],\ldots,2N \qquad (5.42)$$

which can now be used to calculate the response at any single point on the rotor beam.

5.10 Comparison of Results and Further Analysis

The objectives of this section are

i) To perform a comparison of the obtained results with previous experimental and theoretical results essentially the well known results of Lund and Orcutt [53], in order to examine the validity of the present finite element approach combined with a modal analysis in evaluating a rotor-bearing response.

ii) To introduce a comparison between the different effects of the bearing lining flexibility and the bearing support flexibility.

iii) To discuss the proper choice of the suitable number of elements for a typical application and finally,

iv) To provide and to discuss the various ways of interpreting better the stability and dynamic response results of a rotor-bearing.

One of the rotor-bearing configurations that were used by Lund and Orcutt [53] and chosen here for comparison is presented in Fig. 5.6. Tilting pad bearings were utilized and were positioned symmetrically with respect to the load such that their characteristics are symmetric and there are no cross coupling terms which result in circular response orbits. A Hertzian surface-contact stiffness was calculated at a load of 100lb by Lund and Orcutt and found to be 5×10^5lb/in (8.756×10^4N/mm). Also, the unbalance weights were in phase and were positioned on two locations of the rotor beam as shown in Fig. 5.6. In the present procedure the beam is divided into 5 elements with the 6 nodes indicated in Fig. 5.6 while in the event of using only 3 elements the second and fifth nodes are to be excluded.

Using the surface contact stiffness in series with the bearing stiffness, as adopted by Lund and Orcutt, a solution by finite element followed by modal analysis is carried out and presented in Fig. 5.7. Also the theoretical

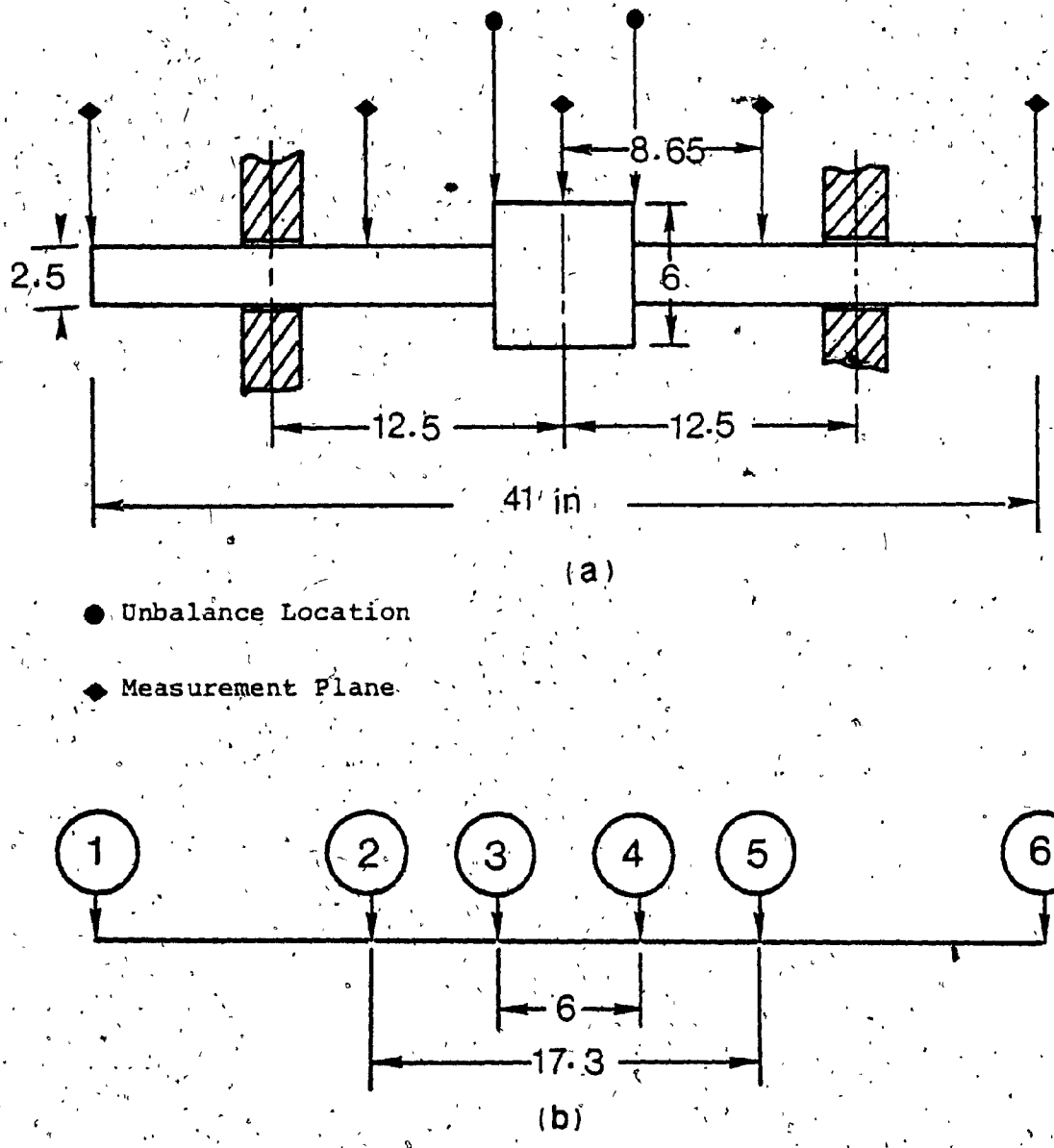

Fig. 5.6 a) Lay-out of the Rotor Bearing System Used for the Comparative Study.

b) Nodes and Elements Arrangement.

results due to Lund and Orcutt [53], which was obtained using a transfer matrix method incorporating continuous shaft segments, are reproduced in Fig. 5.7. As can be seen from the figure, the present results provide a closer agreement with the experimental results than the transfer matrix method, over most of the speed range when only 3 elements are used. This provides a good check on the present procedure and extends the conclusion on the accuracy of the finite element method by Ruhl and Booker [57] who used a simple finite element model.

The fast convergence of the finite element analysis towards the actual solution is also demonstrated by two sets of results for two separate arrangements, one with 3 elements and the other using 5 elements. The results presented in Fig. 5.8 show a little improvement resulting from replacing a 3 element arrangement by a 5 element one, over the entire range. Therefore dividing the beam into 3 elements may be a more suitable choice since this particular arrangement fits the geometrical shape of the rotor-beam. Obviously, the dynamical system (5.27) constructed with 3 elements, will also possess a smaller number of degrees-of-freedom.

The results presented in Fig. 5.8 are arrived at using a bearing support stiffness in place of, and equal in magnitude to, the surface contact flexibility. This specific study is carried out for the sake of bringing out additional features in the finite element procedure. It is interesting

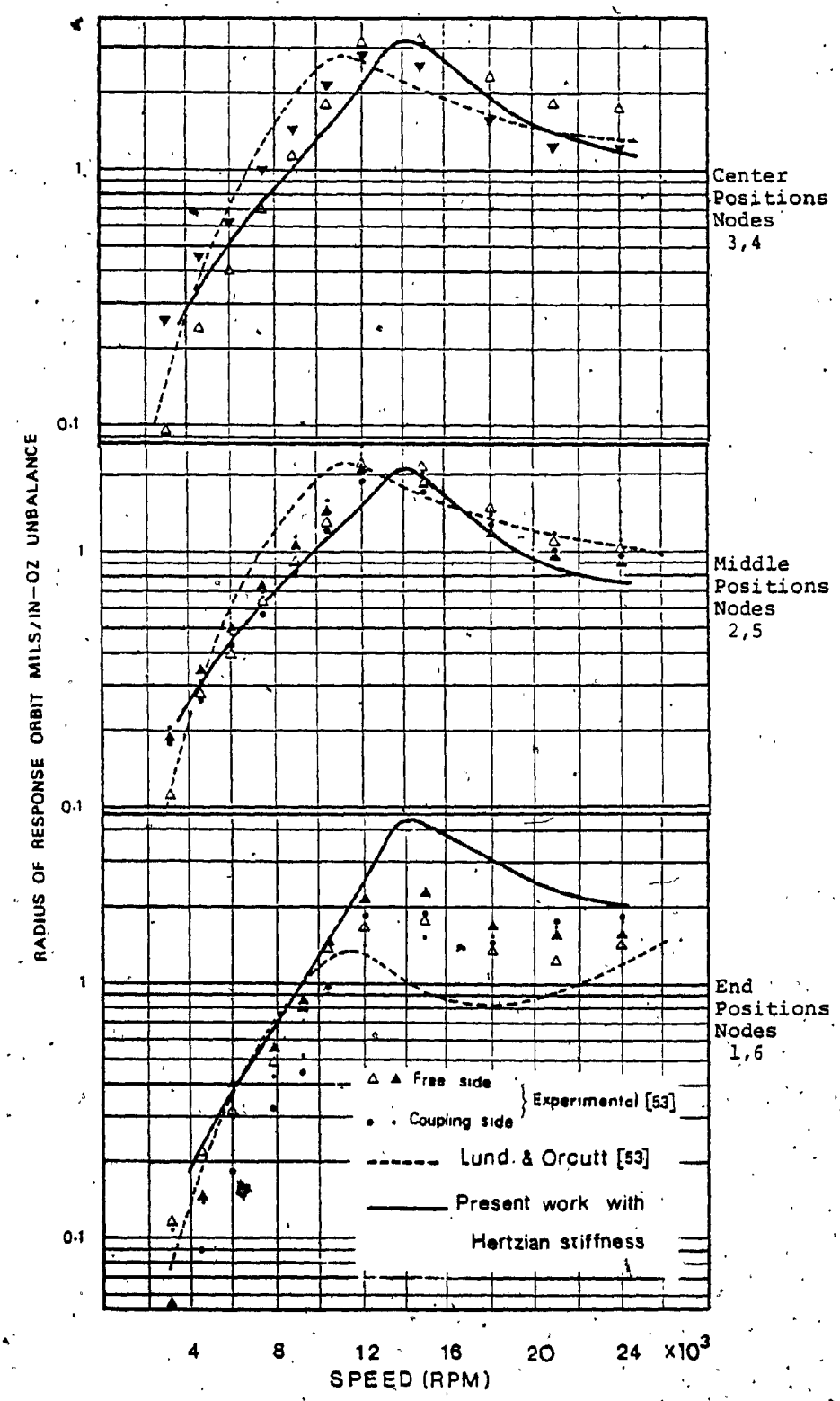

Fig. 5.7 Comparison of the Present Results with Previous Experimental and Theoretical Results.

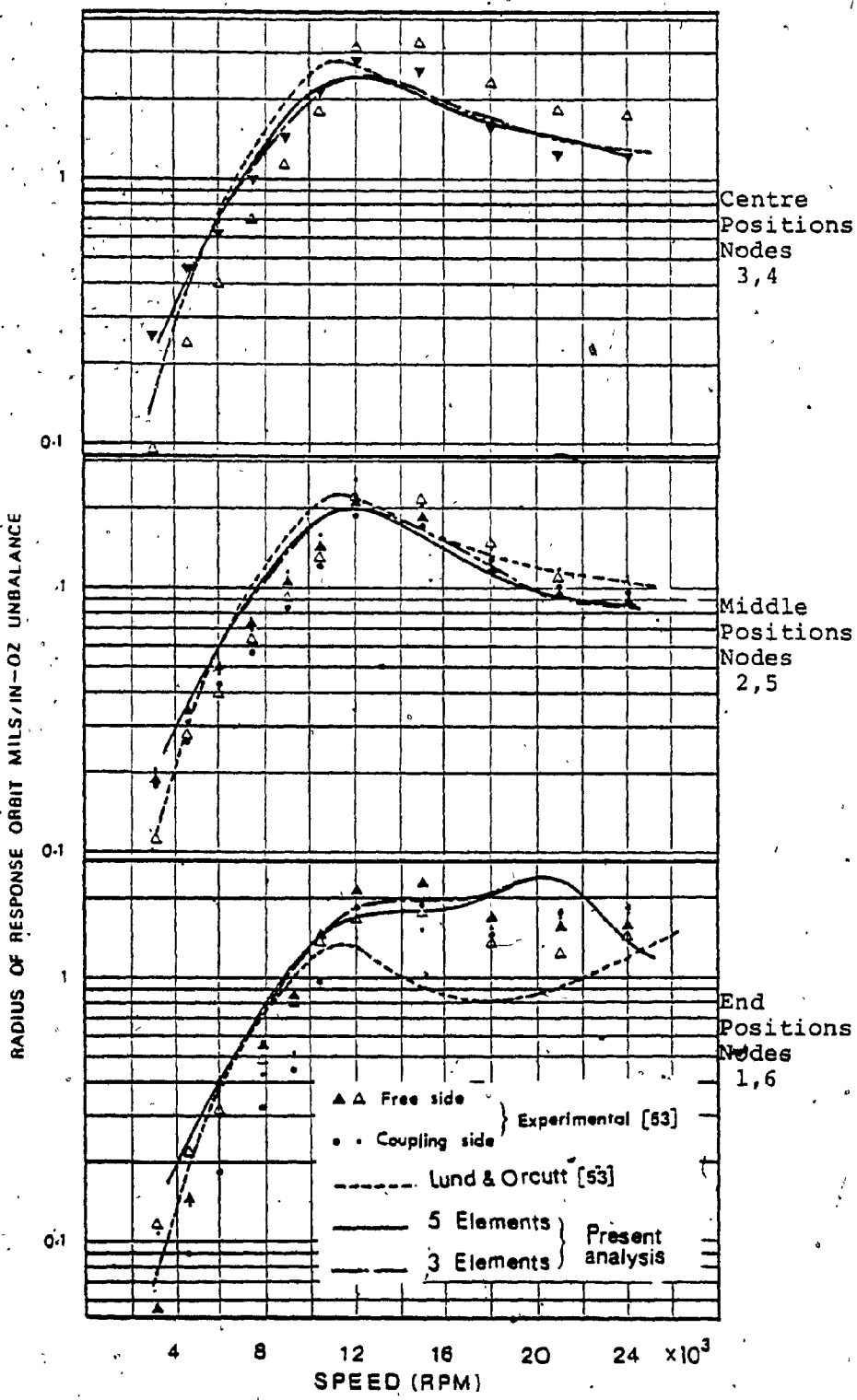

Fig. 5.8 Two Element Arrangements, and the Effect of Bearing Support Flexibility.

to notice the stabilizing effect of the bearing support flexibility in comparison to the effect of the surface contact flexibility, particularly in the range 12000 - 18000 RPM. This stabilizing effect is due to the added degrees-of-freedom to the bearing. This can be explained by the point view-phase diagram (5.9) which shows that the bearing stays almost in phase with the middle nodes, where most of the rotor mass and also the unbalance weights are located, through the speed range specified above, namely 12000 - 18000 RPM, and therefore allowing the soft mounting of the bearing to stabilize the rotor motion.

The end positions in Fig. 5.8 shows a distinct peak at a speed of approximately 20500 RPM where the peaks at the other two positions can hardly be recognized. This can be explained through Fig. 5.9 at a speed of 20000 RPM the end node 1 is almost out of phase by an angle of 90° with the bearing position and therefore remains unaffected by the bearing soft mounting. In such cases where a critical speed can not be easily recognized, a better interpretation of the results can be made. These are achieved by

i) using point-view phase diagram similar to Fig. 5.9 and,

ii) by plotting the inclination angles α and β which are found to be more sensitive than the translational displacements. An example is presented in Fig. 5.10 corresponding to the results of Fig. 5.8, but with the angular displacement α(orβ) in place of the orbit radius which clearly shows

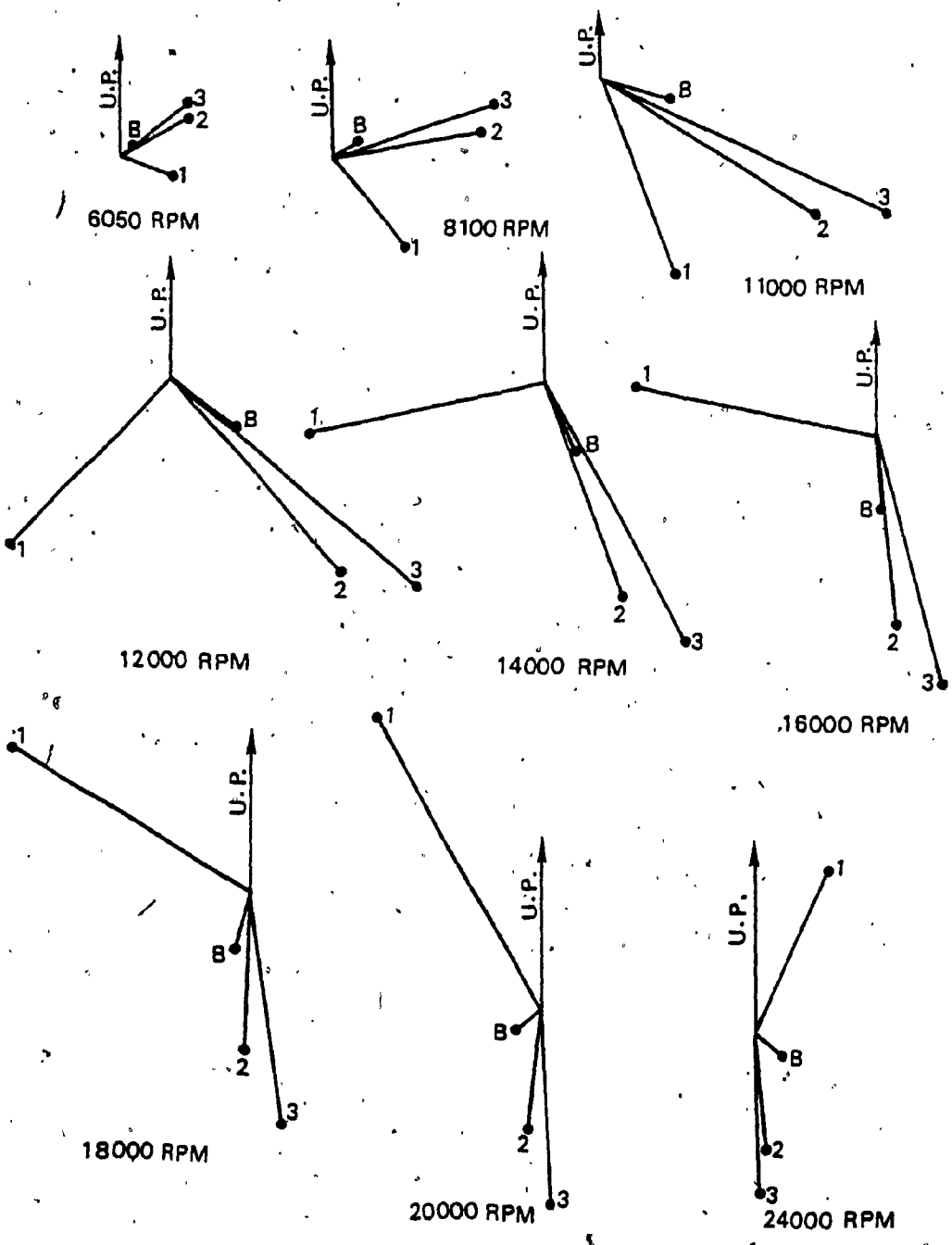

U.P. = Unbalance Plane

1,2,3 and B are nodes 1,2,3 and bearing

Fig. 5.9 Point View Phase Diagram of the Instantaneous Location of the Rotor Nodes.

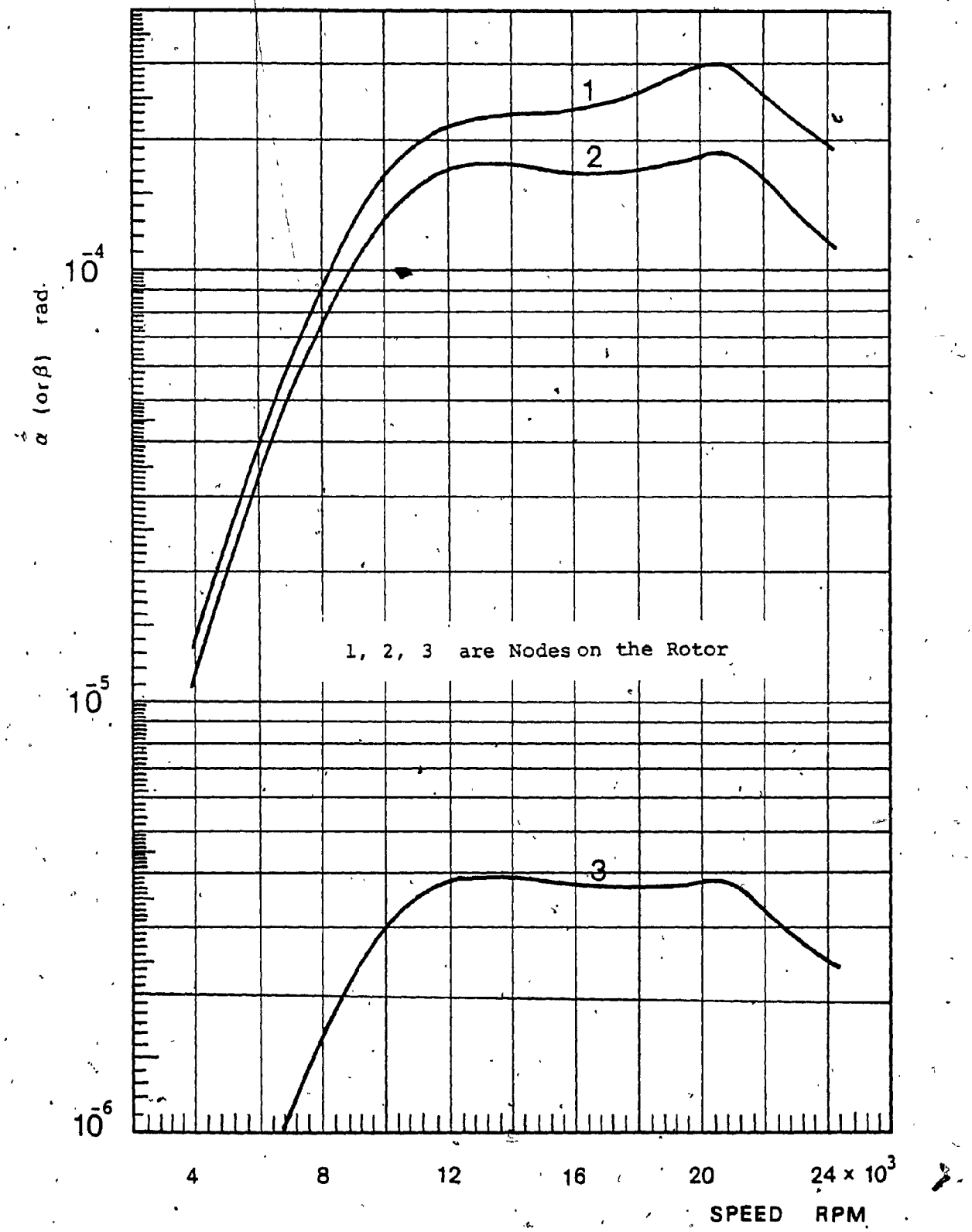

Fig. 5.10 Plot of the Angular Displacements.

peaks at all positions,

iii) finally, the damped natural frequency charts combined with the modal logarithmic decrement, as given by Lund [54], provides comprehensive details about the stability behaviour of a flexible rotor-bearing.

A damped natural frequency chart is presented in Fig. 5.11 for the case with surface contact flexibility shown in Fig. 5.7. The first rotor mode[2], which is an even mode, is heavily[3] damped and has frequencies below the minimum frequency of the chart. The damped critical speeds are defined by the intersections between the synchronous excitation curve under different modes and will only be effective if they are associated with small logarithmic decrements. As can be seen from Fig. 5.11, there are only two damped critical speeds at 14000 and 14200 RPM and both are effective. These results are in good agreement with the experimental observations, within a difference of 500 to 600 RPM, compared to the results of Lund and Orcutt [53] which are within approximately 2000 RPM difference.

Two damped natural frequency charts are presented in Figs. 5.12 and 5.13 for the case of bearing support flexibility using the 3 elements and the 5 element arrangements, respectively. The two rotor modes in both the cases are heavily damped and have very small frequencies. The next 4 rotor

[2]A rotor mode may be composed of two modes, one with backward precession and the other with forward precession.

[3]Associated with large logarithmic decrements.

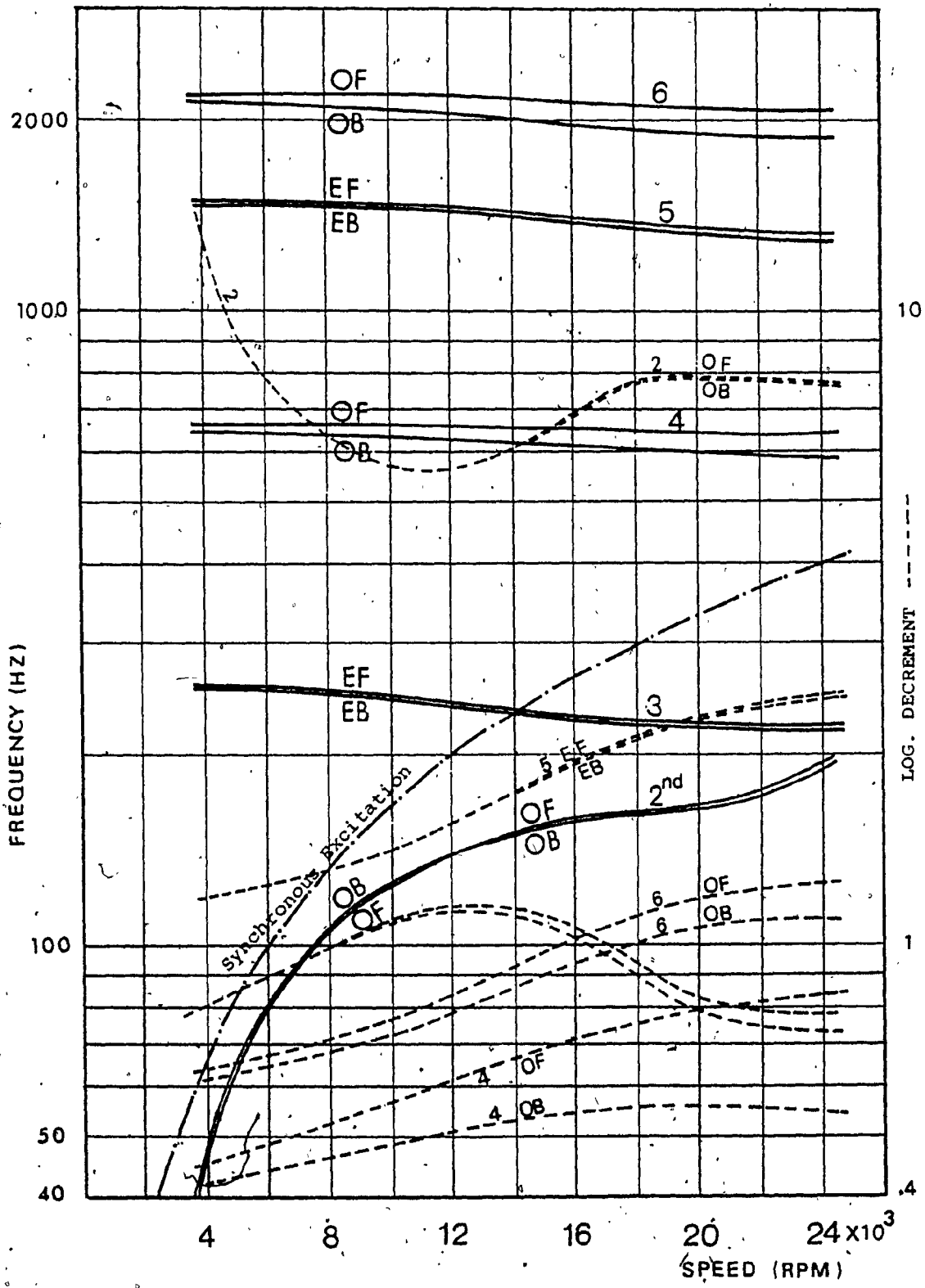

Fig. 5.11 Damped Natural Frequency Chart Corresponding to the Results of Fig. 5.7. (See Page xx).

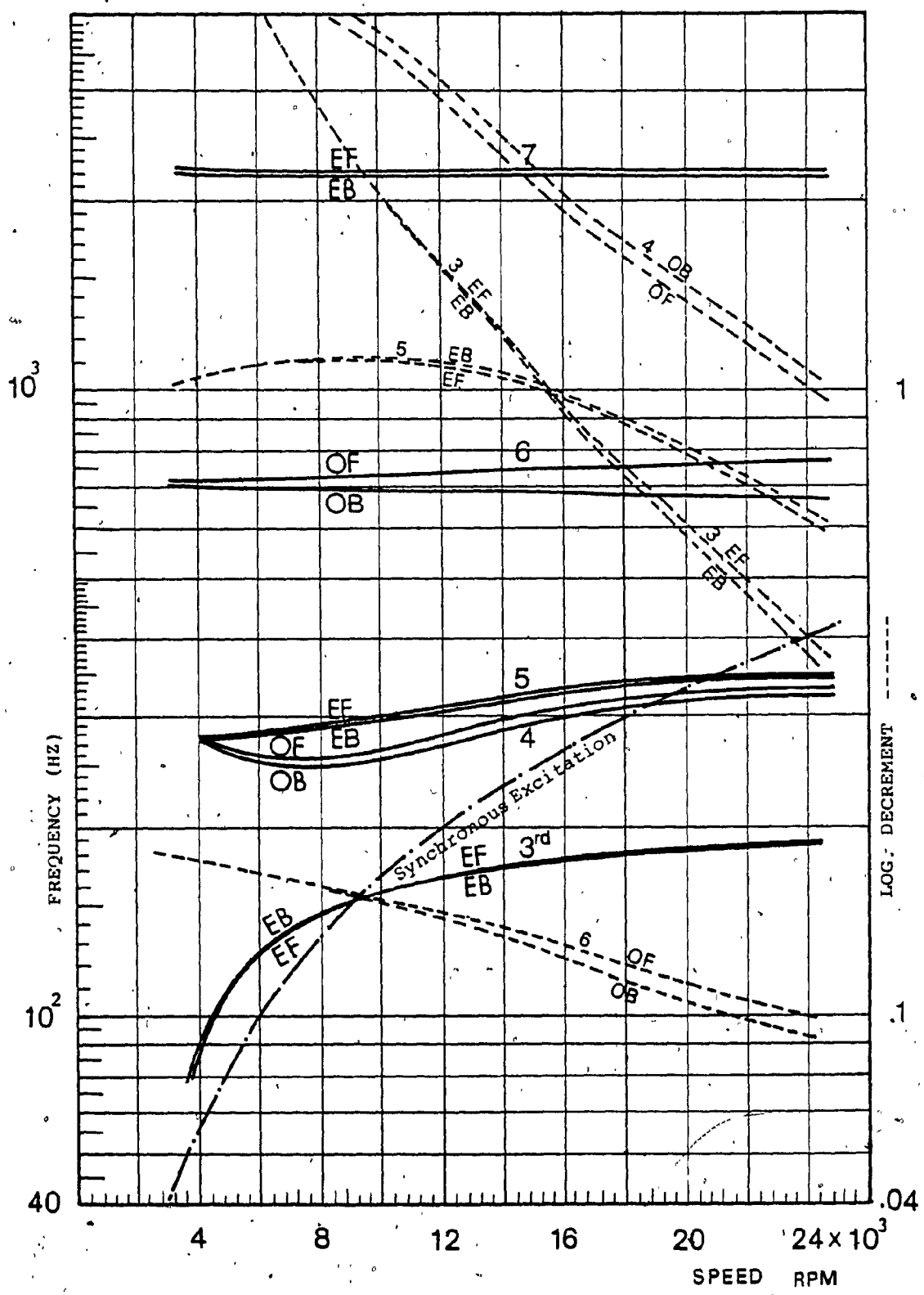

Fig. 5.12 Damped Natural Frequency Chart for the Case of Bearing Support Flexibility, Fig. 5.8, with 3 Elements. (See Page xx).

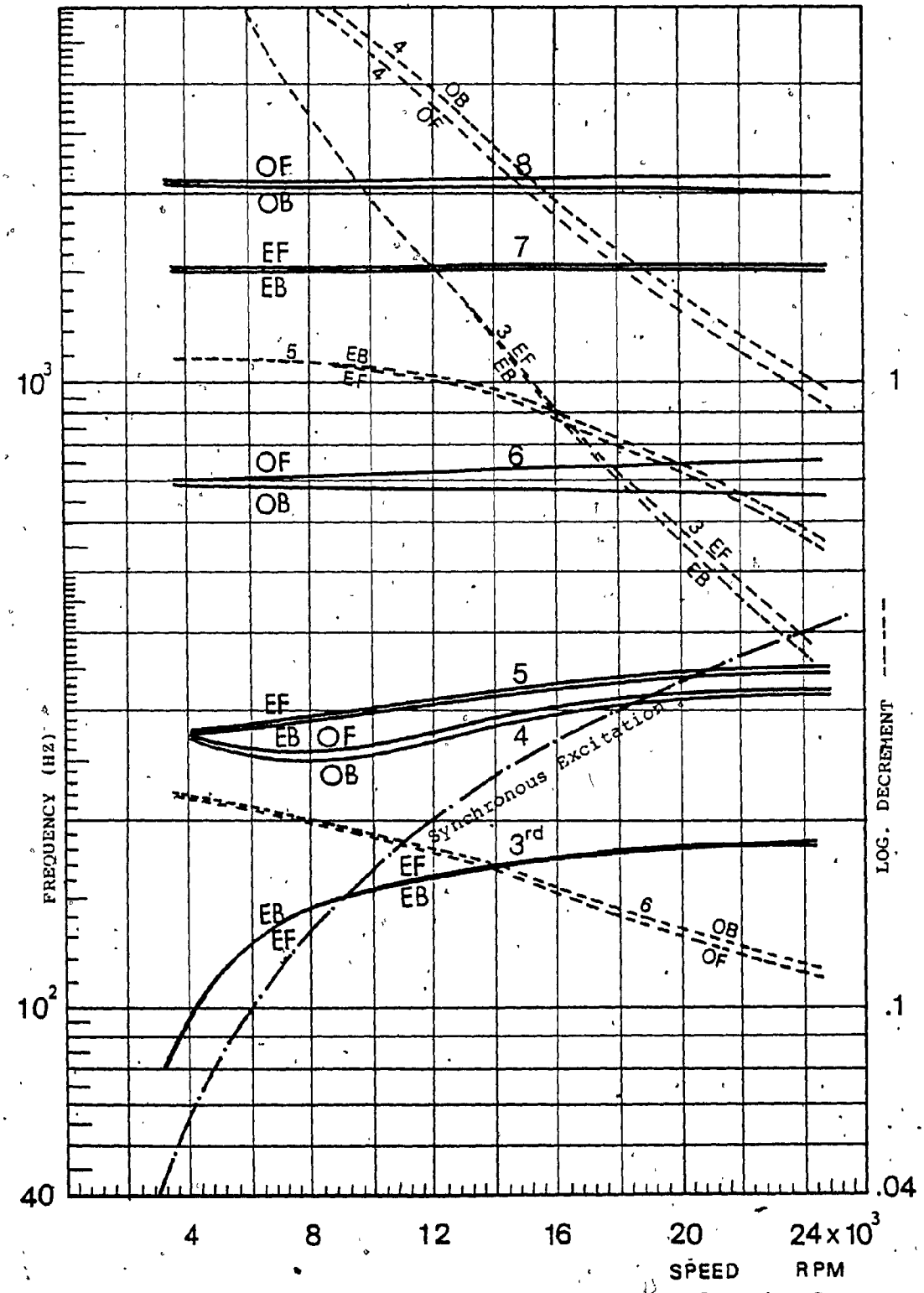

Fig. 5.13 Damped Natural Frequency Chart for the Case of Bearing Support Flexibility, Fig. 5.8, with 5 Elements. (See Page xx).

modes, that is 3rd to 6th, are almost identical in both the plots. In the higher frequency range a new rotor mode, namely the 7th in Fig. 5.13, is generated with the use of 5 elements while the highest modes in both graphs show a slight difference in frequency. Since the lower modes, which are closer to the running speeds, control the rotor bearing more significantly, it can be concluded again that the 3 element arrangement is sufficient for practical considerations.

As can be seen from Fig. 5.12 and/or Fig. 5.13, the damped critical speeds and their characteristics are described by the following:

Speed RPM	Logarithmic Decrement	Mode Nature	Precession Direction
9000	2.32	even	synchronous
18200	1.61	odd	backward
18600	1.47	odd	forward
20200	.718	even	backward
20600	.755	even	forward

Here the synchronous precession refers to a case of mode cross over from backward to forward as can be seen from Figs. 5.12 and 5.13. Only the last two criticals are effective and correspond to the peaks in the unbalance response in in Fig. 5.8. It it also interesting to notice the effect of bearing support flexibility on the rotor-bearing characteristics. This is demonstrated by the chart in Fig. 5.14 which corresponds

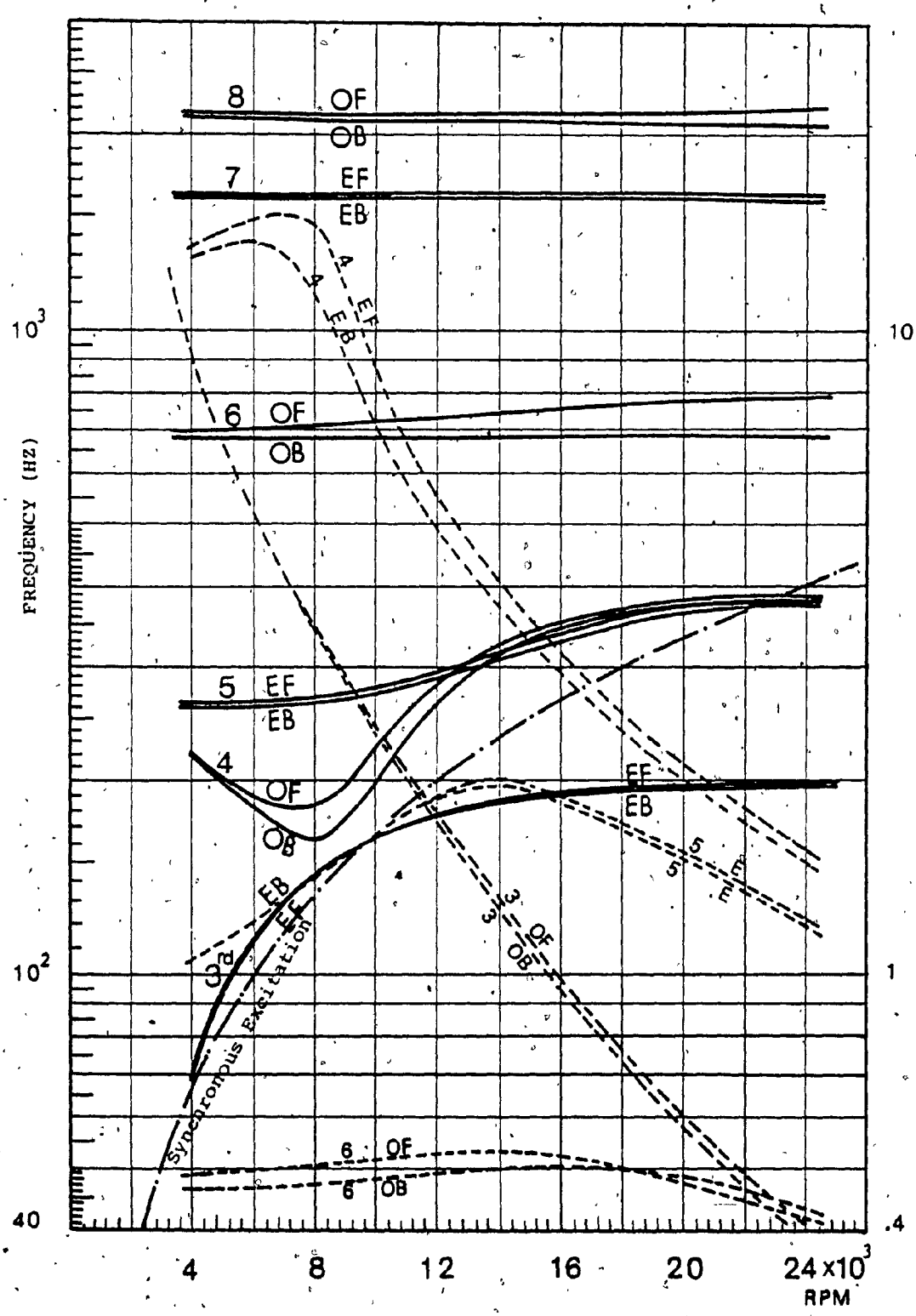

Fig. 5.14 Effect of Stiffening the Bearing Support on the Frequency of the Natural Modes. (See Page xx).

to a bearing support stiffness of 10^6 lb/in, or double the previously used value. For this, the shape of the rotor modes become more complicated. The fourth rotor mode, which is an odd mode, is particularly affected in terms of its shape and logarithmic decrement values. This odd mode may affect the rotor response under input excitations if such excitations on the rotor are unsymmetric in application.

5.11 Conclusions and Discussion

A comprehensive and yet simple modelling of a rotor bearing system is accomplished in this Chapter. All the effects that are associated with the rotor motion are taken into account. The bearings are considered to be supported flexibly in the machine structure which can further be modelled and included into the rotor-bearing system without much difficulty. The basic element used is the simple Timoshenko element which helps in retaining the order of the dynamical system and was previously shown to produce accurate results. The development of the analysis procedure itself is greatly simplified by such natural treatment, because of direct physical interpretation, of the motion planes which are considered analogous. The previous study by Zorzi et al [65], who initially introduced the hysteretic damping into the rotor-bearing system through a finite element procedure did not outline the implementation of the nonconservative moments into the element equations in contrast to the analysis presented here which also employ shape functions that include the

shear deformation effect.

The solution of the dynamical system is carried out using the general modal analysis and a standard proof of the orthogonality properties along with the necessary relations for the analysis are presented for the sake of clarity. The present approach with a fewer number of elements is found to be more accurate than the transfer matrix method which also considered the shaft segments to possess continuous properties. The angular displacements are found to be more sensitive in showing peak responses than the translational displacements, at least for the example presented, and therefore plotting these angular responses along with the translational displacements can provide a better interpretation to the over all system response. Also in the comparison between the surface contact flexibility and the bearing support flexibility, the latter is found to introduce a stabilizing effect to the system behaviour which is related to the added degrees-of-freedom to the bearing mass.

The results for the flexible as well as rigid rotor-bearing system may now be used in an application to the spindle-wheel system of a grinding machine under cutting conditions and is carried out in the next Chapter.

CHAPTER 6

ANALYSIS OF A GRINDING MACHINE SPINDLE SYSTEM UNDER ACTUAL CUTTING CONDITIONS

6.1 General

In this part of the investigation, the results based on rotor dynamic considerations are applied on a grinding machine-spindle-wheel system under actual machining conditions. The cutting forces in machining operations in general, and in grinding in particular, have been shown to be basically random in nature [67,68]. Therefore, the equations of motion form a stochastic system and consequently the spindle response is a stochastic process which is to be prescribed in terms of different statistical averages rather than deterministic expressions. Another type of input under which the system has to be investigated is the disturbance due to residual unbalance which may play an important role in the qualification of the grinding process itself.

As discussed in previous chapters, generally the rotor-bearing system is flexible and possesses nonlinear characteristics, at least due to proper consideration of hydrodynamic film forces. However under certain circumstances the assumptions of rotor rigidity and/or system linearity are quite acceptable. To utilize the simplicity of such cases to practical problems with the contributions elaborated in the present investigation, particularly the mathematical models discussed for the different rotor-bearing conditions,

are summarized in the following paragraphs indicating appropriate selection strategies for representing the overall system.

i) The analysis of the problem can begin by considering the rotor-bearing system as flexible and linear. For this case a conclusive mathematical model and method of solution is outlined in Chapter 5 while a solution to the stochastic system is provided in this Chapter. Once the system critical speeds and the dynamic responses are defined, the rotor may be assumed as rigid if the running speeds are well below the first critical. Also, by examining the rotor response at the bearing centre line, the error involved in using the linear stiffness and damping forces can be checked through error charts such as those presented in Chapter 4.

ii) If the rotor-bearing system is established as flexible but possessing nonlinear characteristics, the nonlinear stiffness and damping given by (B.1) in Appendix B. can be introduced directly in to the equations of motion as described in Chapter 5. However, no solution has been established for this case in the context of the present investigation.

iii) If the assumption of rigid rotor is acceptable but the linear variation of the film force is not valid, the results of Chapters 2 and 3 can be employed providing an accurate analysis enhanced by the use of the improved nonlinear stiffness and damping of the finite bearing. Here

the solution is provided through numerical integration for a deterministic input only.

iv) If the assumptions on rigidity as well as linearity apply, a rather general dimensionless form of solution by modal analysis is established for deterministic inputs in Chapter 4 and is extended to stochastic inputs in the present Chapter.

Before elaborating on the above approach for the problem of the grinding machine, some discussion is devoted for appropriate modelling of the random cutting forces in grinding and later followed by a solution for the stochastic system developed.

6.2 Forces in a Grinding Process

The grinding process in machining is associated with a large number of participating parameters [66]. The most influential parameters are the speed, feed and depth of cut which are established to be in linear relationship with the cutting forces [91,92]. In recent work by Banerjee [82], the cutting forces were shown expressed by the relation

$$F_c = K_c \left(\frac{v_w d_c v_c}{v_h}\right) \tag{6.1}$$

where K_c is a constant of a specific wheel-workpiece combination, d_c is the depth of cut and v_w, v_c and v_h are the work, crossfeed and wheel velocities as explained in Fig. 6.1a.

The relation between the tangential and the normal cutting components F_{ct} and F_{cn} are also found to be [82,91,92]

$$F_{cn}/F_{ct} \cong 2, \text{ for no crossfeed [91]}$$
$$\cong 1.4\text{-}2, \text{ with crossfeed and higher settings [92].} \quad (6.1a)$$

Since it was shown by Peklenik and Kwiatkowski [68] that the metal cutting processes are generally random in nature, the above force specifications given by (6.1a) can be seen, at least in principle, as the mean or the average cutting force. Consequently, the total cutting forces can be treated as the sum $F_c + f_c(t)$ where f_c is a zero mean random dynamic force that represents the stochastic excitation to the spindle-wheel system. The actual pattern of the random cutting force f_c has not been established experimentally so far. However, an analytical definition of the stochastic model of f_c can, however, be made based on the following observations:

i) It was established by Rakhit et al [67] that the cutting forces in fine turning is a random process with a wide band power spectral density and a probability density pattern that is approximately Gaussian.

ii) In a turning process the tool is a single point cutting tool, while in grinding the cutter is of infinite (very large) numer of cutting points. These cutting points (or abrasive grains) are randomly placed in the bonding material.

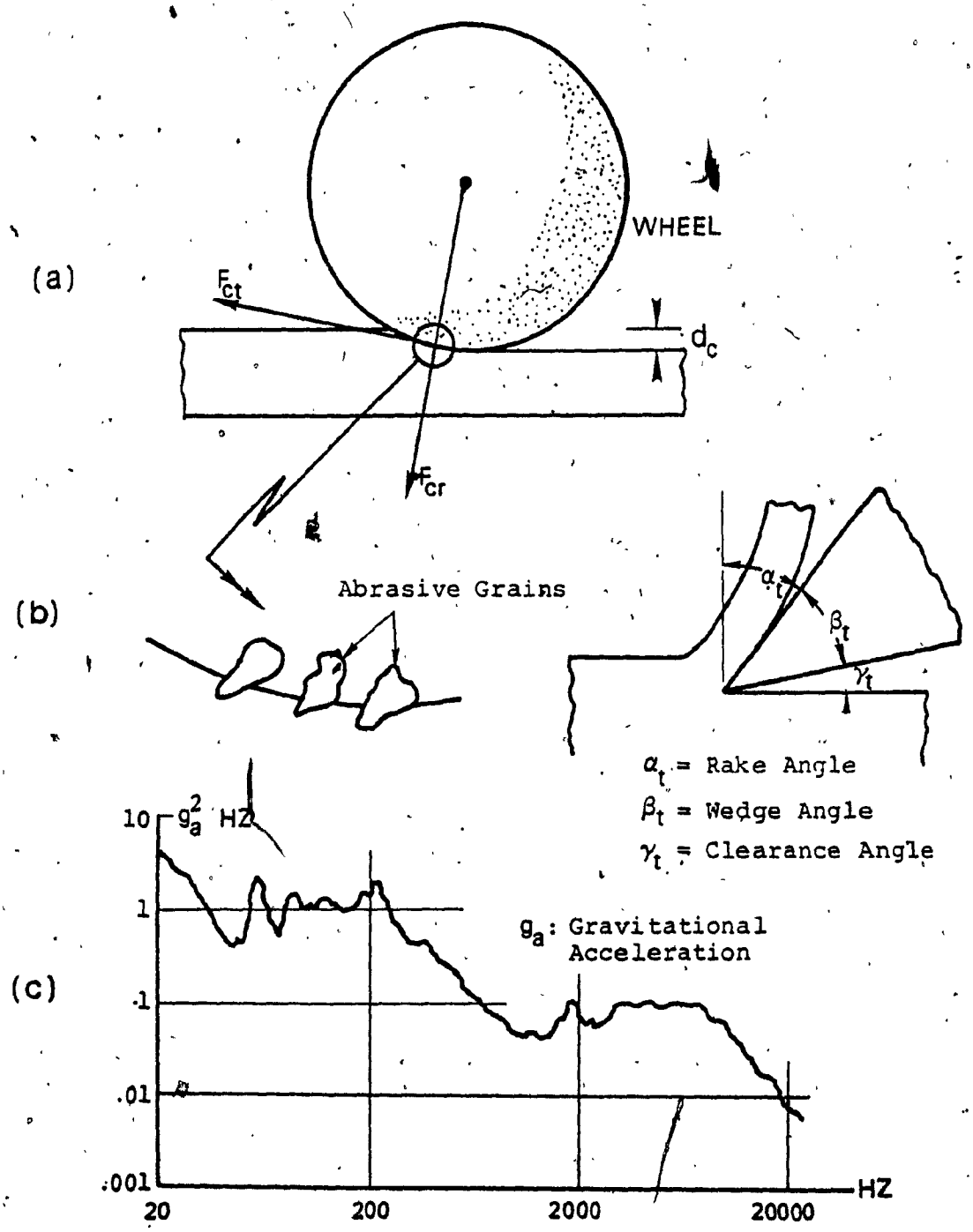

Fig. 6.1 a) Components of the Cutting Forces in Grinding.

b) Tool Points in Grinding and Turning.

c) A Possible Spectral Density Sample of the Forces in Fine Turning [67].

iii) The single point tool may have certain designed angles α_t, β_t and γ_t as can be seen from Fig. 6.1b. In grinding the tool points (grains) are spaced randomly and with random angles, also shown in Fig. 6.1b..

From the above observations, if the random force that is associated with a single point cutting tool is x(t), the random cutting forces in grinding will be a random varibale $f_c(t)$ which is the contribution of each single point tool $x_i(t)$ $(i=1,2,\ldots,n)$. The pattern of the random variable $f_c(t)$ can be extracted from the central limit theorm [83] which can be stated in the following: If a random variable $f_c(t)$ is a product of a large numer of contributing random variables $x_i(t)$ that are statistically independent, whatever the pattern of its probability distribution, and none of these random variables $x_i(t)$ is of particular significance on the whole, the probability density pattern of the output random variable $f_c(t)$ will be Gaussian if the number of the random variables $x_i(t)$ is large enough. Therefore, if the force that is associated with every single grain in the contact area of cut is considered to be a random variable $x_i(t)$, and if these random variables are statistically independent, then the total random cutting force f(t) must be Gaussian.

The cutting force spectral density pattern in fine turning is found to be a wide band process [67], and a possible spectral density sample of cutting forces in fine

turning is shown in Fig. 6.1c. The high degree of randomness in the tool points spacing and the grinding angles can be expected to produce random forces with wider frequency range in the spectral density pattern, thus establishing a nearly white noise type of process.

If the steady state cutting condition is only considered, then the random process f_c can be taken to be stationary. Thus, the definition of the fluctuating random cutting force f_c can be summarized as (i) of zero mean, (ii) stationary and (iii) Gaussian, or with a probability density pattern $p_f(f_c)$ that can be written in the form

$$p_f(f_c) = \frac{1}{\sqrt{2\pi}\sigma_f} \exp\left(\frac{-f_c^2}{2\sigma_f^2}\right) \qquad (6.2)$$

where σ_f is the standard of deviation of f_c. It can also be suggested that f_c is also essentially a wide band process.

6.3 Solution of the Stochastic Equations of Motion of the System

6.3.1 Review of Available Techniques and Procedures

The linear dynamic system on hand can be written in the form

$$\underset{NXN}{[m_s]}\{\ddot{q}_s\} + \underset{NXN}{[c_s]}\{\dot{q}_s\} + \underset{NXN}{[k_s]}\{q_s\} = \underset{NX1}{\{Q_s\}} \qquad (6.3)$$

where Q_s represents the vector of applied random excitation. System (6.3) can be the linear equation of the rigid symmetric rotor (4.1) or the output of the finite element simulation

for flexible rotor (5.27), as the case may be.

A few approaches can be used for evaluating the stochastic response of the system (6.3). These are, namely, the Fokker Plank approach, the impulse response approach and the spectral density approach which are all reviewed by Yang [78] along with an introduction of a matrix algebra approach. All these approaches can be used to determine the correlation matrix $[R_q(\tau)]$ of the response for a stationary Gaussian process except the matrix algebra method which can only determine the instantaneous correlation matrix $[R_q(0)]$ where $[R_q(\tau)]$ is given by

$$[R_q(\tau)] = E\ [\{q_s(t)\}\{q_s(t+\tau)\}^T] \tag{6.4}$$

For a general multidegree-of-freedom system, the Fokker-Plank approach requires the excitation to be stationary, Gaussian and white noise or filtered white noise, in which case the system is combined with a linear damped system, usually a linear filter. This particular approach is effective particularly for nonlinear system. The impulse response approach, involves many complicated integrals to be evaluated analytically especially when the degrees-of-freedom of the system is large. The spectral density approach is just the reciprocal of the impulse response approach and follows the same procedure in the frequency domain. This starts by evaluating the complex frequency response matrix $[H(\omega)]$ which can be constructed through the substitution of [78,83] the

expressions

$$\{Q_s\} = \{Q_0\}\, e^{i\omega t}$$

and

$$\{q_s\} = [H(\omega)]\, \{Q_0\}\, e^{i\omega t}$$

into system (6.3), where $\bar{Q}_0$ is a constant vector. Then $[H(\omega)]$ is given by

$$[H(\omega)] = \left[-\omega^2 [m_s] + i\omega [c_s] + [k_s]\right]^{-1} \qquad (6.5)$$

and the spectral density matrix, in turn, is given as

$$[S_q(\omega)] = [H(\omega)]\, [S_f(\omega)]\, [H^*(\omega)]^T \qquad (6.6)$$

where $[S_f(\omega)]$ is the spectral density matrix of the input excitation and $[H^*(\omega)]$ is the complex conjugate of $[H(\omega)]$. The spectral density matrix and the correlation matrix form a Fourier transform pair (except for the adjustment factor of 2π); then the correlation matrix can be evaluated from the integral

$$[R_q(\tau)] = \int_{-\infty}^{\infty} [S_q(\omega)]\, e^{i\omega\tau}\, d\omega \qquad (6.7)$$

However, the matrix to be inverted in equation (6.5) is a complex matrix and contains the frequency ω. Therefore, the inversion must be done analytically or be evaluated numerically for different values of ω which is possible only for systems with a few degrees-of-freedom. If this complexity is removed, the spectral density approach can be considered as the general approach for a stochastic linear system with

the only restrictions that the input be stationary and be Gaussian distributed.

6.3.2 A Modified Spectral Density Approach

A method that utilizes the modal analysis in the spectral density approach has been used by Lund [72] in the case of a rotor dynamic application that incorporates the transfer matrix method. This approach is extended here for a general dynamic system. The procedure is based on calculating the complex frequency response in the principle coordinates and going back, the complex frequency matrix $[H(\omega)]$ is established in the phase space.

Consider the decoupled first order equation (5.39),

$$\dot{u}_j - \lambda_j u_j = \frac{1}{M_j^*} U_j \quad , \quad j = 1,2,\ldots,2N$$

$$\text{with} \quad U_j = \sum_{\ell=N+1}^{2N} \psi_{\ell j} f_\ell \tag{6.8}$$

Here $\psi_{\ell j}$ is the ℓ^{th} element in the j^{th} left eigenvector $\bar{\psi}_j$ and f_ℓ is the ℓ^{th} element in the force vector $\bar{Q}$.

Further, using the property of superposition, equation (6.8) can be decomposed into N equations, where N is the number of degrees-of-freedom of the dynamical system (6.3), and are

$$\dot{u}_{j\ell} - \lambda_j u_{j\ell} = \frac{1}{M_j^*} \psi_{j\ell} f_\ell(t)$$

$$\text{where} \quad u_j = \sum_{\ell=N+1}^{2N} u_{j\ell} \tag{6.9}$$

The complex frequency function $H_{j\ell}(\omega)$ that corresponds to equation (6.9) can be shown to be

$$H_{j\ell}(\omega) = \frac{\psi_{\ell j}}{M_j^* (i\omega - \lambda_j)} \qquad (6.10)$$

The above formulation of $H_{j\ell}(\omega)$ does not carry the conventional properties that $H_{j\ell}(-\omega)$ is the complex conjugate of $H_{j\ell}(\omega)$, but rather a mathematical convention. Upon projecting the system back into the phase space, the complex frequency function will gain the above property through summation of the complex conjugate pairs.

For every frequency in $f_\ell(\omega)$, the input-output frequency relation is [83]

$$u_{j\ell}(\omega) = H_{j\ell}(\omega)\ f_\ell(\omega)$$

where $u_{j\ell}(\omega)$ and $f_\ell(\omega)$ are the standard Fourier transform of $u_{j\ell}(t)$ and $f_\ell(t)$, respectively. Then

$$u_j(\omega) = \sum_{\ell=N+1}^{2N} H_{j\ell}(\omega)\ f_\ell(\omega) \qquad (6.11)$$

Using the linear transformation (5.42), which is

$$q_k = \sum_{j=1}^{2N} \phi_{kj}\ u_j\ , \qquad k = 1,2,\ldots,2N$$

it can be shown that,

$$q_k(\omega) = \sum_{\ell=N+1}^{2N} H_{k\ell}(\omega)\, f_\ell(\omega) \quad , \quad k = 1,2,\ldots,2N \qquad (6.12)$$

where $H_{k\ell}(\omega) = \sum_{j=1}^{2N} H_{j\ell}(\omega)\, \phi_{kj}$

The spectral density in turn is defined as [84]

$$S_{q_k}(\omega) = \lim_{T \to \infty} \frac{1}{2T} E[q_k(\omega)\, q_k(-\omega)] \qquad (6.13)$$

where $2T$ is the time duration of the sampe q_k and $E[\ ]$ is the expectation operator for ensemble averaging. But

$$q_k(\omega) q_k(-\omega) = \left(\sum_{\ell=N+1}^{2N} f_\ell(\omega) H_{k\ell}(\omega)\right)\left(\sum_{\ell=N+1}^{2N} f_\ell(-\omega) H_{k\ell}(-\omega)\right) \qquad (6.14)$$

$$= \left\{H_k(\omega)\right\}^T \left[\left\{Q_s(\omega)\right\}\left\{Q_s(-\omega)\right\}^T\right]_{NXN} \left\{H_k(-\omega)\right\}$$

Then by taking the expectation of expression (6.14) and utilizing the definition (6.13), the spectral density of the response component q_k can be shown to be

$$S_{q_k}(\omega) = \left\{H_k(\omega)\right\}^T \left[S_f(\omega)\right]^T_{NXN} \left\{H_k(-\omega)\right\} \qquad (6.15)$$

where the transpose of the input spectral density matrix is a consequence of the definition of the cross spectral density [84],

$$S_{f_1 f_1}(\omega) = \lim_{T \to \infty} \frac{1}{2T} E[f_1(-\omega) f_2(\omega)]$$

The final expression for the spectral density (6.15) shows that the approach presented is capable of calculating the spectral density for individual response components, if necessary.

6.3.3 A Check on the Modified Spectral Density Procedure

Consider the example of section 5.10 in Chapter 5 which is concerned with the unbalance response calculations for the rotor. The steady state response at any point on the rotor is harmonic, as discussed before, and is in the form

$$q_k = \rho_k \cos(\omega_{rt} - \theta_k)$$

where ρ_k is the radius of the circular orbit representing the response of a point k on the rotor and θ_k is the phase angle. The mean square value of the response component q_k is given by

$$E[q_k^2] = \lim_{T \to \infty} \frac{1}{2T} \int_{-T}^{T} \rho_k^2 \cos^2(\omega_{rt} - \theta_k)\, dt$$

$$= \frac{\rho_k^2}{2}$$

Two input unbalance forces are acting on the rotor, each with an X and Y component yielding a force vector of order 4. Then the input spectral density matrix $[S_f(\omega)]$ is also of order 4, this is explicitly written in Appendix J. The mean square value, in turn, is as

$$E[q_k^2] = \int_{-\infty}^{\infty} S_{q_k}(\omega)\, d\omega$$

Using the above procedure, the orbit radii ρ_k at different locations on the rotor are checked with those evaluated earlier in Chapter 5. The check is carried out at a single running speed, say 11000 RPM chosen arbitrarly and used here, and the results confirm the procedure explained in the previous section.

6.4 Input Data and Associated Information for the Grinding Machine Spindle System

The grinding machine head shown in Fig. 1.1 is used as the illustrative example for application of rotor-bearing concepts developed previously. Input data and other information are listed below in three parts.

6.4.1 Geometrical Data

The spindle-wheel system is shown in a schematic form in Fig. 6.2 with the grinding wheel and its clamping parts lumped into one single element which will be referred to as the wheel element. Also the pully at the left end is assumed to be one piece along with the spindle end. The rotor beam is divided into 4 elements with lengths and diameters as shown in Fig. 6.2. The modulus of elasticity in tension and shear E and G_s for the material are taken as

$$E = 20.6843 \times 10^4 \text{ N/mm}^2 \quad (30 \times 10^6 \text{ lb/in}^2)$$

$$G_s = 8.2737 \times 10^4 \text{ N/mm}^2 \quad (12 \times 10^6 \text{ lb/in}^2)$$

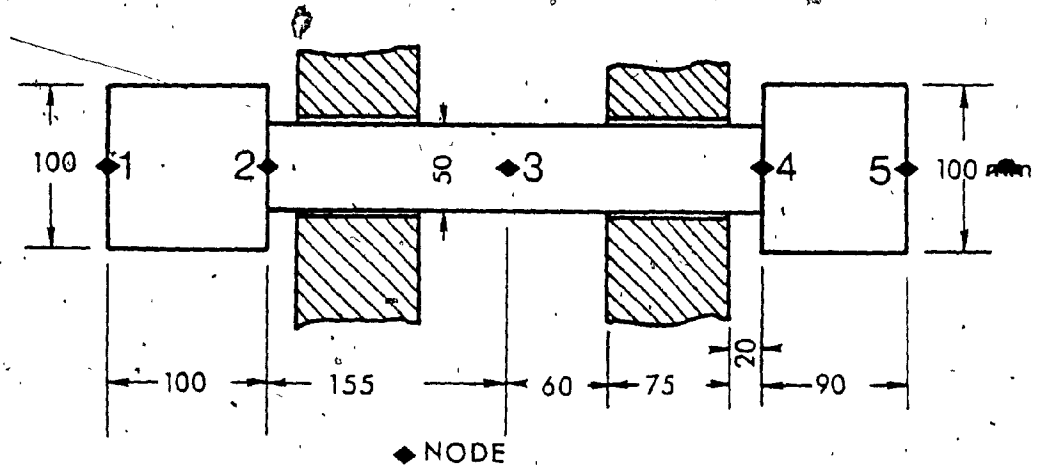

Fig. 6.2 Lumped Spindle-Wheel Systems with Element Arrangement.

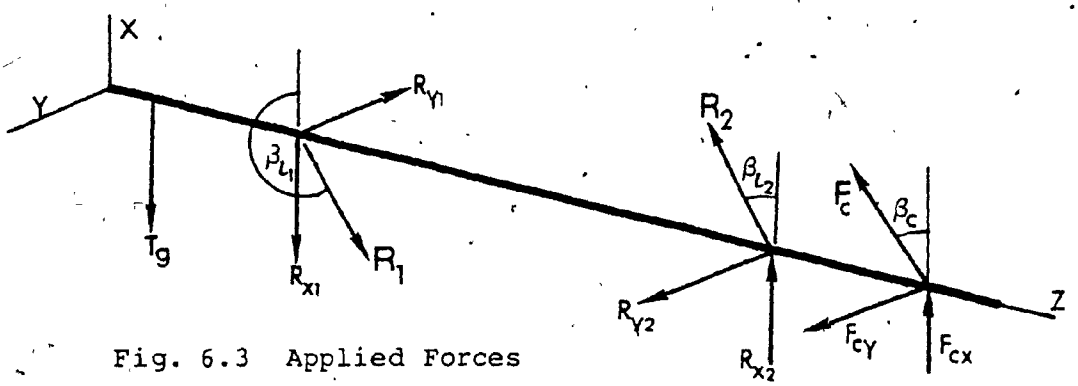

Fig. 6.3 Applied Forces

	F_c = 300 N		F_c = 500 N	
	R	β_L°	R	β_L°
LEFT BEARING	882	183	955	185
RIGHT BEARING	600	15	825	18

Table 6.1 Bearing Reactions and Inclination Angles.

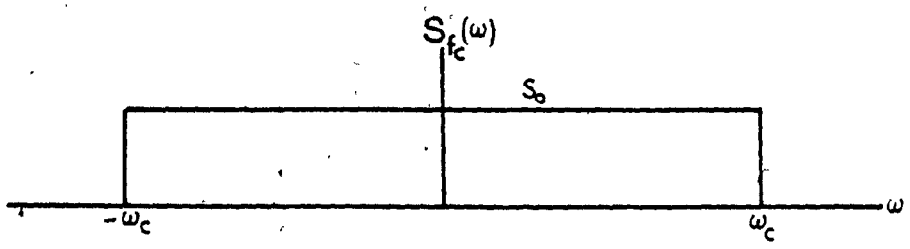

Fig. 6.4 Spectral Density Pattern of the Input Force f_c.

6.4.2 Applied Forces

Some appropriate values are chosen from a recent work on cutting forces in grinding by Banerjee [82] which are presented as corresponding values of the group parameters $v_w d_c v_c / v_h$. These are

$$v_w d_c v_c / v_h = 2.19 \times 10^{-9} \text{ m}^3/\text{m} \quad \text{for} \quad F_c = 300\text{N}$$
$$= 3.8 \times 10^{-9} \text{ m}^3/\text{m} \quad \text{for} \quad F_c = 500\text{N}$$

These values correspond to medium machine settings. The random cutting force f_c is estimated at 20-30% of the average value [67,68]. Since f_c is Gaussian, then the probability that the random variable f_c is between $3\sigma_f$ and $-3\sigma_f$ is almost unity, where σ_f is the standard deviation of the random force f_c. Using this information an approximate value of the standard of deviation σ_f can be estimated as follows

$$6\sigma_f = .3 F_c \quad \text{(30\% of the nominal cutting force } F_c\text{)}$$

Then, $\sigma_f = 15$ N for $F_c = 300$ N

$= 25$ N for $F_c = 500$ N

The force acting on the wheel element is assumed to be concentrated at the element middle point. The tangential and radial cutting force component can be approximated to horizontal and vertical force components [82]. Then the cutting forces $F_c + f_c$ are oriented from the X direction by an angle β_c, as can be seen from Fig. 6.3, which is given by

$$\beta_c = \tan^{-1} \frac{F_{cY}}{F_{cX}} \approx \tan^{-1} \frac{1}{2} \quad , \text{ using relation (6.1a)}$$

The tensile force in the driving belt is adjustable and a value for the tension $T_g = 500N$ is assumed. With these assumptions, the bearing reactions are calculated for the two nominal cutting forces $F_c = 300N$ and $500N$. The bearing reactions are shown as inverted and projected on the spindle in Fig. 6.3 and listed in Table 6.1. The spectral density pattern of the random variable f_c is a wide band type. However, a general practical shape of the input spectral density in terms of finite band can be used and it is seen sufficient to use a simple pattern indicating a band limited or clipped white noise, as the one shown in Fig. 6.4 for the present example. In the figure S_0 is the constant value of the input spectral density and ω_c is the cutoff frequency. The spectral density S_o is related to the variance σ_f^2 by

$$\sigma_f^2 = \int_{-\infty}^{\infty} S_f(\omega)\, d\omega = 2S_0\omega_c$$

The value of ω_c is taken as $\omega_c/2\pi = 20$ KHZ.

The random force components act on the wheel element on nodes 4 and 5, as can be seen from Fig. 6.2, in the X and Y direction and are

$$f_{c4} = f_{c5} = \frac{1}{2} f_c$$

where the subscript refers to the nodes.

Then, $S_{01} = S_{02} = \frac{S_0}{4}$

where S_{01}, S_{02} are the spectral density of the components f_{c4} and f_{c5}. The development of the input spectral density matrix is presented in Appendix K.

6.4.3 Bearing Design Parameters

A speed range of 20-200 rps is used, which is a typical range for a surface grinding machine. Corresponding to this speed range, an applied load of 1112N (250lb) and a 50mm (1.97in) bearing diameter, the optimal design parameters as determined by Seireg and Ezzat [85] are shown approximately to be

average viscosity $\simeq 1 \times 10^{-7}$ Reyns ($\simeq$.6896 centipoises, cp)

radial clearance $\simeq$ .003 in (.076mm)

$L/d \simeq .25$

These values, at least, illustrate the trend for an optimal selection. However, as can be seen from Fig. 1.1 in Chapter 1, the bearings are designed such that L/d = 1.5 which is also used here. According to the above optimal trend a low viscosity oil is chosen which is ASTM60 with a viscosity value $\mu = 9.5 \times 10^{-7}$ Reyns (6,55 cp) at 120°F ($\simeq$49°C) which is assumed to be the inlet oil temperature.

Assuming all the generated heat to be carried away by the oil the calculation of the stiffness and damping coefficients can be carried out as follows:

i) assume a temperature rise,

ii) calculate the average viscosity from standard graphs,

iii) then, calculate the Sommerfeld number and subsequently the eccentricity ratio.

Corresponding to the Sommerfeld number and the eccentricity ratio, the temperature rise can then be evaluated [1,15]. Repeating the iterating procedure until convergence, the eccentricity ratio is subsequently determined along with the average ciscosity value. Using the eccentricity ratio, the linearized stiffness and damping coefficients $k^*_{xx}, k^*_{xy}, \ldots, C^*_{xx}, C^*_{xy} \ldots$ etc can be calculated, where

$$k^*_{xx} = \frac{2k_{xx}}{S}$$

is a function of the eccentricity ratio e only so are $k^*_{xy}, \ldots, C^*_{xx} \ldots$ and $k_{xx}, k_{xy}, \ldots, C_{xx}, C_{xy} \ldots$ are given in Appendix E. The dimensional stiffness and damping coefficients, in turn, are given by

$$k_{xx} = k^*_{xx} \ \omega_r \ \rho_d$$

$$C_{xx} = \rho_d \ C^*_{xx}$$

where $\rho_d = \frac{1}{2} \mu L \left(\frac{d}{c}\right)^3$

Repeating this procedure for every bearing load and running speed, all stiffness and damping coefficients are calculated and listed in Table 6.2.

The above calculations are based on a laminar regime assumption for the oil film. A check on Reynold's number [93] is given by

$$R_e = \frac{\omega_r \ d \ h}{2\nu}$$

speed rps	k_{xx} N/mm	k_{xy} N/mm	k_{yx} N/mm	k_{yy} N/mm	c_{xx} N·sec/mm	c_{xy} N·sec/mm	c_{yx} N·sec/mm	c_{yy} N·sec/mm
Left bearing, F_c = 300 N:								
20	29346.	39175.	-1761.	24668.	529.	304.	234.	300.
40	15374.	33300.	-14431.	21256.	238.	124.	94.	197.
60	11997.	35810.	-23476.	20034.	176.	75.	56.	165.
80	10483.	40492.	-31791.	19126.	153.	52.	39.	150.
100	10346.	47085.	-39765.	19555.	144.	42.	32.	143.
120	10047.	53637.	-47631.	19444.	138.	35.	26.	138.
140	9779.	60419.	-55462.	19208.	134.	29.	22.	135.
160	10000.	67715.	-63172.	19776.	132.	26.	20.	133.
180	9665.	74538.	-70811.	19250.	129.	23.	17.	131.
200	9475.	81379.	-78221.	18947.	127.	20.	15.	129.
Right bearing, F_c = 300 N:								
20	9661.	21513.	-7099.	17865.	251.	181.	139.	293.
40	7028.	23272.	-17092.	15573.	155.	76.	57.	195.
60	6165.	27982.	-25389.	13744.	133.	44.	32.	163.
80	6052.	34538.	-33397.	13203.	127.	32.	23.	151.
100	6043.	41557.	-41262.	12901.	124.	25.	18.	144.
120	6023.	48805.	-49095.	12610.	123.	20.	15.	140.
140	6123.	56188.	-56858.	12632.	122.	17.	13.	137.
160	6185.	63582.	-64557.	12592.	122.	15.	11.	135.
180	6229.	71054.	-72278.	12534.	122.	13.	10.	133.
200	6219.	78272.	-79697.	12381.	121.	12.	9.	132.
Left bearing, F_c = 500 N:								
20	36843.	47462.	1046.	30521.	610.	367.	287.	347.
40	18275.	37512.	-13840.	25303.	258.	146.	111.	218.
60	13914.	38675.	-23410.	23477.	185.	87.	66.	178.
80	12214.	42825.	-31874.	22547.	158.	61.	46.	159.
100	11366.	48301.	-39999.	21941.	145.	47.	35.	149.
120	10927.	54496.	-47900.	21584.	138.	38.	29.	143.
140	10680.	61092.	-55687.	21365.	134.	32.	24.	138.
160	10517.	67956.	-63458.	21193.	131.	28.	21.	136.
180	10446.	74928.	-71101.	21135.	129.	25.	19.	134.
200	10334.	81747.	-78508.	20955.	127.	22.	16.	131.
Right bearing, F_c = 500 N:								
20	17347.	34227.	-4167.	30910.	350.	295.	231.	420.
40	10035.	28692.	-17270.	23268.	173.	109.	81.	241.
60	8682.	31670.	-26206.	20559.	140.	63.	46.	191.
80	8390.	37083.	-34387.	19367.	129.	44.	32.	169.
100	8290.	43339.	-42290.	18556.	124.	34.	24.	157.
120	8334.	50170.	-50147.	18165.	122.	27.	20.	150.
140	8360.	57152.	-57871.	17807.	121.	23.	16.	145.
160	8412.	64273.	-65540.	17573.	120.	20.	14.	142.
180	8487.	71473.	-73162.	17447.	120.	18.	13.	139.
200	8528.	78523.	-80551.	17283.	119.	16.	11.	136.

Table 6.2 Stiffness and Damping Coefficients for Both Bearings with the Two Cutting Force Cases.

where ν is the kinematic viscosity, d is the shaft diameter and h is the film thickness, is made for the maximum speed reaction 955N for which the temperature rise is 6°F. In such a case, the maximum Reynold's number calculated is 323 which defines essentially a laminar operating regime.

6.5 Results and Discussion

6.5.1 Unbalance Response

As a primary step, the rotor response to unbalance force is calculated. An unbalance weight is considered here at the wheel element which is the most significant part of the grinding machine spindle. The major and minor axes of the elliptical response orbit, divided by the bearing radial clearance, per Kg.mm unbalance is plotted in Fig. 6.5 versus the running speed. No effective critical speed can be distinguished from this unbalance response graph.

The middle node (3) moves along the smallest ellipse which, primarily predicts that the rotor runs through a conical mode. To emphasize this the instantaneous mode shape of the rotor shaft under unbalance force is presented in Fig. 6.6 for speeds 20,100 and 200 rps. Results show that the rotor shaft moves in conical mode through all speed range with the deflection taking place in the unbalance plane only. It can therefore, be concluded that the rotor motion is dominated by rigid body modes and the deflection in the rotor shaft is only due to the applied unbalance force without participation from the shaft flexural bending modes.

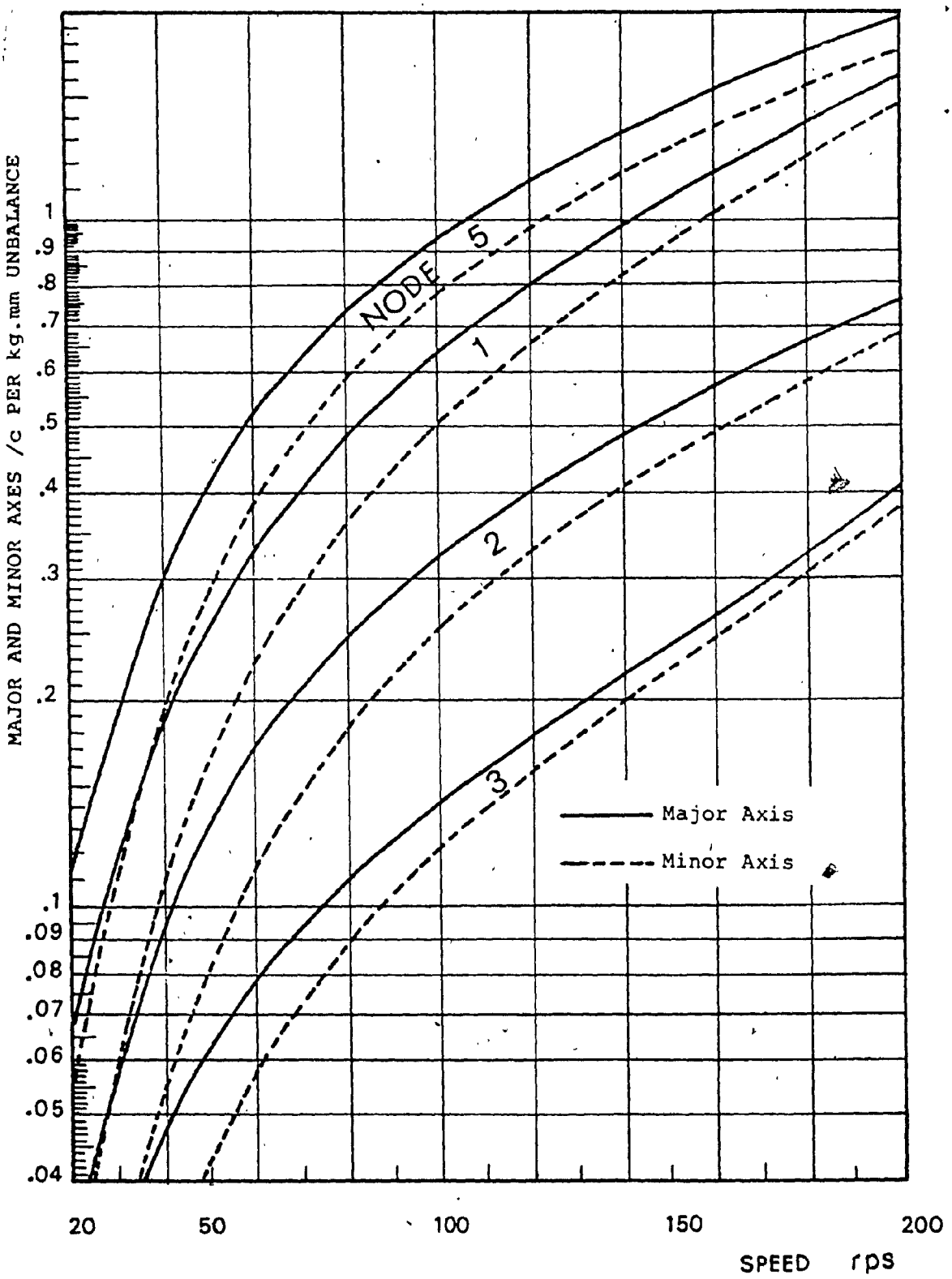

Fig. 6.5 Unbalance Response for a Weight Located at the Grinding Wheel.

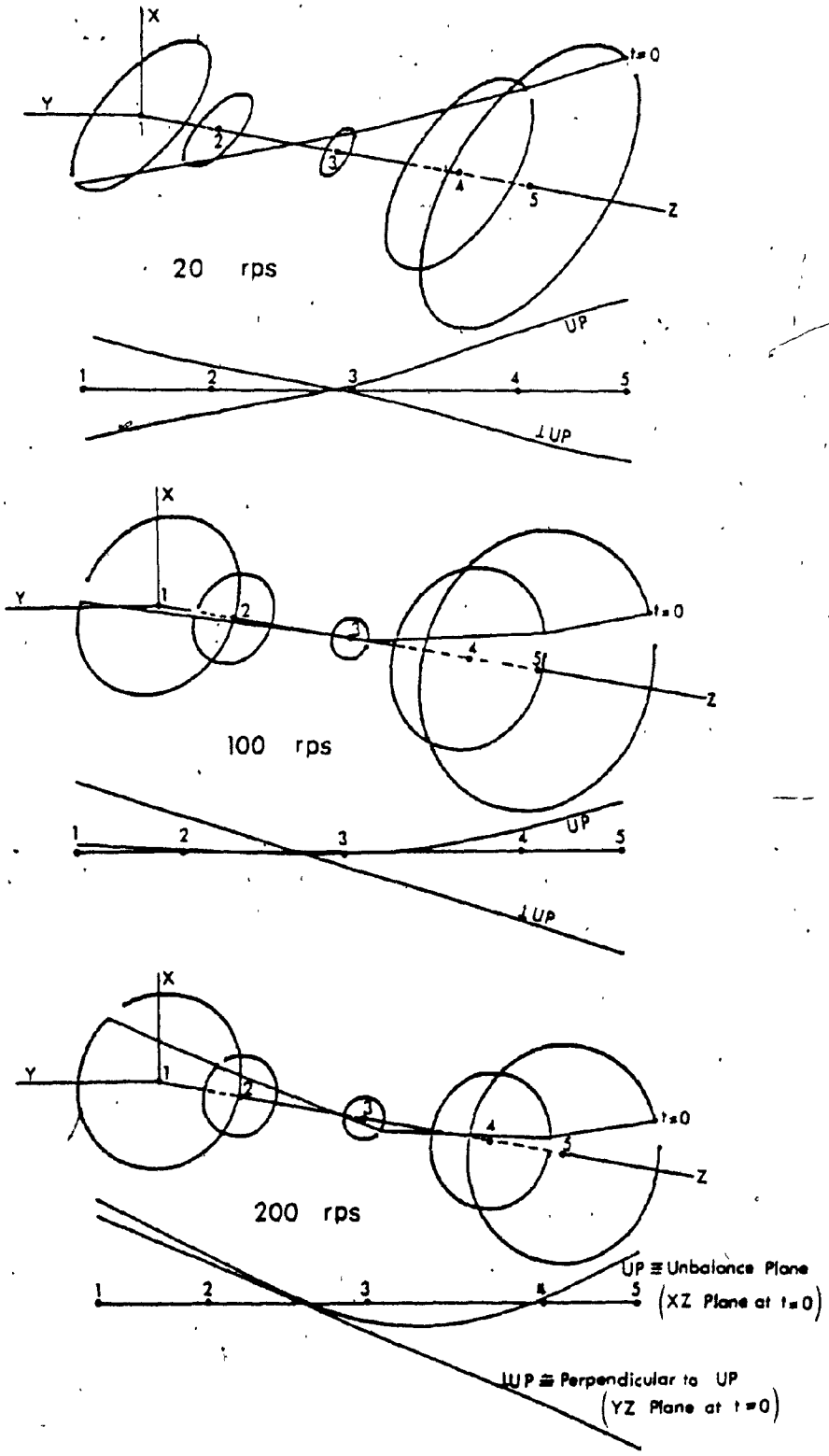

Fig. 6.6 Instantaneous Shape of the Rotor Under Unbalance Forces.

A confirmation on this conclusion requires a qualitative analysis which is presented in a latter part.

6.5.2 Stochastic Response

Since the input cutting force f_c to the grinding spindle-wheel system is a Gaussian random variable, the system response is also Gaussian. Here the random response is completely defined by the variance only since the mean value of the input is zero. The variance of the stochastic response at a particular point on the rotor, say node 5 and X direction denoted by (5X), is evaluated by integrating the spectral density of the random output, $S_{5X}(\omega)$, which in turn is evaluated using the complex frequency response functions.

The four complex frequency functions, whose magnitude actually $\left| H_{5X,i}(\omega) \right|^2$ with i=4X,4Y,5X and 5Y, are necessary to evaluate $S_{5X}(\omega)$ are plotted in Fig. 6.7, for 2 running speeds. The system critical frequencies, which are the effective damped natural frequencies at the respective running speed, can directly be read from such plots. Two critical frequencies are of special significance in both the cases presented in Fig. 6.7. The first occurs at one-half the running speed and becomes more sharp with the higher speed case while the second is fixed at approximately 400HZ. Beyond these two critical frequences, roughly beyond 1000Hz, the complex frequency response drops considerably.

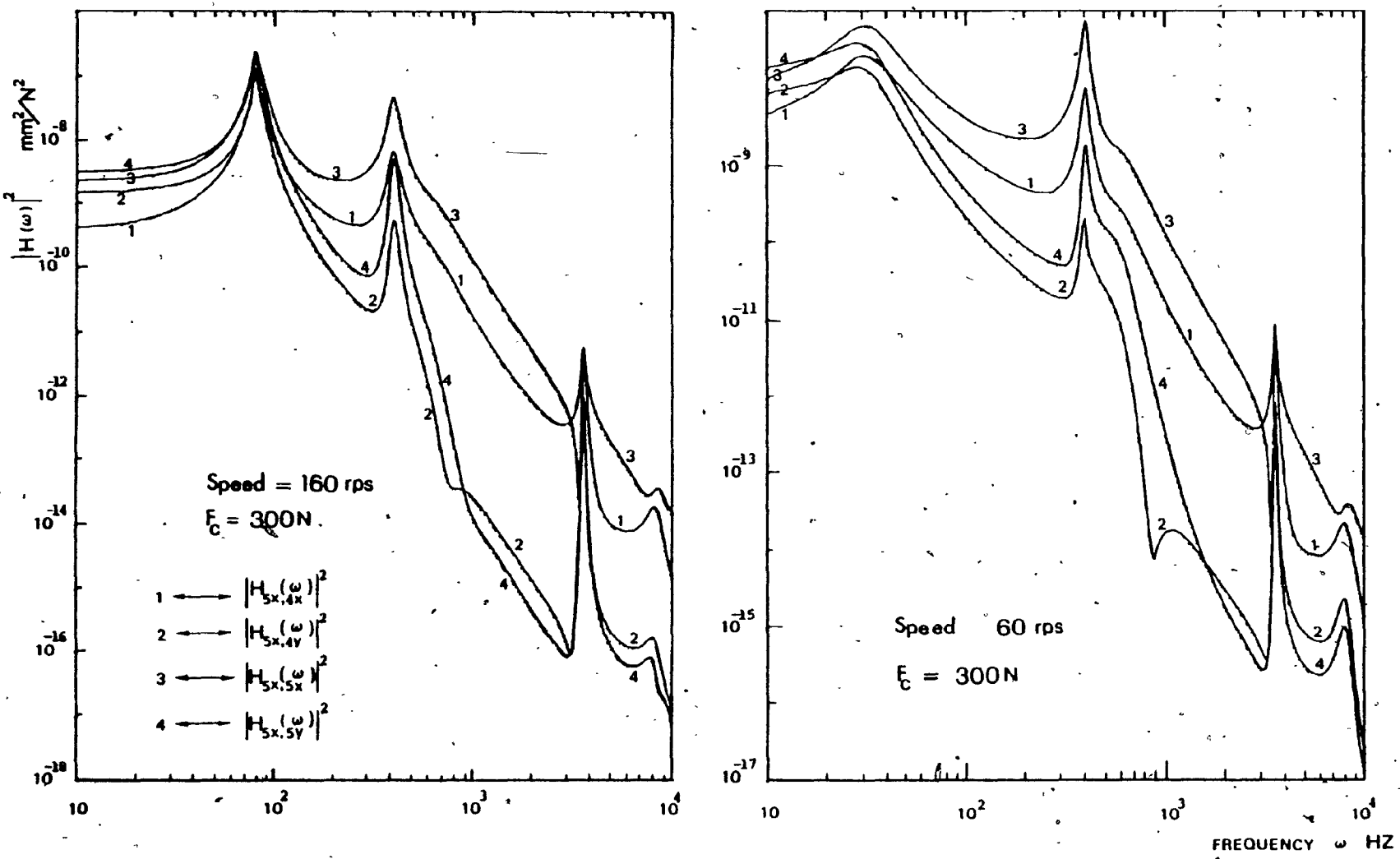

Fig. 6.7 Complex Frequency Response Corresponding the the Wheel Element for the Case with F_c = 300N.

Spectral densities are plotted for that effective frequency range in Fig. 6.8 for the case of $F_c = 500N$ and speeds of 80 and 180 rps. The pattern of these spectral densities is a one of a narrow band process particularly at the higher running speed value. This indicates a growing tendency toward resonance, or instability, as the speed increases. The estimation of the band width $\Delta\omega$ of a spectral density may rely on some assumption such as considering the frequency range outside which the spectral density is a small percentage of the maximum value. For example, consider the spectral density of the response in the fifth node and X directional $S_{5X}(\omega)$ at a speed of 180 rps in Fig. 6.8. The band width $\Delta\omega$ beyond which the spectral density drops below 1% of the maximum value is $\Delta\omega = 600HZ$, as demonstrated in Fig. 6.8.

Before calculating the variances, the participation of the higher modes in the stochastic response is studied through plotting one variance component, say σ^2_{5X}, versus the cut off frequency ω_c, keeping S_0 unchanged, as shown in Fig. 6.9. For both rotor speeds used, the value of the variance σ^2_{5X} remains stationary beyond a (conservative set) frequency of 1000HZ. This means that the effective modes on the rotor random response are those of frequencies below 1000HZ.

A direct result of this fact is that the calculated response will still be applied for different values of the

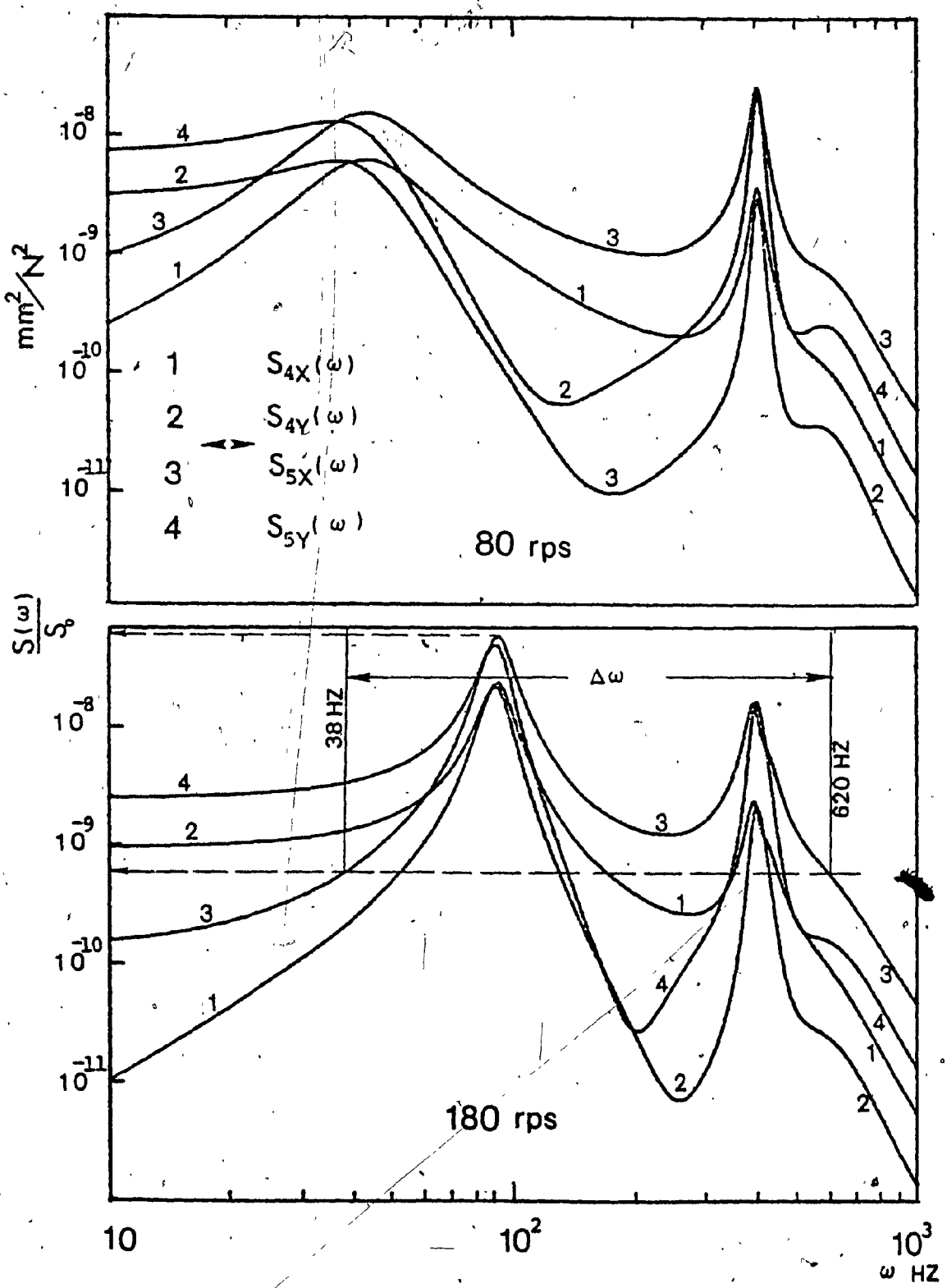

Fig. 6.8 Spectral Density of the Response at the Wheel Element Nodes in Both Directions.

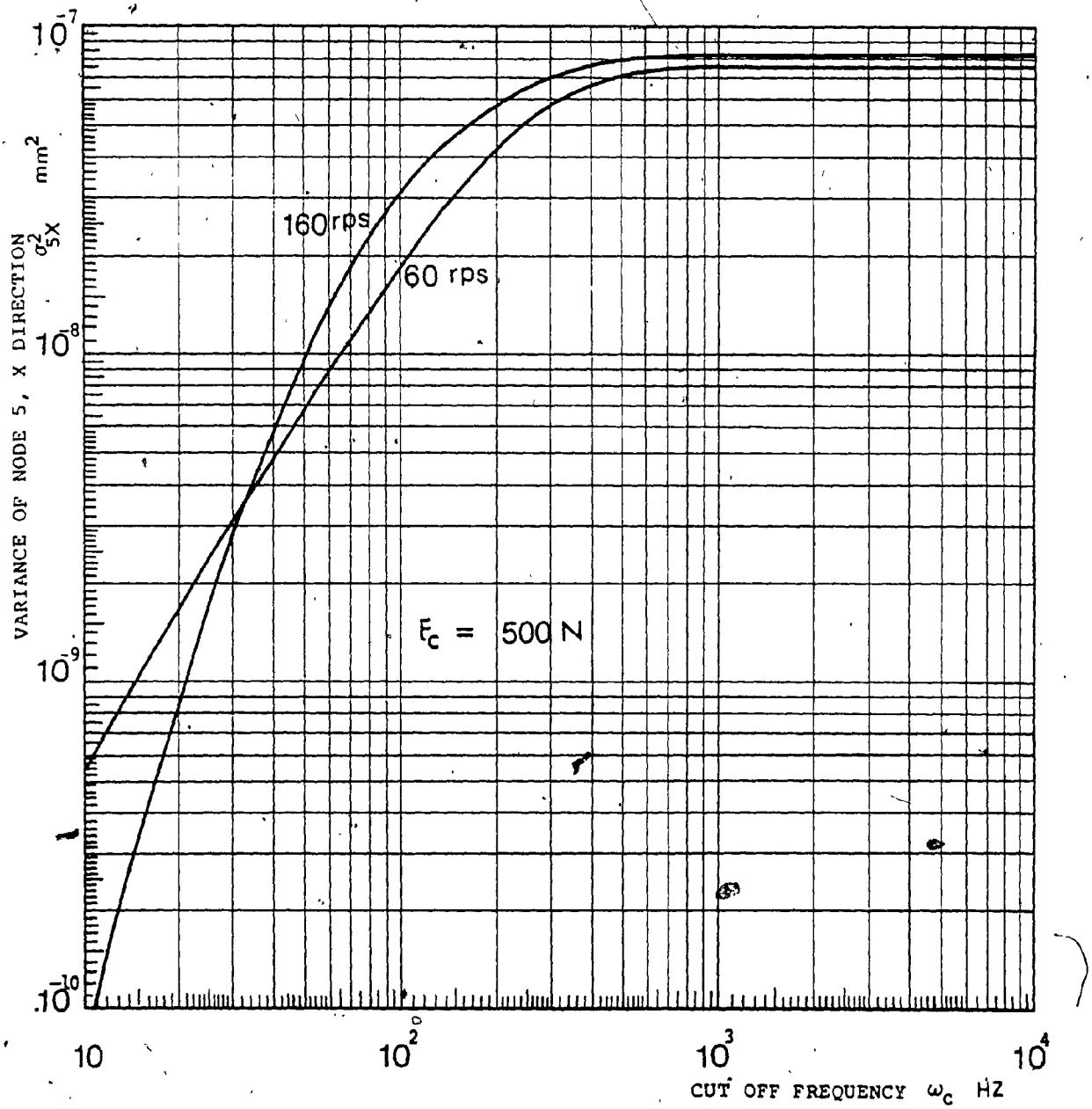

Fig. 6.9 Relation Between the Response Variance and Cut Off Frequency, Effect of Rotor Higher Modes.

cut off frequency ω_c of the input force, anywhere over 1000HZ, except for a multiplication factor. This multiplication factor is ≡ original cut off frequency (20KHZ) divided by the new cut off frequency. The variances of the response at the wheel element nodes 4 and 5 in both X and Y directions are presented in Fig. 6.10 and Fig. 6.11 for the cutting force cases $F_c = 300N$ and $F_c = 500N$ respectively.

For a Gaussian random process, the probability that the amplitude has a value between $-2\sigma_q$ and $2\sigma_q$ is 95.44% and that it is between $-3\sigma_q$ and $3\sigma_q$ is 99.74% [84] where σ_q is the standard deviation of the amplitude. As an example of such an interpretation, consider the value of σ^2_{5X} at 180 rps and for $F_c = 500N$

$$\sigma^2_{5X} = 9.3 \times 10^{-8} \text{ mm}^2 \qquad \sigma_{5X} = 3.05 \times 10^{-4} \text{ mm}$$

The probability that the response amplitude at node 5 in the X direction has a value between -9.15×10^{-4} and 9.15×10^{-4} mm is 99.74%. This particular reponse component X5, is of interest, since it is at the end of the wheel element and in a direction perpendicular to the surface under grinding and therefore will affect the output surface roughness.

A conservative estimation that the input spectral density is limited by the cut off frequency ω_c = 2KHZ (giving S_0 about 10 times the previous value) leads to 10 times the previously calculated variance. For the above, the value will be

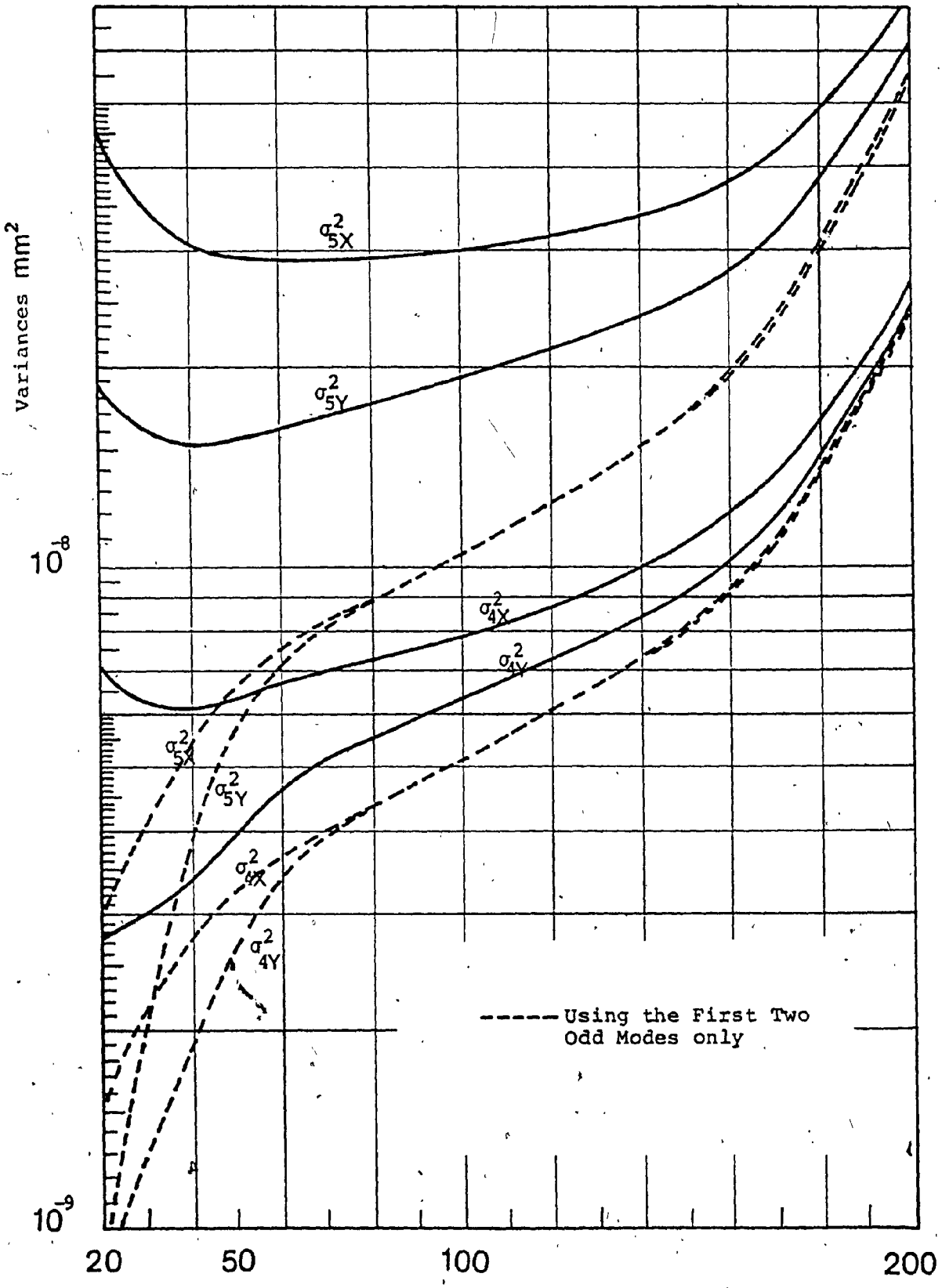

Fig. 6.10 The Variance of the Response at the Wheel Element in X and Y Directions, F_c = 300N.

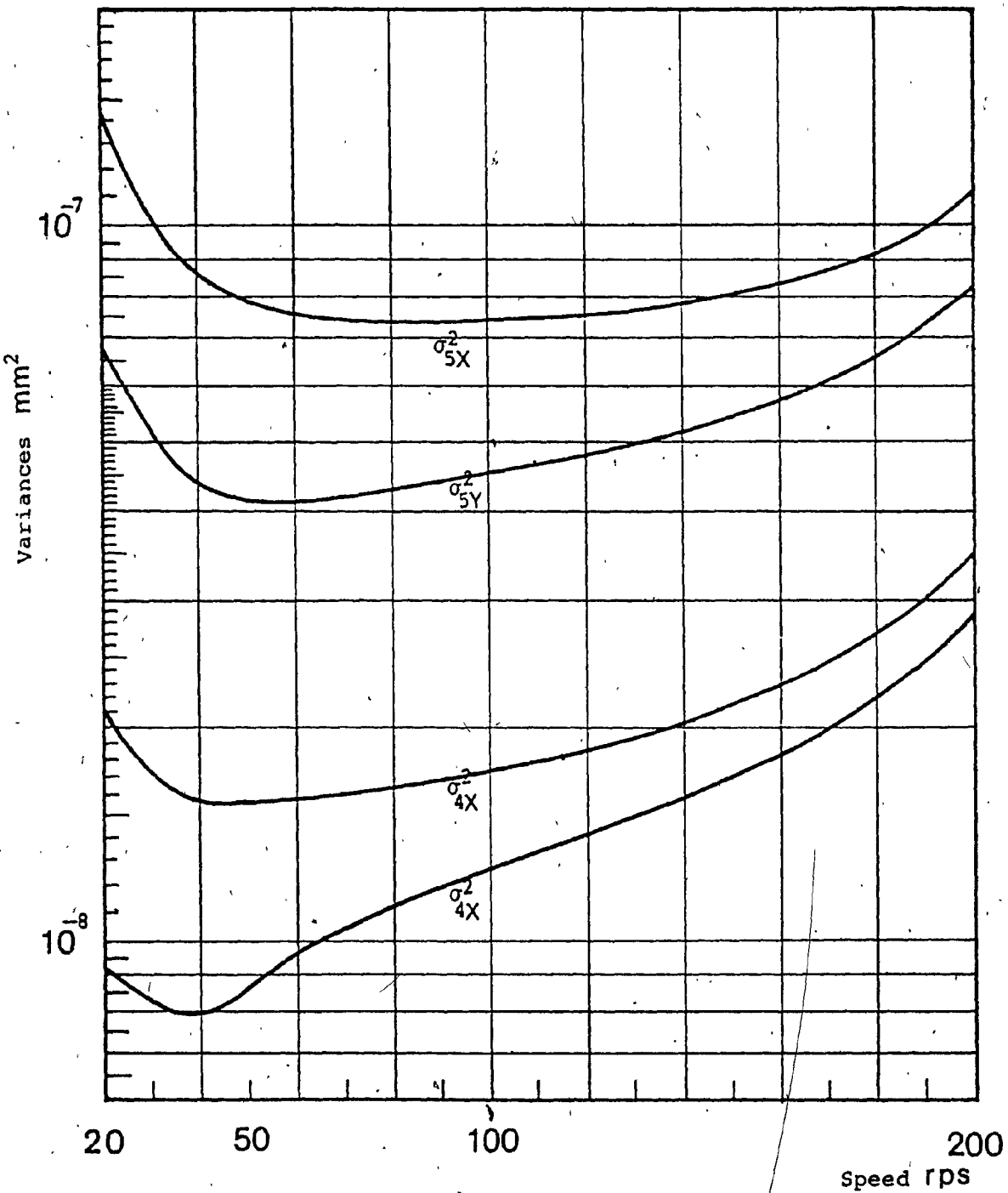

Fig. 6.11 The Variance of the Response at the Wheel Element in X and Y Directions, F_c = 500N.

$$\sigma_{5X}^2 = 93 \times 10^{-8} \text{ mm}^2 \qquad \sigma_{5X} = 9.6 \times 10^{-4} \text{ mm}$$

giving most of the confidence, about 99.74%, that the amplitude will be between -2.89×10^{-3} and 2.89×10^{-3} mm.

Finally, it may be noted that the radial clearance is .076 mm and then without any check on the error involved in the linearization of the bearing hydrodynamic forces, it is directly obvious that such an assumption is quite acceptable. If the amplitudes of the rotor motion are not small enough, still a check on the acceptability of the linearized stiffness and damping of the bearing can be made on an approximate basis by using the results of Chapter 4. In this case, the stochastic response is to be calculated at the bearing centre line and then the probabilities of the response in the X and Y directions, at the bearing centre line, is used to construct a rectangle around the equilibrium point. The sides of the rectangle are $6\sigma_{cX}$ and $6\sigma_{cY}$ where σ_{cX} and σ_{cY} are the standard of deviation of the response in the X and Y directions at the bearing centre line. Then the rotor motion at the bearing centre line will most probably exist inside such enveloping rectangles. Using the size of this rectangle and the deviation error plots of Chapter 4, the error in the linearity assumption can be roughly obtained.

6.5.3 Qualitative Analysis

In the presentation of the unbalance response calculations, it was noted that the rotor does not run through any critical speeds in the specified speed range, namely 20-200rps

and that the beam deflection is mostly due to the unbalance force and otherwise behaves more like a rigid body. It is also noted, from the complex frequency response functions, that the first critical frequency of the system occurs at one-half the running speed which resembles the behaviour of the complex frequency response functions of a rigid rotor presented in Chapter 4.. To elaborate on the behaviour of the rotor bearing on hand, the damped natural frequency charts for both cutting force cases $F_c = 300N$ and $F_c = 500N$, are presented in Figs. 6.12 and 6.13 respectively.

As can be seen from the damped natural frequency charts, the rotor runs free from intersection with any of the rotor modes which explains why no critical speeds are encountered in the unbalance response curves. The first two nodes are over damped, that is nonoscillatory modes or with zero frequency, in both of the cutting force cases and therefore not presented on the charts, in Figs. 6.12 and 6.13, whereas the next two modes, third and fourth, are both odd and with forward precession. The third and fourth modes are of frequencies equal to one-half the running speed $\pm 1\%$ approximately. In this case, the rotor mode is composed of a single mode unlike the higher modes $5^{th}, 6^{th}, \ldots$, etc which split into two components, one with backward precession and the other with forward precession.

Since the rotor runs at speeds that are closer to the frequency of the third and fourth mode compared to any other modes, these two modes are the most influential in affecting

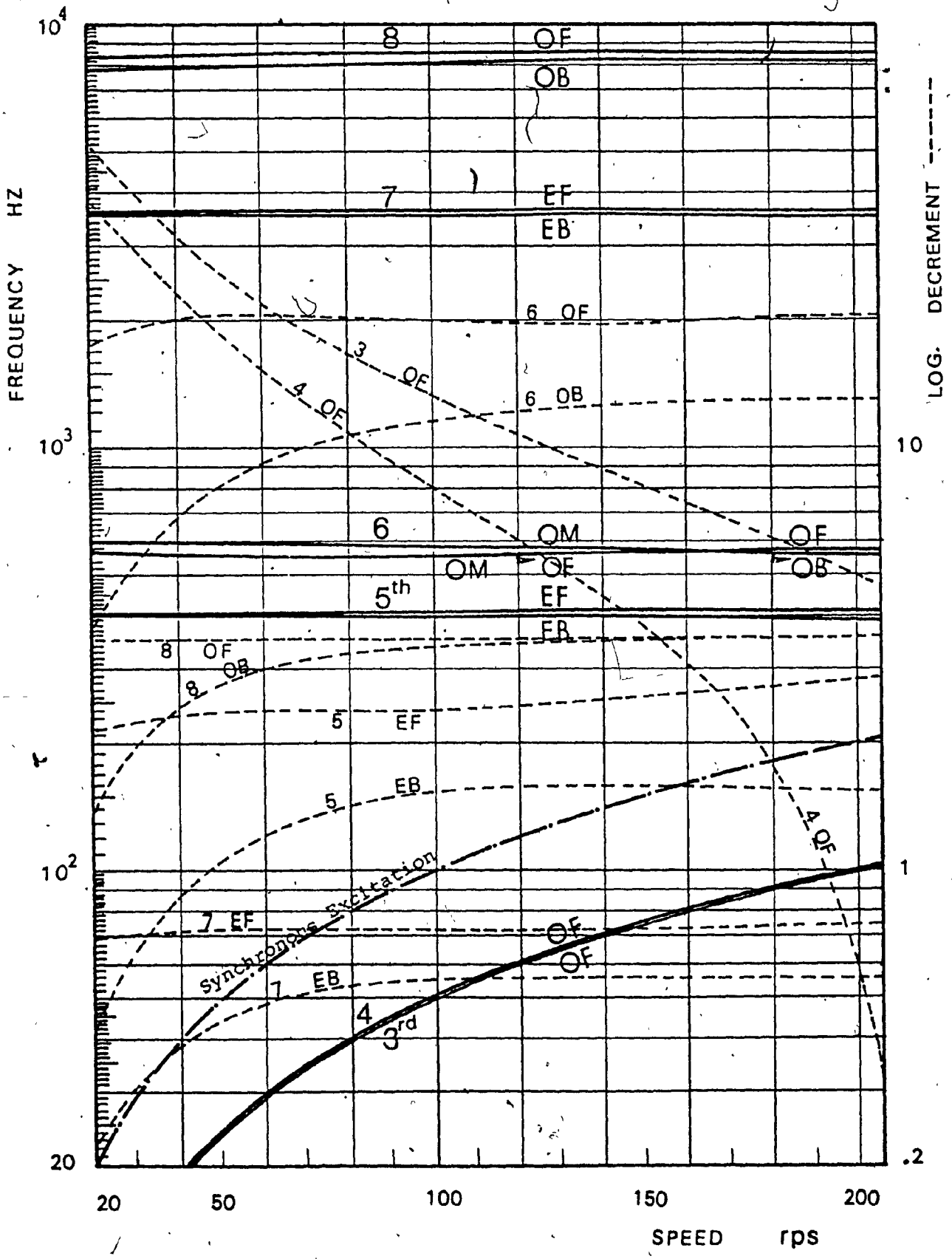

Fig. 6.12 Damped Natural Frequencies for the Case with F_c = 300N. (See Page xx).

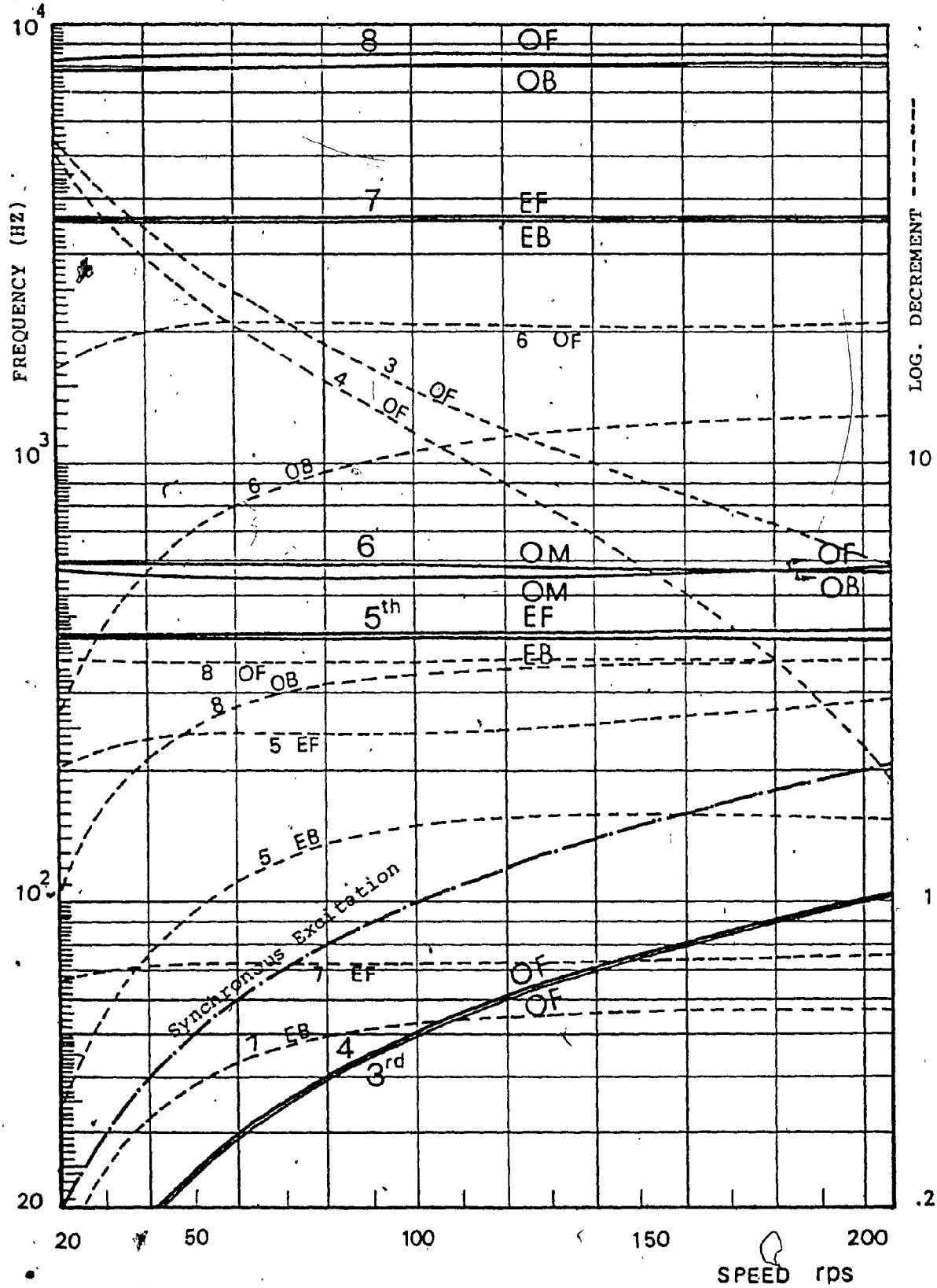

Fig. 6.13 Damped Natural Frequencies for the Case with F_c = 500N. (See Page xx).

the behaviour of the rotor under synchronous excitation. The frequency of the fifth mode is also important and as seen from the complex frequency response functions Fig. 6.7, it is associated with significant magnitude for such transfer functions. It is interesting to note the change in the magnitude of the transfer functions in Fig. 6.7, at the first two peaks relative to each other. The second peak, at 400HZ, is more significant for the low speed case while the first, at half the running speed, becomes more effective at the higher speed.

The first two modes appear to be dominated by the rigid body motion and consequently due to the effect of the hydrodynamic forces in the bearings. Therefore, the growing significance of the third and fourth modes at higher speeds signals that the rotor is approaching a state of instability in oil whip. In fact, this is determined precisely by extrapolating the logarithmic decrement curve for the fourth mode until it reaches a value of zero which defines the onset of instability in oil whip and found to occur at 212 rps for the $F_c = 300N$ case, presented in Fig. 6.12, and at 230 rps for the $F_c = 500N$ case, shown in Fig. 6.13. The onset of instability in oil whip occurs at a running speed that is twice the frequency of the third and fourth mode which are the first and second rotor modes, excluding the overdamped modes. This is also recognized by Lund [54] to be the case other than the occurance of oil whip at twice the first bending critical.

To further elaborate on the nature of the rotor motion, the first and second modes, again excluding the overdamped modes, are plotted in Fig. 6.14 for different speeds. Here, the real parts of the eigenvectors are plotted. As can be seen from the graph, only when higher speeds are reached that some deflection, however negligible, starts to take place. Otherwise these modes can be recognized as mainly dominated by rigid body motion. The reason that these modes are odd is because of the opposite reaction of the two bearings which consequently leads to oppositely acting hydrodynamic forces at both bearings. This results in an unsymmetrical overall configuration despite the almost geometrical symmetry of the rotor-bearing. The first bending critical should take place at a speed of 400 rps (24000 RPM) which can be seen by extrapolating the fifth mode and extending the synchronous excitation curves in either of Figs. 6.12 or 6.13. However, this speed will never be reached due to oil whip.

6.5.4 Further Analysis

Two important points remain for additional discussion. These are reported below.

a) The effect of including further details to the rotor-bearing system on hand is investigated considering bearing support flexibility. The damped natural frequency graph in Fig. 6.15 corresponds to a case of including a flexible support to the bearing with $K_b = 3.5 \times 10^5$ N/mm (2×10^6 lb/in).

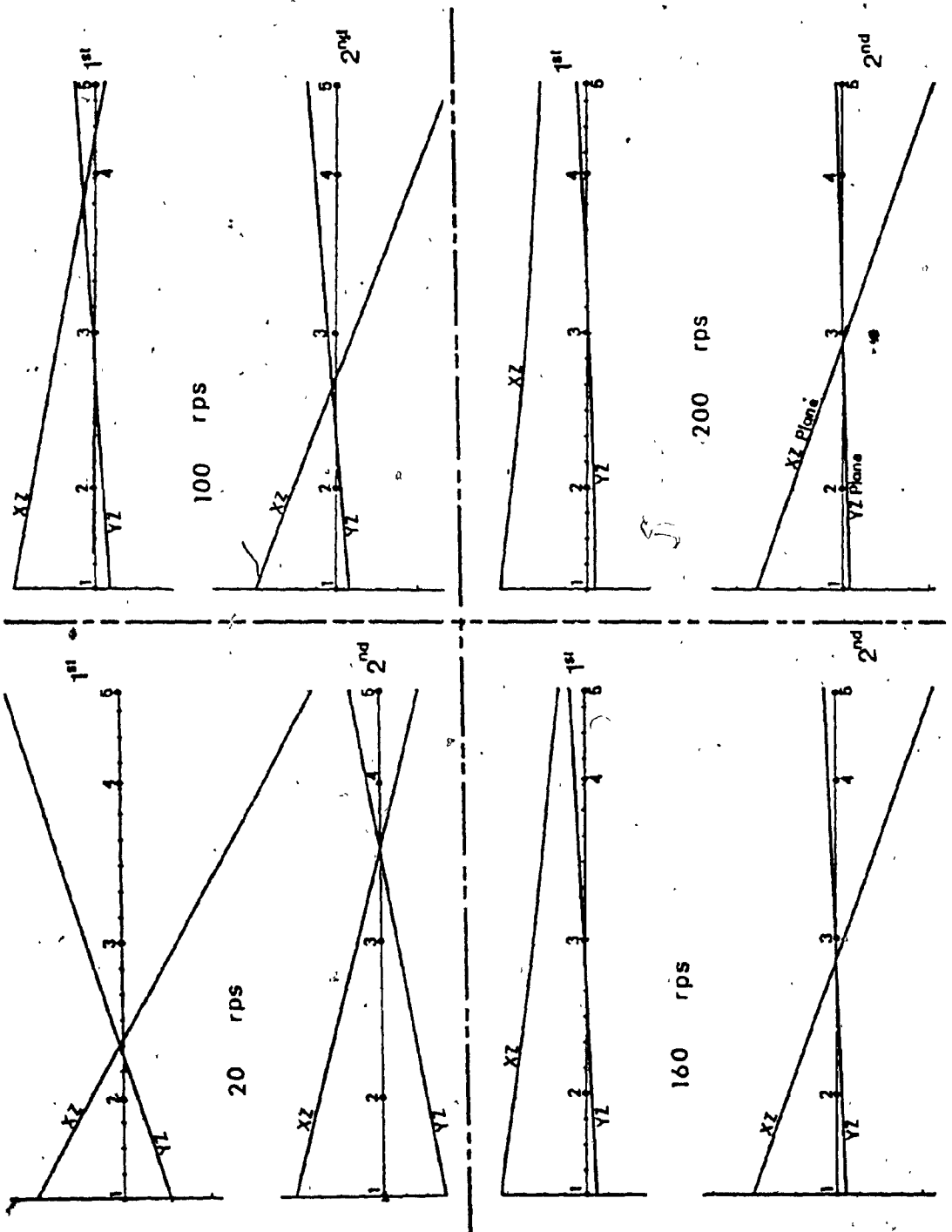

Fig. 6.14 First Two Rotor Natural Modes, Real Parts, at Different Speeds.

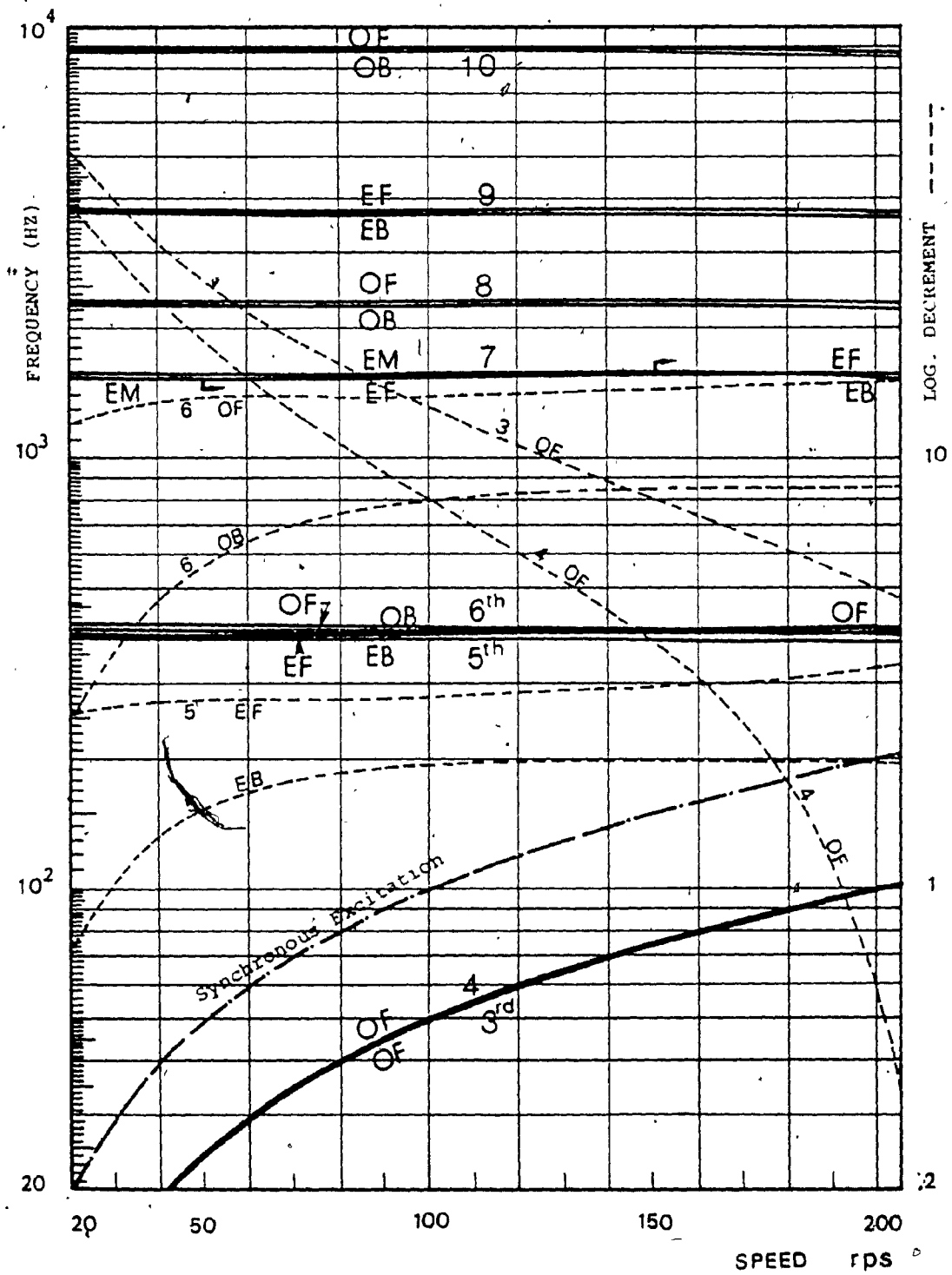

Fig. 6.15 Effect of Bearing Suspension Flexibility on the Natural Modes of the Spindle. (See Page xx).

As can be seen from the graph, only two modes are added in the frequency range above 400HZ, otherwise the picture remains almost identical to that in Fig. 6.12. The onset speed of instability in oil whip occurs at exactly the same previous value, that is 212 rps. Once the hydrodynamic bearing effect is recognized as the most dominant factor on the rotor behaviour, other effects such as hystersis are of minor significance and are needless to be investigated.

b) A rotor-bearing system, that is recognized as being rigid, which is the case on hand, may have critical frequencies which are much higher than the running speeds but are still included in the frequency band of the input spectral density. This will necessitate the inclusion of these frequencies into the calculation of the stochastic response which directly requires the rotor to be treated as flexible. This is demonstrated in Fig. 6.10 where a case is presented for the variances calculated using only the first two modes (next to the overdamped modes) which implies consideration of the rotor to be rigid. As can be seen from the figure the results with this treatment is well off the originally reported results. This is a consequence of neglecting the effect of the critical frequency at 400HZ. In such cases as this, a simple flexible rotor treatment may be recommended, say, by modelling the whole rotor beam as one element.

It can then be concluded that under certain circumstances the assumption of rotor beam rigidity may be quite

appropriate, runs well below its first critical, for unbalance and transient response calculation, but can not always be treated as being rigid for some cases that require a stochastic analysis.

6.6 Conclusions

The modal analysis procedure along with the conventional spectral density approach for stochastic problems, is shown to greatly simplify the approach which is derived with the necessary relations for calculating the stochastic response of the grinding machine rotor system. A check for the procedure is also presented. The spectral pattern of the random cutting force in grinding is specified in view of the previous experimental measurements and using the facts about random variables as specified by the central limit theorm.

With the different mathematical models developed earlier for flexible and rigid rotors, an optimum selection of a model to be employed is discussed. An analysis is then carried out on a given grinding machine spindle. In this example, the spindle responses under both the unbalance and the random inputs are calculated and analyzed. The characteristics of the rotor bearing in this example is distinguished by a small size and opposite bearing reactions. Such a special case has not been discussed in previous investigations. These characteristics enforce a spindle motion that features an odd shape while sustaining a rigid body motion. Therefore

it may seem appropriate to reduce the analysis to the simple case of a rigid rotor so that results of a more general form can be deduced employing simpler calculations.

It is found that the type of input excitation on the system decides the flexibility criterion for the rotor-bearing system. For a stochastic input with a wide band type of spectral density which contains the frequency corresponding to one of the effective damped nature modes of the rotor-bearing system, the rotor beam must be treated as flexible even though its running speeds may be far below the frequency of first bending critical.

CHAPTER 7

CONCLUSIONS AND RECOMMENDATIONS

7.1 Highlights of the Investigation

Comprehensive mathematical models are constructed and presented for light rotor bearing systems with an elaborate emphasis on their stability characteristics. The dynamical systems presented are not only versatile as to represent accurately the various states of the rotor-bearing systems but also a special care has been taken to maintain an overall simplicity for these models in terms of the developed procedures, formulated expressions and dimensional considerations. With such a combination of both accuracy and simplicity, the dynamical systems presented are quite attractive for practical applications. General methods are developed with minimum limitations for calculating the system response to deterministic and stochastic inputs. The procedure can accomodate special requirements for a rigid body treatment as well as linear considerations in an organized manner with appropriate justifications.

An application of the results of the bearing dynamic analysis is carried out on a grinding machine rotor system, and the study is developed in a form for a general practical use since the dynamical systems constructed account for all the effects that may not always be encountered for the range of operating conditions which are normally used in the

design of such machines. Therefore the results of this thesis should serve as an improved tool for present as well as future designs for a better understanding and design of such precision machines as well as other systems.

7.2 Major Conclusions

The contributions made in this investigation may be categorized into two major areas. One part of the analysis considers the rigid body motion of the rotor and the other is extended to flexible rotors. The conclusions drawn from these are first listed under two categories below and in a later part the method of solutions used and their justifications are explained prior to implementation of the analysis to special conditions of the rotor bearing system.

7.2.1 Rigid Rotor Bearing System

The nonlinear stiffness and damping are evaluated using a rather general procedure that makes it possible to carry out a numerical solution in a relatively general form, which requires prespecification of only a few dimensionless parameters with known bounds. Beginning with a decomposition of the Reynolds' equation into appropriate components in a dimensionless form, the equations are solved by the finite element method, integrating for the film forces, using appropriate curve fitting functions and finally taking the cavitation effect into account.

The pressure profile of the dynamic film is identified and is seen as the practical and basic dynamic film model in view of the previous experimental observations. In the place of the basic film model which has a time dependent film profile, two partial film models, namely the π and the $3\pi/2$ film, are developed for a finite bearing and are shown to be the upper and lower bounds for the basic dynamic film. The hydrodynamic forces in these partial film models are decoupled from the Reynolds' equation and thus preserving the simplicity of the known approximate solutions, the long and short bearing approximations, but with an improved accuracy. The $3\pi/2$ film model can be used for the case of light loading in the presence of significant supply pressure and can be reduced quite successfully to the case of squeeze film damper since it contains no distortion in the squeeze pressure component. For other cases, the π film model may be used.

Comparisons with previous work are carried out in detail for the purpose of verification and for bringing out the special nature of the mathematical models. They are listed below in a proper order.

i) A comparison between the developed eccentricity functions and the corresponding functions for the short and the long bearings shows that there exists narrow acceptability limits of such approximations; namely $L/d > 2$ for the long bearing and $L/d < .25$ for the short bearing case.

ii) A comparison with the corrected short bearing theory [13] that extends its validity up to $L/d < 1.25$ has also been carried out for the stationary state and squeeze motion. When compared with the analytical solutions that exist for such special cases using variational methods, the results of the present analysis show a better agreement independent of the L/d ratio.

iii) A comparison with the measured experimental results for the short bearing [2] shows that an approximate solution as given previously can yield correct results for some parameters (in this case, the attitude angle) while introducing considerable error for others and this can only be clarified if other bearing parameters were also measured (in this case, the eccentricity).

iv) A comparison with the available experimental work for the full film case [40] is also carried out and this clearly demonstrates the accuracy of the present approach and the results. Since all the eccentricity functions for all the different film models are developed through a common procedure, it can be stated that such conclusion can also be extended to the partial film models presented.

v) A comparison of the linearized stiffness and damping [5] which employed a weighted sum of the long and short bearing, with the present results showed good agreement for some stiffness and damping coefficients.

The stability behaviour of the finite bearing is investigated using both linear and nonlinear methods and give the following results:

i) Linear stability analysis yields a modified stability boundary that are distinct with a simple trend over the L/d ratios without arbitrary crossovers that were previously reported [43,44].

ii) Through a numerical integration of the nonlinear equations of a bearing with L/d = 1, it is found that the π film is more liable to be destabilized by input disturbances and possesses a smaller orbital stability subregion in comparison to the $3\pi/2$ film model. The large orbital stability subregion of the $3\pi/2$ film model is distinct with a gradual growth in the size of the limit cycle across the orbital stability subregion until the instability boundary is reached where a large circular limit cycle is manifested. This may be used as a logic explanation for the often observed limit cycle for a full film bearing which essentially requires similar circumstances for its formation as those of the $3\pi/2$ film model.

iii) Further extension of the stability results, in the region of stability, is carried out through, and as a by product of, a modal analysis. The logarithmic decrements are calculated as a part of the study of the stable behaviour of the finite bearing.

The solution of the system through modal analysis enabled a focus on the following important statements on the bearing behaviour:

i) The evaluated damped natural frequencies of the system over most of the stable region of the bearing show that one of the two natural frequencies is always overdamped.

ii) The complex frequency response functions are plotted for a rigid symmetric rotor against variations in L/d ratio , dimensionless speed and static eccentricity ratio e_o. The important effect of the unbalance excitation can clearly be seen to be outside the most sensitive frequency region which is located around a frequency equal to one half the running speed.

7.2.2 Flexible Rotor Bearing System

Employing a finite element technique a conclusive dynamical model is built taking into account the gyroscopic moments, rotary inertia, shear deformation, internal viscous damping, hysteretic damping, finite bearing stiffness and damping coefficients as well as the bearing support flexibility. Two main points used in this analysis which greatly simplified the procedure for developing the dynamical system while maintaining its dimensions and accuracy may be stated as following:

i) In all the previous applications of the finite element method on the rotor dynamic problem that took into account the gyroscopic moments and rotary inertia [63-65], a unified spatial system for the angular direction was utilized. Since such a treatment does not solve any existing problem but rather introduces a great deal of complexity, particularly when further details are to be added to the finite element model, the motion planes are treated in an analogous manner in the present investigation. Only matrices of order 4 (instead of usually 8) are needed to be constructed. Further addition of details, particularly shear deformation, is greatly simplified in the present approach.

ii) A simple Timoshenko beam element is utilized here which was previously recognized as to provide accurate results when applied to simple beam problems [59] and requires no change in the dimensions of the dynamic system. This is found to replace elegantly the more detailed element that results in an additional 50% increase in the number of degrees of freedom for the system of element equations and was very recently used in the only application of the finite element on rotor dynamics that accounts for shear deformation [62,63]. The difference in the calculated results between the two type of element arrangement was also shown to be negligible [59].

In addition to the above, the following contributions are worth mentioning. They are:

iii) The shape functions that correspond to the angular displacements of the beam are derived and presented. This makes the development of the finite element procedure more programmable.

iv) The derivation of the nonconservative moments due to the hysteretic damping in the finite element development are also presented.

v) A comparison with previous experimental and theoretircal results due to Lund and Orcutt [53] shows that the present finite element model, using only 3 elements, is in better agreement with the experimental observations than the transfer matrix method employed in [53].

vi) An examination of the two different flexiblity effects, namely the surface contact flexibility and the bearing support flexibility, reveals that the latter stabilizes the rotor motion considerably. This is related to the specified degrees of freedom of the bearing and is explained using a point view phase diagram.

vii) It is also found that the plotting of the angular displacements may help to identify the system criticals that may be hard to distinguish using the translational response only. These are essentially preliminary studies on the system criticals and can lead to comprehensive studies using the damped natural frequency charts due to Lund [54].

7.2.3 Methods of Solution Employed and Special Cases

The method of modal analysis is used in solving the linear systems representing both the rigid and the flexible rotor. A standard proof that is not previously available in the literature is provided. This method is then extended for use in the development of the spectral density approach for the calculation of the stochastic response. A simple check is provided to verify the procedure and to check the program, for the calculation of the stochastic response.

For easy use of the results when the system can be considered linear, the error involved in the calculated response to unbalance excitation is evaluated in detail and a demonstration of how these results can be employed is also outlined.

An application of the results of rotor dynamic study on a grinding machine spindle is carried out. The random cutting force is modeled in view of previous experimental observation on other metal cutting processes and using the properties of random variables as defined by the central limit theorem. The investigation involves: i) the system response to a unit unbalance located at the grinding wheel; ii) the variance of the stochastic response to the input cutting forces; and iii) the bandwidth of spectral density of the random response. The system stability is investigated using different damped natural frequency charts and the

system onset speed of instability in oil whip is calculated.

An interesting conclusion arises from the examination of the results of the study on the grinding machine rotor and may be stated as follows: A rotor bearing system that may be recognized as undergoing a rigid body motion can be considered as such only for calculations such as the unbalance response. But the system must be treated as a flexible rotor for a random input with a spectral density that includes in its band a frequency that corresponds to an effective damped natural frequency of the rotor-bearing system.

7.3 Recommendations for Future Work

The present treatment of the finite journal bearing can be expanded, without much complications, to handle bearings with different film geometry in the incompressible state of the film and perhaps for the compressible film as well. In fact, the present approach is general enough that it can be of immense use in the nonlinear dynamic problem of the journal bearing. A few possible future developments are listed below:

i) A reasonable combination of the π and $3\pi/2$ film models, preserving their simplicity, will certainly provide a better alternative and perhaps an excellent overall model for the general journal bearing problem. It is suggested here that an implementation of the boundary angles (θ_1, θ_2) of the dynamic film for the short and long bearing presented

in Chapter 2, into the general procedure, may produce much improved results.

ii) The case of skewed journal bearing can be handled with ease by using the present approach. Only two parameters will have to be added, namely the two inclination angles in both planes.

Extensive nonlinear analysis for the stability behaviour of the finite bearing is suggested as future work for different L/d ratios. The search for an appropriate Liapunov's function may also be continued for a classical stability analysis.

The errors involved in the calculated response using a linearized system which is constructed here in a chart form is a very valuable tool for the design of rotor bearing systems. It may be attempted in future to generate rather extensive charts and tables to cover the entire range of L/d ratios and dimensionless speeds.

One of the highlights of this thesis is the study of a grinding machine spindle system employing the present and previously available results in the field of rotor bearing dynamics. The input stochastic cutting forces are modelled through an appropriate spectral density function and are based on a study of previously reported cutting force measurements in different machining processes which have to be experimentally verified for a grinding operation. The results of this analysis and the procedures used may be useful in

extending such studies for the design and performance optimization of different machine-tool system in manufacturing. Another follow up of this is the correlation of the rotor - work piece - cutting tool system response to the surface roughness parameters of the resulting product. Perhaps the optimal or desired roughness quality can be achieved through the control of the machining conditions dictated by the spindle response in the cutting directions.

REFERENCES

1. Trumpler, P.R., "Design of Film Bearings", MacMillan, New York, 1966.

2. Ocvirk, F.W., "Short Bearing Approximation for Full Journal Bearing", NACA, TN 2808, 1951.

3. DuBois, G.B. and Ocvirk, F.W., "Short Bearing Approximation for Full Journal Bearing", Trans. ASME, Vol. 77, 1953, p. 1173.

4. Jennings, V.D. and Ocvirk, F.W., "The Simulation of Bearing Whirl on an Analog Computer", Journal of Basic Engineering, Trans. ASME, Series D, Vol. 84, 1962, p. 503.

5. Childs, D., Moes, H. and Leeuwen, H., "Journal Bearing Impedence Descriptions for Rotordynamic Applications", Journal of Lubrication Technology, Trans. ASME, Vol. 99, No. 2, 1977, p. 198.

6. Hays, D.F., "A Variational Approach to Lubrication Problems and the Solution of Finite Journal Bearing", Journal of Basic Engineering, Trans. ASME, Series D, Vol. 81, No. 1, 1959, p. 13.

7. Habata, K., "Theoretical Pressure Distribution in Journal Bearings", Journal of Applied Mechanics, Trans. ASME, Series E, Vol. 83, 1961, p. 497.

8. Ramachandra, S., "A Solution of Reynold's Equation for Full Finite Journal Bearing", Journal of Basic Engineering, Trans. ASME, Series D, Vol. 83, 1961, p. 589.

9. Tao, L.N., "Journal Bearing of Finite Length with Variable Viscosity", Journal of Applied Mechanics, Vol. 26, Trans. ASME, Series E, Vol. 81, 1959, p. 179.

10. Tao, L.N., "General Solution of Reynolds' Equation for Journal Bearing of Finite Width", Quarterly Journal of Applied Mathematics, Vol. 17, 1959, p. 129.

11. Donaldson, R.R., "A General Solution of Reynolds' Equation for a Full Finite Journal Bearing", Journal of Lubrication, Trans. ASME, Series F, Vol. 89, No. 2, 1967, p. 203.

12. Warner, P., "Static and Dynamic Properties of Partial Journal Bearings", Journal of Basic Engineering, Trans. ASME, Series D, Vol. 85, No. 2, 1963, p. 247.

13. Barrett, L.E., Allaire, P.E. and Gunter, E.J., "The Dynamic Analysis of Journal Bearing Using a Finite Length Correction for Short Bearing Theory", "Topics in Fluid Film Bearing and Rotor Bearing System Design and Optimization", ASME, New York, 1978.

14. Day, L., "The Validity of Some Approximate Solutions to the Reynolds' Equation", Journal of Lubrication Technology, Trans. ASME, Series F, Vol. 101, No. 3, July 1979, p. 385.

15. Raimondi, A.A. and Boyd, J., "A Solution for the Finite Journal Bearing and its Application to Analysis and Design - Part I, II and III", Trans. ASLE, Vol. 1, No. 1, 1958.

16. Sternlicht, B., "Elastic and Damping Properties of Cylindrical Journal Bearings", Journal of Basic Engineering, Trans. ASME, Series D, Vol. 18, 1959, p. 101.

17. Lund, J.W. and Sternlicht, B., "Rotor Dynamic with Emphasis on Attenuation", Journal of Basic Engineering, Trans. ASME, Series D, Vol. 84, 1962, p. 491.

18. Huebner, K.H., "The Finite Element Method for Engineers", John Wiley and Sons, New York, 1975.

19. Reddi, M.M. and Chu, T.Y., "Finite Element Solution of the Steady State Compressible Lubrication Problem", Journal of Lubrication Technology, Series F, Vol. 22, No. 3, 1970, p. 495.

20. Reddi, M.M., "Finite Element Solution of the Incompressible Problem", Journal of Lubrication Technology, Trans. ASME, Series F, Vol. 91, No. 3, 1969, p. 524.

21. Booker, J.F. and Huebner, K.H., "Application of Finite Element Method of Lubrication: An Engineering Approach", Journal of Lubrication Technology, Trans. ASME, Series F, Vol. 94, No. 4, 1972, p. 313.

22. Akers, A., Michaelson, S. and Cameron, A., "Stability Contours for a Whirling Finite Journal Bearing", Journal of Lubrication Technology, Trans. ASME, Series F, Vol. 93, 1971, p. 177.

23. Kirk, R.G. and Gunter, E.J., Discussion on "Stability Contours for a Whirling Finite Journal Bearing", Journal of Lubrication Technology, Trans. ASME, Series F, Vol. 93, 1971, p. 186.

24. Singh, D.V., Sinhasan, R. and Tayal, S.P., "Theoretical Prediction of Journal Centre Motion Trajectory", Journal of Lubrication Technology, Trans. ASME, Series F, Vol. 98, No. 4, 1976, p. 620.

25. Etsion, I. and Pinkus, O., "Solution of Finite Journal Bearings with Incompressible Film", Journal of Lubrication Technology, Trans. ASME, Series F, Vol. 97, No. 4, 1975, p. 89.

26. Dawson, D., Godet, M. and Taylor, C.M., "Cavitation and Related Phenomena in Lubrication", Proceedings of the 1st Leeds-Lyon Symposium on Tribology, University of Leeds, England, September 1974.

27. Swales, P.D., "A Review of Cavitation Phenomena in Engineering Situations", Ibid, pp. 3-9.

28. Temperley, H.N.V., "The Tensile Strength of Liquids", Ibid, pp. 11-13.

29. Dawson, D. and Taylor, C.M., "Fundamental Aspects of Cavitation in Bearings", Ibid, pp. 15-25.

30. Floberg, L., "Cavitation Boundary Conditions with Regard to the Number of Streamers and Tensile Strength of the Liquid", Ibid, pp. 31-35.

31. Marsh, H., "Cavitation in Dynamically Loaded Journal Bearings", Ibid, pp. 91-95.

32. Thomsen, K.K. and Lund, J.W., "Consideration of Film Rupture in the Inlet Zone of a Journal Bearing", Ibid, pp. 163-167.

33. Milne, A.A., "Variations of Film Extent in Dynamically Loaded Bearings", Ibid, pp. 79-90.

34. Coyne, J.C. and Elrod, H.G., "Conditions for Rupture of Lubricating Film - Part I Theoretical Model", Journal of Lubrication Technology, Trans. ASME, Series F, Vol. 93, No. 3, 1970, p. 451.

35. Parkins, D.W., "Theoretical and Experimental Determination of the Dynamic Characteristics of a Hydrodynamic Journal Bearing", Journal of Lubrication Technology, Trans. ASME, Series F, Vol. 101, 1979, p. 129.

36. Cole, J.A. and Huges, C.J., "Visual Study of Film Extent in Dynamically Loaded Complete Journal Bearings", Proceedings of the Institution of Mechanical Engineers, Lubrication and Wear Conference, 1957, p. 147.

37. Taylor, C.M., "Research Note : Separation Cavitation, Solution for the Infinite Width Cylinder-Plane Journal Bearing Configuration", Journal of Mechanical Engineering Science, Vol. 15, No. 3, 1973, p. 237.

38. Wade, R.B. and Acosta, A.J., "Experimental Observation on Flow Past a Plano Convex Hydrofoil", Journal of Basic Engineering, Trans. ASME, Series D, Vol. 88, No. 2, 1966, p. 273.

39. Lund, J.W. and Saibel, E., "Oil Whip Whirl Orbits of a Rotor in Sleeve Bearing", Journal of Engineering for Industry, Trans. ASME, Series B, Vol. 89, 1967, p. 813.

40. Mitchell, J.R., Holmes, R. and Byrne, J., "Oil Whirl of a Rigid Rotor in 360° Journal Bearings : Further Characteristics", Proceedings of the Institution of Mechanical Engineers, Vol. 180, Part 1, No. 25, 1965-1966, p. 593.

41. Seireg, A. and Dandage, S., "A Phase-Plane Simulation for Investigating the Effect of Unbalance Magnitude of the Whirl of Rotors Supported on Hydrodynamic Bearings", Journal of Lubrication Technology, Trans. ASME, Series F, Vol. 97, No. 4, 1975, p. 605.

42. Reddi, M.M. and Trumpler, P.R., "Stability of the High Speed Journal Bearing Under Steady Load : I - The Incompressible Film", Journal of Engineering for Industry, Trans. ASME, Series B, Vol. 84, 1962, p. 351.

43. Holmes, R., "Instability Phenomena Due to Circular Bearing Oil Films", Journal of Mechanical Engineering Science, Vol. 8, No. 4, 1966, p. 419.

44. Badgley, R. and Booker, J.F., "Turborotor Instability Effect of Initial Transient on Plane Motion", Journal of Lubrication Technology, Trans. ASME, Series F, Vol. 91, No. 2, 1969, p. 625.

45. Sweet, J. and Genin, J., "Nonlinear Rotor Bearing Behaviour", Journal of Nonlinear Mechanics, Vol. 7, Pergamon Press, England, 1972, p. 407.

46. Singh, D.V. and Sinhasan, R., "Stability and Relative Stability of Porous Journal Bearing System with Axes Skewed", Journal of Lubrication Technology, Trans. ASME, Series F, Vol. 96, 1974, p. 621.

47. Eshleman, R.L., "Flexible Rotor-Bearing System Dynamics - I Critical Speeds and Response of Flexible Rotor Systems", ASME Report, New York, 1972.

48. Gunter, E.J., "The Influence of Internal Friction on the Stability of High Speed Rotors", Journal of Engineering for Industry, Trans. ASME, Series B, Vol. 89, 1967, p. 683.

49. Gunter, E.J., "Dynamic Stability of Rotor-Bearing Systems", NASA SP-113, 1966.

50. Vance, J.M. and Lee, J., "Stability of High Speed Rotors with Internal Friction", Journal of Engineering for Industry, Trans. ASME, Series B, Vol. 96, No. 1, 1974, p. 960.

51. Kirk, R.G. and Gunter, E.J., "Transient Response of Rotor Bearing Systems", Journal of Engineering for Industry, Trans. ASME, Series B, Vol. 96, No. 1, 1974, p. 682.

52. Kirk, R.G., "Nonlinear Transient Analysis of Multi-Mass Flexible Rotors", Ph.D. Dissertation, University of Virginia, June 1972.

53. Lund, J.W. and Orcutt, F.K., "Calculations and Experiments on the Unbalance of a Flexible Rotor", Journal of Engineering for Industry, Trans. ASME, Series B, Vol. 89, No. 4, 1967, p. 785.

54. Lund, J.W., "Stability and Damped Critical Speeds of a Flexible Rotor in Fluid Film Bearings", Journal of Engineering for Industry, Trans. ASME, Series B, Vol. 96, No. 1, 1974, p. 509.

55. Lund, J.W., "Modal Response of a Flexible Rotor in Fluid Film Bearings", Journal of Engineering for Industry, Trans. ASME, Series B, Vol. 96, No. 1, 1974, p. 525.

56. Bansal, R.N. and Kirk, R.G., "Stability and Damped Critical Speeds of Rotor Bearing Systems", Journal of Engineering for Industry, Trans. ASME, Series B, Vol. 97, No. 1, 1975, p. 1325.

57. Ruhl, R. and Booker, J.F., "A Finite Element Model for Distributed Parameter Turborotor Systems", Journal of Engineering for Industry, Trans. ASME, Series B, Vol. 94, 1972, p. 126.

58. Archer, J.S., "Consistent Mass Matrix of Distributed Mass Systems", Journal of the Structural Division, Proceedings of the ASCE, Vol. 89, ST4, 1963, p. 161.

59. Thomas, D.L., Wilson, J.M. and Wilson, R.R., "Timoshenko Beam Finite Elements", Journal of Sound and Vibration, 1973, Vol. 31, No. 3, p. 315.

60. Przemieniecki, J.S., "Theory of Matrix Structural Analysis", McGraw Hill, New York, 1968.

61. Davis, R., Henshell, R.D. and Warburton, G.B., "A Timoshenko Beam Element", Journal of Sound and Vibration, Vol. 22, No. 4, 1972, p. 475.

62. Rouch, K.E. and Kao, J.S., "A Tapered Beam Finite Element for Rotor Dynamic Analysis", Journal of Sound and Vibration, Vol. 66, No. 1, 1979, p. 119.

63. Rouch, K.E. and Kao, J.S., "Dynamic Reduction in Rotor Dynamics by the Finite Element Method", Journal of Mechanical Engineering Design, Trans. ASME, Vol. 102, 1980, p. 360.

64. Nelson, H.D. and McVaugh, J.M., "The Dynamics of Rotor-Bearing Systems Using Finite Elements", Journal of Engineering for Industry, Trans. ASME, Series B, Vol. 98, No. 2, 1976, p. 593.

65. Zorzi, E.S. and Nelson, H.D., "Finite Element Simulation of Rotor-Bearing Systems with Internal Damping", Journal of Engineering for Power, Trans. ASME, Series A, Vol. 99, No. 1, 1977, p. 71.

66a. Framer, A., Becker, J.N. and Shaw, M.C., "Study of the Finish Produced in Surface Grinding : Part 1 - Experimental", Proceedings of the Institution of Mechanical Engineers, Oxford, April 1968, p. 171.

66b. Nakayama, K. and Shaw, M.C., "Study of the Finish Produced in Surface Grinding : Part 2 - Analytical, Ibid.

67. Rakhit, A.K., Sankar, T.S. and Osman, M.O.M., "The Influence of Metal Cutting Forces on the Formation of Surface Texture in Turning", International Journal of Machine Tool, Vol. 16, Pergamon Press, 1976, p. 281.

68. Peklenik, J. and Kwiatkowski, A.W., "New Concepts in Investigating the Manufacturing Systems by Means of Random Process Analysis", Proceedings of the 7th International M.T.D.R. Conference, University of Birmingham, September 1966, p. 683.

69. Klaiszer, H. and Sindwani, A.D., "The Effect of Grinding Wheel Unbalance on Workpiece Waviness", Proceedings of the 10th International M.T.D.R. Conference, University of Manchester, September 1969, p. 395.

70. Tessarzik, J.M., Chiang, T. and Badgley, R.H., "The Response of Rotating Machinery to External Random Vibration", Journal of Engineering for Industry, Trans. ASME, Series B, Vol. 96, No. 1, 1974, p. 477.

71. Sankar, T.S. and Osman, M.O.M., "Flexural Stability of Machine Tool Spindles Under Randomly Fluctuating Cutting Forces", Proceedings of the 3rd World Congress for the Theory of Machines and Mechanisms, Kupari, Yugolsavia, September 1971, Vol. G, Paper G-19, p. 269.

72. Lund, J.W., "Response Characteristics of a Rotor with Flexible Damped Supports", Proceedings of IUTAM Symposium, Lyngby, Denmark, August 1974, p. 319.

73. Allaire, R.E., Barrett, L.E. and Gunter, E.J., "Variational Method for Finite Length Squeeze Film Damper Dynamics with Applications", Wear, Vol. 42, No. 1, 1977, p. 9.

74. Dimarogonas, A.D., "A General Method for Stability Analysis of Rotating Shafts", Ingenieur Archiv, Vol. 41, 1975, p. 9.

75. Meirovitch, L., "Analytical Methods in Vibration", MacMillan Book Co., New York, 1967.

76. Foss, K.A., "Co-ordinates Which Uncouple the Equations of Motion of Damped Linear Dynamic Systems", Journal of Applied Mechanics, Vol. 25, 1958, p. 361.

77. Lancaster, P., "Lambda-Matrices and Vibrating Systems", Pergamon Press Inc., Oxford, 1966.

78. Yang, I.M., "Stationary Random Response of Multidegree of Freedom Systems", California Institute of Technology, Ph.D. Thesis, 1970.

79. Meirovitch, L., "Elements of Vibration Analysis", McGraw Hill, New York, 1975.

80. LaSalle, J. and Lefschetz, S., "Stability by Liapunov's Direct Method with Applications", Academic Press, New York, 1961.

81. Barbashin, E.A., "Introduction to the Theory of Stability", Translated from Russian by Transcripta Service, London, Ed. by Likes, T., Wolters-Noordhoff, 1970.

82. Banerjee, K.K., "Some Aspects of Flat Surface Grinding with Intermittent Cross-Feed", Journal of Engineering for Industry, Trans. ASME, Series B, Vol. 101, No. 2, 1979, p. 135.

83. Crandall, S.H. and Mark, W.D., "Random Vibrations in Mechanical Systems", Academic Press, New York, 1973.

84. Cooper, G. and McGillon, C., "Probabilistic Methods of Signal and Systems Analysis", Holt, Rinehart and Winston Inc., New York, 1971.

85. Seireg, A. and Ezzat, H., "Optimum Design of Hydrodynamic Journal Bearings", Journal of Lubrication Technology, Trans. ASME, Series F, Vol. 91, No. 2, 1969, p. 516.

86. Kirk, R.G., Dechoudhury, P. and Gunter, E.J., "The Effect of Support Flexibility on the Stability of Rotors Mounted in Plain Cylindrical Journal Bearing", IUTAM Symposium, Lyngby, Denmark, 1974.

87. Parszewski, Z., "Dynamic Interaction Between Machine and Support", First World Conference in Industrial Tribology, New Delhi, Paper E5, 1972.

88. Thomson, W., "Theory of Vibration with Applications", Prentice Hall, New Jersey, 1972.

89. Rohde, S.M., "Bounds for the Solution of Reynolds' Equation", Journal of Lubrication Technology, Trans. ASME, Series F, Vol. 95, 1973, p. 102.

90. Hori, Y., "A Theory of Oil Whip", Journal of Applied Mechanics, Trans. ASME, Vol. 81, 1959, p. 189.

91. Marshall, E.R. and Shaw, M.C., "Forces in Dry Surface Grinding", ASME, Vol. 74, 1952, p. 51.

92. Banerjee, J.K. and Hillier, M.T., "Forces in Surface Grinding with Intermittent Cross-Feed" Journal of Tool and Manufacturing Engineers, ASTME, 1969, p. 63.

93. King, K.F. and Taylor, C.M., "A Theoretical Estimation of the Performance of Journal Bearings Operating in the Turbulent Lubrication Regime", Journal of Mechanical Engineering Science, I.Mech.E., Vol. 17, No. 2, 1975, p. 52.

APPENDIX A

TABLES OF COEFFICIENTS OF THE ECCENTRICITY FUNCTIONS

The eccentricity functions are curve fitted using the polynomial form (2.16) in Chapter 2. The curve fitting accuracy is demonstrated in Table A.1 for chosen 10 values of the eccentricity ratio in the range $0 \leq e \leq .9$ in terms of the percentage error. The coefficient B_i for the eccentricity functions E_1, E_2, E_3, E_4 and E_6 are listed in Tables A.2 through A.6.

Q	ORIGINAL FUNCTION	CURVE FITTED FUNCTION	PERCENT. ERROR
SETS OF FUNCTION E_1 ,G=L/D= .25			
0.0	0.0000000	0.0000000	0.0000000
.1	-.0096627	-.0096629	.0018348
.2	-.0201678	-.0201672	.0030032
.3	-.0325737	-.0325749	.0036689
.4	-.0484887	-.0484872	.0030832
.5	-.0707599	-.0707611	.0017259
.6	-.1052000	-.1051994	.0006119
.7	-.1659110	-.1659112	.0001243
.8	-.2968480	-.2968480	.0000116
.9	-.7196600	-.7196600	.0000003
SETS OF FUNCTION E_1 ,G=L/D= .50			
0.0	0.0000000	0.0000000	0.0000000
.1	-.0359420	-.0359436	.0044846
.2	-.0745730	-.0745675	.0073878
.3	-.1191900	-.1192009	.0091242
.4	-.1746030	-.1745894	.0077937
.5	-.2489120	-.2489231	.0044667
.6	-.3577110	-.3577051	.0016384
.7	-.5361140	-.5361159	.0003503
.8	-.8835340	-.8835337	.0000356
.9	-1.8328200	-1.8328200	.0000010
SETS OF FUNCTION E_1 ,G=L/D= 1.00			
0.0	0.0000000	0.0000000	0.0000000
.1	-.1125900	-.1125926	.0023290
.2	-.2308880	-.2308790	.0038819
.3	-.3616500	-.3616677	.0048921
.4	-.5142020	-.5141799	.0043055
.5	-.7032470	-.7032651	.0025722
.6	-.9551770	-.9551675	.0009983
.7	-1.3251900	-1.3251931	.0002306
.8	-1.9573700	-1.9573695	.0000262
.9	-3.4225000	-3.4225000	.0000008
SETS OF FUNCTION E_1 ,G=L/D= 1.50			
0.0	0.0000000	0.0000000	0.0000000
.1	-.1866870	-.1866901	.0016568
.2	-.3798800	-.3798694	.0027817
.3	-.5872660	-.5872868	.0035503
.4	-.8193950	-.8193689	.0031828
.5	-1.0927800	-1.0928013	.0019492
.6	-1.4368000	-1.4367888	.0007813
.7	-1.9122000	-1.9122036	.0001880
.8	-2.6756700	-2.6756694	.0000225
.9	-4.3377000	-4.3377000	.0000008
SETS OF FUNCTION E_1 ,G=L/D= 2.00			
0.0	0.0000000	0.0000000	0.0000000
.1	-.2433300	-.2433325	.0010335
.2	-.4927700	-.4927614	.0017478
.3	-.7557300	-.7557470	.0022537
.4	-1.0426400	-1.0426187	.0020477
.5	-1.3702800	-1.3702975	.0012751
.6	-1.7689000	-1.7688908	.0005215
.7	-2.3015700	-2.3015730	.0001286
.8	-3.1305900	-3.1305895	.0000159
.9	-4.8853800	-4.8853800	.0000006
SETS OF FUNCTION E_1 ,G=L/D= INIFINITY			
0.0	0.0000000	0.0000000	0.0000000
.1	-.4712500	-.4712533	.0007069
.2	-.9430500	-.9430386	.0012076
.3	-1.4181500	-1.4181725	.0015853
.4	-1.9043000	-1.9042719	.0014774
.5	-2.4183800	-2.4184030	.0009505
.6	-2.9951200	-2.9951079	.0004046
.7	-3.7099800	-3.7099839	.0001047
.8	-4.7596200	-4.7596193	.0000137
.9	-6.9234000	-6.9234000	.0000005

Table A.1 Percentage Error in the Curve Fitting of Eccentricity Function E_1.

	BEARING L/D RATIO					
	.25	.5	1	1.5	2	∞
B0	0.00000	0.00000	0.00000	0.00000	0.00000	0.00000
B1	-.09565	-.35842	-1.12211	-1.86271	-2.42978	-4.71822
B2	.00745	.06983	.11481	.13393	.13269	.12567
B3	-.18403	-.92793	-1.74019	-2.00336	-1.92157	-.90418
B4	.12336	1.36243	2.25340	2.61440	2.56392	2.34962
B5	-.91544	-6.96496	-11.76742	-13.51001	-13.54758	-15.03429
B6	1.96661	16.89081	28.70699	32.94091	33.04329	35.92761
B7	-1.78748	-16.10134	-27.57606	-31.56757	-31.78780	-34.01855
B8	.59817	5.93515	10.34210	11.82667	11.97340	12.71939

Table A.2 Coefficients of Polynomial E_1.

B0	.19059	.71025	2.23346	3.71279	4.84692	9.42477
B1	-.25231	-.30819	-.27815	-.26936	-.26862	-.42277
B2	6.20143	9.43272	13.19476	15.56370	16.71547	23.16368
B3	-39.20965	-48.04302	-43.37067	-42.08294	-41.87024	-65.98620
B4	112.91920	141.89000	134.45390	133.17810	133.35290	205.44630
B5	-472.54560	-580.98660	-520.60300	-505.58460	-500.86080	-791.86890
B6	1213.98500	1505.72100	1361.78800	1327.80100	1316.30900	2067.27200
B7	-1165.92000	-1453.97600	-1315.45100	-1283.97300	-1271.96800	-1991.68100
B8	433.93480	546.61820	495.93480	484.73740	480.13310	746.74900

Table A.3 Coefficients of Polynomial E_2.

B0	0.00000	0.00000	0.00000	0.00000	0.00000	0.00000
B1	-.00339	-.00179	.00048	.00111	.00157	.00030
B2	.12990	.23160	.48343	.70131	.85215	1.49311
B3	-.52869	-.28371	.06998	.17016	.24321	.04206
B4	1.61384	1.13274	.43172	.26624	.09713	.66386
B5	-6.41526	-3.39210	1.15620	2.51344	3.39956	.80779
B6	16.81220	9.58445	-1.69247	-5.07512	-7.23552	.02144
B7	-16.33940	-9.51671	1.46842	4.80998	6.86289	-.30171
B8	6.21282	3.79020	-.35185	-1.63176	-2.39318	.25817

Table A.4 Coefficients of Polynomial E_3.

B0	.09529	.35513	1.11673	1.85639	2.42346	4.71240
B1	-.01352	.55028	2.13399	3.33376	4.02379	5.67186
B2	5.78537	8.01758	9.92150	10.77066	11.29338	14.22412
B3	-38.60522	-46.16279	-41.29381	-37.10107	-36.15049	-45.91631
B4	112.29220	140.13390	136.75810	129.97190	129.20090	168.20140
B5	-471.58010	-578.55650	-537.86190	-504.74560	-497.96180	-687.34420
B6	1212.05800	1500.88100	1404.18200	1327.92900	1312.17400	1837.71000
B7	-1164.51600	-1450.41800	-1352.99600	-1285.46100	-1270.30200	-1809.40600
B8	433.49070	545.46850	508.36760	485.25920	479.70400	689.45740

Table A.5 Coefficients of Polynomial E_4.

B0	0.00000	0.00000	0.00000	0.00000	0.00000	0.00000
B1	-.11185	-.44957	-1.31206	-1.93841	-2.28532	-2.99790
B2	-.21720	-.07283	.09183	.10771	.13548	-.03979
B3	1.35663	-.26044	-2.54052	-3.11200	-3.40436	-2.67227
B4	-4.57891	-1.78989	1.48568	1.92696	2.28356	-1.31044
B5	18.77970	5.17605	-11.83398	-14.65571	-16.19597	-2.70561
B6	-49.17346	-16.42022	25.54869	32.47599	36.14563	.80592
B7	47.76571	17.03657	-23.60149	-30.41079	-33.93311	-.17587
B8	-18.09264	-7.13342	8.25662	10.87173	12.22121	-.26370

Table A.6 Coefficients of Polynomia E_6.

APPENDIX B

NONLINEAR STIFFNESS AND DAMPING PARAMETERS OF THE FINITE BEARING

The journal equation of motion in the cartesian coordinates (3.1) can be derived from the polar form with the transformations

$$X = e\cos\psi \quad , \quad Y = e\sin\psi$$

and their derivatives. The nonlinear damping and stiffness functions, C_{XX}, C_{XY}, ..., and K_{XX}, K_{XY}, ... can then be written as

$$\begin{Bmatrix} C_{XX} \\ C_{XY} \\ C_{YX} \\ C_{YY} \end{Bmatrix} = \frac{S}{2e^3} \begin{bmatrix} 2XY & X^2e & -2Y^2 & -XYe \\ -2X^2 & XYe & 2XY & -Y^2e \\ 2Y^2 & XYe & 2XY & X^2e \\ -2XY & Y^2e & -2X^2 & XYe \end{bmatrix} \begin{Bmatrix} E_i \\ E_j \\ E_k \\ E_\ell \end{Bmatrix} \tag{B.1}$$

and

$$K_{XX} = \frac{S}{2e} E_i = K_{YY}$$

$$K_{XY} = -\frac{S}{2e} E_k = -K_{YX}$$

Here the eccentricity functions E_i, E_j, E_k and E_ℓ are listed in Table 2.2 for all film bearings, namely, the full film, the $3\pi/2$ film and the π film cases, and S is the bearing dynamic parameter given by equation (2.18a).

APPENDIX C

THE EQUATIONS OF MOTION OF THE FINITE BEARING IN THE PHASE SPACE

The equations of motion of the journal bearing can be written in terms of the phase variables $\bar{z}^*$ and in the general dimensionless form

$$\left\{\overset{0}{z}{}^*\right\}_{4x1} = \left\{Z^*(z_1^*, z_2^*, \ldots)\right\}$$

which can be written explicitly in the cartesian coordinates as

$$\begin{Bmatrix} \overset{0}{z}{}_1^* \\ \overset{0}{z}{}_2^* \\ \overset{0}{z}{}_3^* \\ \overset{0}{z}{}_4^* \end{Bmatrix} = - \begin{bmatrix} 0 & -1 & 0 & 0 \\ K_{XX} & C_{XX} & K_{XY} & C_{XY} \\ 0 & 0 & 0 & -1 \\ K_{YX} & C_{YX} & K_{YY} & C_{YY} \end{bmatrix} \begin{Bmatrix} z_1^* \\ z_2^* \\ z_3^* \\ z_4^* \end{Bmatrix} + \begin{Bmatrix} 0 \\ W_{nX} \\ 0 \\ W_{nY} \end{Bmatrix} \quad (C.1)$$

Here C_{XX}, ..., K_{XX}, ... are the nonlinear damping and stiffness terms, given by expressions (B.1) in Appendix B. The corresponding set in the polar coordinates for equations (C.1) can be written as

$$\begin{aligned}
\overset{0}{z}{}_1^* &= z_2^* \\
\overset{0}{z}{}_2^* &= z_1^* z_4^{*2} - \frac{S}{2}(1 - 2z_4^*)\, E_i(z_1^*) - \frac{S}{2} z_2^*\, E_j(z_1^*) \\
&\quad + W_n \cos(z_3^* - \beta_\ell) \\
\overset{0}{z}{}_3^* &= z_4^* \\
\overset{0}{z}{}_4^* &= \frac{1}{z_1^*}\left[-2z_2^* z_4^* - \frac{S}{2}(1 - 2z_4^*)\, E_k(z_1^*) - \frac{S}{2} z_2^* E_\ell(z_1^*)\right. \\
&\quad \left. -W_n \sin(z_3^* - \beta_\ell)\right] \qquad (C.2)
\end{aligned}$$

where the eccentricity functions E_i, E_j, E_k and E_ℓ are listed in Table 2.2 for all the different film models and β_ℓ is the load angle as seen from Fig. 2.1.

APPENDIX D

THE COEFFICIENTS OF THE MATRIX $[A_\ell]$ OF THE LINEARIZED SYSTEM (3.4)

Expanding the nonlinear functions in equation (3.4) by a Taylor series, retaining the first order derivatives and using the equilibrium state relations, the matrix $[A_\ell]$ is constructed as

$$[A_\ell] = -\frac{S}{2e}\begin{bmatrix} 0 & 1 & 0 & 0 \\ eE_i' & eE_j & -eE_k & -2eE_i \\ 0 & 0 & 0 & 1 \\ E_k' & E_\ell & E_i & -2E_k \end{bmatrix}$$

Here all the terms are evaluated at the equilibrium point and the eccentricity functions listed in Table 2.2 are used with the adjustments

$$E_5 = E_4$$

$$\zeta = 1$$

for the linearized system considered.

APPENDIX E

STIFFNESS AND DAMPING COEFFICIENTS IN THE LINEARIZED EQUATION FOR THE FINITE BEARING

The damping and stiffness coefficients of the linearized bearing system is obtained by expanding the non-linear hydrodynamic forces around an equilibrium point $(X_0, Y_0, \overset{0}{X}_0 = 0, \overset{0}{Y}_0 = 0)$ using Taylor series and keeping only the first order derivatives. Using equation (3.1) of Chapter 3, it directly follows that the damping coefficients of the linear system c_{xx}, c_{xy}, ..., are exactly those nonlinear damping functions C_{XX}, C_{XY}, ..., given by equation (B.1) in Appendix B, evaluated at the respective equilibrium points. The stiffness coefficients k_{xx}, k_{xy}, ..., though, are to be evaluated by expanding the terms $(K_{XX}X + K_{XY}Y)$ in F_X and similarly in F_Y and can be shown to be

$$\begin{Bmatrix} k_{xx} \\ k_{xy} \\ k_{yx} \\ k_{yy} \end{Bmatrix} = \left(\frac{S}{2}\right)\left(\frac{1}{e^3}\right) \begin{bmatrix} X^2e & Y^2 & -XYe & XY \\ XYe & -XY & -Y^2e & -X^2 \\ XYe & -XY & X^2e & Y^2 \\ Y^2e & X^2 & XYe & -XY \end{bmatrix} \begin{Bmatrix} E_i' \\ E_i \\ E_k' \\ E_k \end{Bmatrix} \quad (E.1)$$

Here, the primes denote the derivative $\frac{d}{de}$ and all the quantities are evaluated at the equilibrium point (X_0, Y_0).

APPENDIX F

THE SUBMATRICES OF THE EQUATIONS OF A FINITE ELEMENT

The submatrices $[M_{t_1}]$, $[M_{r_1}]$ and $[k_1]$ of the equations system (5.12) for the simple Timoshenko element are evaluated, as explained in Chapter 5, and can be written explicity as

$$[M_{t_1}] = \frac{m_z \ell}{420(1+\gamma)^2} \begin{bmatrix} a_1 & & & \\ a_2 & a_5 & \text{Symmetric} & \\ a_3 & -a_4 & a_1 & \\ a_4 & a_6 & -a_2 & a_5 \end{bmatrix}$$

$$[M_{r_1}] = \frac{J_T}{(1+\gamma)^2 30\ell} \begin{bmatrix} 36 & & & \\ a_7 & a_8 & \text{Symmetric} & \\ -36 & -a_7 & 36 & \\ a_7 & a_9 & -a_7 & a_8 \end{bmatrix}$$

$$[k_1] = \frac{EI}{\ell^3(1+\gamma)} \begin{bmatrix} 12 & & & \\ 6\ell & a_{10} & \text{Symmetric} & \\ -12 & -6\ell & 12 & \\ 6\ell & a_{11} & -6\ell & a_{10} \end{bmatrix}$$

where

$a_1 = 156 + 294\gamma + 140\gamma^2$ $\qquad$ $a_2 = (22 + 38.5\gamma + 10\gamma^2)\ell$

$a_3 = 54 + 126\gamma + 70\gamma^2$ $\qquad$ $a_4 = -(13 + 31.5\gamma + 10\gamma^2)\ell$

$a_5 = (4 + 7\gamma + 3.5\gamma^2)\ell^2$ $\qquad$ $a_6 = -(3 + 7\gamma + 3.5\gamma^2)\ell^2$

$a_7 = (3 - 15\gamma)\ell$ $\quad$ $a_8 = (4 + 5\gamma + 10\gamma^2)\ell^2$

$a_9 = (-1 - 5\gamma + 5\gamma^2)\ell^2$ $\quad$ $a_{10} = \ell^2(4 + \gamma)$

$a_{11} = \ell^2(2 - \gamma)$

Submatrices $[M_{t_2}]$, $[M_{r_2}]$, $[k_2]$ and $[G^*]$ of system (5.15) may be constructed as given below

$$[M_{t_2}] = \frac{m_z \ell}{420} \begin{bmatrix} 156 & & \text{Symmetric} & \\ -22\ell & 4\ell^2 & & \\ 54 & -13\ell & 156 & \\ 13\ell & -3\ell^2 & 22\ell & 4\ell^2 \end{bmatrix}$$

$$[M_{r_2}] = \frac{J_T}{30\ell} \begin{bmatrix} 36 & & \text{Symmetric} & \\ -3\ell & 4\ell^2 & & \\ -36 & 3\ell & 36 & \\ -3\ell & -\ell^2 & 3\ell & 4\ell^2 \end{bmatrix}$$

$$[k_2] = \frac{EI}{\ell^3} \begin{bmatrix} 12 & & \text{Symmetric} & \\ -6\ell & 4\ell^2 & & \\ -12 & 6\ell & 12 & \\ -6\ell & 2\ell^2 & 6\ell & 4\ell^2 \end{bmatrix}$$

$$[G^*] = \frac{\omega_r J_z}{30\ell} \begin{bmatrix} 36 & & \text{Skew Symmetric} & \\ 3\ell & -4\ell^2 & & \\ -36 & 3\ell & 36 & \\ 3\ell & \ell^2 & -3\ell & -4\ell^2 \end{bmatrix}$$

APPENDIX G

HYSTERETIC DAMPING MATRIX $[D_h]$ OF THE COUPLING TERMS IN EQUATIONS (5.22)

Equation (5.25) is expanded in terms of the shape functions of the angular displacement α and β to give the hysteretic matrix $[D_h]$ such that

$$[D_h]_{8x8} \{q^e\} = EI \sin\gamma_h \begin{bmatrix} [0] & [k_h] \\ -[k_h] & [0] \end{bmatrix}_{8x8} \{q^e\}$$

The entry (i,j) of the submatrix $[k_h]$ is given by

$$k_h(i,j) = \int_0^{\ell} N'_{ri} \, N'_{rj} \, dZ$$

and the submatrix $[K_h]$, in turn, is constructed as follows:

$$[k_h] = \frac{1}{\ell^3(1+\gamma)^3} \begin{bmatrix} 12 & & \text{Symmetric} & \\ 6\ell & \ell^2(4+2\gamma+\gamma^2) & & \\ -12 & -6\ell & 12 & \\ 6\ell & \ell^2(2-2\gamma-\gamma^2) & -6\ell & \ell^2(4+2\gamma+\gamma^2) \end{bmatrix}$$

APPENDIX H

CONSTRUCTION OF MATRICES FOR THE BEARING ELEMENT AND THE BEARING SUSPENSION

The linearized hydrodynamic forces F_x can be written as

$$F_x = -(k_{xx}x + k_{xy}y + c_{xx}\dot{x} + c_{xy}\dot{y})$$

and similarly for F_y where F_x and F_y are dimensional in the present case. The forces F_x and F_y are assumed acting at a distance Z_c from the bearing left end. Then all the displacements and the velocities at $Z = Z_c$ are evaluated in terms of the shape functions N_i such that

$$N_i = N_i(Z)\Big|_{Z=Z_c} \quad , \quad i = 1,2,3,4$$

But since the coordinate x and y are given by

$x = X_j - X_b$ and $y = Y_j - Y_b$ with reference to Fig. 5.4

then $F_x = F_{Xj} - F_{Xb}$ and similarly for F_y.

Using the virtual work expressions (5.11) and displacing the resulting expressions to the left hand side of the element equations, one gets the stiffness term in the equation as

$$\left[[K_j]_{8x8} + [K_b]_{8x2}\right]\{q^e\} \qquad \text{(H.1)}$$

and similarly for the damping term.

The above expressions are composed of submatrices $[k_j]$ and $[k_b]$ such that

$$[k_j]_{2x2} \quad (\text{row } n, \text{ column } m) = N_n N_m [a_k]_{2x2} \quad , \quad n,m = 1,2,3,4$$

$$[k_b]_{2x2} \quad (\text{row } n) = -N_m [a_k]_{2x2} \quad ; \quad n = 1,2,3,4$$

where

$$[a_k] = \begin{bmatrix} k_{xx} & k_{xy} \\ k_{yx} & k_{yy} \end{bmatrix}$$

The equations for the bearing mass are given by

$$m_b \ddot{X}_b + c_b \dot{X}_b = k_b X_b = -(F_{Xj} - F_{Xb}) \quad , \text{ on the XZ plane}$$

and similarly for the YZ plane.

Again, using the virtual work expressions (5.11) for the forces on the right hand side and moving the resulting elements to the left hand side, one gets the term

$$[K_b]^T_{2x8} + [a_k] \begin{Bmatrix} X_b \\ Y_b \end{Bmatrix}$$

and similarly for the damping term.

It should be noted that the matrix $[K_b]$ is as given in expression (H.1), on the element side, whereas the transpose applies on the submatrices rather than on the individual elements. Also the column locations refer to the bearing element coordinates in the global assembly of the rotor-bearing system. The column locations of the submatrix $[a_k]$ above are also X_b and Y_b.

APPENDIX I

ROTOR RESPONSE TO UNBALANCE EXCITATION

Consider a coordinate system (e_r, e_t) fixed to the rotor. The unbalance force components in the X and Y direction, namely U_{nX} and U_{nY} respectively, can be specified in terms of the unbalance components in the coordinate system (e_r, e_t), which are U_{nr} and U_{nt}, as

$$U_{nX} = U_{nr} \cos \omega_{rt} - U_{nt} \sin \omega_{rt}$$

$$U_{nY} = U_{nr} \sin \omega_{rt} + U_{nt} \omega_{rt}$$

This transformation allows a simple introduction of the phase angle between mass unbalance at different axial locations. The forces in the principal coordinates are

$$\{U(t)\} = [\Psi]^T \{Q\}$$

which gives the individual relations

$$U_j = A_j^c \cos \omega_{rt} + A_j^s \sin \omega_{rt} \quad , \quad j = 1,2,\ldots,2N$$

where A_j^c and A_j^s are generally complex.

Carrying out the integration (5.40), the steady state response is

$$u_j = \frac{1}{M_j^*(\lambda_j^2+\omega_r^2)} \left[(\lambda_j A_j^c + \omega_r A_j^s)\cos \omega_{rt} + (-\omega_r A_j^c + \lambda_j A_j^s)\sin \omega_{rt}\right], \quad j = 1,2, \ldots, 2N$$

The response in the phase space coordinates $\bar{q}$ can then be obtained using equation (5.42).

APPENDIX J

EVALUATION OF THE SPECTRAL DENSITY OF THE INPUT UNBALANCE FORCES

The input force is a unit unbalance distributed over two nodes. Then considering the X and Y direction, the input force vector can be written as

$$\bar{f} = \frac{U_b}{2} (\cos \omega_{rt} \quad \sin \omega_{rt} \quad \cos \omega_{rt} \quad \sin \omega_{rt})^T$$

The spectral density matrix $[S_f(\omega)]$ can be evaluated from the Fourier transform of the correlation matrix $[R_f(\tau)]$. For example,

$$R_{f_1 f_1}(\tau) = E[f_1(t) f_1(t+\tau)] = \left(\frac{U_b}{2}\right)^2 \underset{T\to\infty}{\text{limit}} \frac{1}{2T} \int_{-T}^{T} \cos \omega_{rt} \cos \omega_{rt}(t+\tau)\, dt$$

$$= \frac{U_b^2}{8} \cos \omega_r \tau$$

Then the spectral density $S_{f_1 f_1}(\omega)$ is given by the Fourier

$$S_{f_1 f_1}(\omega) = \frac{1}{2\pi} \int_{-\infty}^{\infty} \frac{U_b^2}{8} \cos \omega_r \tau \exp(-i\omega\tau)\, d\omega$$

$$= \frac{U_b^2}{16} [\delta(\omega-\omega_r) + \delta(\omega+\omega_r)]$$

where $\delta(\cdot)$ refers to the Dirac delta function.

It can then be shown that the spectral density matrix of the input force vector $\bar{f}$ is given by:

$$[S_f(\omega)] = \frac{U_b^2}{16} \begin{bmatrix} \delta_1 & i\delta_2 & \delta_1 & -i\delta_2 \\ i\delta_2 & \delta_1 & i\delta_2 & \delta_1 \\ \delta_1 & -i\delta_2 & \delta_1 & -i\delta_2 \\ i\delta_2 & \delta_1 & i\delta_2 & \delta_1 \end{bmatrix}$$

where

$$\delta_1 = \delta(\omega - \omega_r) + \delta(\omega + \omega_r)$$

$$\delta_2 = \delta(\omega - \omega_r) - \delta(\omega + \omega_r)$$

and $i = \sqrt{-1}$

APPENDIX K

EVALUATION OF THE INPUT SPECTRAL DENSITY MATRIX OF THE GRINDING SPINDLE-WHEEL SYSTEM

The input force vector is $(f_{cX4}\ f_{cY4}\ f_{cX5}\ f_{cY5})^T$ where X,Y refer to the direction and 4,5 are the boundary nodes of the wheel element with reference to Fig. 6.2.

The spectral density matrix is evaluated starting from the correlation matrix $[R_f(\tau)]$. Consider the element $R_{X4,Y4}(\tau)$ in the correlation matrix which can be written as

$$R_{X4,Y4}(\tau) = E[f_{X4}(t)\ f_{Y4}(t+\tau)]$$

where E is the expectation or ensemble averaging operator. Then,

$$R_{X4,Y4}(\tau) = \frac{1}{4} \cos\beta_c \sin\beta_c\ E[f_c(t)\ f_c(t+\tau)]$$

$$= \frac{\sin 2\beta_c}{8}\ R_{f_c}(\tau)$$

where β_c is the angle of the cutting force f_c with the X-direction and $R_{f_c}(\tau)$ is the autocorrelation of the random cutting force f_c. The spectral density element $S_{X4,Y4}(\omega)$, in turn, is

$$S_{X4Y4} = \frac{\sin 2\beta_c}{8}\ S_{f_c}(\omega) = S_0 \frac{\sin 2\beta_c}{8}$$

For $\beta_c = \tan^{-1}(\frac{1}{2})$, the spectral density matrix $[S_f(\omega)]$ can be shown to be

$$[S_f(\omega)] = \frac{S_0}{20} \begin{bmatrix} 4 & 2 & 4 & 2 \\ 2 & 1 & 2 & 1 \\ 4 & 2 & 4 & 2 \\ 2 & 1 & 2 & 1 \end{bmatrix}$$